UNIVERSITY OF NOTTINGHAM

The University of
Nottingham

UNITED KINGDOM · CHINA · MALAYSIA

SCHOOL OF MATHEMATICAL SCIENCES

Transmission Lines, Quantum Graphs and Fluctuations on Complex Networks

Mubarack Ahmed

A thesis submitted to the University of Nottingham for the

degree of

DOCTOR OF PHILOSOPHY

DECEMBER 2020

I dedicate this thesis to Mum and Dad

and to my children

Abubakar Siddik, Zulaikha and Bashir

Abstract

High-frequency devices are commonplace and at their foundations often lie cable networks forming fundamental sub-systems with the primary role of transferring energy and information. With increasing demand for "more electric" systems, the emerging trends in Internet of Things (IoT), as well as the surge in global mobile data traffic, the complexities of the underlying networks become more challenging to model deterministically. In such scenarios, statistical approaches are best suited because it becomes daunting to accurately model details of such networks.

In this thesis, I present a quantum graph (QG) approach of modelling the transfer of energy and information through complex networks. In its own right, the graph model is used to predict the scattering spectrum in wired communications, as well as statistical predictions in wireless communication systems. I derive a more generalised vertex scattering matrix that takes into account cables of different characteristics connected at a common node. This is significant in real applications where different kinds of cables are connected. For example, in digital subscriber line (DSL) networks, the final loop drop may consist of cables with different characteristics.

The proposed graph model is successfully validated both with a Transmission Line (TL) approach, and with laboratory experiments. The model agrees well with the universal predictions of Random Matrix Theory (RMT).

In particular, the statistics of resonance is compared with the predictions of Weyl's law, while the level-spacing distribution is compared with the Wigner's surmise, which is a telltale signature of chaotic mixing of the underlying waves.

In addition, I propose an analogue of the so-called random coupling model (RCM), which is important in the study of electromagnetic waves propagating in chaotic cavities. To achieve this, I present a procedure for symmetrising the transfer operator, which we use to modify the QG model in order for it to be comparable to RCM. Unlike the RCM which depends on Gaussian random variables, the graph model works for both Gaussian and non-Gaussian statistics. We use the analogue model to investigate the impact of different boundary conditions on the distribution of energy in networks with different topologies and connectivities.

I further present a novel technique of using quantum graphs to predict the statistics of multi-antenna wireless communication systems. In this context, I present three different ways of calculating the probability density function of Shannon channel capacity. The analytical calculations compares favourably with numerical simulations of networks of varying complexities.

In the area of wired communications, the graph model is used to model the distribution of data in G.fast networks (the fourth-generation Digital Subscriber Line (DSL) networks), using realistic cable parameters from the so-called TNO-Ericsson model. In particular, we show that quantum graph formalism can be used to simulate the in-premises distribution network

at G.fast frequencies. The parameters of CAD55 (or B05a) cables and the in-house distribution network reported in the International Telecommunication Union documentation were used in the simulations.

ACKNOWLEDGEMENTS

CONTENTS

Contents

Contents

Contents

1

INTRODUCTION

In this chapter, we present the motivation and the problems we seek to address in this work. Since the central theme of this thesis is about modelling the propagation of microwaves in complex networks through the use of quantum graphs (QGs), we will review the literature on QGs and highlight some of the main achievements of previous studies.

1.1 MOTIVATION

High frequency cables commonly connect modern devices and sensors. Interestingly, the proportion of electrical components is rising fast in an attempt to achieve lighter, quieter and greener devices. Significant research has focused on this area, aimed at replacing hydraulics and mechanical linkages with electric components [1, 2]. There is an on-going paradigm shift from combustion chambers because of their negative impact on climate [3]. Alternative propulsion concepts have been proposed, but *distributed electric*

propulsion [4] is the most commonly accepted concept with a promising future. The "*all-electric*" and "*more-electric*" vehicles have become a household terminology in every department of our lives. This ranges from aeroplanes, cars, motorbikes, trams to flying cars. For example, UberAir was originally scheduled to be launched by the end of this year (i.e. 2020) in Los Angeles, USA [4]. A prototype has been out-doored in 2018 and it is shown in Figure 1. Although the initial schedule of 2020 has not been met (as the new schedule date is 2023 [5]), it will only be a matter of time when air taxis become commonplace.

Figure 1.: Uber's prototype flying car [4].

Currently, the aerospace industry is compelled to reduce its carbon emission levels by 2.6 billion metric tons under the *Carbon Offsetting and Reduction Scheme for International Aviation* [6]. As a result, GE Aviation's head of electrical power, Hao Huang, was awarded a certificate of honour in 2019 by IEEE for his role towards achieving cleaner airways through 'more electric' engines [6] and through a programme whose ultimate target is to

reduce each of their Boeing Dreamliners' weight by approximately 450 kg. Apart from the engines, airliners typically have two other non-electrical supplementary subsystems that augment the engines. The pneumatic system guides and propagates energy through compressed air to power the environmental control devices and the de-icing systems. On the other hand, the hydraulic system transmits energy through pressurised fluid to power the majority of the aerodynamic devices of aeroplanes. According to Huang, the idea is to replace these non-electrical systems as shown in Figure 2.
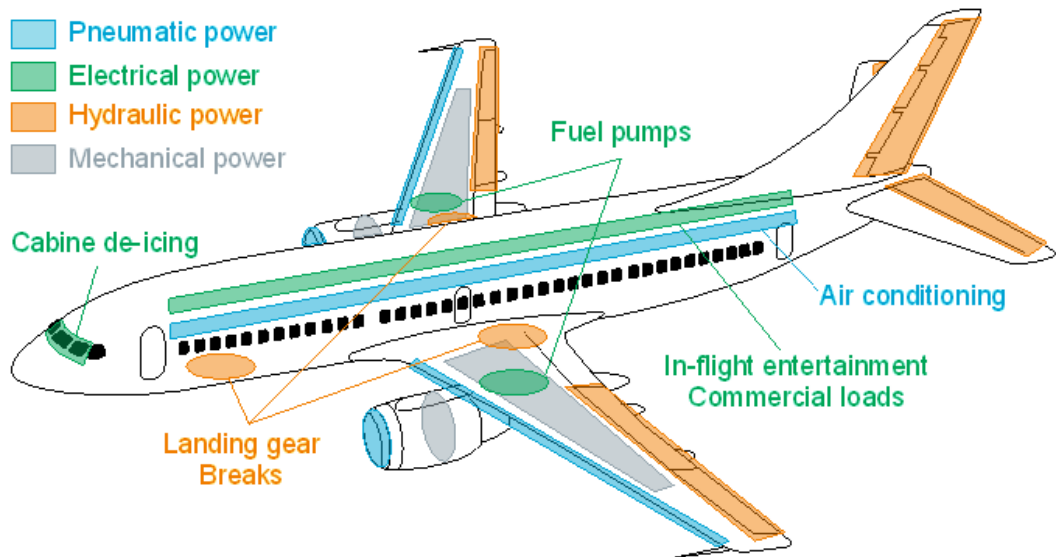
Figure 2.: Commercial airplane's architecture showing pneumatic, hydraulic and partly mechanically driven systems that needs to be changed and systems that are already electrical [7].

However, we are still at the *early adopters* stage of Rogers innovation adoption curve [8] as indicated by Plotz et al. [9]. For example, in electric vehicles, this is attributable to high life cycle cost [10–12] of the vehicles. There is therefore the need to drive the overall cost down. One way to achieve low

Rogers Adoption / Innovation Curve

Early Adopters · Early Majority · Late Majority

2,5% · 13,5% · 34% · 34% · 16%

Innovators · Laggards
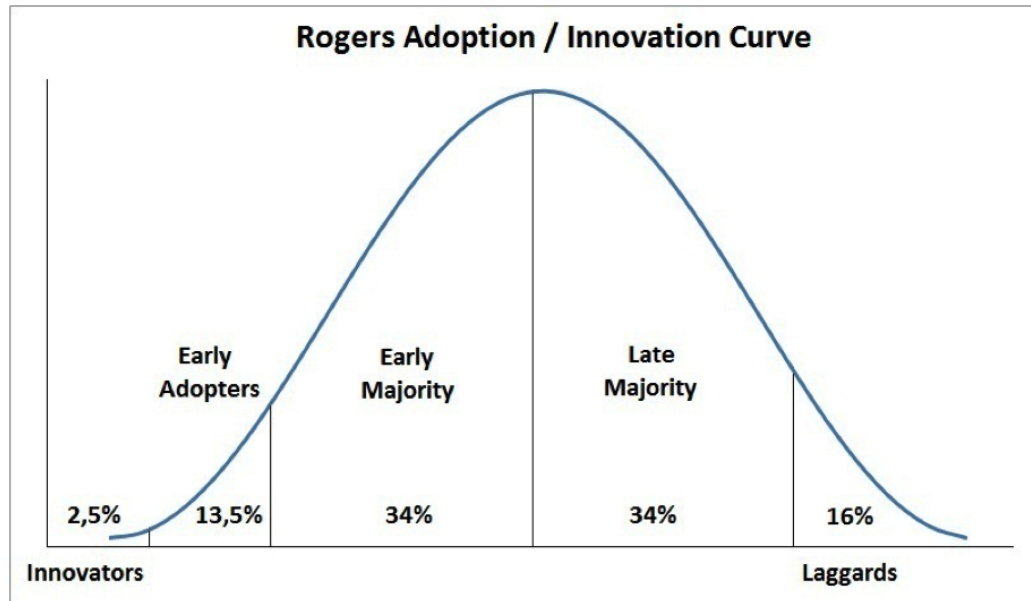
Figure 3.: Rogers innovation adoption curve [13].

cost electric components is to engage in further research to develop efficient cables and linkages. This will enable us to gain more insight into the way signals propagate through these cables. Direct laboratory experimentations with real cables are ideal; but they are often not the most cost-effective way during the initial stages of research. Scientists and industry players often do not want to commit significant amounts of resources (in terms of time and money) in laboratory measurements for the fear of 'exercise-in-futility'. Modelling has always been the way forward because of its ability to save time and cost.

Our second motivation for modelling signal propagation in cable networks is related to the so-called Digital Subscriber Line (DSL) communication networks. A DSL network uses copper cables as a channel to transmit data between the central office (CO) and subscribers (DSL end-users). DSL

technology is by far the most widely-used medium for broadband internet access, with more than 1 billion fixed broadband users worldwide [14]. Although the DSL access network has undergone step-by-step revolutions (driven largely by the need for high data rates transmission), the final loop drop (i.e. the network from the street cabinets to end-users) has remained a network of copper cables [15], with the International Telecommunication Union ITU-T G.9701 as the latest standard for the network [16]. The demand for higher data rates has necessitated the use of high frequency sub-carriers and wider bandwidth implementations.

For example, while the first, second, and third generations DSL networks utilise frequencies of up to 1.1 MHz, 2.2 MHz, and 30 MHz, respectively, the ITU-T G.9701 standard, under the working name G.fast (i.e. to denote fast access to DSL subscribers), uses up to 300 MHz with the aim of achieving data rates as high as 1 Gb/s [17]. Quantum graph theory will be used to model such networks, especially the in-premises data distribution networks of G.fast. In particular, we aim to analytically predict the channel capacity statistics of such networks using realistic, ITU-approved cable parameters.

Modelling the propagation of high frequency signals through cable networks is a real challenge. At low frequencies, accounts of lumped elements (resistors, inductors and capacitors) can be easily used to analyse the behaviour of signals because the electrical wavelengths are assumed to be large compared to the physical dimensions of the network. However, when frequencies rise, the lump-element circuitry assumptions no longer hold be-

cause the circuit attributes are not *concentrated* - but rather *distributed* - into ideal elements. Since a significant number of recent applications in communications require high frequency regimes [18–22], there is the need for appropriate techniques to deal with current trends. Distributed-parameter (infinite-dimensional systems) networks like the transmission lines (TL) has been used in that regard. The method is named "*distributed*" because attributes of the circuits like inductance, resistance, and capacitance are no longer concentrated at a single point on the circuits.

Transmission line models have been used in applications ranging from coaxial cables, strip lines, wave guides, to optical fibres [19, 23, 24]. However the method usually requires the use of impedance, admittance or the so-called ABCD matrices which are very difficult to obtain at high frequencies. This is because the measurement of such parameters require ideal conditions, where the network has to be terminated in open or short circuit. Additionally, TL modelling becomes extremely difficult to use when the topology of the underlying network increases in complexity. For example, it will be extremely difficult to use the TL theory to model the reflection or transmission spectrum of the cable network illustrated in Figure 4 (a). The figure is an illustration of fully-connected graph with 10 vertices (also known as the K10 network).

However, at high frequencies, one can measure power with high reliability and accuracy. The scattering matrix is therefore an ideal approach to overcome this difficulty [25, 26]. One way of achieving this is through quan-

tum graph (QG) formalism, which is the central theme of this research. In addition, QG modelling goes round the problem of complexity in topology by breaking down the underlying network into simple Vertex Scattering Matrices (VSM) and aggregating the VSM in an elegant way to form the graph scattering matrix. This way, the topological complexity of the underlying network does not affect the ability of the graph framework to be used in modelling such networks.

Fortunately, in laboratories, the amplitude and phase characteristics of microwave devices may be measured using an instrument called a *Vector Network Analyser* (VNA). Figure 4 (b) shows a picture of a typical VNA. With this instrument, we can validate the QG approach of modelling the propagation of microwaves in these complex networks. The theory of Quantum graphs, and how to use them to model propagating microwaves are presented in Chapters 3 and 4 respectively. The usage of the VNA is presented later in Chapter 5, where we discuss the experimental measurements and results used in validating the QG approach.

Although these underlying cable networks in electrical systems are mostly deterministic by nature, the continuous increase in the density of cables of such systems makes it numerically expensive to solve deterministically. Additionally, the advent of the Internet of Things (IoTs) has also introduced similar challenges in the area of wireless communications [28–30]. As the number of connected devices in IoTs increases, deterministically modelling the details of propagation of electromagnetic waves in such wireless sys-

(a)   (b)
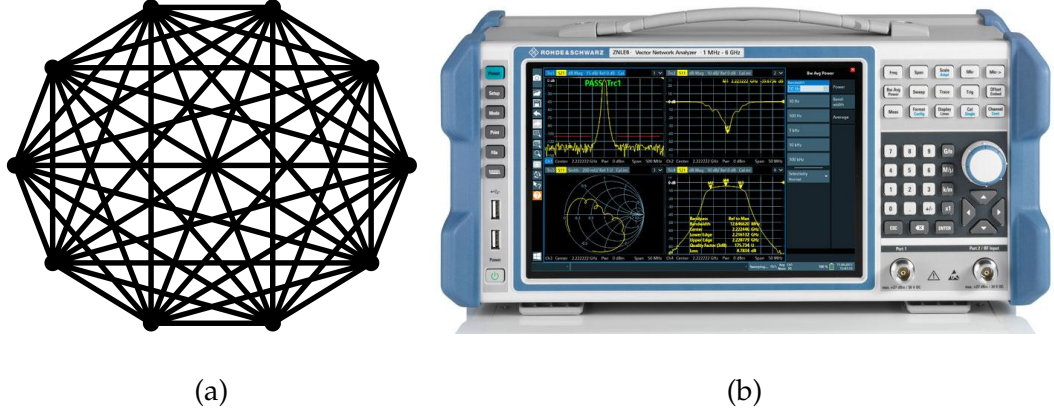
Figure 4.: (a) is an example of a fully-connected cable network with 10 ver-
tices (K10 network). The reflection spectrum of the graph is ex-
tremely difficult to model using TLM. (b) is a picture example of
a Vector network analyser for measuring the reflection spectrum
of cable networks [27].

tems is often inaccurate. This is because, at high frequencies, small changes
in the location and/or geometry of connected devices result in a signifi-
cant change in the electromagnetic field distribution within the underlying
system. Statistical approaches are therefore employed to overcome such
challenges [31].

The Random Coupling Model (RCM) is one such statistical approach
[32–34]. The RCM effectively uses an impedance method to model the
propagation of electromagnetic waves in irregular cavities coupled to ei-
ther single [33] or multiple [34] channels. It has since attracted attention of
several researchers that contributed to the model both theoretically [35] and
experimentally [31, 36, 37]. For example, in [35], the effect of electromag-
netic induction on electronic components inside large wave-chaotic cavities

has been studied, while [31] experimentally examined the effectiveness of wave coupling of radio frequencies on partially shielded large electronic components. There is also a comprehensive review by Gradoni et al. [38] on RCM, where the relationship between RCM and other electromagnetic formulations has been thoroughly discussed. These include areas such as optical communications and acoustics.

Although RCM was formulated to study the properties of chaotic cavities, which are wireless systems by nature, we propose an analogue of RCM, which is suitable for modelling both wireless and wired communication channels. In Chapters 6 and 7, we discuss the applications of this analogue model to calculate the statistics of wireless communication channels. Similarly, the applications to wired communications is treated subsequently in Chapter 8, where we analytically predict the distribution of data rates in DSL networks.

1.2 LITERATURE REVIEW

The idea of quantum graphs is well established. It has been used to model a variety of systems including propagation of waves of different kinds (acoustic, electromagnetic, etc.) and in complex structures (cars, aeroplanes, PC system units, etc.) [39–44]. Quantum graphs in general have been used to model ideal (i.e. lossless) networks where the width of the wire is assumed to be negligible [45] compared to all other lengths of the system. A signif-

icant number of applications has already been achieved [46–62]. We begin with a brief history of quantum graphs, and what have been the achieved over the years.

The journey was started by Pauling in 1936 when he used quantum graphs to model organic molecules (benzene and other aromatic hydrocarbons) [46]. Organic molecules consist of atoms that are connected together by idealised paths (referred to as bonds in this case) along which the so-called p_z electrons move according to one-dimensional Schrödinger equation [39, 40, 45, 46].

The idea behind his work was further developed by Kuhn a decade later [47]. By 1972, the idea has generated significant interest with diverse applications from the worlds of both theoretical and experimental physics [49–53]. For example in [49], Platt studied the classification of π-orbitals in condensed aromatic systems. The works of Ruedenberg and Scherr [50] in 1953, concentrated on the network model for free electrons. They focused on the "limiting case of a three dimensional quantum-mechanical treatment of the π-electrons" where they derived the boundary conditions for the free end points of the network. This idea was extended to apply to metals in research conducted by Coulson [51] a year later.

In the early 1970s , Montroll [52] generalised the network model to include both the *tight binding* and the *free-electron* models. Richardson and Balazs [53] showed how to calculate the secular equation for all periodic lattices. The next decade (in the 1980s) saw further remarkable advances in

quantum graph applications. Alexander [54] showed a difference equation method which is applicable to the Schrödinger equation. This is very important as we will use the Schrödinger operator on QGs quite extensively in this thesis during the modelling stage in chapters 3 and 4. There was a numerical study of propagating waves in networks of waveguides [55] in 1987 and in 1988, the works of Chalker and Coddington [56] introduces the famous Anderson localisation model to QGs.

In the late 1990s to early 2000s, there was a surge of interest in quantum graphs [39–42, 45, 58–61, 63–99], but I find the works of Kottos et al. from 1997 to 2003 [40, 41, 45, 59, 60] by far the most relevant works related to this research. Those papers generally studied the chaotic (or pseudo-chaotic) scattering in quantum graphs, which is the focal point in this research. In [45] for example, two main ways of quantizing graphs have been presented. Such methods will be employed to derive two secular equations and a justification of our choice will be provided in Section 3.3.4. In addition, the magnetic terms were assumed to be zero so that time reversal symmetry (TRS) is maintained. This research also deals with systems that maintains TRS. Finally, the types of graphs treated in all the afore mentioned papers are *simple* and *connected* graphs.

There are other publications with direct relevance to this research. For instance, in Barra's work [68, 69], a closed expression for level spacing distribution for graphs with Dirichlet boundary condition was derived. In both publications, only systems with no magnetic fields terms were consid-

ered, which falls in line with one of the assumptions made in this research. Tanner conjectured in [84] (proven by [64]) that the spectral statistics of an ensemble of unitary stochastic processes on graphs largely depends of the spectral gap. The conjecture is based on condition that the spectral gap $\Delta_g = \max(1 - |\lambda_b|)$ is either constant or varies slower than $1/2B$, where B is the total number of bonds in the underlying quantum graph, and $\lambda_b < \lambda_1$ is a non-principal eigenvalue for any $b \in \{2, 3, \cdots, B\}$, such that $\lambda_1 = 1$ is the principal eigenvalue.

Some other studies also considered quantum graphs with leads attached [60, 61, 69, 75, 100–102] from which I draw insight when I discuss systems with coupled leads. From the coupling-of-leads scenario, the scattering matrix, which helps in spectral analysis discussed in later chapters, is constructed. Several papers [41, 65, 66, 78–80, 98, 103] were also published which concentrated only on spectral analysis of the underlying graph system. Some of them used direct methods while others used the inverse problem approach.

One can find exact expressions for both the vertex scattering matrix and the trace formulae that establishes the link between the quantum graph spectral statistics and the predictions of random matrix theory (RMT). Similar results were reported in a comprehensive review by Gnutzmann [39] in 2006, while the works of Pluha et. al [104] conjectured a universal description of chaotic scattering, and applications of RMT predictions in the transmission channels of communication networks [105, 106]. Relevant portions of RMT

predictions will be highlighted when they are needed in subsequent chapters.

The story of QGs will not be complete without mentioning some of the recent works in the field. For example, in [107, 108], the scattering problem of high-speed radiation pulses on complex targets was modelled. In particular, they studied the probability distribution of delay-time in such scattering systems. According to their definition, delay-time was defined as "the difference between the time it would take the scattered particle (or wave) to transit through the domain of interaction and the time of transit when the interactions is switched off." Interestingly, they derived an expression of the mean delay-time that unifies the quantum expressions obtained by Wigner [109] and Smith [110] in one hand, and the expression obtained in classical mechanics on the other. In [111], Brewer et al. have used elastic graphs to study the dynamics on networks of beams (or plates), which support different modes propagating at different velocities within the same structure.

Finally, the work of Drinko in [112] investigated how quantum graphs may be used to model quantum devices such as filters. I envisaged their approach may be applied in a fairly new area in telecommunications [20–22, 113, 114], where metamaterials may be used as reconfigurable intelligent surfaces (RIS). This will be discussed as a future outlook. Although the use of quantum graphs in terms of RIS-aided communication does not feature in the current thesis, it may be a good idea for future research.

Since this literature review is meant to be brief, the following review papers are a good starting point for someone interested in the study of quantum graphs [39, 44, 74, 89, 115].

1.3 OPEN QUESTIONS AND CONTRIBUTION TO BODY OF KNOWLEDGE

In most works reported in literature so far, the assumption is that the underlying graph networks are uniform with equal characteristic impedances and propagation constants across the entire network. We will drop that assumption and derive a general scattering formula for quantum graphs with different cables forming different segments of the network. This scenario finds applications in DSL networks (DSL applications are treated in Chapter 8), where the final loop drop (i.e. the cables from the street cabinets to homes) may not necessarily be uniform [16]. This will mean that the cables in the networks need not be of same characteristics, but are allowed to vary.

In addition, we are going to study systems with losses, unlike in most previous work where the systems are assumed to be lossless. We will introduce a parameter that quantifies the losses in the underlying systems, and the impact of such a parameter on communication channel statistics. This is important because realistic systems significantly deviate from idealised assumptions and are inherently lossy. The loss parameter and its effects on channel statistics are described in Chapters 6 and 7.

Furthermore, we will establish a novel framework (under quantum graphs) of modelling open systems, where the amount of losses can be controlled without violating the vertex unitary conditions. This is important in modelling random media whose characteristics can be adequately compared with the predictions of random matrix theory. The quasi-closed system so constructed will be 'closed' enough to exhibit all the necessary chaotic behaviours predictable under RMT predictions, yet open enough to communicate to other systems through coupling of leads.

The problem of scattering from networks of cables can also provide an analogue model for wireless communication in highly reverberant environments. In this context we provide analysis of the statistics of communication capacity for communication across cable networks. We specialise this analysis in particular for the case of Multiple-Input Single-Output (SIMO or MISO) protocols. To the best of our knowledge, this is the first time such a connection has been established.

1.4 STATEMENT OF PURPOSES

The goals of this thesis are to:

- develop the idea of MISO/SIMO wired networks and analyse their associated data rate performance;

- show how the scattering problem from network of cables can be used as an analogue model (to the so-called random coupling model) for wireless communications;

- directly compare the predictions of the graph model, in terms of scattering response, with experimental measurements;

- apply the graph model in the digital subscriber line (DSL) networks

1.5 THESIS OUTLINE

Chapter 2 deals with the theory of transmission lines (TL). There are two reasons for discussing the fundamentals of TL theory. First, it is to provide the reader with the explanation of basic concepts in TL Modelling. This is important because the information in that chapter will be used to numerically validate the QG Model (to be discussed in Chapter 4) which is central to this thesis. In addition, the derivation of the wave equations from first principle, starting from the lumped-element circuitry and working all the way through Telegrapher's equations will be discussed here. Secondly, the basic understanding of TL theory will be essential to understanding how cable characteristics are measured. This will become apparent in Chapter 5, when we discuss laboratory measurements and how the characteristics of the cables involved are modelled, and under Section 8.3 of Chapter 8, where we treat DSL networks and how their cables are modelled.

In Chapter 3 we deal with the theory of quantum graphs. First, the discussion of basic definitions and terminologies regarding quantum graphs are presented. This will be followed by the presentation of how Schrödinger operator acts on graphs, and the discussions of the types of boundary conditions that may apply on graph vertices. Two secular equations will then be derived and their advantages and disadvantage compared and contrasted. We will then make a choice of secular equation to be used in this research based on the advantages and disadvantages. There will be a separate section where a generalised expression of Vertex Scattering Matrix (VSM) will be derived. This will be a novel expression of VSM which unifies all previously reported VSM by dropping some previous assumptions.

Chapter 4 presents the mathematical derivation of the quantum graph model, starting from the wave equations derived in Chapter 2. The physical interpretation of the model will be presented, while the derived model is modified to serve as an analogue of the so-called random coupling model [38, 116]. In the same chapter, the TL model and the QG model will be numerically compared in terms of reflections spectra, using graph topologies that are simple enough to be solved under TLM, but complex enough to reveal the necessary complexities of the scattering response over a wide range of frequencies. Additionally, losses in graph systems is discussed, and a formulation of open systems that minimise system losses will be introduced.

After the numerical validation, Chapter 5 is based on laboratory measurements of real cables of varying topologies. The system set-up and the

measurement procedures are outlined. The experimental results forms a second layer of validation of QG model.

In Chapters 6 and 7, the graph model is applied to wireless communication channels in reverberant environments. The existence of multiple random reflections and transmissions of signals through these types of environments make it difficult to use deterministic approaches to solve the scattering problem. Statistical methods in these situations have been proven to be effective [35, 38], where the electromagnetic field quantities are represented by random variables. In this chapter, the graph model is compared to RMT predictions.

Unlike Chapters 6 and 7, which focused on applications in wireless communication, Chapter 8 presents an application of quantum graphs in wired networks. In particular Chapter 8 model wave propagation in DSL networks, using recommended ITU cable parameters and network topologies [16]. Finally, the concluding chapter contains the summary of what this research has achieved, and the future outlook. This is presented in Chapter 9.

2

TRANSMISSION LINES

2.1 INTRODUCTION

This chapter presents an overview of transmission line theory. The wave equation will be derived from first principles beginning with basic circuit theories through to the Telegrapher's equations. The TL modelling is an impedance-based modelling of the propagation of high frequency waves. As mentioned in Chapter 1, there are limitations to the usage of TL model. The main idea here is to use the TL model to numerically validate the QG method using cable networks of simple topologies. Such networks will be formed by cascading several simple T-junction network so that the overall network could still be modelled using TL model. This is discussed in details in Section 4.4, where we numerically compare the predictions of TL and QG models in terms of reflection spectrum.
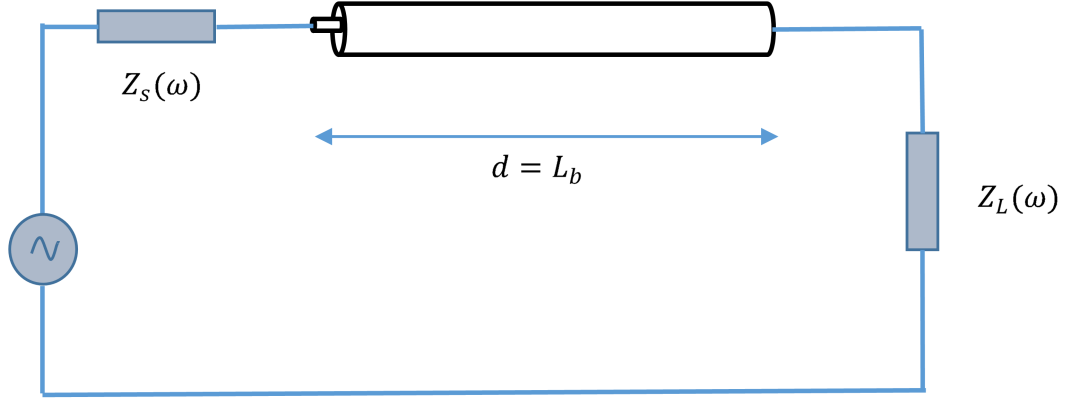
Figure 5.: Uniform TL of length d.

2.2 THE WAVE EQUATIONS

Figure 5 shows a transmission line of length $d = L_b$ with frequency-dependent internal source and load impedances Z_s and Z_L, respectively. The transmission line could be a coaxial cable or any suitable line as mentioned in the introductory chapter. Coaxial cables are used here because it feeds directly into what is investigated in this research, and the theory remains the same regardless of the medium of transmission.

An infinitesimal segment Δx from the transmission line, which can be schematically drawn as a two-wire line to represent the two parallel conductors in the line [18]. The segment is normally modelled as a lumped-element circuit [18, 19, 23, 26] as seen in Figure 6. Here, the cable characteristics R,L,G and C are the primary per unit length parameters of the TL, where they represent the *resistance, inductance, conductance* and *capacitance* of the cables respectively. The voltage V and the current I are both depen-
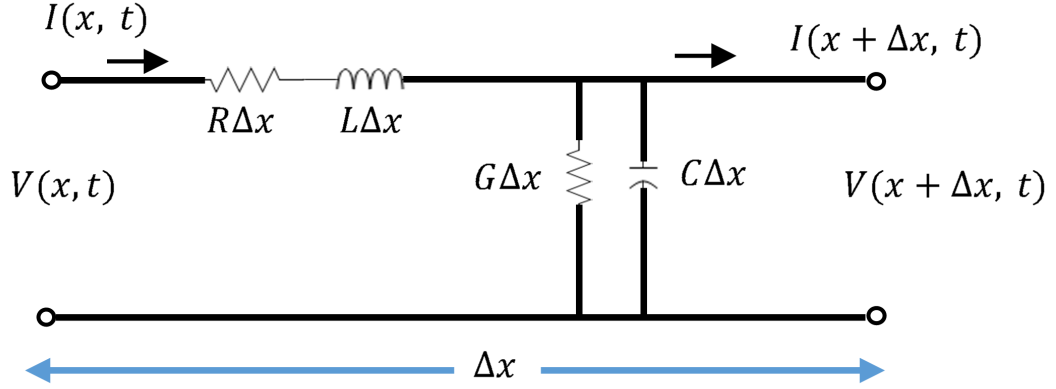
Figure 6.: General model of an infinitesimal segment of TL.

dent on position x and time t. The initial voltage applied from the left hand side across the segment is denoted by $V(x,t)$, while the final voltage experienced at the right hand side is $V(x+\Delta x,t)$. The famous Telegrapher's equations [18,19,23,26] could be derived by applying Kirchoff's laws.

Applying Kirchoff's law on voltages, we can write

$$V(x,t) - I(x,t)R\Delta x - \frac{\delta I(x,t)}{\delta t}L\Delta x - V(x+\Delta x,t) = 0, \qquad (1)$$

where $I(x,t)$ is the current associated with $V(x,t)$. In addition, a second equation can also be written from Figure 6 using Kirchoff's law on currents in a similar fashion. This is given by

$$I(x,t) - V(x+\Delta x,t)G\Delta x - \frac{\delta V(x+\Delta x,t)}{\delta t}C\Delta x - I(x+\Delta x,t) = 0, \qquad (2)$$

where $I(x+\Delta x,t)$ is the current at a distance Δx from $I(x,t)$. Rearranging (1) and (2) and dividing through both equations by Δx and allowing Δx to approach zero, we get the following two equations

$$\lim_{\Delta x \to 0} \frac{V(x,t) - V(x+\Delta x,t)}{\Delta x} = \lim_{\Delta x \to 0} \left[I(x,t)R + \frac{\delta I(x,t)}{\delta t}L \right] \qquad (3)$$

and

$$\lim_{\Delta x \to 0} \frac{I(x,t) - I(x + \Delta x, t)}{\Delta x} = \lim_{\Delta x \to 0} \left[V(x + \Delta x, t)G + \frac{\delta V(x + \Delta x, t)}{\delta t}C \right]. \quad (4)$$

Equations (3) and (4) could be written as

$$-\frac{\delta V(x,t)}{\delta x} = I(x,t)R + \frac{\delta I(x,t)}{\delta t}L \quad (5)$$

and

$$-\frac{\delta I(x,t)}{\delta x} = V(x,t)G + \frac{\delta V(x,t)}{\delta t}C \quad (6)$$

respectively.

In phasor forms, the voltage and current may be written as [18]

$$V(x,t) = \Re\left[V(x)e^{j\omega t} \right] \quad (7)$$

and

$$I(x,t) = \Re\left[I(x)e^{j\omega t} \right], \quad (8)$$

where ω is the angular frequency of the signal which can be written in terms of linear frequency f as $\omega = 2\pi f$ and $j = \sqrt{-1}$. Differentiating (7) with respect to x and (8) with respect to t, gives

$$\frac{\delta V(x,t)}{\delta x} = \Re\left[\frac{dV(x)}{dx}e^{j\omega t} \right] \quad (9)$$

and

$$\frac{\delta I(x,t)}{\delta t} = \Re\left[j\omega I(x)e^{j\omega t} \right], \quad (10)$$

respectively. The full derivative in (9) resulted from the fact that the voltage amplitude $V(x)$ depends only on x. Substituting (8), (9) and (10) into (5) and simplifying, one retrieves the first Telegrapher's equation as

$$\frac{dV(x)}{dx} = -ZI(x), \quad (11)$$

where the impedance $Z = R + j\omega L$. Similarly, the second Telegrapher's equation is obtained by differentiating (7) with respect to t and (8) with respect to x and performing similar substitution and simplification to arrive at

$$\frac{\mathrm{d}I(x)}{\mathrm{d}x} = -YV(x), \tag{12}$$

where the admittance $Y = G + j\omega C$. Equations (11) and (12) are the two fundamental equations governing TL theory from which one can derive the wave equations. In Section 5.2, we will discuss how the Telegrapher's equations can be used to calculate the cable characteristics (i.e. R,L,G and C) of a given coaxial cable, and use the values of the cable characteristics to validate our QG model (QG model will be derived in chapter 4).

For now, we proceed to derive the wave equations as follows. From (11),

$$I(x) = -\frac{1}{Z}\frac{\mathrm{d}V(x)}{\mathrm{d}x}, \tag{13}$$

and

$$\frac{\mathrm{d}^2V(x)}{\mathrm{d}x^2} = -Z\frac{\mathrm{d}I(x)}{\mathrm{d}x}. \tag{14}$$

Substituting (12) into (14) and rearranging gives the wave equation as

$$\frac{\mathrm{d}^2V(x)}{\mathrm{d}x^2} - YZV(x) = 0, \tag{15}$$

whose general solution in terms of progressive and regressive propagating voltage waves is given by

$$V(x) = V^+\mathrm{e}^{\kappa x} + V^-\mathrm{e}^{-\kappa x}, \tag{16}$$

where the frequency-dependent complex propagation constant

$$\kappa = \sqrt{YZ}$$

$$= \sqrt{(R + j\omega L)(G + j\omega C)} \qquad (17)$$

$$= \alpha_\kappa + j\beta_\kappa$$

Here, α_κ represents the attenuation constant (i.e. a measure of how a propagating wave is damped.), while β_k is the phase constant. Amplitudes of the outgoing and incoming voltages are represented by V^+ and V^- respectively. The purpose of the subscript in α_κ is to differentiate this attenuation constant with another loss parameter α that will be discussed in Chapter 4. Again, the propagation constant κ as defined here must not be confused with the k in Chapters 3 and 4. We will clarify whenever there is a possibility of confusion in subsequent chapters.

2.3 TRANSMISSION LINE MODEL

In this section we show how to model the complex-valued reflection spectrum S_{11} of a cable network, using TL modelling. Figure 7 illustrates a cable network consisting of a cascade of T-junction networks, where n is the number of vertices in the cable network, and L_b is the length of cable b. The reflection spectrum of these types of networks are simple enough to be handled by TL model. As mentioned in the introductory chapter, graphs with more complex topologies may not be amenable to TL modelling. The goal here is to give an example of a graph that is simple enough to be handled by
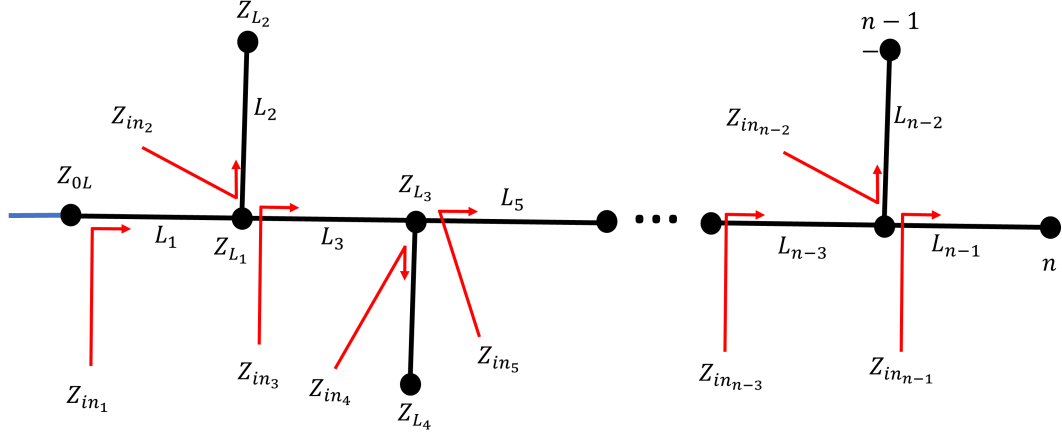
Figure 7.: TL Model.

TL modelling so we could compare it with quantum graph model (quantum graph model is treated in Chapter 4).

We denote the input and load impedances of bond b by Z_{in_b} (as indicated by the red arrows in Figure 7) and Z_{L_b}, respectively. The blue cable represents the lead connected to a VNA. If the reference plane is moved to the point where the lead connects to the rest of the cable network, then [18]

$$S_{11} = \frac{Z_{in_1} - Z_{0L}}{Z_{in_1} + Z_{0L}}, \tag{18}$$

where Z_{0L} is the load impedance at the point of connection, calculated by looking at the VNA (on the left of Figure 7) at that point. For a perfectly matched systems, $Z_{0L} = Z_{0b}$, where Z_{0b} is the characteristic impedance of cable b in the network. Since all cables in the network are uniform in this example, $Z_{0b} = Z_0$. Most commonly used coaxial cables have $Z_0 = 50\ \Omega$. Also, the input impedance of the VNA is $50\ \Omega$.

In addition to (18), it is easy to show that

$$Z_{in_b} = Z_{0b} \frac{Z_{L_b} + Z_{0b} \tanh(\kappa_b L_b)}{Z_{0b} + Z_{L_b} \tanh(\kappa_b L_b)}. \tag{19}$$

A detailed proof of (19) can be found in [18]. Furthermore, if we consider the first T-junction in Figure 7, then Z_{L_1} is equal to the parallel combination of Z_{in_2} and Z_{in_3} and so

$$Z_{L_1} = \frac{Z_{in_2} Z_{in_3}}{Z_{in_2} + Z_{in_3}}. \tag{20}$$

Generally, the load impedance on cable b may be written as

$$Z_{L_b} = \frac{Z_{in_{b+1}} Z_{in_{b+2}}}{Z_{in_{b+1}} + Z_{in_{b+2}}}. \tag{21}$$

Therefore S_{11} can be calculated by cascading the results of parallel combinations of $Z_{in_{b+1}}$ and $Z_{in_{b+2}}$ from the last T-junction up to Z_{L_1}, while accounting for the phase shifts between Z_{in_b} and Z_{L_b} for any arbitrary cable b in the network. Subsequently, (19) is used to find Z_{in_1} by noting that $b = 1$. Finally, the reflection coefficient S_{11} is calculated using (18).

As an example, Figures 8(a) and (b) show the S_{11} spectrum of a single T-junction and a cascade of two T-junctions cable networks respectively. All the cables in (a) have equal lengths (1 m each), while the lengths in (b) are incommensurate. From left to right of the inset in (b), the lengths are given by $1/(5\pi)$ m, $\sqrt{3}/5$ m, $(\sqrt{5}+3\sqrt{6})/9$ m, $\pi/10$ m and $1/\sqrt{2}$ m, respectively. Unlike Figure 8(a), the lengths in Figure 8(b) are linearly independent, and are therefore expected the have an aperiodic resonances. The blue cable in inset of each figure denotes the leads that are assumed to be connected to a VNA, and the reference plane where the S_{11} values are calculated is at the point of connection between the lead and the rest of the cable network.

(a)   (b)
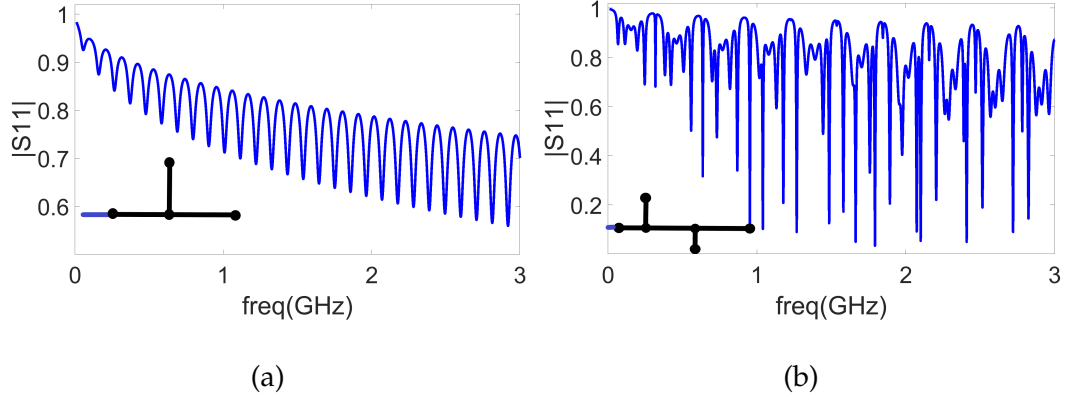
Figure 8.: The $|S_{11}|$ response across frequency range $0 - 3$ GHz of a (a) single T-junction and (b) a cascade of two T-junctions cable networks. In (a), each cable has a length of 1 m, while the incommensurate lengths (in metres) of cables in (b) are $1/(5\pi)$, $\sqrt{3}/5$, $(\sqrt{5} + 3\sqrt{6})/9$, $\pi/10$ and $1/\sqrt{2}$.

In chapter 4, the predictions of the transmission line approach will be compared with the quantum graph approach as a way of validating the graph model.

2.4 CONCLUSION

We have derived the two Telegrapher's equations and specialised them to coaxial cables from first principles. The Telegrapher's equations are the fundamental equations in transmission line modelling. We have used the two equations to derive the equations governing the propagations of microwaves in cable networks.

Finally, we have shown how to use the transmission line modelling to predict the reflection spectrum of microwave networks. In particular, we have calculated the S_{11} of a cascade of T-junction networks and given the numerical calculations of two examples. This calculations will be compared with the predictions of quantum graph modelling, which will be discussed in chapter 4. Before then, the next chapter discusses the background theory of quantum graphs, which serves as the preamble to chapter 4.

3

QUANTUM GRAPH THEORY

3.1 INTRODUCTION

Quantum Graph (QG) theory has been established as a successful paradigm for studying complex scattering problems [39–41, 45, 59, 60, 107, 108]. This chapter presents a summary of the theoretical background of quantum graphs (QGs), which are fundamental to the understanding of this thesis. Other theories and definitions that are not directly related to this thesis are not presented here. For a more in-depth study of quantum graphs, the reader is referred to a review paper on QGs by Gnutzmann and Smilansky [39].

The rest of the chapter is organised as follows. In Section 3.2, we discuss basic definitions and terminologies that are used in the field of quantum graphs and are directly relevant to this research. Also, all graphs treated in this thesis will be categorised in Section 3.2 according to a connectivity index γ. Section 3.3 presents the theoretical backgrounds of quantum graphs,

where the action of the Laplacian on graphs is introduced. This is followed by treating the various boundary conditions and the corresponding expressions for the vertex scattering matrices as used in this research and can be found in Section 3.3.2. In Section 3.3.3, we generalise the calculations of the vertex scattering matrix to include non-uniform bonds. For the purpose of spectral analysis of quantum graphs, two spectral functions are derived and compared in Section 3.3.4, and our choice is justified. The chapter conclusion is presented in Section 3.4.

3.2 DEFINITIONS AND TERMINOLOGIES

A graph $\mathcal{G}(n, B)$ is defined as a linear, network-shaped structure endowed with a differential operator and consisting of a number of bonds B and vertices n [42]. The number of vertices n is also known as the *order* of the graph. A bond may be specified completely by the pair of vertices (i, j) it connects. If the bonds are directed, then the direction of propagation of waves along the bond must be specified. Under such circumstance, each bond is counted twice [44].

For example, bond (i, j) starts from vertex i to vertex j, and it is different from the reverse bond (j, i). We take the positive direction to be from $\min(i, j)$ to $\max(i, j)$, while the negative direction is the reverse from $\max(i, j)$ to $\min(i, j)$. Loops are formed when $i = j$. In general, multiple bonds may connect a pair of vertices, but in this thesis each unique ordered

pair of vertices is connected by a single bond. Furthermore, unless other-wise stated, all bonds in this research are undirected and one does not need to specify the direction of propagation on each bond.

Graphs drawn in a two-dimensional plane are not necessarily embedded in the plane. Two or more bonds crossing one another at points other than vertices are ignored and assumed not to be touching one another [39, 42]. That is, the fact that two bonds crosses each other does not mean they create a vertex at the crossing point. Figure 9(a) shows an example of a graph with $V = 5$ and $B = 10$, while (b) shows a graph with $V = 10$ and $B = 45$. It is important to note that the centre of the graph in (b) does not constitute a vertex. We refer to these types of graphs as *non-planar* because they are not embedded in 2D plane. Unless otherwise stated, all graphs treated in thesis are non-planar.

An $n \times n$ square matrix is used to describe the topology of a graph as follows [39]:

$$C_{ij} = \begin{cases} m & \text{if } i \neq j \text{ where } i \text{ and } j \text{ are connected by } m \text{ bonds} \\ 2m & \text{if } i = j \text{ and there are } m \text{ loops at vertex } i \\ 0 & \text{if } i \text{ and } j \text{ are not connected} \end{cases} \tag{22}$$

The matrix as described in (22) is called *connectivity matrix* or *adjacency ma-trix*, and we shall use both nomenclature interchangeably. This thesis fo-cuses on *simple* graphs, where each unique pair of vertices (i, j) is connected

(a)   (b)
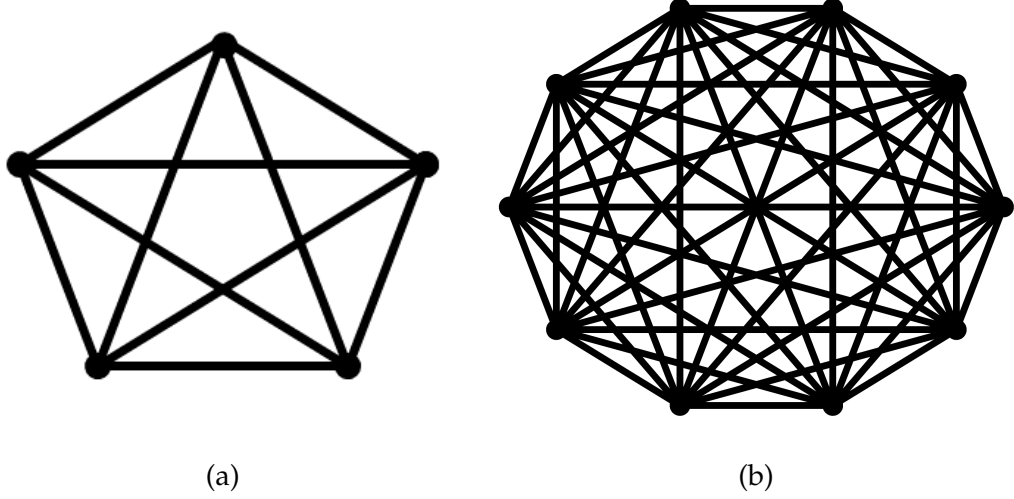
Figure 9.: Examples of graphs consisting of bonds and vertices. In graph (a) there are 5 vertices and 10 bonds, while graph (b) consists of 10 vertices and 45 bonds. Note that the centre of the graph in (b) does not constitute a vertex.

by at most one bond, and no vertex is connected to itself. In such simple graphs, the elements of the connectivity matrix C_{ij} are defined by

$$C_{ij} = \begin{cases} 1 & \text{if } i \text{ and } j \text{ are connected} \\ 0 & \text{if } i \text{ and } j \text{ are not connected} \end{cases} . \tag{23}$$

Let E_i denote the set of all bonds arriving at vertex i, then the *valency* (or *degree*) v_i of vertex i is defined as the cardinality ($|E_i|$) of E_i. This may also be written in terms of the connectivity matrix as

$$v_i = |E_i| = \sum_{j=1}^{V} C_{ij}, \tag{24}$$

while the number of bonds in the whole graph, B is written as

$$B = \frac{1}{2} \sum_{i=1}^{V} \sum_{j=1}^{V} C_{ij}. \tag{25}$$

A vertex with zero valency is an *isolated vertex*. If the valency of each vertex in a graph is v, then the graph said to be a $v-regular$. For example, Figure 9(a) is a $4-regular$ graph, while Figure 9(b) is a $9-regular$ graph. If $v = n - 1$ in a $v-regular$, then the graph is said to be *complete*. By *complete* graph, we mean any graph where each vertex is connected to all other vertices of the graph. Again, Figure 9(a) and (b) are complete graphs of orders 5 and 10 respectively. In this thesis, we will represent such complete graphs by Kn, where n is the order of the graph. Examples of a K5 and K10 are shown in Figure 9.

A graph $\mathcal{G}(n, B)$ is said to be a metric graph if, to each bond b, there exists a positive length L_b assigned to it [42,43]. A function defined on a graph $\mathcal{G}$ is a collection of functions on individual bonds which make the graph. The *neighbourhood* $\Gamma(i)$ of a vertex i, is the set of all vertices connected to i. The boundary $\Gamma(\hat{\mathcal{G}})$ of a sub-graph $\hat{\mathcal{G}}$ of graph $\mathcal{G}$ is defined in the usual sense as the union of all neighbourhoods of the vertices of $\hat{\mathcal{G}}$ that are not in $\hat{\mathcal{G}}$ [39].

Every non-isolated vertex i forms a *star* graph with the vertices in its neighbourhood $\Gamma(i)$. That is

$$S^{(i)} = \bigcup_{j \in \Gamma(i)} (i, j). \tag{26}$$

Although a *compact* graph was formally defined in [117,118] as any graph $\mathcal{G}$ which contains no *isolated* vertices and for each pair i, j of non-adjacent vertices of $\mathcal{G}$, there exists a vertex q such that $\Gamma(i) \cup \Gamma(j) \subseteq \Gamma(q)$, we loosely define a *compact* graph in this thesis as any graph consisting of finite number of vertices connected by finite bonds. The later definition is consistent

with what is reported in [119]. Therefore, whenever semi-infinite leads are attached to graphs, the phrase "*compact part of the graph*" will be used to denote the part of the graph without the leads attached. Figure 10 shows an example of a graph connected to two leads, where the 'compact' part of the graph is demarcated by the red rectangle.
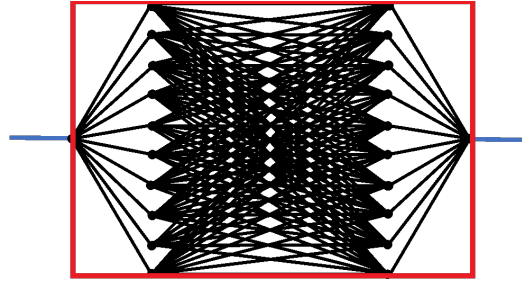
Figure 10.: An illustration of a graph attached to two leads. The solid red box indicates the *compact part of the graph*, while the two blue lines indicate the semi-infinite leads attached to the graph.

3.2.1 *Classification of Graphs By Connectivity*

In graph theory, connectivity indices are topological indices used to quantify the extent to which graph vertices are connected. These indices have been studied extensively in different forms and in several fields of study such as chemical graph theory [120–123], fuzzy graphs [124], street networks [125] and transport systems [126, 127].

However, the index we chose to use in this thesis is the γ index reported in [127]. The γ index takes the values between 0 and 1, with $\gamma = 1$ indi-

cating a complete (i.e. fully connected) graph. The index may therefore be interpreted as the percentage of a fully connected graph of the same *order*. For a non-planar graph (i.e. graphs which are not embedded in 2D plane) consisting of B bonds and n vertices, the γ index is defined by

$$\gamma := \frac{2B}{n(n-1)}. \tag{27}$$

Although no single connectivity index is completely adequate in comparing graph complexities, the γ index is sufficient for the purpose of this thesis, where we broadly classify the graphs as *high*, *medium* and *low* connectivity graphs.

3.2.1.1 *High connectivity (fully-connected) graphs*

We define high connectivity graphs as graphs with $\gamma = 1$. This is also known in some other literature as fully-connected graphs [39] or complete graphs [118]. In fully-connected graphs with no loops, the number of bonds $B = n(n-1)/2$, and so substituting that in (27) always gives $\gamma = 1$.

For example, Figures 11(a) and (b) show examples of two high connectivity graphs, one of order $n = 10$ and $B = 45$ bonds, and the other of order $n = 4$ and $B = 6$ respectively. It is important to note in Figure 11(a) that, although bonds appear to cross one another at the centre of the polygon, the centre does not constitute a node of the graph. However, in the tetrahedral network in Figure 11(b), the centre constitutes a vertex. Therefore, in Figure 11(a) the connectivity index is calculated as $\gamma = 2 \times 45/(10 \times 9) = 1$, while $\gamma = 2 \times 6/(4 \times 3) = 1$ in Figure 11(b).

(a) Fully-connected Decagon. (b) Tetrahedral network
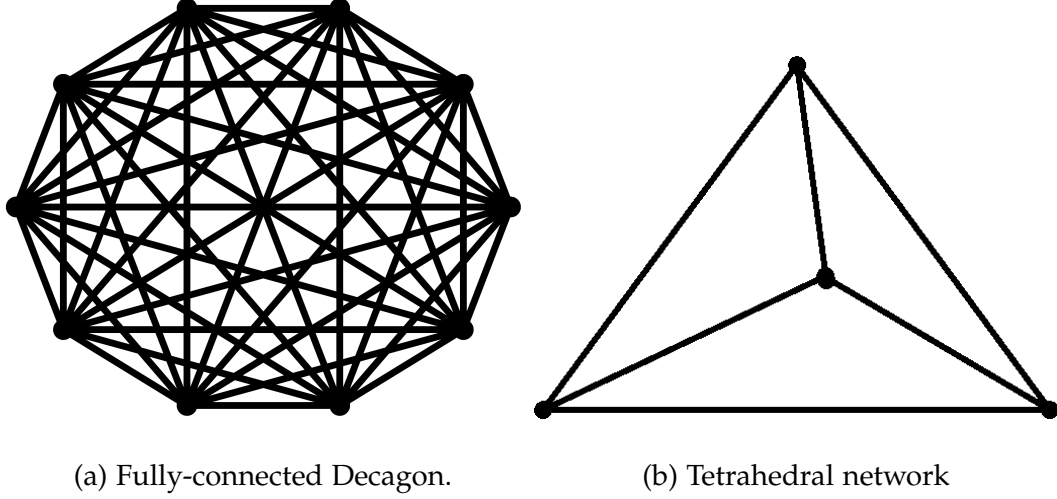
Figure 11.: Illustration of full-connected graphs.

3.2.1.2 *Medium connectivity (Hexagonal) graphs*

We classify graphs whose connectivity index $\gamma \approx 0.5$ as graphs with medium connectivity. For the purposes of this thesis, we introduce a class of graphs with hexagonal topology and call them *HEXv* graphs (or half-connected graphs) where v is the valency of the first node as well as the last node. For example, a *HEX6* graph has six bonds attached to both the first vertex and the last vertex as shown in Figure 12(a). Similarly Figure 12(b) shows a *HEX10* graph. Although *HEX10* graph has more bonds than *HEX6* graph, both have $\gamma \approx 0.5$. In general the number of bonds B for *HEXv* graphs is given by $B = v(v+2)$ while the number of vertices is $n = 2(v+1)$. Therefore the connectivity index for *HEXv* graphs is calculated in terms of v as

$$\begin{aligned}
\gamma &= \frac{2B}{n(n-1)} \\
&= \frac{v(v+2)}{(v+1)(2v+1)}.
\end{aligned} \tag{28}$$

Factorising v in both the numerator and the denominator, and simplifying the expression by applying the limiting case of large v, we get

$$\gamma = \frac{1 + 2/v}{(1 + 1/v)(2 + 1/v)} \qquad (29)$$
$$\approx \frac{1}{2} \quad \text{as} \quad v \to \infty.$$

This implies that, for $v > 1$, the connectivity index of $HEXv$ graphs is such that $1/2 \leq \gamma \leq 15/28$, where the maximum is attained when $v = 3$. Figure 13(a) shows how γ asymptotically approaches 0.5 in the limit of large graph sizes. The topology of $HEXv$ graphs is constructed so that the line-of-sight (LoS) transmission is avoided whenever leads are attached to the first and last nodes. This is discussed further in chapters 4 and 6. For now, it suffices to say that $HEXv$ ensures that waves travelling through the graphs needs at least three bounces to get from one lead to another. Graphs of $HEXv$ topology will be central when it comes to the discussion of statistics of channel capacity of both wireless (see chapters 6 and 7).

(a) $HEX6$ graph.   (b) $HEX10$ graph.
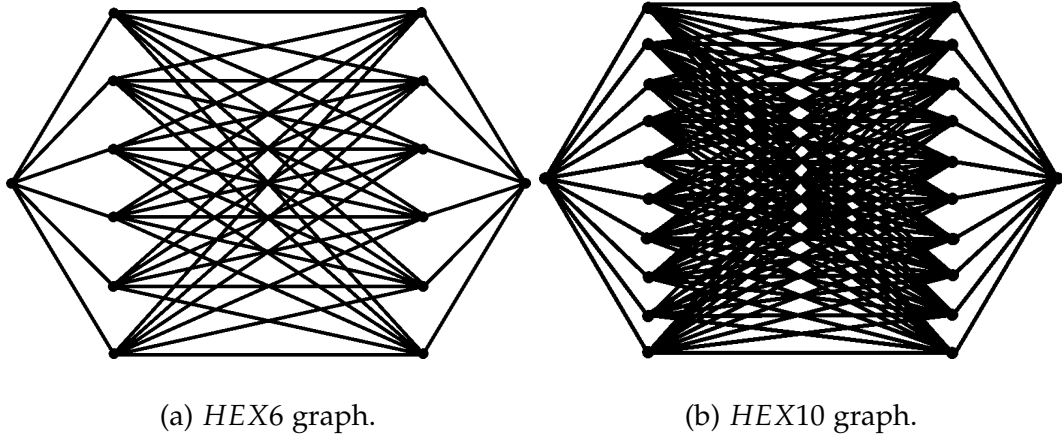
Figure 12.: Illustrations of graphs with $HEXv$ topologies for $v = 6, 10$ without leads attached.

(a) *HEXv* graphs.

(b) Cascade of T-junction graphs.
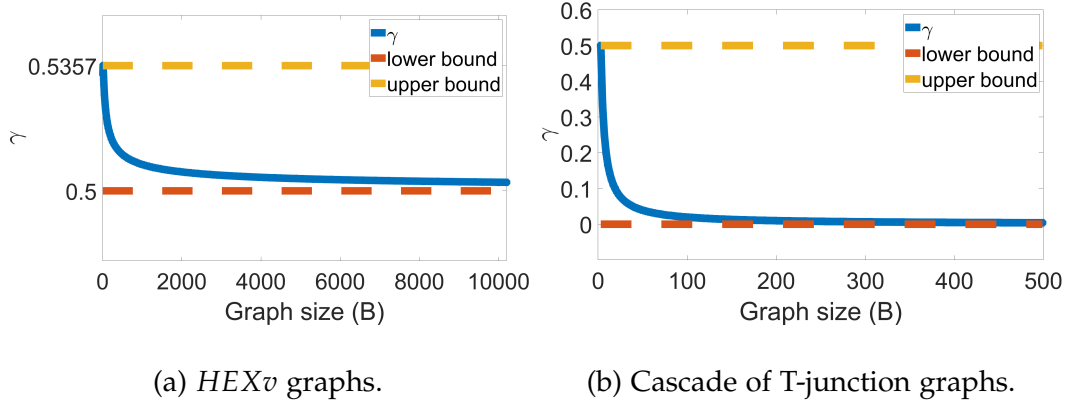
Figure 13.: Limits of connectivity index for (a) *HEXv* graphs and (b) cascade of T-junction graphs. The yellow dashed curve is the upper bound of the connectivity index while the red dashed curve represent the lower bound in both plots.

3.2.1.3 *Low connectivity (cascaded T-junction) graphs*

Low connectivity graphs are non-planar graphs with $\gamma < 0.5$. In particular we concentrate on graphs consisting of cascades of star networks. This network architecture is abundant in applications such as Digital Subscriber Line (DSL) and its variants like the Symmetric DSL (SDSL) and Asymmetric DSL (AVSL). The statistics of low connectivity networks is discussed in Chapter 8.

Figure 13(b) shows how γ changes with increasing graph size for a cascade of T-junction (i.e. star graphs with three branches each) networks. It is worth noting that the connectivity index asymptotically approaches zero as the number of stars in the network increases. This is because the number of

bonds B is related to the number of vertices n by $B = n - 1$. Therefore the connectivity index is given by

$$\gamma = \frac{2B}{n(n-1)}$$

$$= \frac{2}{n} \tag{30}$$

$$\rightarrow 0 \quad \text{as} \quad n >> 1.$$

From (30), it is obvious that a single T-junction network has the maximum connectivity (i.e. $\gamma = 0.5$) in this class of graph networks. The higher the number of stars cascaded, the lower the connectivity index. In this thesis, we refer to the cascade of such star graphs as *low connectivity graphs*. An illustration of is a single T-junction is shown in Figure 14(a), while (b) represents a graph consisting of a cascade of five T-junctions with $\gamma = 1/6$. Applications of the graphs with low connectivity is presented in Chapter 8, where we look at the digital subscriber networks.

(a)   (b)
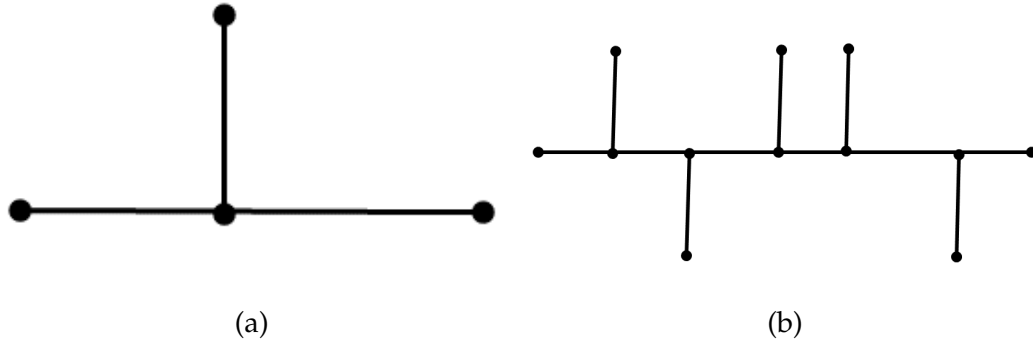
Figure 14.: Low connectivity graphs with (a) single T-junction and (b) a cascade of five T-junctions. The graph in (a) has the connectivity index $\gamma = 0.5$, while (b) has $\gamma = 1/6$.

With these definitions and terminologies in mind, we can now proceed to study the different theories of quantum graphs.

3.3 THEORETICAL BACKGROUND

The theories of quantum graphs have been widely reported. As usual, emphasis will be put on the theories that are essential to this thesis. We begin the discussion with the action of the Laplacian on graphs, followed by the boundary conditions at the vertices; subsequently, we generalise the expression for the vertex scattering matrix and finally discuss the analysis of spectrum of quantum graphs through two spectral functions.

3.3.1 *The Laplacian Operator on Graphs*

The Schrödinger operator on $\mathcal{G}$, defined on each bond b, consists of one dimensional operators

$$H_b = \left(\frac{1}{j} \frac{d}{dx_b} + A_b \right)^2 , \tag{31}$$

where A_b are real and positive constants representing an external magnetic flux. In this research, as in many other reported studies, we assume zero magnetic flux. The characteristics of these cables are presented in Section 5.2. The symbol $j = \sqrt{-1}$, while x_b is the position of a point on bond b whose length is denoted by L_b. Therefore, for each bond b, $0 \leq x_b \leq L_b$.

For any arbitrary wave function $\varphi(x)$ which may correspond either to voltage $V(x)$ or current $I(x)$, the wave equation reads

$$\left(\frac{1}{j}\frac{d}{dx_b}\right)^2 \varphi(x) = k^2\varphi(x), \tag{32}$$

which has general solution given by

$$\varphi(x) = Ae^{jkx} + Be^{-jkx}, \tag{33}$$

where k is the wave number. This wave number is slightly different from the κ defined in Chapter 2. Unlike κ (where the $\Re(\kappa)$ denotes the attenuation), the $\Im(k)$ here characterises the damping experienced by the propagating waves. The κ definition is commonly used by the Engineering communities, while the current definition is common in mathematics and physics communities.

With appropriate boundary conditions, the constants A and B can be determined so that a specific solution is obtained. The next subsections shed more light on these boundary conditions. We start by considering two simply-connected bonds and then work our ways to more complex topologies. Without loss of generality, we take the wave function to be the voltages $V(x)$ here. This could also be applied to currents *mutatis mutandis*. Equation 33 can therefore be re-written in terms of outgoing V^+ and incoming V^- voltages on bond b as

$$V_b(x_b) = V_b^+ e^{jkx_b} + V_b^- e^{-jkx_b}. \tag{34}$$

Equation (34) applies to each bond b of the graph and we can therefore form a system of differential equations to represent the entire graph. From such a system, we are able to derive two different spectral ζ functions (also

known as *secular* equations) [39] and justify our choice. The zeroes of these secular equations are in one-to-one correspondence with the resonances of our graph and therefore forms an important tool that will be used during spectral analysis of the underlying graph networks. The quantization of these metric graphs can be found in Section 4.5, which allows us to examine features of graphs that are predicted by random matrix theory [45,59,64]. For now, we will deal with boundary conditions that are relevant to this thesis and their implications on energy distribution within the graph network.

3.3.2 *Boundary conditions at vertices*

Boundary conditions describe the behaviour of travelling waves at boundaries (i.e. vertices) of graph networks. The proportion of the propagating waves that are reflected and/or transmitted on each bond connected to the vertex is governed by the conditions at the boundaries. A variety of boundary conditions have been reported in the literature. The two most important conditions that must be satisfied at a vertex are the *continuity* and *current conservation*.

The continuity condition at vertex i requires that the potential ϕ_i at i remains the same regardless of the bond from which one approaches the vertex. That is, $V^i(x_b) = \phi_i$ for all b connected to i. For example, Figure 15 shows a star graph where the central node is the reference point, and the potential at the centre remains unchanged. That is, $\phi_1 = V(x_1 = L_1) =$

$V(x_2 = L_2) = \cdots$, and $V(x_1 = 0) = \phi_2$, $V(x_2 = 0) = \phi_3$ and so on. For example, a wave starting from vertex 2 (i.e. at $x_1 = 0$) with potential ϕ_2 will end up with a potential of ϕ_1 at vertex 1 when $x_1 = L_1$.
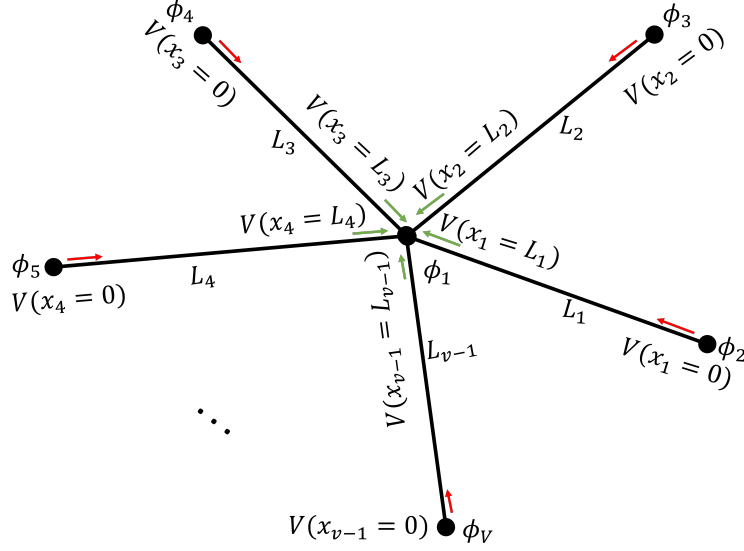
Figure 15.: Star graph showing continuity at the central vertex. In this particular way of labelling the vertices, $V(x_b = L_b) = \phi_1$ for all $b \in \{1, 2, 3, \cdots, v - 1\}$. Other ways such as labelling the central potential as ϕ_0 and the peripheral nodes from ϕ_1 may be used.

The current conservation condition is applied to the derivatives of the wave functions, and is given by [39, 45]

$$\sum_{b \in S^{(i)}} \pm \left. \frac{\mathrm{d}V(x_b)}{\mathrm{d}x_b} \right|_i = \lambda_i \phi_i, \tag{35}$$

where λ_i is a free parameter known (in some literature) as the *vertex scattering potential*. Its name originate from the fact that it is analogous to the potential strength obtained from the boundary conditions of a δ-function potential. For example, the valency of vertex i to which two bonds are at-

tached is $v_i = 2$. If we choose $x_b = 0$ at i, then (35) takes the simple form

$$\lim_{\epsilon \to 0^+} \left[\frac{dV(x_b)}{dx_b} \bigg|_{0+\epsilon} - \frac{dV(x_b)}{dx_b} \bigg|_{0-\epsilon} \right] = \lambda_i \phi_i. \tag{36}$$

Equation (36) is a well-known matching condition for a δ-potential of strength λ_i [39, 45].

The summation in (35) is over two types of waves. The outgoing waves are assumed to move in the positive direction (i.e. takes the $+$ sign at $x_b = 0$), while the incoming waves takes the negative direction at $x_b = L_b$ for vertex i. Although the vertex scattering potential $\lambda_i \in [-\infty, \infty]$, two specific values of λ_i have interesting applications and are by far the commonly used. These are the *Neumann* boundary conditions where $\lambda_i = 0$ and Dirichlet boundary conditions where $\lambda_i = \infty$. In the case of Dirichlet boundary conditions, the potentials of the vertex under consideration are zeros (i.e. $\phi_i = 0$).

From the boundary conditions above, the expression for reflection and transmission amplitudes at a vertex can be found. These transmission and reflection amplitudes are given in the form of a matrix known as the vertex scattering matrix (VSM). The elements of VSM, at vertex m with valency v_m, are given by [39]

$$\sigma_{pq}^{(m)} = \frac{2k}{v_m k + j\lambda_m} - \delta_{pq}, \tag{37}$$

where $p, q \in 1, 2, \cdots, v_m$ and k is the frequency-dependent wave number. Equation (37) is the most general expression of VSM one can find in literature [39]. The most commonly reported VSMs are the Neumann and Dirichlet VSMs [40, 41, 59, 101, 128]. It is important to note that the expres-

sion in (37) is valid only when the cables involved are uniform (i.e. when all the cables connecting at m have the same characteristics). We will later derive a more unifying expression to include non-uniform bonds.

From (37), it is easy to see that both Neumann and Dirichlet scattering matrices are independent of frequency. The effects of Dirichlet and Neumann boundary conditions on energy distribution are discussed in subsections 3.3.2.1 and 3.3.2.2, respectively.

3.3.2.1 *Dirichlet boundary condition*

When $\lambda_m = \infty$ in (37), the node is said to be subjected to Dirichlet boundary condition. This is equivalent to having a short circuit at the node so that any signal at the vertex is totally reflected (i.e. the vertex scattering matrix, $\sigma_{pq}^{(m)} = -\delta_{pq}$). This makes the entire graph behave as if it was made up of a set of disconnected bonds and there is nothing interesting to analyse under such circumstance. However, if the graph network has dead ends and it is desirable to prevent energy leakage at that end, then Dirichlet boundary condition become useful.

3.3.2.2 *Neumann boundary condition*

If $\lambda_m = 0$ in (37), then we have Neumann boundary conditions and this is equivalent to open circuits. The sum of all currents at the vertex is zero

(Kirchoff's law for currents). In this case, the vertex scattering matrix in (37) simplifies to

$$\sigma_{pq}^{(m)} = \frac{2}{v_m} - \delta_{pq}. \tag{38}$$

In the limit of large v_m, the scattering amplitudes of Neumann graphs favours reflection (i.e. back scattering) instead of transmission as shown in Figure 16 by the red arrows. The weights of the red arrows depict the strength of transmission or reflection at the vertex. Neumann boundary conditions therefore result in an unequal distribution of energy and hence introduce abnormal behaviour of the wave functions. The ultimate consequence of this unfair distribution is discussed in Section 4.6.
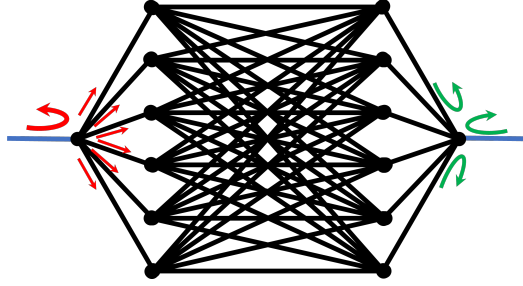
Figure 16.: Effects of Neumann (red arrows) and Dirichlet (green arrows) boundary conditions at graph vertices.

In order to avoid such a non-democratic distribution of energy, we introduce a third boundary condition known as the *Fourier* boundary condition. This is treated in subsection 3.3.2.3.

3.3.2.3 *Fourier boundary condition*

The Discrete Fourier Transform vertex scattering matrix [39,84] is given by

$$\sigma_{pq}^{(m)} = \frac{1}{\sqrt{v_m}} e^{\frac{j2\pi pq}{v_m}} .$$

(39)

This makes the transition probabilities $|\sigma_{pq}^m|^2 = 1/v_m$ and therefore reflections and the transmissions are uniform and democratic across edges. Consequently, the energies are equally distributed at all the vertices. This effect is illustrated in Figure 17 by the red arrows. The equi-distribution of energy improves the ability of the wave to mix within the connected graph network and therefore allows us to use the quantum graph theory more readily to model chaotic phenomena. More details are found in Chapters 4 and 6, where we use quantum graphs to model the distribution of information transfer rates in idealised communication channels. This paves the way for an effective treatment of a more realistic communication channel in Chapter 7.
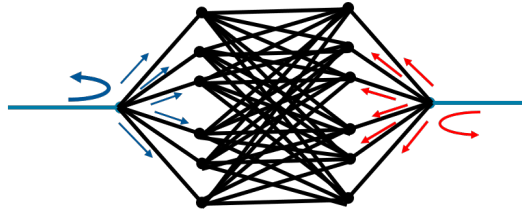
Figure 17.: Effect of Fourier boundary condition on energy distribution at a vertex. The equi-distribution of energy is shown in red, while the effect of Neumann bc is shown in blue.

Another vertex scattering matrix, which ensures equal transmission of amplitudes, has been studied [91]. Unfortunately, back-scattering is not al-

lowed here and it makes the scattering in such systems less favourable compared to the Fourier scattering when modelling propagation of microwaves. Nevertheless, I envisaged the so-called equi-transmitting scattering matrix to be useful in modelling other systems, where the underlying waves are required to flow in one direction. For this reason, this thesis will focus on the first three scattering matrices (i.e. Neumann, Dirichlet and Fourier).

3.3.3 *Generalisation of Vertex Scattering Matrix*

Consider an arbitrary vertex m with valency v_m and potential ϕ_m in a graph $\mathcal{G}$ as represented in Figure 18. All the outgoing and incoming voltages are colour-coded in red and green respectively as V_b^+ and V_b^-. The solution to
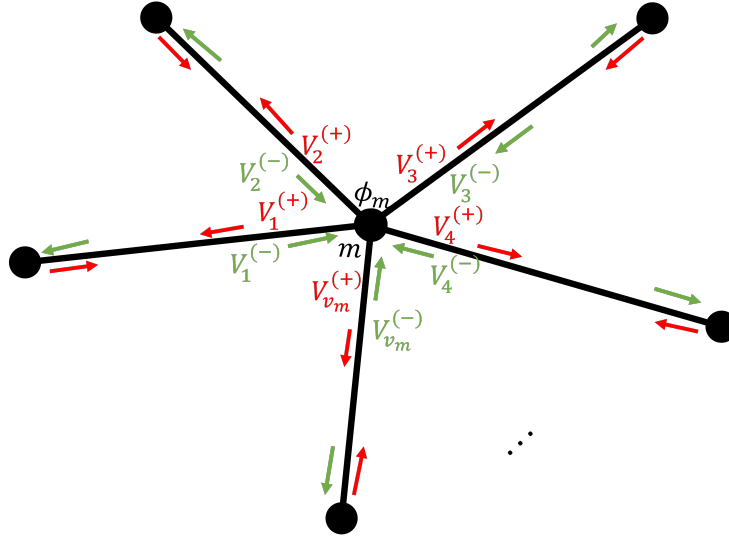
Figure 18.: A vertex with valency v_m.

the Schrödinger equations on each bond is given by

$$V_b(x_b) = V_b^+ e^{jk_b x_b} + V_b^- e^{-jk_b x_b}, \tag{40}$$

48

and therefore

$$\frac{\mathrm{d}V_b(x_b)}{\mathrm{d}x_b} = \mathrm{j}k_b\left(V_b^+ \mathrm{e}^{\mathrm{j}k_b x_b} - V_b^- \mathrm{e}^{-\mathrm{j}k_b x_b}\right). \tag{41}$$

Applying the continuity condition to (40) at $x_b = 0$ yields

$$V_b(x_b = 0) = \phi_m = V_b^+ + V_b^-, \qquad \forall b \in \{1,2,3,\cdots,v_m\}, \tag{42}$$

and therefore

$$\sum_{b=1}^{v_m}\left(V_b^+ + V_b^-\right) = v_m\phi_m. \tag{43}$$

Similarly, we can apply the current conservation condition to (41) to achieve

$$\sum_{b=1}^{v_m}\frac{\mathrm{d}V_b(x_b)}{\mathrm{d}x_b}\Bigg|_{x_b=0} = \sum_{b=1}^{v_m}\mathrm{j}k_b\left(V_b^+ - V_b^-\right) = \lambda_m\phi_m. \tag{44}$$

Using (43) and (44) to eliminate ϕ_m, we have

$$\sum_{b=1}^{v_m}\mathrm{j}k_b\left(V_b^+ - V_b^-\right) = \frac{\lambda_m}{v_m}\sum_{b=1}^{v_m}\left(V_b^+ + V_b^-\right). \tag{45}$$

Equation (45) may be rearranged, according to incoming and outgoing voltages, as

$$\sum_{b=1}^{v_m}\left(\mathrm{j}k_b + \frac{\lambda_m}{v_m}\right)V_b^- = \sum_{b=1}^{v_m}\left(\mathrm{j}k_b - \frac{\lambda_m}{v_m}\right)V_b^+. \tag{46}$$

From (42), we can form $v_m - 1$ equations of the form

$$V_1^+ + V_1^- = V_2^+ + V_2^-$$

$$V_1^+ + V_1^- = V_3^+ + V_3^-$$

$$V_1^+ + V_1^- = V_4^+ + V_4^- \tag{47}$$

$$\vdots \quad = \quad \vdots$$

$$V_1^+ + V_1^- = V_{v_m}^+ + V_{v_m}^-,$$

which may also be rearranged as

$$V_1^- - V_b^- = V_b^+ - V_1^+ \qquad \forall \quad b \in \{2,3,\cdots,v_m\}. \tag{48}$$

Equation (46) can be combined with (48) to form a system of v_m equations, which may be written in compact form as

$$AV^- = CV^+,\tag{49}$$

which implies

$$V^+ = \sigma V^-,\tag{50}$$

where

$$\sigma = C^{-1}A\tag{51}$$

is the *Vertex Scattering Matrix* (VSM). A careful examination of (46) and (48) reveals that the $v_m \times v_m$ matrices A can be written in compact form as

$$A = \begin{bmatrix} a_1 & \boldsymbol{a} \\ \boldsymbol{1} & -\mathbb{I} \end{bmatrix},\tag{52}$$

where $\mathbb{I}$ is a $(v_m - 1) \times (v_m - 1)$ unit matrix. If we define $a_b := \mathrm{j}k_b + \lambda_m/v_m$ for all $b \in \{1,2,3,\cdots,v_m\}$, then $\boldsymbol{a}$ is a $v_m - 1$ row vector with components $\begin{pmatrix} a_2 & a_3 & a_4 & \cdots & v_m \end{pmatrix}$; $\boldsymbol{1}$ is a $v_m - 1$ column vector with each component as 1. On the other hand,

$$C = \begin{bmatrix} c_1 & \boldsymbol{c} \\ -\boldsymbol{1} & \mathbb{I} \end{bmatrix},\tag{53}$$

where $\boldsymbol{c}$ is a $v_m - 1$ row vector with components $\begin{pmatrix} c_2 & c_3 & c_4 & \cdots & v_m \end{pmatrix}$ such that $c_b := \mathrm{j}\, k_b - \lambda_m/v_m$ for all $b \in \{1,2,3,\cdots,v_m\}$.

From (51)

$$\sigma = \frac{1}{|C|}\mathrm{Adj}(C)A,\tag{54}$$

where the determinant of C is

$$
\begin{aligned}
|C| &= \sum_{b=1}^{v_m} c_b \\
&= \sum_{b=1}^{v_m} \left(\mathrm{j}k_b - \frac{\lambda_m}{v_m} \right) \\
&= \sum_{b=1}^{v_m} \mathrm{j}k_b - \lambda_m.
\end{aligned} \tag{55}
$$

Furthermore, the adjoint of C is found to be

$$
\mathrm{Adj}(C) = \begin{bmatrix} 1 & -\mathbf{c} \\ \mathbf{1} & \mathbb{B} \end{bmatrix}, \tag{56}
$$

where the elements of $\mathbb{B}$ are given by

$$
B_{pq} = \delta_{pq} |C| - c_q. \tag{57}
$$

We now calculate the vertex scattering matrix as

$$
\sigma = \frac{1}{|C|} \begin{bmatrix} 1 & -c_2 & -c_3 & \cdots & -c_{v_m} \\ 1 & |C| - c_2 & -c_3 & \cdots & -c_{v_m} \\ 1 & -c_2 & |C| - c_3 & \cdots & -c_{v_m} \\ \vdots & \vdots & \vdots & \ddots & \vdots \\ 1 & -c_2 & -c_3 & & |C| - c_{v_m} \end{bmatrix} \begin{bmatrix} a_1 & a_2 & a_3 & \cdots & a_{v_m} \\ 1 & -1 & 0 & \cdots & 0 \\ 1 & 0 & -1 & \cdots & 0 \\ \vdots & \vdots & \vdots & \ddots & \vdots \\ 1 & 0 & 0 & \cdots & -1 \end{bmatrix} \tag{58}
$$

This implies

$$
\sigma = \frac{1}{|C|} \begin{bmatrix} a_1 + c_1 - |C| & a_2 + c_2 & a_3 + c_3 & \cdots & a_{v_m} + c_{v_m} \\ a_1 + c_1 & a_2 + c_2 - |C| & a_3 + c_3 & \cdots & a_{v_m} + c_{v_m} \\ a_1 + c_1 & a_2 + c_2 & a_3 + c_3 - |C| & \cdots & a_{v_m} + c_{v_m} \\ \vdots & \vdots & \vdots & \ddots & \vdots \\ a_1 + c_1 & a_2 + c_2 & a_3 + c_3 & & a_{v_m} + c_{v_m} - |C| \end{bmatrix} . \tag{59}
$$

51

But from $a_b = \mathrm{j}\,k_b + \lambda_m/v_m$ and $c_b = \mathrm{j}\,k_b - \lambda_m/v_m$, $a_b + c_b = 2\mathrm{j}k_b$ for all

$b \in \{1, 2, 3, \cdots, v_m\}$. Therefore

$$
\sigma = \frac{1}{|C|}
\begin{bmatrix}
2\mathrm{j}k_1 - |C| & 2\mathrm{j}k_2 & 2\mathrm{j}k_3 & \cdots & 2\mathrm{j}k_{v_m} \\[6pt]
2\mathrm{j}k_1 & 2\mathrm{j}k_2 - |C| & 2\mathrm{j}k_3 & \cdots & 2\mathrm{j}k_{v_m} \\[6pt]
2\mathrm{j}k_1 & 2\mathrm{j}k_2 & 2\mathrm{j}k_3 - |C| & \cdots & 2\mathrm{j}k_{v_m} \\[6pt]
\vdots & \vdots & \vdots & \ddots & \vdots \\[6pt]
2\mathrm{j}k_1 & 2\mathrm{j}k_2 & 2\mathrm{j}k_3 & & 2\mathrm{j}k_{v_m} - |C|
\end{bmatrix},
\tag{60}
$$

and the elements of σ at vertex m may be written as

$$
\begin{aligned}
\sigma_{pq}^{(m)} &= \frac{2\mathrm{j}k_q}{|C|} - \delta_{pq} \\[8pt]
&= \frac{2\mathrm{j}k_q}{\sum_{b=1}^{v_m}\left(\mathrm{j}k_b - \frac{\lambda_m}{v_m}\right)} - \delta_{pq} \\[8pt]
&= \frac{2\mathrm{j}k_q}{\mathrm{j}\sum_{b=1}^{v_m} k_b - \lambda_m} - \delta_{pq} \\[8pt]
&= \frac{2k_q}{\sum_{b=1}^{v_m} k_b + \mathrm{j}\lambda_m} - \delta_{pq}.
\end{aligned}
\tag{61}
$$

When uniform bonds are assumed (i.e. $k_b = k$ for all b), then (37) is re-

trieved. It must be noted that the vertex scattering matrix constructed by

the formula in (61) is not guaranteed to be symmetric. Symmetry is guaran-

teed only when the wave numbers k_b are equal. Also, unlike (37), the ver-

tex scattering matrix in (61) is frequency-dependent even under Neumann

boundary conditions.

3.3.4 *Quantization of Graphs*

Now that we have understood how the various boundary conditions affect the energy distribution at the vertex, we turn to the spectral properties of quantum graphs through *secular* equations. Two such secular equations are treated below.

3.3.4.1 *Secular Equation I*

As we have seen earlier, in (34), an arbitrary pair of vertices connected by bond b has the following general solution to the wave equation in (32)

$$V_b(x_b) = V_b^+ e^{jkx_b} + V_b^- e^{-jkx_b}. \tag{62}$$

An outgoing wave from vertex m becomes an incoming wave to vertex n. We derive the first secular equation in the following way.

If we choose $x_b = 0$ at m and $x_b = L_b$ at n, then we can write the following two equations at m and n respectively

$$V_b(x_b = 0) = V_b^+ + V_b^- = \phi_m$$

$$V_b(x_b = L_b) = V_b^+ e^{jkL_b} + V_b^- e^{-jkL_b} = \phi_n, \tag{63}$$

which may be written in matrix form as

$$\begin{bmatrix} 1 & 1 \\ e^{jkL_b} & e^{-jkL_b} \end{bmatrix} \begin{bmatrix} V_b^+ \\ V_b^- \end{bmatrix} = \begin{bmatrix} \phi_m \\ \phi_n \end{bmatrix}. \tag{64}$$

This implies

$$\begin{bmatrix} V_b^+ \\ V_b^- \end{bmatrix} = \frac{1}{-2\sin kL_b} \begin{bmatrix} \phi_m e^{jkL_b} - \phi_n \\ \phi_m - \phi_n e^{-jkL_b} \end{bmatrix}. \tag{65}$$

Substituting (65) into (62) and simplifying gives the solution in terms of the nodal potential as

$$V_b(x_b) = \frac{1}{\sin kL_b} \left[\phi_m \sin k(L_b - x_b) + \phi_n \sin kx_b \right]. \tag{66}$$

Differentiating (66) with respect to x_b gives

$$\frac{dV_b(x_b)}{dx_b} = \frac{k}{\sin kL_b} \left[\phi_n \cos kx_b - \phi_m \cos k(L_b - x_b) \right] \tag{67}$$

Applying the current conservation conditions at vertex m (i.e. at $x_b = 0$) and n (i.e. at $x_b = L_b$) respectively results in the following two equations

$$\sum_{b \in \Gamma(m)} \frac{k}{\sin kL_b} \left[\phi_n - \phi_m \cos kL_b \right] = \lambda_m \phi_m \tag{68}$$

and

$$\sum_{b \in \Gamma(n)} \frac{-k}{\sin kL_b} \left[\phi_n \cos kL_b - \phi_m \right] = \lambda_n \phi_n. \tag{69}$$

The expression $b \in \Gamma(m)$ refers to all bonds that connect vertex m to the vertices in its neighbourhood. Therefore the sum is over such bonds. While the coefficients of ϕ_n in (68) remain as $k/\sin kL_b$ for each b, the coefficient of ϕ_m becomes $-k \sum \cot kL_b$. The reverse happens to the coefficients of ϕ_m and ϕ_n in (69).

Consequently, (68) and (69) can be written in matrix form as

$$\begin{bmatrix} \sum_{b \in \Gamma(m)} \cot kL_b & -\frac{1}{\sin kL_b} \\ -\frac{1}{\sin kL_b} & \sum_{b \in \Gamma(n)} \cot kL_b \end{bmatrix} \begin{bmatrix} \phi_m \\ \phi_n \end{bmatrix} = \begin{bmatrix} -\frac{\lambda_m}{k} \phi_m \\ -\frac{\lambda_n}{k} \phi_n \end{bmatrix}. \tag{70}$$

This is simplified and written in compact form as

$$h(k)\boldsymbol{\phi} = 0, \tag{71}$$

where the elements of the matrix $h(k)$ are generated as

$$h_{mm}(k) = \frac{\lambda_m}{k} + \sum_{b \in \Gamma(m)} \cot kL_b, \tag{72}$$

and

$$h_{mn}(k) = -C_{mn}\frac{1}{\sin kL_b}, \quad m \neq n. \tag{73}$$

Here, C_{mn} are the elements of the connectivity matrix C, which was defined in section 3.2; and $h(k)$ has the same dimension as C.

Equation (71) has a non-trivial solution only when

$$\zeta_h(k) := \det[h(k)] = 0, \tag{74}$$

where the spectral function $\zeta_h(k)$ is called the *secular function* [39]. The zeroes of the secular function are symmetrically distributed on the real k plane. This is due to the symmetric nature of the wave equation, which is immediately visible in (66) (i.e. $V_b(x_b; k) = -V_b(x_b; -k)$). The spectrum of the Schrödinger equation is $\{k_n^2\}$, which is in one-to-one correspondence with the zeroes of the secular function $\zeta_h(k)$.

However, the presence of $\sin kL_b$ in the denominator in (73) will result in poles appearing in the spectrum at $k = 0$. Note that $k = 0$ gives the same vertex scattering matrix as Dirichlet boundary condition would in (37). This means that poles will appear at Dirichlet spectrum. In order to avoid the appearance of these poles, another secular equation is derived below.

3.3.4.2 *Secular Equation II*

Here, we derive the second secular function with no poles. We begin with some notation to label the vertices and the bonds in the underlying network. Consider, as an example, the simple T-junction network shown in Figure 19. There are $2B$ outgoing and incoming voltages respectively, where B is the

55
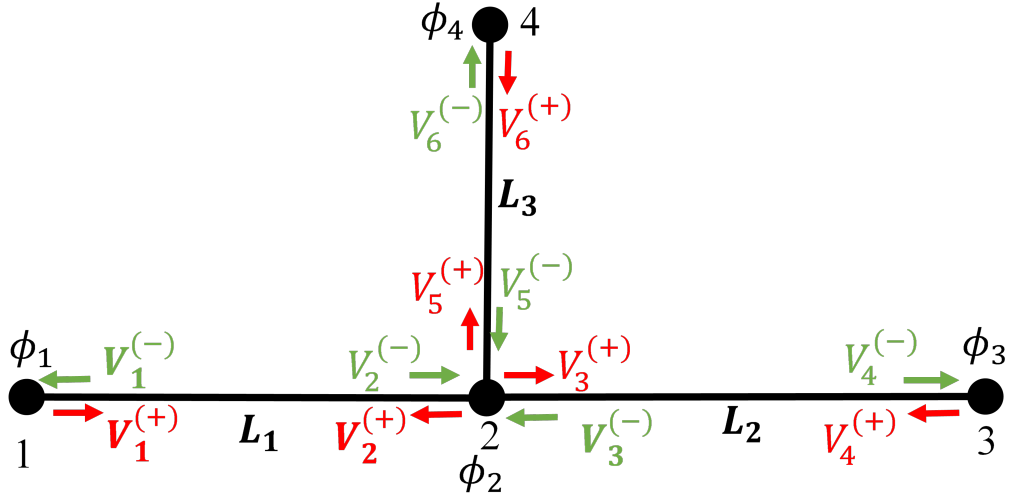
Figure 19.: An illustration of a single T-junction with out-going $(V_b^{(+)})$ and incoming $(V_b^{(-)})$ voltages on each bond b.

total number of bonds in the network. For book-keeping purposes, we label the voltages on each bond in this special way: if V_m^+ and V_{m+1}^+ are two outgoing voltages on a bond, then the incoming voltages on that particular bond are labelled V_m^- and V_{m+1}^-, respectively. With this method of labelling, it is easy to observe that the outgoing and incoming voltages in the network are related in a simple way by phase shifts. In general, we can form $2B$ equations as

$$
\begin{aligned}
V_2^- &= e^{jkL_1}V_1^+ \\
V_1^- &= e^{jkL_1}V_2^+ \\
&\vdots \\
V_{2B}^- &= e^{jkL_B}V_{2B-1}^+ \\
V_{2B-1}^- &= e^{jkL_B}V_{2B}^+,
\end{aligned}
\tag{75}
$$

where L_b is the length of bond b.

The system of equations may be written in matrix form as

$$
\begin{bmatrix} V_2^- \\ V_1^- \\ \vdots \\ V_{2B}^- \\ V_{2B-1}^- \end{bmatrix} = \begin{bmatrix} e^{jkL_1} & 0 & 0 & \cdots & 0 \\ 0 & e^{jkL_1} & 0 & \cdots & 0 \\ 0 & 0 & \ddots & \cdots & 0 \\ \vdots & \vdots & 0 & e^{jkL_B} & \vdots \\ 0 & 0 & 0 & \cdots & e^{jkL_B} \end{bmatrix} \begin{bmatrix} V_1^+ \\ V_2^+ \\ \vdots \\ V_{2B-1}^+ \\ V_{2B}^+ \end{bmatrix}.
\tag{76}
$$

It can be noticed that the vector in the left hand side of (76) is not arranged in ascending order as is the case in the right hand side. To rearrange, we multiply both sides of (76) by a block diagonal matrix of the form

$$
C = \begin{bmatrix} 0 & 1 & 0 & \cdots & 0 \\ 1 & 0 & 0 & \cdots & 0 \\ 0 & 0 & \ddots & \cdots & 0 \\ \vdots & \vdots & 0 & 0 & 1 \\ 0 & 0 & 0 & 1 & 0 \end{bmatrix}.
\tag{77}
$$

For the purpose of this research, we call the $2B \times 2B$ matrix C the *connection* matrix. Like the connectivity (or adjacency) matrix, it contains topological information of the cable network. Unlike the connectivity matrix, it contains a single entry of 1 in each row and each column and it has twice

the dimension of the connectivity matrix. The matrix equation in (76) is rearranged as

$$
\begin{bmatrix}
V_1^- \\
V_2^- \\
\vdots \\
V_{2B-1}^- \\
V_{2B}^-
\end{bmatrix}
=
\begin{bmatrix}
0 & e^{jkL_1} & 0 & \cdots & 0 \\
e^{jkL_1} & 0 & 0 & \cdots & 0 \\
0 & 0 & \ddots & \cdots & \vdots \\
\vdots & \vdots & 0 & 0 & e^{jkL_B} \\
0 & 0 & 0 & e^{jkL_B} & 0
\end{bmatrix}
\begin{bmatrix}
V_1^+ \\
V_2^+ \\
\vdots \\
V_{2B-1}^+ \\
V_{2B}^+
\end{bmatrix}.
\tag{78}
$$

In compact form, we write

$$
V^- = S V^+,
\tag{79}
$$

where the shift matrix, S is a block diagonal matrix of the form in (78) containing the phase shifts. From the definition of scattering matrix σ, we can write

$$
V^- = \sigma^{-1} V^+.
\tag{80}
$$

Using (80) to eliminate V^- in (79), we have

$$
V^+ = T V^+,
\tag{81}
$$

where the transfer matrix $T = \sigma S$. Therefore

$$
\left(I_{2B} - T \right) V^+ = 0.
\tag{82}
$$

Equation (82) has a non-trivial solution if and only if

$$
\zeta_T(k) := \det \left(I_{2B} - T \right) = 0.
\tag{83}
$$

The function $\zeta_T(k)$ is the second secular function whose zeroes must coincide with the zeroes of the first secular function $\zeta_h(k)$ since they describe the same physical system. Figure 20 shows an example of complex eigenvalue behaviour for a single T-junction graph network (as shown in Figure 19)

with $L_b = 1$ for all the three bonds in the network, and $0 \leq k \leq 2\pi$. Since the lengths of the bonds are commensurate, the resonances are expected to be periodic as seen in Figure 19. In this case the resonances occurred at $kL_b = 0, \quad \pi/2, \quad \pi, \quad 3\pi/2 \quad$ and $\quad 2\pi$. Figure 20(a) shows the 3D plot, while (b) shows the bird's eye view of the figure in (a).
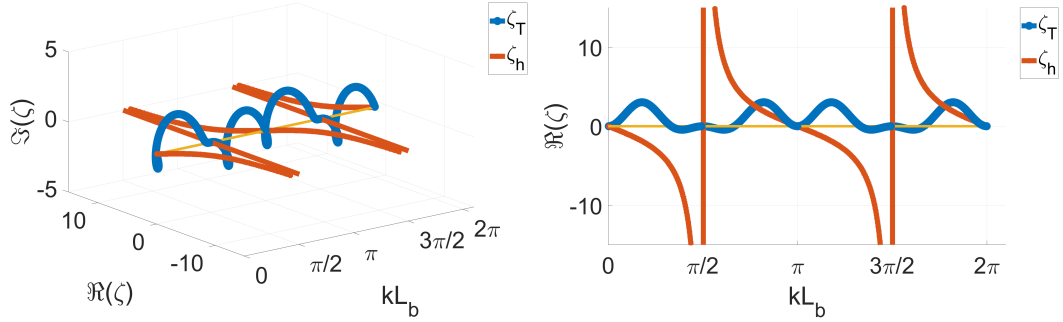
Figure 20.: Comparing the zeroes of first and second secular functions.

Comparing the first $\zeta_h(k)$ and the second $\zeta_T(k)$ secular functions reveals the following. Unlike $\zeta_h(k)$, which depends on the determinant of a $V \times V$ matrix, the $\zeta_T(k)$ depends on the determinant of matrix with a dimension of $2B \times 2B$, which is significantly larger than $\zeta_h(k)$. This is true especially with regards to graphs of high connectivity. Additionally, $\zeta_h(k)$ is real when the boundary conditions are Neumann or Dirichlet. It is easier to find the zeroes of a real function than complex.

On the other hand $\zeta_T(k)$ does not results in poles in the spectrum of the Schrödinger operator. Furthermore, $\zeta_T(k)$ can be converted from a complex function into a real one by noting the general expression for the determinant of T, which is given by

$$\det(T) = - e^{j2k\mathcal{L}}, \tag{84}$$

where $\mathcal{L} = \sum L_b$ for all b, is known as the volume of the graph. With this in mind, we can write

$$\zeta_T(k) = \det\left(I_{2B} - T\right)$$

$$= -2je^{jk\mathcal{L}}\sin(k\mathcal{L}) \tag{85}$$

$$= -2\sqrt{\det(T)}\sin(k\mathcal{L}).$$

There we can redefine $\zeta_T(k)$ by scaling it with $\sqrt{\det(T)}$ to make it a real function as

$$\zeta_T(k) = \frac{\det\left(I_{2B} - T\right)}{\sqrt{\det(T)}}. \tag{86}$$

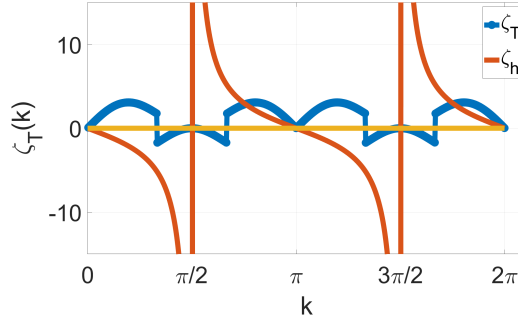An example is shown in Figure 21 which compares (86) with $\zeta_h(k)$.

Figure 21.: Comparing the zeroes of $\zeta_h(k)$ and purely real $\zeta_T(k)$.

Therefore the only advantage of $\zeta_h(k)$ over $\zeta_T(k)$ is with regards to its smaller dimension. But the existence of poles in the spectrum of $\zeta_h(k)$ derails the advantage of this secular function, hence our choice to use $\zeta_T(k)$ in subsequent chapters.

3.4 CONCLUSION

We have introduced the most important theory and background knowledge of QGs relevant to this research. This was done by first discussing the terminologies and definitions used in this thesis. In addition, the Laplacian operator on graphs was introduced, and the various boundary conditions that may be applied to the vertices of these graphs has been extensively discussed. The application of these boundary conditions was used to derive mathematical expressions for the vertex scattering matrix for both uniform and non-uniform cable networks.

Finally, we have presented two ways of quantising graph networks, which resulted in two spectral functions. First secular equation involved finding the determinant of a smaller matrix but consist of poles in its spectrum, while the second secular equation has the overriding advantage of having no poles in its spectrum. The theory behind the second secular equation is used in Chapter 4 to derive a model which predicts the propagation of high frequency waves in cable networks.

4

QUANTUM GRAPH MODEL

4.1 INTRODUCTION

In this chapter, we model the propagation of microwaves in complex systems using quantum graph theory, which we introduced in Chapter 3. This method is useful in modelling not only wired systems but also wireless systems. For example, the propagation of microwaves in chaotic cavities has been researched extensively by several authors using what is commonly known as the *random coupling model* (RCM) [31–33, 35, 37, 38, 116, 129, 130]. The RCM is an impedance model and consists of two main parts. The non-statistical part is made up of system-specific features of the underlying system, while the statistical part has universal characteristics that do not depend on the system under consideration, but rather, can be predicted by the random matrix theory.

The main objective of this chapter is to create an analogue of the RCM using graph theory. In this analogue model, we use scattering matrices

instead of the impedance matrices typically used in RCM. We leverage the simplicity of quantum graphs as a model to create a tool which can be used as a test-bed for simulating realistic systems. All the features in RCM are available analogously in the graph model and will be compared in this chapter.

The chapter is organised as follows. We begin with the brief introduction of RCM and its main characteristics. In Section 4.3, we model the propagation of microwaves in cable networks that are coupled to leads. This model is numerically validated by comparing it with the theoretical predictions of the well-known transmission line (TL) model [25, 26]. This is presented in Section 4.4, where we compare and contrast the performance of the two methods. The fact that we intend to use quantum graph theories to model chaotic (or pseudo chaotic) systems requires that we test the model for its ability to model chaotic phenomena. This is discussed in Section 4.5. In the same section, we propose a mechanism which allows us to attached leads *weakly* to graphs. This is important in reducing energy leakages from the system under consideration in order to produce idealised models. It is also a fundamental requirement in electromagnetic compatibility studies where the interference effects between nearby systems are supposed to be minimised. Moreover, in order compare the graph model with the predictions of RMT, we need the underlying system to be as close to a lossless system as possible. This can be achieved through the weak coupling of leads to graphs.

In Section 4.6, we discuss how to create the graph-scattering analogue of RCM by symmetrising the model in Section 4.3. We also show how to analytically derive the characteristic features of the constituent variables in the graph model. Finally, in Section 4.7, we introduce how losses may be incorporated into the graph model to allow for modelling realistic systems. This makes the graph model a complete analogue of the random coupling model, which will be used later to predict the distribution of the channel capacity of wireless communication systems.

4.2 RANDOM COUPLING MODEL

The Random Coupling Model (RCM) provides a basis for understanding the properties of high-frequency electromagnetic field quantities coupled into chaotic cavities through a number of ports or terminals. These ports may be in the form of sensors or antennas. The theory takes into account two separate phenomena. The *deterministic* part on one hand, depends only on the non-statistical properties of the coupling port. On the other hand, the *non-deterministic* part depends on universal statistical properties of wave-chaotic systems, which can be predicted using random matrix theory (RMT) by the properties of ensembles of large random matrices [131]. The model equation is based on an impedance matrix Z^{cav} defined for M channels as follows [33, 35]:

$$Z^{\text{cav}} = j\Im\left[Z^{\text{rad}}\right] + \left[R^{\text{rad}}\right]^{\frac{1}{2}} \cdot \xi_Z \cdot \left[R^{\text{rad}}\right]^{\frac{1}{2}}, \tag{87}$$

where

$$Z^{\mathrm{rad}} = R^{\mathrm{rad}} + j\Im\left[Z^{\mathrm{rad}}\right] \tag{88}$$

is an $M \times M$ complex-valued and experimentally accessible port *radiation impedance* matrix, whose diagonal elements represent the non-statistical and system-specific features of the coupling between the irregular cavity and its ports [38]. The crosstalk between the coupled ports are represented by the off-diagonal elements of Z^{rad} [34, 35]. In this research, we assume zero crosstalk between the ports. Therefore Z^{rad} is simply a diagonal matrix whose diagonal elements represent the radiation impedances of the corresponding ports. This is a realistic assumption since the ports are assumed to be perfectly coupled and the only way electromagnetic waves would move from one port to another is through the chaotic cavities. The matrix R^{rad} on one hand (i.e. the real part of Z^{rad}) can be interpreted as a *radiation resistance* because it quantifies the ability of far-field radiation of the ports. On the other hand $\Im\left[Z^{\mathrm{rad}}\right]$ quantifies the stored near-field reactive energy of the ports [35].

The normalised impedance matrix

$$\xi_Z = \frac{j}{\pi} W \frac{1}{j\alpha I - \Lambda_Z} W^{\dagger}, \tag{89}$$

denotes the statistical part of the model. The elements W_{nm} of the $M \times N$ coupling matrix W represent the coupling between the mth driving port and the nth eigen mode [35,38], and have the following characteristics. They are

1. Gaussian-distributed with zero mean and unit variance, and

2. uncorrelated.

The maximum number of eigenmodes of the enclosure is N, $j = \sqrt{-1}$, I is an $N \times N$ identity matrix, and $W^\dagger$ is the conjugate transpose of W. The normalised diagonal matrix Λ_Z is an $N \times N$ matrix, whose diagonal elements are the eigenvalues of the underlying transfer matrix. The spacing of the eigenvalues are distributed according Wigner's "semicircle law" are obtainable through a random matrix Monte Carlo simulation [35, 37].

The Monte Carlo approach, which was first proposed by [37] and later published in [35] may be implemented by creating a large random matrix with the following properties.

1. The matrix is $5N \times 5N$ real symmetric, where N is the size of the diagonal matrix Λ_Z.

2. The elements are independent and identically distributed.

3. The diagonal elements are Gaussian distributed with zero mean and unit variance.

4. The off-diagonal elements are Gaussian distributed with zero mean and a variance of $1/2$.

For each randomly generated matrix with properties as outlined above, there will be $5N$ eigenvalues out of which the middle N eigenvalues are chosen and normalised to have a unit average spacing. The spacings of these eigenvalues have been shown to follow the Wigner's "semicircle law". For a more detailed description, see Appendix A of [35].

Figure 22 shows an example where $N = 200$ and a sample of 1000 matrices were used. The solid red curve is the theoretical prediction of a semicircle with radius 31.5, and it agrees well with Monte Carlo simulation of a random matrix with properties as described above.
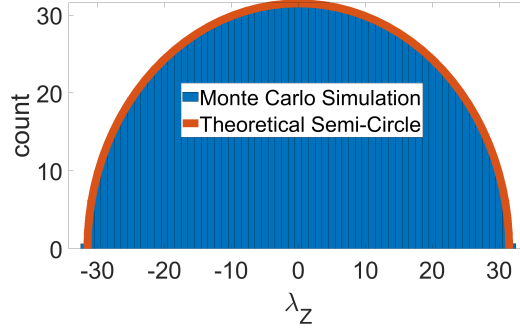

Figure 22.: An example of Wigner's semicircle law, where $N = 200$ and an ensemble of 1000 samples were used. The red curve is the theoretical prediction, while the histogram is the results of the Monte Carlo approach summarised in 4.2.

The universal random variable ξ_Z is an $N \times N$ matrix which depends neither on the geometrical shape of the cavity nor the positions of the scatterers inside the cavity, but rather depends only on a dimensionless parameter α. The α parameter quantifies losses in the system and we shall refer to it as the *loss parameter*. From the theory of RCM, the loss parameter is given by

$$\alpha = \frac{k^2}{\Delta k_n^2 Q}, \tag{90}$$

where k is the wave number, Δk_n^2 is the mean level spacing, and Q is the quality factor of the chaotic cavity. The variance of real and imaginary parts of ξ_Z was predicted in [33] and validated experimentally in [116], to be

$$\sigma^2_{\Re[\xi_Z]} = \sigma^2_{\Im[\xi_Z]} = \frac{1}{\alpha\pi} \quad \text{for} \quad \alpha \gg 1. \tag{91}$$

For a more detailed discussion of the theoretical underpinnings of RCM, I refer the reader to [32, 34–38, 129, 130].

In Section 4.6, we will derive the quantum graph analogue of the RCM, and use the analogue model in chapters 6, 7 and 8 to model both wireless and wired communication channels. We achieve this by first using quantum graph theory to model the propagation of microwaves in complex networks, and then derive the analogue of RCM in (87) from the graph model.

4.3 MODELLING WAVE PROPAGATION USING QUANTUM GRAPH THEORY

In this section, we model the propagation of waves through cable networks by estimating the scattering parameters. In Chapter 3, we derived expressions for the vertex scattering matrix. Here, we seek the scattering parameters of the entire graph networks when leads are attached. Figure 23 shows a schematic of a graph attached to a lead (i.e. the solid blue cable).

Now, we can consider the graph part and the lead part as two systems coupled together. We refer to the underlying graph *without* leads as the *compact* part of the graph. To simplify the algebra, we label the compact part of the graph as a black box, x, and use a subscript of 0 to denote the lead side. We can write two equations connecting the voltages on the lead side to the voltages on the compact graph side as
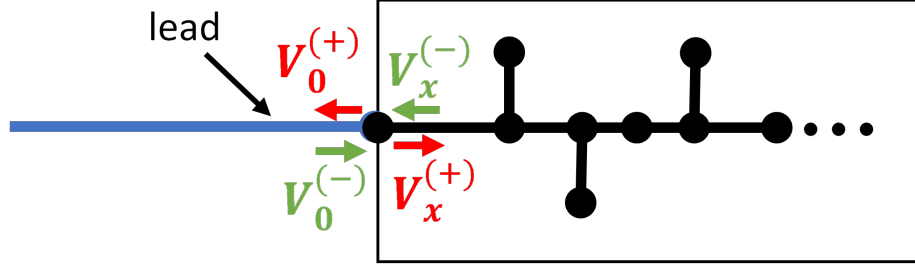
$$V_0^+ = \sigma_{00} V_0^- + \sigma_{0x} V_x^-$$
(92)

68

Figure 23.: Illustration of a cable network connected to a lead.

and

$$V_x^+ = \sigma_{x0}V_0^- + \sigma_{xx}V_x^-. \tag{93}$$

Substituting (79) into both (92) and (93) gives

$$V_0^+ = \sigma_{00}V_0^- + \sigma_{0x}S_{xx}V_x^+ \tag{94}$$

and

$$V_x^+ = \sigma_{x0}V_0^- + \sigma_{xx}S_{xx}V_x^+. \tag{95}$$

Making V_x^+ the subject in (95) and substituting back into (94), we have the

quantum graph (QG) model equation for the reflection coefficient as

$$\begin{aligned}
\hat{S}_{11} &= \sigma_{00} + \sigma_{0x}S_{xx}\frac{1}{I_{2B} - \sigma_{xx}S_{xx}}\sigma_{x0} \\
&= \sigma_{00} + \sigma_{0x}S_{xx}\sum_{n=1}^{\infty}T^n\sigma_{x0},
\end{aligned} \tag{96}$$

where $T = \sigma_{xx}S_{xx}$ is the transfer matrix (as discussed previously in Chapter

3) which is unitary for a closed graph network and sub-unitary when leads

are attached. The matrix T will be extensively discussed later in Section 4.6.

The model in (96) may be explained in the following way. The network is

excited, by the voltage $V_0^{(-)}$, through the lead. At node 0 (i.e. the node con-

necting the lead to the graph), the signal undergoes both a *prompt* reflection which is modelled by σ_{00}, and a transmission from the lead to the compact part of the graph. This transmission is modelled by σ_{x0}. While inside the network, the signal undergoes multiple reflections and transmissions represented by $(I_{2B} - \sigma_{xx}S_{xx})^{-1}$. Finally, the signal is transmitted back onto the lead. The bond-lead transmission is modelled by σ_{0x}. The shift matrix S_{xx} now encodes the topology of the network as well as the phase shifts the signal undergoes while in transit. Additionally, we can denote losses in the system by writing the phases as $\exp\left(j\Re(k)L - \epsilon\right)$, where $\exp(-\epsilon)$ is the damping factor that will be discussed in Section 4.7. In this context, it is important to note that $\epsilon = \Im(k)$ is a real number and its value is dictated by the underlying cable characteristics. The matrix σ_{xx} is the graph scattering matrix containing all the vertex scattering matrices. I_{2B} is a $2B \times 2B$ identity matrix. A measuring instrument like the Vector Network Analyser (VNA) may be used to both excite the system and detect the signal when it is finally transmitted onto the lead. This setup is illustrated in Figure 23. We will discuss the setup further in Chapter 5, which deals with experimental measurements.

When multiple leads are attached, (96) can be generalised as an $M \times M$ scattering matrix

$$S^M = \sigma_{00} + \sigma_{0x}S_{xx}\frac{1}{I_{2B} - T}\sigma_{x0}, \tag{97}$$

where the transfer matrix $T = \sigma_{xx}S_{xx}$, M is the number of leads attached, σ_{00} is now an $M \times M$ diagonal matrix containing prompt reflections, while

σ_{0x} and σ_{x0} are $M \times 2B$ and $2B \times M$ respectively. The matrices S_{xx}, σ_{xx} and I_{2B} are all of dimensions $2B \times 2B$. As a result of the multiple scattering modelled by $(I_{2B} - T)^{-1}$, S^M is effectively a sum over a large collection of interfering waves which brings about the typical fluctuations across frequencies. The model is doubly-validated by comparing it numerically with Transmission Line modelling, which was presented in Chapter 2. We present the numerical validation in Section 4.4. However, experimental validation of the model is presented subsequently in Chapter 5.

4.4 NUMERICAL VALIDATION OF QG MODEL

Although limited in its ability to model complicated networks, the transmission line (TL) method can be used to model a cascade of T-junction networks as we discussed in Chapter 2. In this section, we compare the predictions of the graph model with the TL model. To reiterate, TL model is based on the impedance matrix, while the QG model uses the scattering matrix. All the advantages of scattering methods over impedance methods enumerated in Chapter 1 still apply. Additionally, this graph method decomposes the modelling problem into a local vertex scattering and then provides an elegant way of aggregating them into a global graph scattering. This way, graphs of arbitrary complexity or topology are easily treated. As we shall see in subsequent chapters, graph topologies that are insurmountable using TL model, have been implemented using QG modelling. However, for the purpose

of comparison, we use graphs with low connectivity indices (i.e. $\gamma < 0.5$) which can be implemented by both methods. Classification of graphs by their connectivity index γ has been discussed in Chapter 3, Section 3.2.1.

Although this is a numerical comparison, we used characteristics (R, L, G, and C) of real cables (Farnell coaxial cable PP000663), which are frequency-dependent, to find the coaxial cable wave number,

$$\kappa(\omega) = \sqrt{(R + j\omega L)(G + j\omega C)}, \tag{98}$$

where R, L, G and C are the per unit length resistance, inductance, conductance and capacitance respectively, and ω is the angular frequency. Figure 24 shows the dependence of the cable characteristics on frequency up to the limit allowed by the VNA, which is 3 GHz. The details of the experimental set-up and measurements will be discussed in chapter 5. For now, it is sufficient to note that the realistic wave number of the coaxial cable (i.e. Farnell PP000663) was used in the numerical calculations.

Figure 25 shows the comparison between the QG and TL models for a single T-junction. Predictably, all the plots have perfect agreement. This is because both are solutions of the same problem. The regularly-spaced (periodic) resonances of Figure 25(a) occur as a result of commensurate lengths of cables used. When the cables lengths are incommensurate, the resonances become irregular as in the case of Figure 25(b) where the bond lengths, L_b, were generated so that $0 < L_b < 1$ with values of 0.5508 m, 0.7081 m and 0.2909 m.
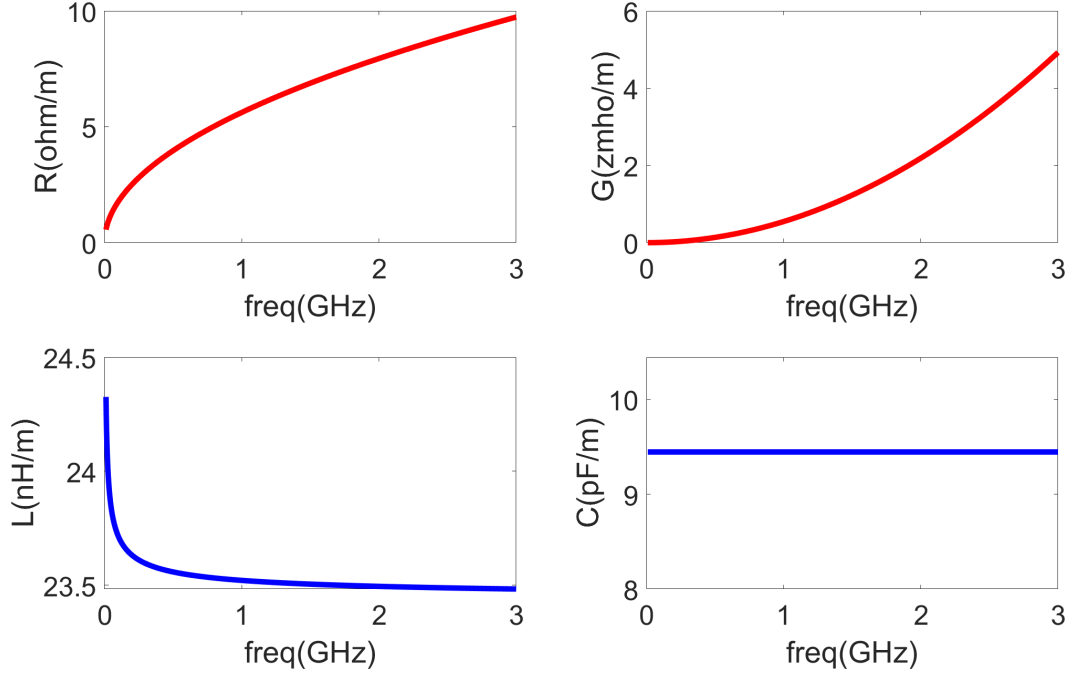
Figure 24.: A plot of cable characteristics as they vary with frequency.

We apply two types of boundary conditions and it is important to note where they are applied. If one end of a cable is not connected to any another, we require all the energy to be reflected back into the cable network without escaping. The boundary condition required at that point is the Dirichlet boundary condition (DBC), where $\lambda = \infty$ in (37). This corresponds to a short circuit in electronics, where the load impedance, $Z_L = 0$. However, if two or more cables are connected at a junction, then the amount of energy transmitted or reflected is determined by the vertex scattering matrix which is generated after applying Neumann boundary condition (NBC) (i.e. $\lambda = 0$ at that node). The schematic diagram showing how the cables are connected and terminated is given in Figure 26. The red arrows denote out-
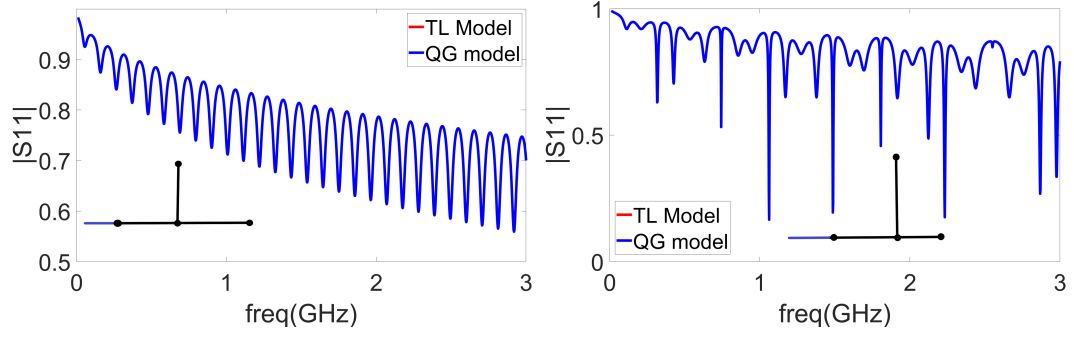
(a) $|S_{11}|$ for a T-Junction network with each bond lengths.

(b) $|S_{11}|$ for a T-Junction network with different bond lengths

Figure 25.: Comparison between the $|S_{11}|$ predictions of quantum graph and transmission line modelling for a single T-junction network connected to a lead. In (a), all cables in the network are $1m$ each, while in (b), the cables have lengths 0.5508 m, 0.7081 m and 0.2909 m.

going waves leaving a vertex, while the green arrows represent the incoming waves.

As the size of the graph B is increased, by cascading more and more of the T-junctions, the number of resonances increases within a given frequency window. This is seen in the cascade of 2 and 3 T-junctions shown in Figure 27(a) and (b), respectively. The lengths used for the a cascade of 2 T-junctions are 0.9670 m, 0.5472 m, 0.9727 m, 0.7148 m, 0.6977 m and 0.2161 m, while those in the 3 T-junctions architecture are 0.8929 m, 0.3320 m, 0.8212 m, 0.0417 m, 0.1077 m, 0.5951 m, 0.5298 m, 0.4188 m and 0.3354 m. With increasing connectivity, such as in the case of large complete graphs,
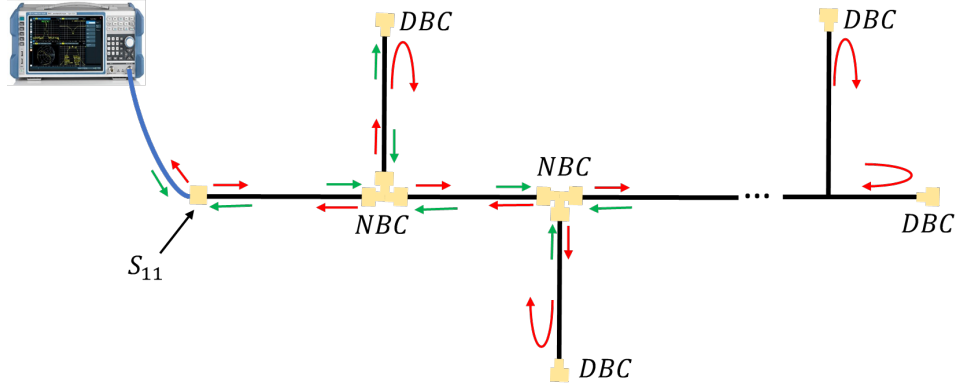
Figure 26.: An illustration of a cascade of T-junction networks. Dirichlet boundary conditions are applied at the dead-ends, while Neumann boundary conditions are applied at the other vertices. The out-going waves are labelled by the red arrows, while the green arrows represent the incoming waves.

signatures of chaotic systems begin to emerge. Some of these signatures are examined next.

4.5 WAVE CHAOS ON GRAPHS

We will use the graph theory in (97) to model both wired and wireless networks. With regards to wireless networks, we would like to model the propagation of electromagnetic waves in chaotic cavities. In order to do that, the graph model must be shown to be capable of modelling the chaotic behaviour of waves in such systems.

Chaotic systems exhibit universal characteristics which can be predicted accurately by random matrix theory (RMT). The most widely-used signa-
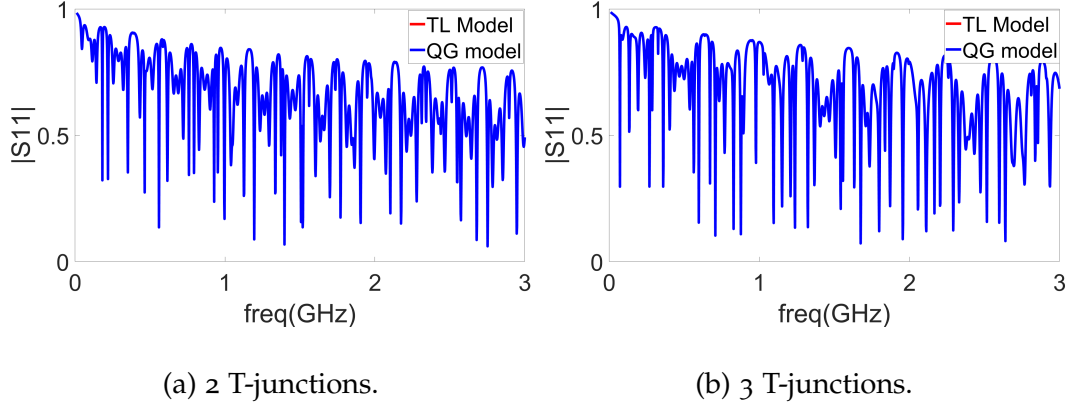
(a) 2 T-junctions. (b) 3 T-junctions.

Figure 27.: Comparison between QG model and TL model for a cascade of 2 and 3 T-junctions. The set of lengths for (a) and (b) in metres are $\{0.9670, 0.5472, 0.9727, 0.7148, 0.6977, 0.2161\}$ and $\{0.8929, 0.3320, 0.8212, 0.0417, 0.1077, 0.5951, 0.5298, 0.4188, 0.3354\}$

ture of chaos is the *resonance spacing distribution* [132] which will be treated later in this section. Additionally, the distribution law governing the asymptotic behaviour of eigenvalues of the transfer operator will be examined.

Before we begin the discussion of the characteristics of chaotic systems, it is important to note that the RMT predictions are for ideal (i.e. lossless) systems. Unfortunately, attaching leads to quantum graphs makes the system open, and some amount of energy is radiated through the leads. In order to mitigate the effects of these losses, we require a different, idealised boundary condition that will allow us to control the strength of coupling between the compact part of the graph and the leads. When graphs are weakly-coupled, then the amount of radiation through the leads reduces. The weaker the coupling, the smaller the radiation. In the next section, we propose how weak-coupling may be imposed on our model.

4.5.1 *Weak Coupling of Leads*

We now construct an idealised coupling matrix between leads and graph which allows us to treat and limit of the amount of loss from graph to leads. Whenever a lead is attached to a node (with valency v) of a compact graph, we look for a $v \times v$ unitary vertex scattering matrix, σ, of the form

$$\sigma = \begin{bmatrix} \cos\delta & \sin\delta\boldsymbol{a}^\dagger \\ -\sin\delta\boldsymbol{b} & \cos\delta\boldsymbol{V} \end{bmatrix}, \tag{99}$$

where $\boldsymbol{a}$ and $\boldsymbol{b}$ are column vectors of dimension $v - 1$ and $\boldsymbol{V}$ is a $(v - 1) \times (v - 1)$ matrix. The unitarity of σ requires that

$$\begin{aligned}
\boldsymbol{I}_v = \sigma^\dagger \sigma &= \begin{bmatrix} \cos\delta & -\sin\delta\boldsymbol{b}^\dagger \\ -\sin\delta\boldsymbol{a} & \cos\delta\boldsymbol{V}^\dagger \end{bmatrix} \begin{bmatrix} \cos\delta & \sin\delta\boldsymbol{a}^\dagger \\ -\sin\delta\boldsymbol{b} & \cos\delta\boldsymbol{V} \end{bmatrix} \\
&= \begin{bmatrix} \cos^2\delta + \sin^2\delta\boldsymbol{b}^\dagger\boldsymbol{b} & \cos\delta\sin\delta\left(\boldsymbol{a}^\dagger - \boldsymbol{b}^\dagger\boldsymbol{V}\right) \\ \cos\delta\sin\delta\left(\boldsymbol{a} - \boldsymbol{V}^\dagger\boldsymbol{b}\right) & \cos^2\delta\boldsymbol{V}^\dagger\boldsymbol{V} + \sin^2\delta\boldsymbol{a}\boldsymbol{a}^\dagger \end{bmatrix}
\end{aligned} \tag{100}$$

where $\boldsymbol{I}_v$ is a $v \times v$ identity matrix. Therefore σ is unitary if and only if the following three conditions are satisfied simultaneously:

$$\boldsymbol{b}^\dagger\boldsymbol{b} = 1, \tag{101}$$

$$\boldsymbol{a} = \boldsymbol{V}^\dagger\boldsymbol{b}, \tag{102}$$

and

$$\boldsymbol{I}_{(v-1)} = \cos^2\delta\boldsymbol{V}^\dagger\boldsymbol{V} + \sin^2\delta\boldsymbol{a}\boldsymbol{a}^\dagger, \tag{103}$$

where $I_{(v-1)}$ is a $(v-1) \times (v-1)$ unit matrix. Furthermore, (101) implies b is a unit vector, while (102) is true if and only if

$$a^\dagger = b^\dagger V. \tag{104}$$

Keeping the three equations (101), (102) and (103) in mind, we can write

$$
\begin{aligned}
I_{(v-1)} &= \cos^2 \delta V^\dagger V + \sin^2 \delta a a^\dagger \\
&= \cos^2 \delta V^\dagger V + V^\dagger b b^\dagger V \sin^2 \delta \\
&= V^\dagger \left(\cos^2 \delta + \sin^2 \delta b b^\dagger \right) V \\
&= U^\dagger U,
\end{aligned}
\tag{105}
$$

where U is a unitary matrix such that

$$U = \left[\cos^2 \delta I_{(v-1)} + \sin^2 \delta b b^\dagger \right]^{\frac{1}{2}} V. \tag{106}$$

That is, for any arbitrary unitary matrix U, we can define

$$V = \left[\cos^2 \delta I_{(v-1)} + \sin^2 \delta b b^\dagger \right]^{-\frac{1}{2}} U. \tag{107}$$

It is easy to show that, if b is any unit vector, then

$$\left[\cos^2 \delta I_{(v-1)} + \sin^2 \delta b b^\dagger \right]^{-\frac{1}{2}} = b b^\dagger + \frac{1}{\cos \delta} \left[I_{(v-1)} - b b^\dagger \right], \tag{108}$$

which gives

$$\left[\cos^2 \delta I_{(v-1)} + \sin^2 \delta b b^\dagger \right]^{\frac{1}{2}} = b b^\dagger + \cos \delta \left[I_{(v-1)} - b b^\dagger \right]. \tag{109}$$

This holds because b is an eigenvector of $b b^\dagger$ with eigenvalue 1 and all other eigenvalues are zero, with $b b^\dagger$ and $I_{(v-1)} - b b^\dagger$ acting as projections onto the respective eigenspaces.

Next, from (102) and definition of V, we can write

$$a = V^\dagger b$$

$$= U^\dagger \left[\cos^2 \delta I_{(v-1)} + \sin^2 \delta bb^\dagger \right]^{-\frac{1}{2}} b \qquad (110)$$

$$= U^\dagger b.$$

The last line in (110) implies $b = Ua$, and so a is also a unit vector.

In summary, we can form a $v \times v$ unitary matrix σ by implementing the following steps:

1. Choose an arbitrary unit vector b and an arbitrary $(v - 1) \times (v - 1)$ unitary matrix U.

2. Define V as in (107).

3. Find a by using (102).

4. Construct σ as in (99).

Alternatively, we can form σ by choosing any unit vector a and any $(v - 1) \times (v - 1)$ unitary matrix U and then finding b through $b = Ua$. Finally, V is found as defined in (107).

However, for a lead connected to a compact graph as illustrated in Figure 28, we construct σ by specifically choosing b as a unit vector of the form

$$b = \frac{1}{\sqrt{v-1}} \left. \begin{bmatrix} 1 \\ 1 \\ 1 \\ \vdots \\ 1 \end{bmatrix} \right\} (v-1)\text{entries.} \qquad (111)$$
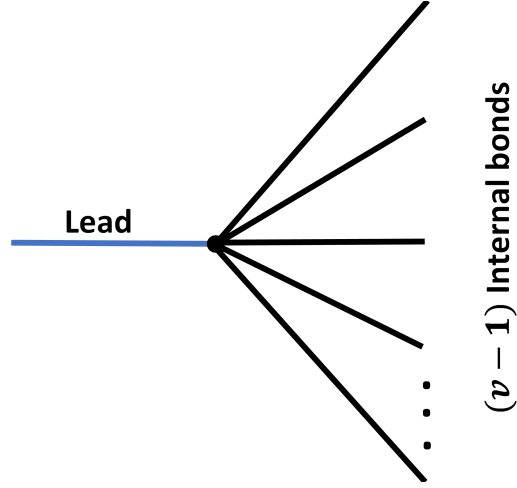
Figure 28.: Illustration of a lead (blue line) connected to $v - 1$ internal bonds of a compact graph at a vertex with valency v.

Furthermore, U is chosen to be a $(v - 1) \times (v - 1)$ Fourier matrix which is unitary by definition. We therefore continue to find V and then a as defined above.

The advantage of constructing σ this way is that it allows us to control the lead-bond transmission amplitudes, by changing δ, while maintaining the unitarity of σ. The δ parameter is therefore a free parameter, the choice of which does not affect the unitarity of σ. This way, we can make the coupling strength as weak as we desire.

In general, the coupling strength depends on the lead-bond amplitude (i.e. $\sin \delta a^\dagger$ in this case). The lead-bond amplitude also depends on the type of boundary conditions imposed at the graph nodes that are coupled to the lead. The definition and the expressions of the coupling strengths are defined in Section 4.6.3 for all the three boundary conditions (i.e. weak-, Fourier-, and Neumann-coupling) that are considered in this thesis.

Now that we are able to implement approximately closed graphs, we can proceed with the spectral analysis. As indicated before, we begin with *resonance spacing distribution* which is a litmus test when it comes to testing the presence of chaos. The treatment of the asymptotic distribution law of eigenvalues follows immediately after that.

4.5.2 *Resonance Spacing Distribution*

The resonance spacing distribution is one of the most commonly referred-to signatures of chaotic systems [132, 133]. The QG model implicitly takes into account the chaotic behaviour of the propagating signals. In this section, we investigate the nearest-neighbour level spacing distribution of the resonances and compare our results with the RMT predictions. The Wigner surmise regarding level spacing distribution of chaotic systems is given by

$$P_\beta^{\text{Wig}}(s) \propto s^\beta e^{-(A/2)s^2}, \tag{112}$$

where the value of the Dyson index β determines the symmetry class of the underlying system. The index $\beta = 1$ for systems with preserved time-reversal symmetry (TRS) and its statistics are predictable by those from Gaussian Orthogonal Ensemble (GOE) of large random matrices. $\beta = 2$ for systems where TRS is broken and can be predicted by the statistics of Gaussian Unitary Ensemble (GUE). With Gaussian Symplectic Ensemble (GSE), $\beta = 4$. Matrices considered under GOE, GUE and GSE are real symmetric, hermitian and real quaternions respectively [132, 134].

Since our graph model assumes zero external magnetic field, TRS is preserved. For closed (or at least weakly coupled) systems, the eigenvectors of the transfer matrix T are real (or approximately real). Therefore, we use the probability distribution

$$P_1(s) = \frac{\pi}{2} s e^{-(\pi/4)s^2}, \tag{113}$$

which provides a good approximation to the Wigner surmise [33]. Figure 29 shows the comparison between the Wigner distribution in (113) and a single realisation of a K6 network shown in the inset. Here, the value of the free parameter, which determines the coupling strength (coupling strengths are discussed in Section 4.6.3), is $\delta = 0.1$. The idea here is to show that weakly-coupled graphs are can be compared with the predictions of closed graphs (i.e. Wigner predictions). By way of emphasis, the transfer matrix of a K6 network is only 30×30 because the number of bonds in K6 is $B = 15$. However, there is still a remarkable agreement considering the fact that the size of the matrix is small and the fact that only one realisation of the graph is shown. The main reason we are showing the chaotic behaviour in graphs is because, in subsequent sections, we are going to use quantum graphs to model chaotic microwave cavities and wireless communication channels which have inherent wave chaos in them. This modelling will be done through random coupling model (RCM) discussed previously in Section 4.2. The quantum graph analogue of RCM is one of the main results of this thesis and is proposed in Section 4.6. In the meantime, we continue
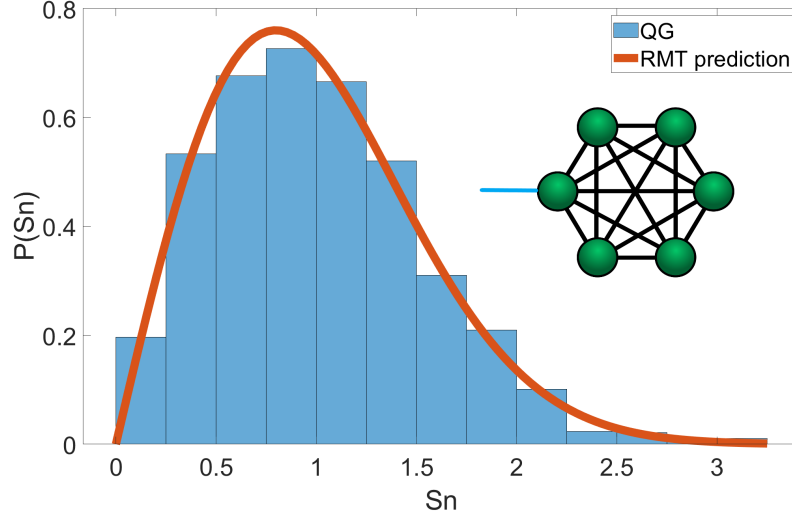
Figure 29.: Level spacing distribution of a K6 network compared with the Wigner surmise [132]. The free parameter $\delta = 0.1$.

with the spectral analysis, where we discuss the asymptotic behaviour of eigenvalues of the transfer matrix.

4.5.3 *Asymptotic Distribution Law of Eigenvalues*

From Chapter 3, we know that the complex zeroes of the secular function $\zeta(k) = \det(I_{2B} - T(k))$ are in one-to-one correspondence with the resonances of the S^M spectrum. When leads are coupled to a graph, the transfer matrix $T(k)$ becomes sub-unitary. As a result, the Perron-Frobenius theorem guarantees that the eigenvalues are located inside a unit circle [108]. This implies that all the resonances are located in the lower half of the complex k plane. On the other hand, $T(k)$ is unitary for closed systems and the eigenvalues are distributed on the unit circle. In such closed systems,

the asymptotic distribution of k was originally predicted by Hermann Weyl more than a century ago [135]. This is popularly known as the Weyl's law. Since then, significant amount of work has been done to derive the equivalence of the law in specific applications. For example, [103] is a review paper on 100 years of Weyl law and how it is implemented in a variety of applications. For quantum graphs, the Weyl's law is given by the counting function [102]

$$N(k) = \frac{\mathcal{L}}{\pi}k + A, \tag{114}$$

where $N(k)$ is the number of resonances less than or equal to k, and A is the intercept. In general, A is function that is bounded by a constant in the limit of large k. However, in Figure 30, we chose the best value of A that fits the staircase. The total length of the graph $\mathcal{L} = \sum_{b=1}^{B} L_b$ is known as the *'volume'* of the graph.

Effectively, the counting function is a form of a staircase function which increases by one whenever it encounters a resonance along the frequency spectrum. Figure 30(a) shows a single realisation of a weakly coupled K6 network (as shown in the inset), where 1509 resonances were counted and compared with the prediction of Weyl law. By *weakly-coupled* graphs, we mean graphs whose losses through the leads to the external environment are negligible.

The details of how to mathematically achieve weak coupling while maintaining unitarity at the vertex was proposed in Section 4.5.1. After investigation, we found the intercept term in Figure 30 to be $A = -5$ for this example.

(a) Weyl law for a K6 network.

(b) Blow up.
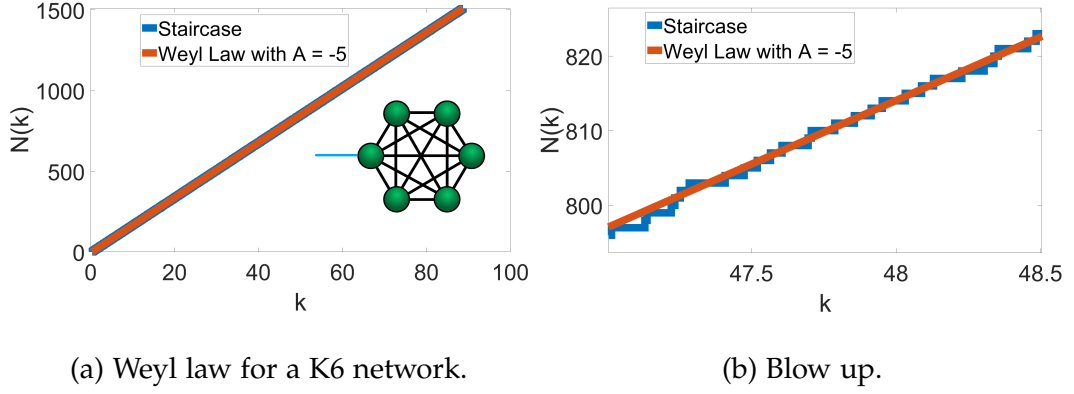
Figure 30.: Comparison between staircase function and the prediction of Weyl law for a weakly coupled K6 network where the lengths in metres are randomly generated with uniform distribution between 0 and 10 where 1509 resonances were counted in a single realisation.

The blue curve is a staircase function which goes up one step whenever a resonance is encountered. The red line is the plot Weyl's prediction in (114). Bond lengths in this example were chosen to be uniformly distributed between 0 and 10 m. Figure 30(b) is the magnified version of (a) and it only shows the resonances from the 800th to 820th. This allows for the details of the staircase to be displayed. We could see that the resonance count fits the prediction of Weyl law so well.

4.6 GRAPH ANALOGUE OF RCM

In this section, we propose a graph analogue of RCM which is useful in the study of propagating microwaves in irregular chaotic cavities. It also

provides a flexible platform in the study of interference effects as the coupling regimes create avenues for signal leakages. This is central to the study of electromagnetic compatibility (EMC). Additionally, this model will provide us with tractable alternatives regarding rate of information transfer in multichannel communication systems. In particular, we will derive, from this model, closed-form solutions for the distribution of channel capacity in low-loss systems as well as systems with high losses. We begin with the procedure for symmetrising the transfer matrix $T = \sigma_{xx} S_{xx}$ in (97). The symmetrised transfer matrix $\hat{T}$ is an alternative of T which allows for direct comparison with the transfer matrix in RCM.

4.6.1 *Symmetrised QGM*

If we write $S_{xx} = \sqrt{S_{xx}}\sqrt{S_{xx}}$, then (97) can be written as an infinite sum. That is

$$
\begin{aligned}
S^M &= \sigma_{00} + \sigma_{0x}\sqrt{S_{xx}}\sqrt{S_{xx}}\frac{1}{I_{2B} - \sigma_{xx}\sqrt{S_{xx}}\sqrt{S_{xx}}}\sigma_{x0} \\
&= \sigma_{00} + \sigma_{0x}\sqrt{S_{xx}}\sqrt{S_{xx}}\left[I + \sigma_{xx}\sqrt{S_{xx}}\sqrt{S_{xx}} + \right. \\
&\qquad\qquad\qquad \left. \sigma_{xx}\sqrt{S_{xx}}\sqrt{S_{xx}}\sigma_{xx}\sqrt{S_{xx}}\sqrt{S_{xx}} + \cdots\right]\sigma_{x0}.
\end{aligned}
\tag{115}
$$

By multiplying the terms in the square bracket by $\sqrt{S_{xx}}$ from the left hand side and factorising same from the right hand side, we can write the scattering matrix S^M in terms of a symmetrised transfer matrix $\hat{T}$ as below.

$$
\begin{aligned}
S^M &= \sigma_{00} + \sigma_{0x}\sqrt{S_{xx}}\left[\sqrt{S_{xx}} + \left(\sqrt{S_{xx}}\sigma_{xx}\sqrt{S_{xx}}\right)\sqrt{S_{xx}} + \right. \\
&\qquad \left. \left(\sqrt{S_{xx}}\sigma_{xx}\sqrt{S_{xx}}\right)\left(\sqrt{S_{xx}}\sigma_{xx}\sqrt{S_{xx}}\right)\sqrt{S_{xx}} + \cdots\right]\sigma_{x0} \\
&= \sigma_{00} + \sigma_{0x}\sqrt{S_{xx}}\left[I + \left(\sqrt{S_{xx}}\sigma_{xx}\sqrt{S_{xx}}\right) + \right. \\
&\qquad \left. \left(\sqrt{S_{xx}}\sigma_{xx}\sqrt{S_{xx}}\right)\left(\sqrt{S_{xx}}\sigma_{xx}\sqrt{S_{xx}}\right) + \cdots\right]\sqrt{S_{xx}}\sigma_{x0} \\
&= \sigma_{00} + \sigma_{0x}\sqrt{S_{xx}}\frac{1}{I_{2B} - \hat{T}}\sqrt{S_{xx}}\sigma_{x0},
\end{aligned}
$$

$$(116)$$

where $\hat{T} = \sqrt{S_{xx}}\sigma_{xx}\sqrt{S_{xx}}$.

Furthermore we can use eigenvalue decomposition to write $\hat{T}$ as $\hat{T} = V^\dagger \Lambda V$, where V is a $2B \times 2B$ matrix whose ith column forms the ith eigenvector of $\hat{T}$. Λ is a $2B \times 2B$ diagonal matrix with diagonal elements forming the respective eigenvalues. Since $\hat{T}$ is unitary for closed (or weakly coupled) systems, the eigenvalues lie on a complex unit circle. We are therefore able to write (116) as

$$
\begin{aligned}
S^M &= \sigma_{00} + \sigma_{0x}\sqrt{S_{xx}}V\frac{1}{I_{2B} - \Lambda}V^\dagger\sqrt{S_{xx}}\sigma_{x0} \\
&= \sigma_{00} + Y\frac{1}{I_{2B} - \Lambda}Y^\dagger,
\end{aligned}
$$

$$(117)$$

where $Y = \sigma_{0x}\sqrt{S_{xx}}V$ and the symbol $\dagger$ is the conjugate transpose.

In order for (117) to qualify as an analogue of RCM, which was presented as (87), we need to compare the variables and parameters of both equations to ensure that they model the same events. At this point, σ_{00} in (117) and $j\Im[Z^{rad}]$ in (87) are both diagonal matrices modelling the prompt reflections

(radiation impedances); Λ in (117) and Λ_Z in (87) are both diagonal matrices with their diagonal elements constituting the eigenvalues of their respective transfer matrices. What is left at this stage is to answer the question of whether or not Y is a vector of non-correlated Gaussian random variables with zero mean and unit variance just like the variable W which has been presented in (89). The analysis of variable Y, which is analogous to variable W in (87), is treated in Section (4.6.2).

4.6.2 *Distribution of Y*

In Section 3.3.2, we have seen how the type of boundary condition affects the distribution of energy in graphs, which also dictates the distribution of Y. For example, we have seen that the Neumann boundary condition results in unequal scattering of energy at vertices of graphs. The scattering events at the nodes favours reflection (back scattering) when $v > 4$. The unequal distribution of energy affects the distribution of Y.

As you recall from the theory of RCM, the random variable W, which is analogous to Y is assumed to be Gaussian distributed. The assumption of 'Gaussianity' is based on effective mixing of the underlying waves, which Neumann boundary conditions do not satisfy. This culminates in making Y non-Gaussian. Investigating the distribution of Y further, we found Y, empirically, to be Laplace distributed for Neumann graphs. A random variable

Y is said to be a Laplace distribution, with *location* and scale (or *diversity*) parameters μ and b respectively, if the probability distribution is given by

$$f(Y) = \frac{1}{2b}\exp\left(-\frac{|Y - \mu|}{b}\right),\tag{118}$$

with variance $2b^2$.

The distribution of the real part of Y is shown in Figure 31(a) for a graph with Neumann nodes and the topology of a HEX6 graph as shown in the inset. The histogram is obtained by simulating an ensemble of 8000 HEX6 graphs each with uniformly distributed random lengths. The lengths l are chosen such that $0 \le kl \le 2\pi$, where k is the wave number. The red curve is a Laplace distribution with parameter $b = 0.0425$. To reiterate, the real and imaginary parts are independent and identically distributed (iid) random variables and therefore it is enough to show only the real part. In addition to HEX6 graph, the distribution of Y has been investigated for HEXv graphs, which have larger numbers of bonds and each case resulted in the same distribution of Y. Specifically, we simulated HEX8, HEX10, HEX14, HEX18 and HEX20. These are large graphs in terms of the number of bonds B they contain. For example, the number of bonds in the HEX20 graph is 440.

However, because HEXv graphs are graphs with a medium level of connectivity (i.e. connectivity index $\gamma \approx 0.5$), it is not enough to use only HEXv graphs to make a general statement about the distribution of Y. Therefore, we further investigated fully-connected graphs, which have the maximum level of connectivity. These are graphs where each node is connected to every other node in the graph network. Therefore the connectivity index for

fully-connected graphs is always 1. In particular we have looked at $K(v+1)$ graphs. These graphs generally contains $v+1$ vertices, which each vertex has a valency of v. Specifically, we have considered K10 and K16, and Y is Laplace distribution in both cases. Although it is not possible to consider each and every type of graph, it is reasonable to hypothesise that the distribution of Y is generally Laplace distributed at least for large graphs with medium to high connectivity.

The variance of Y is defined for a Laplace distribution as $2b^2$. The analytical expression for the variance of Y, for Neumann graphs, is calculated later in Section 4.6.2.2 as $2(v-1)/v^2B$. Relating $2b^2$ with the analytical expression, it is easy to establish the relationship between the parameter b with the graph size B and the valency of the node v to which an external lead is attached.

Figure 31(b) shows the distribution of Y for the same HEX6 graphs, as in (a), but with Fourier nodes. It is apparent that Y is normally distributed with zero mean but with a variance that is different from unity. However, the variance of Y can always be standardised to unity. Therefore, with Fourier graphs, we can always find a standardised version of the random variable Y which satisfies all the properties discussed in section 4.2 for random coupling model. The standardisation process will be discussed after deriving the variance of Y for Fourier graphs.
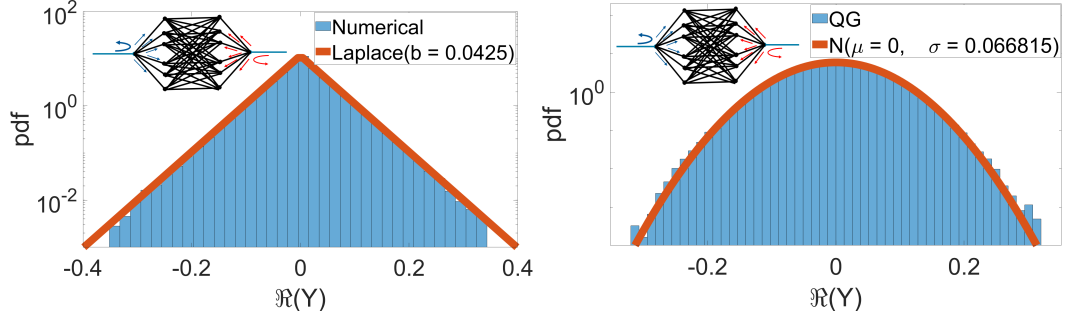
(a) Real part of Y for Neumann graph.

(b) Real part of Y for Fourier graph.

Figure 31.: (a) is the distributions of Y for HEX6 Neumann graph, while
(b) is the distribution of Y for the same graph as (a) but with
Fourier boundary conditions. In each case, an ensemble average
of 8000 graphs were used with lengths randomly generated from
a uniform distribution such that $kL \in [0 \quad 2\pi]$.

4.6.2.1 *Variance of Y for Fourier graphs*

Before finding the variance of $Y = \sigma_{0x}\sqrt{S_{xx}}V$, we need to first calculate the
square root of the shift matrix $\sqrt{S_{xx}}$ which is one of the constituent variable
of Y. From (78) and (79), we know that S_{xx} is a block diagonal matrix where
the *ith* block is given by

$$S_{xx_{(i)}} = \begin{bmatrix} 0 & e^{jkL_i} \\ e^{jkL_i} & 0 \end{bmatrix}. \tag{119}$$

Therefore calculating $\sqrt{S_{xx}}$ reduces effectively to finding the matrix-square-
root of each block. Hence we focus on one of such blocks first and then

generalise later. Each block of S_{xx} is a unitary matrix and therefore it is diagonalisable as

$$S_{xx_{(i)}} = \frac{1}{\sqrt{2}} \begin{bmatrix} 1 & -1 \\ 1 & 1 \end{bmatrix} \begin{bmatrix} e^{jkL_i} & 0 \\ 0 & -e^{jkL_i} \end{bmatrix} \frac{1}{\sqrt{2}} \begin{bmatrix} 1 & 1 \\ -1 & 1 \end{bmatrix}. \tag{120}$$

Therefore a square root can be written as

$$\sqrt{S_{xx_{(i)}}} = \frac{1}{2} \begin{bmatrix} 1 & -1 \\ 1 & 1 \end{bmatrix} \begin{bmatrix} e^{jkL_i/2} & 0 \\ 0 & je^{jkL_i/2} \end{bmatrix} \begin{bmatrix} 1 & 1 \\ -1 & 1 \end{bmatrix}$$

$$= \frac{1}{2} e^{jkL_i/2} \begin{bmatrix} 1+j & 1-j \\ 1-j & 1+j \end{bmatrix} \tag{121}$$

By noting that $1+j = \sqrt{2}\exp(j\pi/4)$, and $1-j = -j\sqrt{2}\exp(j\pi/4)$, we can write

$$\sqrt{S_{xx_{(i)}}} = \frac{1}{\sqrt{2}} e^{j(kL_i/2+\pi/4)} \begin{bmatrix} 1 & -j \\ -j & 1 \end{bmatrix}. \tag{122}$$

This implies

$$\left(\sqrt{S_{xx_{(i)}}}\right) \left(\sqrt{S_{xx_{(i)}}}\right)^\dagger = \left|\sqrt{S_{xx_{(i)}}}\right|^2 = I_2, \tag{123}$$

where I_2 is a 2×2 unit matrix. Therefore $\sqrt{S_{xx}}$ is a unitary matrix and therefore preserves the inner product of complex vectors. Now if we represent the nth eigenvector as V_n, then its variance is $\langle |V_n|^2 \rangle = 1/2B$, where $2B$ is the size of the underlying matrix. Consequently

$$\left\langle |\sqrt{S_{xx}}V_n|^2 \right\rangle = \left\langle |V_n|^2 \right\rangle = \frac{1}{2B}. \tag{124}$$

Figure 32 shows the distributions of the real and the imaginary parts of $\sqrt{S_{xx}}V_n$ of a HEX6 Fourier graph with $B = 48$ bonds. The red curve in each case represents a normal distribution with the standard deviation $1/2\sqrt{B} = 0.072169$ as shown in the legends of the figure.
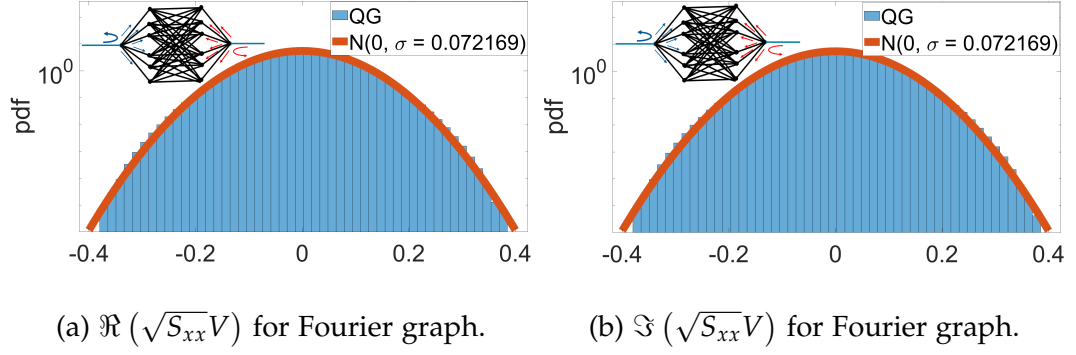
(a) $\Re\left(\sqrt{S_{xx}}V\right)$ for Fourier graph.

(b) $\Im\left(\sqrt{S_{xx}}V\right)$ for Fourier graph.

Figure 32.: (a) and (b) are the distributions of $\Re\left(\sqrt{S_{xx}}V\right)$ and $\Im\left(\sqrt{S_{xx}}V\right)$ respectively. The Fourier graph is made up of HEX6 architecture (as illustrated in the inset) with $B = 48$. The red curve is the distribution of a zero mean Gaussian random variable with variance of $1/4B$. The distribution is generated from an ensemble of 5000 of such Fourier graphs.

For a Fourier graph connected to a lead at a vertex with valency v, the variance of Y is calculated as

$$
\begin{aligned}
\left\langle |Y_n|^2 \right\rangle &= \left\langle |\sigma_{0x}|^2 \right\rangle \left\langle |\sqrt{S_{xx}}V_n|^2 \right\rangle \\
&= \left(\sum_{i=1}^{v-1} \frac{1}{v} \right) \left(\frac{1}{2B} \right) \\
&= \frac{v-1}{2vB}.
\end{aligned}
\tag{125}
$$

From (125), we have seen that $\left\langle |Y_n|^2 \right\rangle \neq 1$. But we can always standardise Y to have a unit variance by using the transformation $X = (1/\sigma_Y)Y$, where $\sigma_Y = \sqrt{(v-1)/2vB}$ is the standard deviation of Y. That is, if Y is a Gaussian random variable with zero mean and standard deviation σ_Y, then its probability density function is given by

$$
f_Y(y) = \frac{1}{\sigma_Y\sqrt{2\pi}} e^{-\frac{1}{2}\left(\frac{y}{\sigma_Y}\right)^2}.
\tag{126}
$$

Now let $X = (1/\sigma_Y)Y$. Then

$$f_X(x) = f_Y(y)\frac{dY}{dX}$$

$$= \frac{1}{\sigma_Y\sqrt{2\pi}}e^{-\frac{1}{2}\left(\frac{y}{\sigma_Y}\right)^2}\sigma_Y \tag{127}$$

$$= \frac{1}{\sqrt{2\pi}}e^{-\frac{1}{2}x^2}.$$

Therefore X is a standard normal random variable with zero mean and unit variance.

For a HEX6 Fourier graph, standard deviation of the real part of Y is $\sqrt{(v-1)/(4vB)} = 0.066815$. This is shown in Figure 31(b) where the theoretical prediction accurately described the numerical simulation. In that case the random variable $X = (1/\sigma_Y)Y \sim N(0,1)$ and has all the properties of the random variable W as discussed in the random coupling model in (89). The distributions of $\Re(X)$ and $\Im(X)$ are shown in Figure 33.

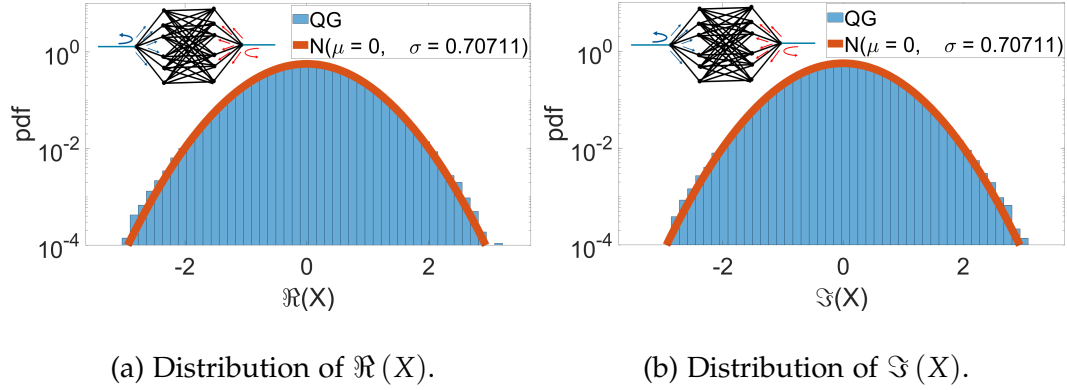(a) Distribution of $\Re(X)$.   (b) Distribution of $\Im(X)$.

Figure 33.: (a) and (b) are the distributions of real and imaginary parts of X respectively. The red curve is the distribution of a zero mean Gaussian random variable with standard deviation $1/\sqrt{2}$.

We are now able to re-write our graph model in (117) in terms of the random variable X as an analogue of random coupling model as follows:

$$
\begin{aligned}
S^M &= \sigma_{00} + Y \frac{1}{I_{2B} - \Lambda} Y^\dagger \\
&= \sigma_{00} + \sigma_Y X \frac{1}{I_{2B} - \Lambda} X^\dagger \sigma_Y \\
&= \sigma_{00} + \sqrt{\frac{v-1}{2vB}} \xi \sqrt{\frac{v-1}{2vB}},
\end{aligned}
\tag{128}
$$

where $\xi = X(I_{2B} - \Lambda)^{-1}X^\dagger$ is the analogue of the normalised impedance matrix ξ_Z, representing the statistical part of the model. Detailed discussions of the statistics of ξ are presented in Chapter 6 for Fourier graphs, and in Chapter 7 for Neumann graphs. For now, it suffice to note that, the distribution of ξ (depending on losses and boundary conditions) interpolates between t-distribution and Gaussian distribution.

The statistics of both ξ and ξ_Z are system independent with characteristics that are predictable by random matrix theory. The expression $\sqrt{(v-1)/2vB}$ represents the system specific part of the graph model and it is non-statistical. This is analogous to the real part of the radiation impedance $[\Re\left(Z^{\mathrm{rad}}\right)]^{1/2}$ in (87) which is also non-statistical and contains the system-specific features of the random coupling model. Finally, σ_{00} is a diagonal matrix with the diagonal elements representing the prompt reflections of the graph model and this plays the role of the imaginary part of the radiation impedance $[\Im\left(Z^{\mathrm{rad}}\right)]$ matrix which is also diagonal and impedes the flow of energy.

Now, the only thing left is the question of how we incorporate losses (apart from those due to radiating leads) into the graph model. We will

discuss that after calculating the variance of Y for Neumann graphs and for weakly-coupled graphs.

4.6.2.2 *Variance of Y for Neumann Graphs*

For a Neumann graph, the bond-lead transmission amplitudes are given by $\sigma_{0x} = 2/v$. Therefore

$$
\begin{aligned}
\left\langle |Y_n|^2 \right\rangle &= \left\langle |\sigma_{0x}|^2 \right\rangle \left\langle |\sqrt{S_{xx}} V_n|^2 \right\rangle \\
&= \left(\sum_{i=1}^{v-1} \left(\frac{2}{v} \right)^2 \right) \left(\frac{1}{2B} \right) \\
&= \frac{2(v-1)}{v^2 B}.
\end{aligned}
\tag{129}
$$

This implies that the real and imaginary parts of Y will each have a variance given by $(v-1)/(v^2 B)$. Similarly, we can scale Y to have unit variance as before. We call this scaled variable X. In this case, the graph analogue of RCM as written in (128) will change for Neumann graphs. The modified formula is therefore given by

$$
\begin{aligned}
S^M &= \sigma_{00} + Y \frac{1}{I_{2B} - \Lambda} Y^\dagger \\
&= \sigma_{00} + \sigma_Y X \frac{1}{I_{2B} - \Lambda} X^\dagger \sigma_Y \\
&= \sigma_{00} + \sqrt{\frac{2(v-1)}{v^2 B}} \xi \sqrt{\frac{2(v-1)}{v^2 B}}.
\end{aligned}
\tag{130}
$$

A closer look at (128) and (130) reveals that, although the distribution of Y for Fourier and Neumann graphs remains different, their variance coincides when the valency is $v = 2$. Equations (128) and (130) are valid for fully-connected graphs, as well as the hexagonal graphs (i.e. graphs with medium connectivity index as defined in Chapter 3). A large ensemble (above 2000) of these randomly selected graphs are required to simulate the statistics of ξ.

The bond lengths are randomly selected from a uniform distribution such that the phases of the underlying waves $0 \leq kl \leq 2\pi$. Additionally, the number of bonds B of the graphs must large enough (graphs with $B > 48$ have been found to be sufficient in this thesis).

From Figure 31(a), we have seen that for Neumann graphs, Y is Laplace-distributed with zero mean. The variance of Laplace distribution is given by $2b^2$, and so the real (or the imaginary) part of the scaled variable X will have a variance of $1/2$. This corresponds to $b = 1/2$, when one equates the two variances.

Figure 34 shows the distribution of the real part of X for HEX10 Neumann graph with $B = 120$ as shown in the inset. We used an ensemble of 5000 of such Neumann graphs with their lengths randomly selected from a uniform distribution such that $kL_i \in [0 \quad 2\pi]$, where k is the wave number and L_i is the length of bond i.
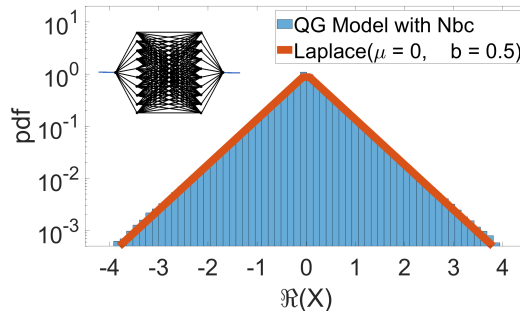

Figure 34.: Distribution of the standardised random variable $\Re(X)$ for a HEX10 Neumann graph. The red curve represents the pdf of Laplace random variable with variance $1/2$.

4.6.2.3 *Variance of Y for Weakly Coupled Graphs*

For a weakly-coupled graph, the bond-lead transmission amplitudes are given by $\sigma_{0x} = \sin\delta/\sqrt{v-1}$. Therefore

$$
\begin{aligned}
\langle |Y|^2 \rangle = \sigma_Y^2 &= \langle |\sigma_{0x}|^2 \rangle \langle |\sqrt{S_{xx}} V_n|^2 \rangle \\
&= \sum_{b=1}^{v-1} \frac{\sin^2\delta}{v-1} \left(\frac{1}{2B} \right) \\
&= (v-1) \frac{\sin^2\delta}{v-1} \left(\frac{1}{2B} \right) \\
&= \frac{\sin^2\delta}{2B}.
\end{aligned}
\tag{131}
$$

Equation (131) is the variance of Y for a weakly-coupled graph regardless of whether the boundary conditions in the compact part of the graph are Fourier or Neumann. Again, Y can be scaled to have unit variance as previously discussed. Consequently the graph analogue of RCM, for a weakly-coupled graph is given by

$$
S^M = \sigma_{00} + \sqrt{\frac{\sin^2\delta}{2B}} \, \xi \sqrt{\frac{\sin^2\delta}{2B}}.
\tag{132}
$$

Figure 35(a) shows the distribution of Y, while (b) shows the distribution of the scaled variable X for a weakly-coupled HEX10 Fourier graph. We chose the free parameter, which controls the level of energy leakage through the leads, to be $\delta = 0.1$.

After finding the variance of Y for various boundary conditions, we define the coupling strength next.

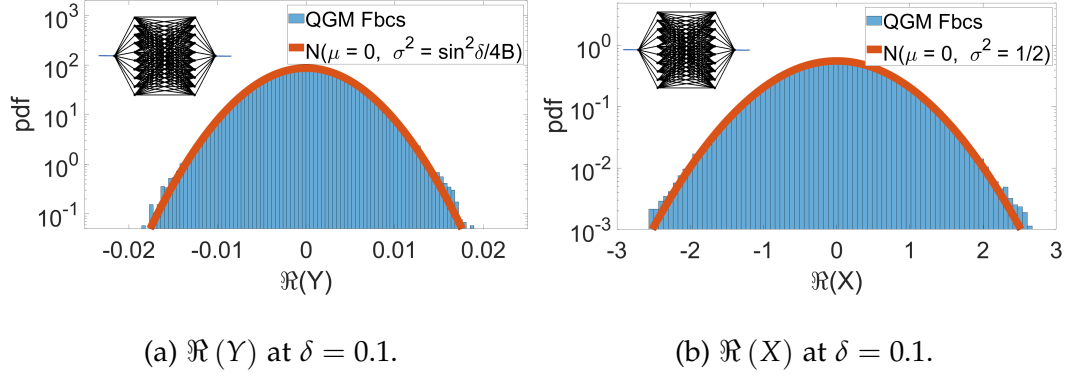(a) $\Re(Y)$ at $\delta = 0.1$.   (b) $\Re(X)$ at $\delta = 0.1$.

Figure 35.: (a) is the distribution of real part of Y compared with the pdf of a normal distribution with zero mean and variance $\sin^2 /4B$ (red solid curve), while (b) the distribution of the standardised random variable X. The red curve is the pdf of a zero mean Gaussian random variable with variance $1/2$.

4.6.3 Graph Coupling Strengths

From the second line of (128) the off-diagonal, S_t^M, of S^M is given by $\sigma_Y^2 \xi$. Therefore

$$|S_t^M|^2 = \sigma_Y^4 |\xi|^2$$
$$= \tau |\xi|^2,$$

$$(133)$$

where we define the coupling strength τ as the square of the variance of Y. That is,

$$\tau = \sigma_Y^4. \tag{134}$$

Consequently, we have three expressions for coupling strengths each corresponding to a specific boundary condition at the graph node that is connected to a lead.

From (128), (130), (132), the expressions for the coupling strength of Fourier, Neumann, and weakly-coupled graphs are respectively given by the equations

$$\tau = \left(\frac{v-1}{2vB}\right)^2, \tag{135}$$

$$\tau = \left(\frac{2(v-1)}{v^2 B}\right)^2, \tag{136}$$

and

$$\tau = \left(\frac{\sin^2 \delta}{2B}\right)^2. \tag{137}$$

Finally, the next item which will complete the graph model is how losses are incorporated into the graph system. This is discussed next.

4.7 LOSS PARAMETER

In the random coupling model, the loss parameter, α is a dimensionless parameter which determines the level of losses in chaotic systems [31, 35]. This has been discussed for chaotic cavities in (90).

In this section, we derive a corresponding expression of the loss parameter in quantum graphs. Before we begin these calculations, we note that there are two main sources of losses. These are radiation through the leads to the outside environment and internal losses we introduce at the local vertex scattering. For lossless systems, the eigenvalues λ_n of the transfer matrix $\hat{T}$ are uniformly distributed on the unit circle. This is because $\hat{T}$ is unitary and the Perron-Frobenius theorem guarantees that $|\lambda_n| = 1$ for all values of

$n \in 1, 2, \cdots, 2B$ [108]. This implies that, for a graph consisting of B bonds, we can write $\lambda_n = \exp(j\phi_n)$ for $n = 1, 2, 3, \cdots, 2B$ and $\phi = kL$.

However, for lossy systems where $\hat{T}$ is sub-unitary, $|\lambda_n| = r$, where $r < 1$ is the spectral radius of $\hat{T}$ and the eigenvalues lie strictly inside the unit circle. In this case we write $\lambda_n = r\exp(j\phi_n)$, where $r = \exp(-\epsilon_0 - \epsilon)$. ϵ_0 and ϵ are small positive real numbers such that $\exp(-\epsilon_0)$ and $\exp(-\epsilon)$ represent the external losses due to radiating leads, and the internal losses in the compact part of the graph, respectively. This is generalised as $\lambda_n = \exp(j\theta_n)$, where $\theta_n = \phi_n + j(\epsilon_0 + \epsilon)$. Therefore, the imaginary part of the complex phase represents the losses in the system. We therefore define the loss parameter as

$$
\begin{aligned}
\alpha &= \frac{\langle \Im(\theta_n) \rangle}{\langle \Delta\theta_n \rangle} \\
&= \frac{\epsilon_0 + \epsilon}{2\pi/(2B)} \\
&= \frac{B}{\pi}(\epsilon_0 + \epsilon) \\
&= \alpha_0 + \alpha_1
\end{aligned}
\tag{138}
$$

where $\langle \Delta\theta_n \rangle$ is the average spacing between the complex phases, $\alpha_0 = B\epsilon_0/\pi$ characterises losses due to radiations through the leads, and $\alpha_1 = B\epsilon/\pi$ characterises the losses within the internal (compact) part of the graph.

As we have seen earlier in Section 4.2 of this chapter, the analogue loss parameter in RCM is given by

$$
\alpha = \frac{k^2}{\Delta k_n^2 Q},
\tag{139}
$$

where k is the wave number, Δk_n^2 is the mean level spacing, and Q is the quality factor of the chaotic cavity, which is defined as the ratio of energy stored in the cavity to the power losses within the cavity (i.e. ohmic and dielectric losses) as well as losses due to radiating ports [35]. Similarly, the loss parameter in the graph model also depends on the average spacing of the complex phases, and losses in the internal part of the graph (i.e. ohmic and dielectric losses) as well as losses due to radiating leads. It is clear that, both parameters characterise the same types of losses within the system under consideration.

It must be noted that unlike ϵ that depends on the ohmic and dielectric losses, the value of ϵ_0 is dictated by the boundary conditions at the nodes to which the leads are attached. To be able to control α_0, we use the weak-coupling mechanism we discussed in section 4.5.1. This will allow us to control the amount of energy that goes in and out of the graph while maintaining unitarity of the vertex scattering matrix. Refer to section 4.5.1 for details of how we implemented weak-coupling of leads to graphs.

Figure 36 shows the distribution of eigenvalues for a HEX10 graph with $\alpha \in \{0, 5, 10\}$. To achieve $\alpha = 0$ (shown as blue curve), we weakly coupled the lead to the graph so that the graph behaves as if it were a closed graph. The red and yellow curves represent the same graph topology but with losses introduced such that $\alpha = 5$ and $\alpha = 10$ respectively. The larger the losses the smaller the radius of the circle. This is in conformity with the Perron-Frobenius theorem.
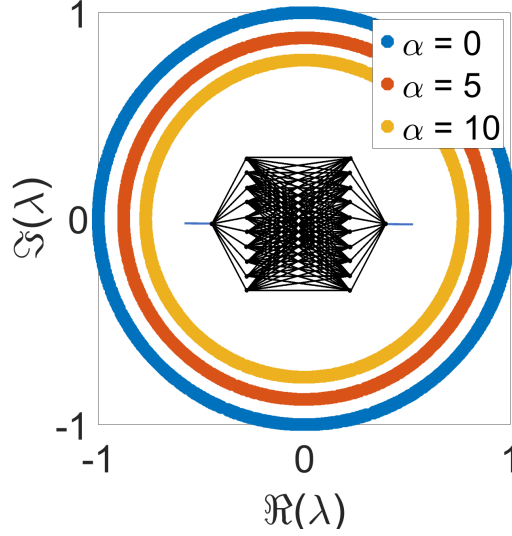
Figure 36.: Distribution of eigenvalues on a complex plane for a HEX10 Fourier graphs with $\alpha = 0, 5, 10$.

In the random coupling model, although the chaotic cavities are open systems (because they are coupled to multiple channels), losses are added through a perturbative approach so that it allows the use of statistical predictions of closed systems from RMT. This means that the statistical properties of the normalised impedance matrix ξ_Z are predicted by that of a closed system even though the cavity is open [36]. Similarly, attaching leads to graphs cause them to behave as open systems just like in the case of RCM.

For example, Figure 37 shows the losses due to radiating leads α_0 with increasing graph size B. We used HEXv graphs (as discussed in Chapter 3) with Fourier boundary condition for which $v = 2, 4, 6, \cdots, 20$. From (138), α_0 represent losses that are purely as a result of radiating leads when the compact part of the graph is entirely made up of lossless cables. This

implies that the losses through the leads are not negligible especially as the graph size increases.

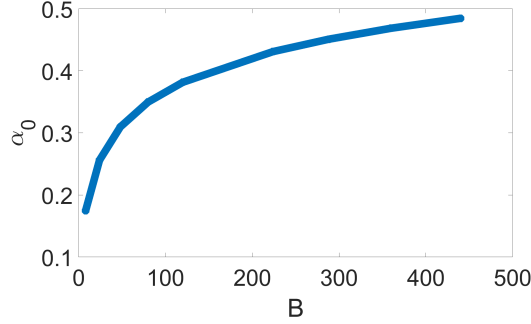Figure 37.: Variation of α_0 with increasing graph size, B. The values shown are averages of an ensemble of 5 randomly chosen HEXv Fourier graphs.

However, we are able to implement an approximately closed graph, using the weak-coupling mechanism discussed in this chapter, and that was the reason why the Weyl and Wigner predictions worked so well in sections 4.5.

4.8 CONCLUSION

We have derived an analogue of the random coupling model (RCM) using graph theory. This graph model has all the characteristics of RCM if Fourier boundary conditions are applied at vertices of the graph. This model is useful in modelling the propagation of microwaves in both wired network and wireless communication systems. The application of this model is discussed in subsequent chapters. For example, in Chapter 5, we use the model to predict the scattering parameters of a cable network with experimental

validation. We also use the graph model to predict the distribution of capacity of wireless communication channels in Chapter 6.

Although the Fourier boundary conditions are not accessible experimentally, they provide us with a useful conceptual tool for predicting the propagation of microwaves through both wired and wireless networks. However, for graphs with Neumann boundary conditions, the normalised random variable X in (130) assumes a Laplace distribution instead of being a Gaussian-distributed as assumed in the RCM. Therefore not all the assumptions of RCM can be achieved with Neumann graphs. Nevertheless, we have achieved a new statistical model for the distribution of the un-scaled random variable Y, which was presented in (130).

Additionally, we have shown how losses are introduced into graph networks. The loss parameter α which depends only on the graph size is dimensionless and measures the level of losses in the entire graph system. This is analogous to the loss parameter as discussed in Section 4.2, which focused on random coupling model.

Finally, we have successfully implemented an approximately closed graph. This is important because of two main reasons. The predictions of RMT for chaotic systems are based on closed systems and by implementing quasi-closed graphs, we can effectively test for the presence of wave chaos. Secondly, coupling of leads create avenues for energy leakages in the underlying system. By reducing these leakages through weak-coupling, we are able to reduce the interference effects on (or from) other systems. This is an im-

portant subject and remains an active field in electromagnetic compatibility studies.

5

LABORATORY EXPERIMENTS

5.1 INTRODUCTION

We measure the reflection coefficient, S_{11}, of microwaves interacting with networks of cables through a single port. The aim is to compare the experimental measurements with the graph model predictions developed in Chapter 4. Measurements of several network topologies have been carried out. These include a simple T-junction network, where two arms of the three constituent cables have equal lengths. This network was designed to have periodic resonances. This has been compared with the theoretical model predictions focusing on the resonance spectrum. Another measurement is made of a T-junction network but with cables of unequal lengths. Additionally, the S_{11} response of cable networks with a more complex topologies has been measured, where we selected a cable network consisting of a single loop as well as of double-loop architecture.

Before starting the main experimental measurements, there was the need to characterise the cables used in the experiments. These include the per unit length resistance (R), capacitance (C), conductance (G) and inductance (L) over a wide range of frequencies (usually $0 - 3$ GHz.) The values of the cable characteristics are required in the theoretical model in order to predict a more realistic propagation of microwave in cable networks. The results of the model predictions has been compared eventually with the experimental measurements. We used a procedure by Smartt et. al [136], which enables the calculation of such cable characteristics as explained in Section 5.2.

After characterising the cables, Section 5.3 focuses on the main laboratory measurements, which determine the reflection coefficients S_{11} of the cable networks as a whole. The discussion of the experimental results, together with the theoretical model predictions, is presented in Section 5.4. Finally, the concluding section presents a summary of the key results from the chapter and establish a link to subsequent chapters.

5.2 MEASUREMENT OF CABLE CHARACTERISTICS

The measurements of the cable characteristics, as well as of the scattering parameters of the whole cable networks have been conducted at the Cable Network Laboratory, George Green Institute for Electromagnetic Research (GGIEMR). In both experiments, Farnell coaxial cables PP000663 and Agilent 59657917E *Vector Network Analyser* (VNA) were used. Although the

cable characteristics were obtained through the method described in [136], here we summarise the main ideas behind the method for completeness.

From TL model discussed in Chapter 2, the transmission of currents and voltages on a shielded cables with braided screens may be modelled by the following Telegrapher's equations in matrix form [137–139] as

$$\frac{\partial}{\partial z}\begin{bmatrix} I_s(z) \\ I_w(z) \end{bmatrix} = \begin{bmatrix} Y_s & 0 \\ 0 & Y_w \end{bmatrix}\begin{bmatrix} V_s(z) \\ V_w(z) \end{bmatrix}, \tag{140}$$

$$\frac{\partial}{\partial z}\begin{bmatrix} V_s(z) \\ V_w(z) \end{bmatrix} = \begin{bmatrix} Z_s & Z_m \\ Z_m & Z_w \end{bmatrix}\begin{bmatrix} I_s(z) \\ I_w(z) \end{bmatrix} \tag{141}$$

where I_w, I_s V_w and V_s are the inner wire and external shield currents and voltages respectively. The cable impedances per unit lengths of the inner wire, external shield and mutual coupling are Z_w, Z_s and Z_m respectively. Similarly,

$$Y_w = G_w + j\omega C_w, \qquad Y_s = G_s + j\omega C_s \tag{142}$$

are the per unit length admittance of the inner wire and the external shielding. Here, G_w, C_w and G_s, C_s are the conductance and capacitance of the inner coaxial and the external shield respectively.

Also, the frequency dependent parameters may be represented in the form

$$Z_s, Z_w, Z_m \approx \frac{\sum_{i=0}^{\infty} a_i(j\omega/\omega_0)^i}{1 + \sum_{i=1}^{\infty} b_i(j\omega/\omega_0)^i}, \tag{143}$$

where $j = \sqrt{-1}$ and ω_0 is the frequency normalisation constant. In practice, the first or second order approximation of (143) is adequate enough to model the transfer impedance matrix [136]. The admittance matrix is mod-

elled in a similar fashion. Although the admittance equations in (142) may be approximated to have purely capacitive admittance

$$Y_w = j\omega C_w, \qquad Y_s = j\omega C_s \tag{144}$$

for the majority of cables [136], in this experiment we used the more accurate equations where $G_w, G_s \neq 0$, as stated in (142).

The cable characteristics are determined by first measuring the scattering parameters of the cable under test. Figure 38 shows an illustration of the experimental setup for measuring the scattering parameters. The propagation of the internal coaxial mode is characterised by the measured S_{11}, while that of the shielding is characterised by S_{22}. The mutual coupling between the shielding and the coaxial cable, which are assumed to be symmetrical, is characterised by S_{21} or S_{12}. In order to determine values of the scattering parameters accurately, care must be taken to connect the VNA ports correctly to the cable under test. Here, port 1 is connected to the internal coaxial cable, while the port 2 is connected to the external shielding or the ground circuit as shown in Figure 38.

Effectively, only three (i.e. S_{11}, S_{22} and S_{21} or S_{12}) out of the total four scattering parameters are required to find the cable characteristics. By measuring the S parameters over a wide range of frequencies in this way, it is easy to transform them to impedances and admittances per unit length. For example, the relationship between the scattering matrix S and the impedance Z is given by [140]

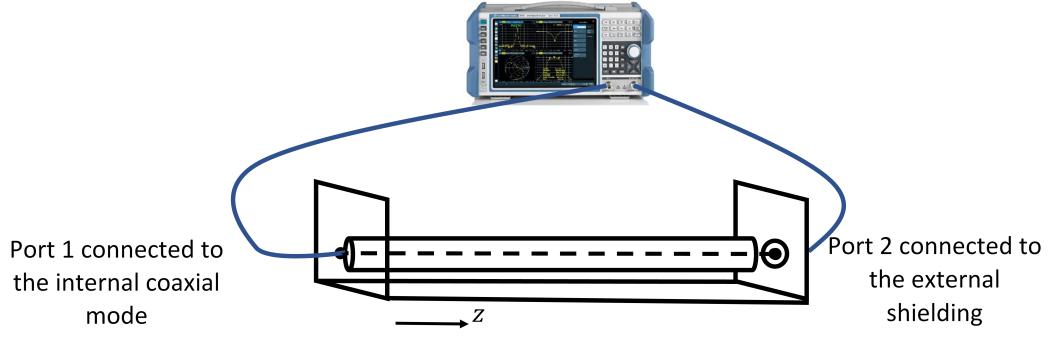$$Z = Z_0^{1/2}(I_2 + S)(I_2 - S)^{-1}Z_0^{1/2}, \tag{145}$$

Figure 38.: Experimental setup for measuring the scattering parameters of a shielded cable. Port 1 is connected to the internal coaxial cable mode, while port 2 is connected to the external shielding.

where Z_0 is a 2×2 diagonal matrix with diagonal elements representing the characteristics impedances of the coaxial cable and the external shielding; I_2 is a 2×2 identity matrix.

Finally, from $Z = R + j\omega L$, we can find the resistance per unit length R, and inductance per unit length L of the cable. The conductance and capacitance per unit lengths may also be calculated mutatis mutandis. Figure 39 shows the results of the cable characteristics. It is important to note that the values of the conductance per unit length are non zeros in this experiment. This increases the accuracy of the measurement as mentioned earlier in this chapter.

By knowing the values of the wave number and the graph scattering matrices σ_{00}, σ_{0x}, σ_{xx} and σ_{x0} in (97) across a frequency range, we can accurately predict the behaviour of propagating microwaves across the cable network. This theoretical prediction is compared with experimental measurements in
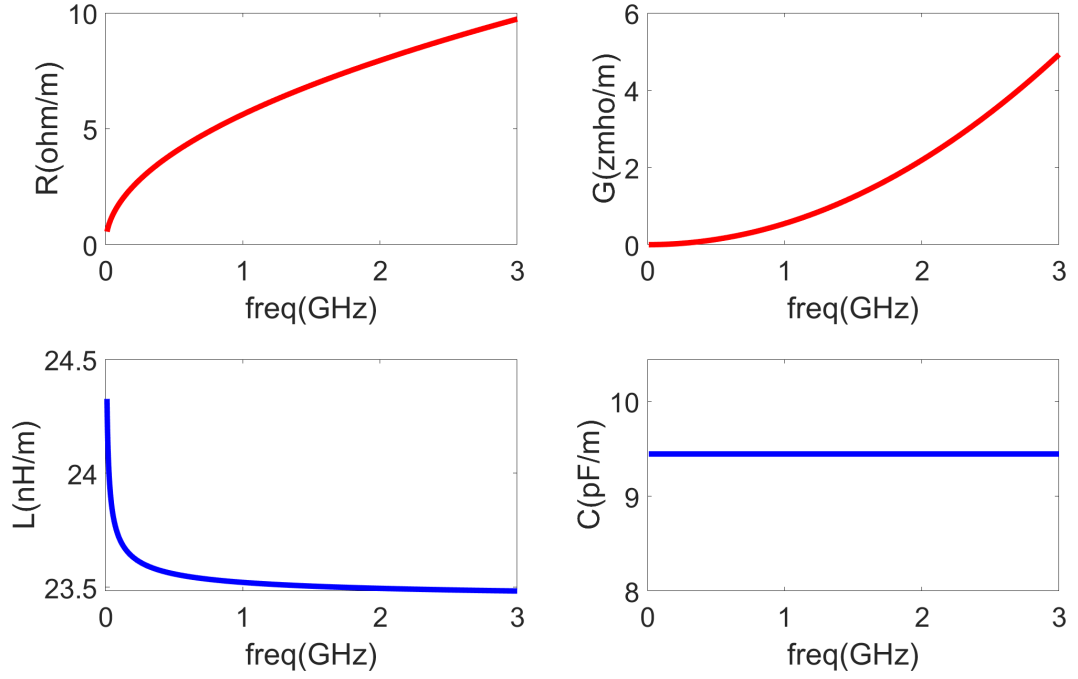
Figure 39.: Cable characteristics of Farnell coaxial cables PP000663 and their dependence on frequency.

the following sections. In particular, we focus on the measurement of the S_{11} parameter for selected topologies of the cable network.
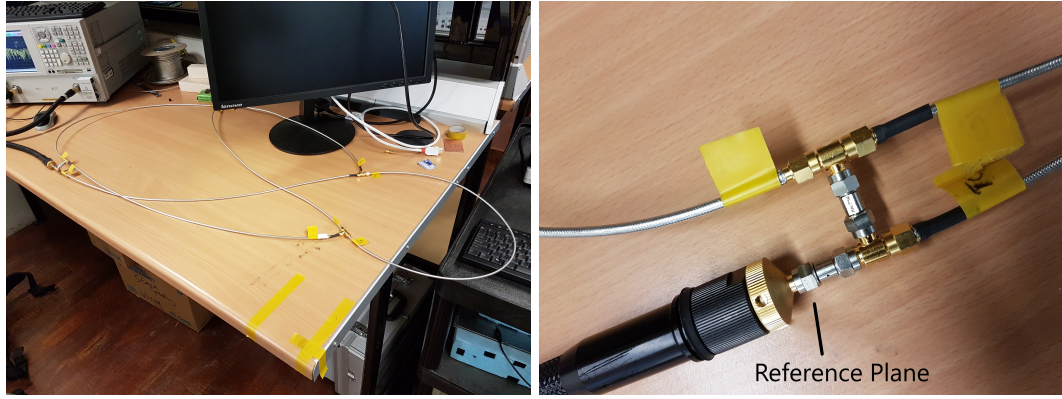
5.3 MEASUREMENT OF S_{11} IN CABLE NETWORKS

In this section, the experimental set-up and the measurement procedures are introduced. This is followed in section 5.4 by the results of measurement as compared with the theoretical model predictions from the model in (97).

5.3.1 *Experimental set-up*

Figure 40 shows a picture of the cable laboratory layout adopted in our experiments. Figure 40(a) shows the general set-up, where the network of cables is connected to the a VNA through a probe. The probe connection is shown in Figure 40(b). The VNA is calibrated in such a way that the point of probe-cable contact is set as the reference point of the measurement. If there is the need for more than three cables to be connected a vertex, then several T-junction connectors may be used to implement such vertex. For example, Figure 40(b) shows how four cables may be connected to one another at a common vertex. These types of connections are tricky because of the limitations imposed by the geometry of the T-junction connectors. It is important to note that each T-junction connector in a network increases the effective lengths of the cable. This increase in length was carefully measured and found to be 0.012 m on each arm of the connector. Figure 41 illustrates the extra length contribution from a T-junction connector.

In order to provide an extra layer of precaution, the T-junction connectors were further secured in place with black tapes as seen in Figure 41. It is important to note the length of the cable that is directly connected to the probe, so that the correct cable length can be used in the theoretical model. To achieve that, all cables were labelled with a yellow tape and their positions noted. This yellow labels are visible in Figure 40(b) and in Figure 41. After taking all the above precautions, a procedure used in measuring

(a)   (b)

Figure 40.: Experimental set-up to measure reflection coefficients (S_{11}). (a) shows a photo of how the cable networks are connected to the measuring instrument (i.e. the VNA), while (b) shows a cable connection to the probe (i.e. the measurement reference point).

the S_{11} scattering parameter is outlined in subsection 5.3.2.

5.3.2 *Measurement Procedure*

The measurement procedure is made of three steps. The first step involves making some initial settings on the measuring equipment (i.e. VNA). These settings include frequency range, number of sweep points, scale of frequency sweep, sweep time, and format of the measurement output. Most of these settings can be made by navigating through the *Sweep Setup* dialogue box on the VNA. Although there may be slight differences in achieving these settings, depending on the model type of VNA used, the steps generally involves either using a set of buttons on the VNA or using a computer
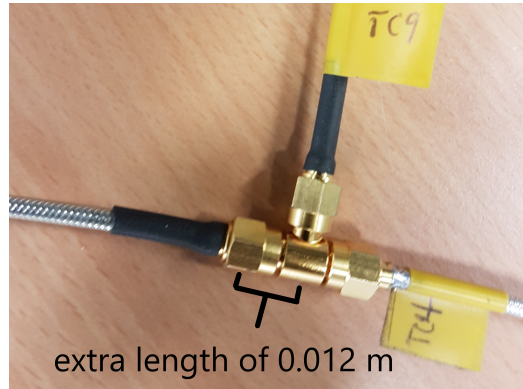
Figure 41.: A photo of how a T-junction connector adds an extra length of 0.012 m to each cable connected to it.

monitor and a mouse connected to the VNA. More information on how to navigate the settings may be found at [141]. In this experiment, the following initial settings were made:

1. Frequency range: 10 MHz - 3 GHz

2. Number of sweep points: 1601

3. Scale of Frequency: Linear

4. Power level: 0 dBm (default)

5. IF Bandwidth: 100 kHz

6. Time of sweep: Auto

7. Output format: Linear (i.e. complex S_{11} values in linear format)

After the initial settings, the second step is to perform a suitable calibration using an instrument called electronic calibration module (ECal). By connecting the ECal to the VNA, it is easy to set the position of the reference

plane and to transfer the factory accuracy of the ECal to the VNA. The ECal ensures consistency in measurement for repeatability and also minimises the errors introduced by human interaction with the measurements. In this experiment the ECal was used to set the reference measurement plane at the probe-cable connection point as shown in Figure 40(b).

The third and last step is to connect the device under test (DUT), which in our case is the network of cables whose S_{11} parameter is to be measured. A photo of this is shown in Figure 40(a). It is important to note that out of the three boundary conditions discussed in chapter 3, only two are experimentally accessible. These are the Neumann and Dirichlet boundary conditions (or any impedance boundary condition which interpolates between them).

In this experiment, we require a total reflection at dead-end vertices, where the valency is unity. This is equivalent to Dirichlet boundary condition (or short circuit). All other vertices have Neumann boundary conditions. For example, Figure 42(a) shows a diagram of a T-junction network connected to a VNA. The Neumann and Dirichlet boundary conditions are labelled as *NBC* and *DBC*, respectively.

The Fourier boundary condition on the other are idealised boundary conditions which ensures equal distribution of power at every vertex of the network. However, they can be implemented as an average scattering matrix of a large, overmoded, mode stirred enclosure connecting the ports through antennas radiating inside the cavity. In this case, the attenuation due to cavity losses and energy diffusion need to be modelled in the equivalent

node. While this is not central in this experiment, the condition is common in experiments involving reverberation chambers [142, 143].

The experimental results and analysis of cable networks are discussed in Section 5.4 for various network topologies.

5.4 MEASUREMENT RESULTS AND MODEL PREDICTIONS

We start with the simple case of a single T-junction network consisting of three cables of lengths 0.767 m, 0.778 m and 0.778 m as shown in Figure 42(a). The 0.767 m cable was connected to the VNA at one vertex, while the other vertex is connected to two cables of equal lengths. The red arrows represent the out-going waves, while the green arrows depict the in-coming waves. The boundary conditions at the first two vertices are Neumann, while the other two vertices have Dirichlet boundary conditions as shown. Since the 0.767 m cable only contribute to a phase shift $\exp(jkL)$, where $L = 0.767$ m, we expect the S_{11} response to be periodic because the other two cables have equal lengths.

The absolute value of S_{11} are plotted against frequency (in GHz) and the plot is shown in Figure 42(b). The solid green curve represents the experimental measurement, while the solid blue curve is the theoretical predictions of the graph model in (97). As it can be seen from the results, the QG model predicts the resonances of $|S_{11}|$ with high degree of accuracy. The nearest neighbour spacing distribution of these resonances is an important

feature of cable networks, and has been discussed in chapter 4 section 4.5. The minor differences between the measured and the simulated results have to do with machine precision, the noise level from the measured data, the non-symmetrical nature of the T-junction connectors' geometry, and the fact that we assumed the connectors to have the same characteristics (i.e. R, L, C, G) as the cables.

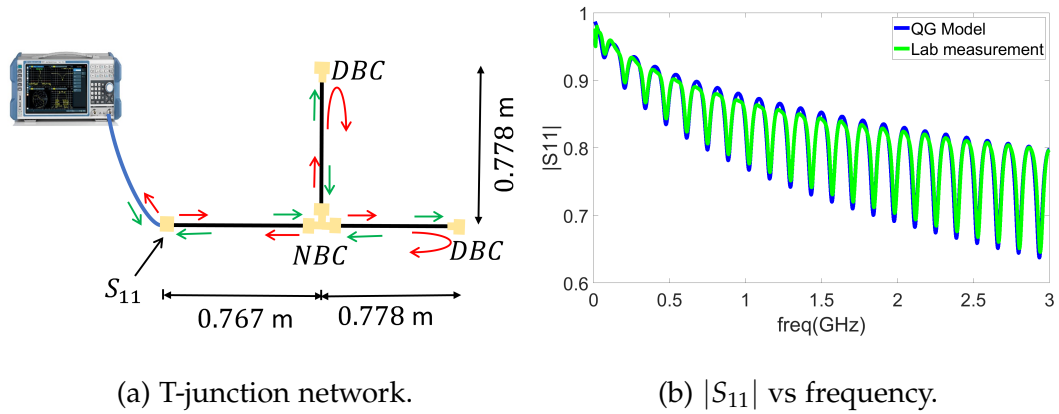(a) T-junction network.

(b) $|S_{11}|$ vs frequency.

Figure 42.: Comparison of experimental results with QG model predictions. (a) illustrates a T-junction network where the two arms of the network have equal cable lengths of 0.778 m and the third cable of length 0.767 m is connected to the VNA.

Next, the results of a more complicated graph topology is shown in Figure 43. The network architecture, together with the cable lengths and boundary conditions, is shown in Figure 43(a), while the laboratory measurement is compared with theoretical prediction in Figure 43(b). The boundary condition at each of the three vertices are Neumann. The effective lengths of the cables are 0.012 m, 0.774 m, 0.774 m, 0.774 m and 0.784 m as shown in Figure 43(a). The blue and the green curves, in Figure 43(b), represent

the results of theoretical predictions and the experimental measurements respectively. Again, the theoretical model is able to predict accurately the S_{11} laboratory measurements.

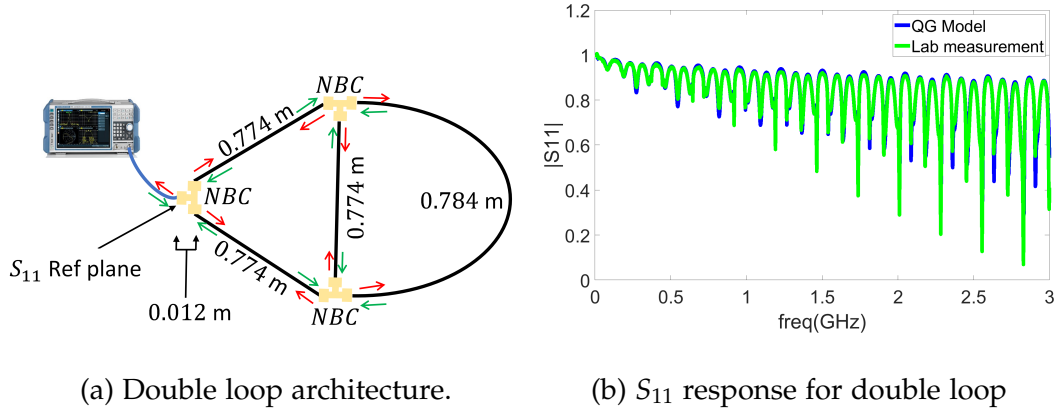(a) Double loop architecture.

(b) S_{11} response for double loop

Figure 43.: Diagram and S_{11} response for double loop.

In order to achieve an accurate comparison between the theory and measurement, it is important to include the extra length of 0.012 m introduced by the T-junction connectors. For example, Figure 44 shows the comparison between the theoretical predictions and the laboratory measurements when the extra length of 0.012 m is not taken into account. It is easy to observe a significant difference between the measurement and theoretical predictions when the effective lengths are not used in the graph model.

The results of other networks of different topologies are shown in appendix A. The main idea of this chapter is to validate the graph model with experimental results. At this stage, there is no doubt that the theoretical model adequately predicts the propagation of microwaves in cable networks.
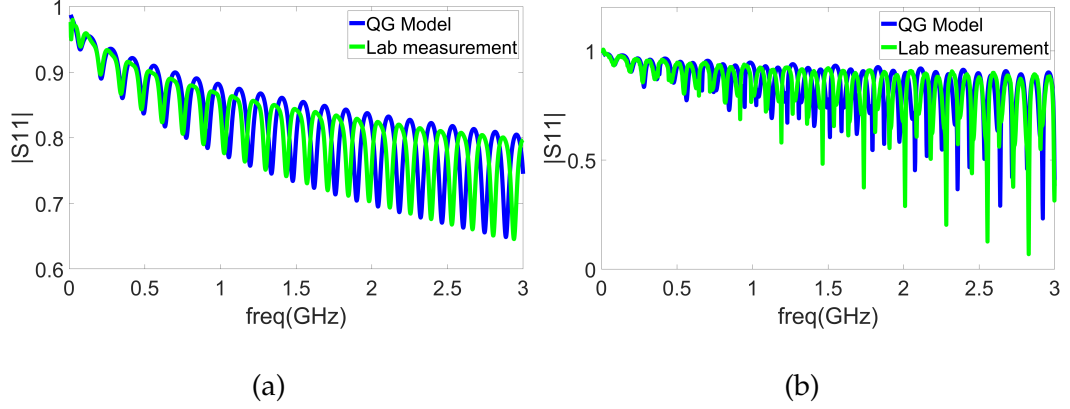
Figure 44.: $|S_{11}|$ response with *non-effective* cable lengths. (a) is the results of a T-junction network with cable lengths 0.743 m, 0.754 m and 0.754 m, while (b) is the results of a cable network with the double loop architecture. The non-effective lengths in (b) are 0.75 m, 0.75 m, 0.75 m and 0.76 m.

5.5 CONCLUSION

We have been able to successfully compare the theoretical predictions of quantum graph model with experimental measurements. The graph model was able to predict, in great detail, the reflection coefficient S_{11} of cable networks of various topologies. This ranges from T-junction networks to double loop cable networks. In all cases, except for negligible differences, the graph model agrees well with the experimental results.

The graph model therefore provides a flexible model, which can be used to predict the propagation of microwaves in complex networks of arbitrary topology. Modelling the coupling of leads to graph networks can provide

a significant insight when investigating interference effects. This is because energy may leak out of the cable network at the point where leads are coupled to the network.

Additionally, the graph model may be used to effectively predict the propagation of microwaves in wireless communication channels such as multiple-input multiple-output (MIMO) wireless communication channels. This is discussed in Chapter 6 for idealised Fourier graphs and in Chapter 7 for realistic Neumann graphs.

Finally, in its own right, the graph model may be used as a test-bed to predict the scattering parameters in wired communications. This has been discussed in Chapter 8 to predict the distribution of channel capacity in Digital Subscriber Line (DSL) technologies, which is chiefly used in providing internet access to various households and for commercial purposes.

6

DISTRIBUTION OF CHANNEL CAPACITY ON FOURIER GRAPHS

6.1 INTRODUCTION

We are interested generally in communication across wired networks for a number of reasons. In its own right, wired communication has a wide range applications such as Digital Subscriber Line (DSL) and its variants like the Asymmetric DSL (ADSL) and very high bit-rate DSL (VDSL) [144]. Additionally, the wired model can be used as a theoretical model to learn about Multiple-Input Multiple-Output (MIMO) systems in chaotic cavities. Realistic cable models have behaviour that is non-generic from the point of view of existing theories such as random matrix theory (RMT), and random coupling model (RCM).

We therefore start with idealised boundary condition which allows us to establish more simple connections with the existing theories. These idealised boundary conditions are Fourier boundary conditions which are ap-

plied at the vertices of the compact part of the graph. As discussed in Chapter 3, Fourier boundary condition ensures democratic scattering at the vertices and hence enables the waves to mix properly as they will in chaotic cavities. At vertices to which leads are attached, we implement vertex scattering matrices which allow us to weakly couple the leads to the rest of the graph (see section 4.5.1 for details of how this is achieved.) By Fourier graphs, we refer to graphs with Fourier boundary conditions at the vertices of the compact part of the graph. In Chapter 7, these assumptions are relaxed to go towards more realistic models.

In this chapter, the distribution of channel capacity is determined for Fourier graphs that are weakly connected to leads. In telecommunications for example, the leads represent the input and output devices like transmitters and receivers. In general, MIMO systems are communication systems involving multiple input systems and multiple output systems coupled to the communication channel. MIMO systems have been used as a strategy to increase both *reliability* and *throughput* of the communication link [145].

In particular, we focus our attention, in this work, on the special case of MIMO systems with either Single-Input Multiple-Output (SIMO) or Mutiple-Input Single-Output (MISO). Both SIMO and MISO abound in real life applications. For instance, in Digital Subscriber Line (DSL) network and its variants (i.e. ADSL and VDSL) [144], data transmission from street cabinets to households is an example of a SIMO application. Similarly, in mobile communications, the *downlink* in the physical layer is responsible for data

transmission from base stations to mobile devices. This is an example of a SIMO system. The reverse transmission, the *uplink*, is a MISO system. Generally, all broadcast networks are examples of SIMO systems. Mathematically SIMO and MISO systems are equal since one is easily converted to the other by swapping the role of the transmitters and receivers. Therefore all calculations done for one are applicable to the other.

The aim of this chapter is to show how quantum graphs (QGs) can be used, as an analogue of random coupling model (RCM) (see Chapter 3) Section 4.2, to analytically predict field properties of these communication channels. Therefore QGs may be used to simulate propagation of microwaves in cable networks as well as information transfer in chaotic cavities. The ultimate aim is to calculate, from first principles, the distribution of channel capacity, which serves as the main measure of maximum allowable rate of data transmission.

The following summarises the steps towards achieving this goal:

1. We first model the communication matrix H by the symmetrised graph scattering matrix S^M calculated in Chapter 4.

2. We then replace H with S^M in the channel capacity formula and use the distribution of S^M to analytically determine the distribution of the channel capacity depending on whether we are in the low loss regime or high loss regime.

3. We test the validity of the analytical calculations with numerical simulation of graphs networks of various topologies.

The rest of this chapter is organised into four sections. Section 6.2 gives a summary of background information about the channel capacity and the communication matrix, and then establishes the link to the RCM formulation. We explain how the scattering matrix is extracted and used as an analogue of the transfer matrix H traditionally used communications theory. This is followed in Section 6.3 by the discussion of methods and mathematical manipulation required to obtain the distribution of channel capacity, starting from systems with single input and single output devices. This is then generalised in Section 6.4 to cover systems with multiple inputs (or outputs). The final section in this chapter summarises the key achievements of the chapter by comparing and contrasting the various methods of predicting the channel capacity using weakly-coupled Fourier graph.

6.2 CHANNEL CAPACITY AND THE COMMUNICATION MATRIX

Channel capacity may be defined as the maximum rate at which data can be transmitted reliably through a communication channel. There are two formulas for calculating capacity of a channel. For a noiseless channel, the Nyquist bit rate formula is used, while the Shannon Capacity formula is used for a realistic noisy channel. In reality, there are no ideal noiseless channels and therefore we concentrate on the Shannon channel capacity formula in all our discussions in this chapter. The Shannon channel capacity formula and its variants have been widely researched [146–149]. However,

the one which is linked directly to MIMO systems has been derived in the Appendix of [146] and it is given, in bits per second per Hertz, by

$$C = \log_2 \left[\det \left(I_{n_r} + \frac{\rho}{n_t} HH^\dagger \right) \right] \text{bps/Hz,} \tag{146}$$

where I_{n_r} and H are the $n_r \times n_r$ identity matrix and $n_r \times n_t$ transfer matrix [146] respectively; n_t and n_r are the number of transmit and receive antennas, respectively. H is generally a complex matrix also referred to as the communication matrix; we shall use both terminologies interchangeably. The transfer matrix connects the received signal, y, to the transmitted signal x through the equation

$$y = Hx + \varsigma, \tag{147}$$

where ς is the received noise. This means that the received signal is made up of both the transmitted signal as well as the noise from the channel. $HH^\dagger$ therefore represents the normalised channel power transfer characteristic [146]. The symbol $\dagger$ denotes the complex-conjugate transposition. ρ is the signal-to-noise ratio (SNR) and is defined as the ratio of the total power transmitted from the antennas to the noise power at each of the receiving antennas. The SNR is usually given in dB. In this case, it is the difference between the received power (measured in dBm) and the noise floor (in dBm). The relationship between SNR in dB and ρ is given by

$$\text{SNR}_{\text{dB}} = 10 \log_{10}(\rho). \tag{148}$$

This means that if the SNR is given in dB, then the value of ρ in (146) is calculated from

$$\rho = 10^{\left(\frac{\text{SNR}_{\text{dB}}}{10}\right)}. \tag{149}$$

Higher values of SNR indicate better signal quality and channel condition. For example, two separate telephone lines with equal channel bandwidths will have two different data rates depending on the SNR values of each channel.

Furthermore, we assume that signals propagating through the channel, undergo Rayleigh fading. Rayleigh fading is based on the assumption that signals that arrive at the receiver, after undergoing multiple reflections and transmissions, randomly vary in magnitude. In Rayleigh fading, the independent paths taken by signals are such that, there is no dominant line of sight transmission [150]. This type of fading is the most widely used to model propagating signals in environments such as urban cities. In experimental settings, it is not uncommon to model such multipath environments in reverberation chambers [151] and chaotic cavities [32, 38]. Unless otherwise stated, the transmission medium are assumed to be Rayleigh channels.

Coming back to our case where there are multiple transmitters coupled to a single receiver, the Shannon capacity formula in (146) simplifies to

$$C = \log_2 \left[\det \left(1 + \frac{\rho}{n_t} \sum_{i=1}^{n_t} |h_{1i}|^2 \right) \right] \text{bps/Hz}, \qquad (150)$$

where the communication matrix $H = \left(h_{11}, h_{12}, h_{13}, ..., h_{1n_t} \right)$ is now a vector of length n_t such that $HH^\dagger = \sum_{i=1}^{n_t} |h_{1i}|^2$. This case is not different from the scenario of multiple receivers combined with a single transmitter. In the random coupling model discussed in Chapter 4, the Z^{cav} is used to model H. We propose using the symmetrized scattering matrix S^M, introduced in Section 4.6, to model H. It is important to note from (128) that, the prompt

reflection matrix σ_{00}, is diagonal; and so the off-diagonal elements which represent the transmission part of the model are all zeroes. Therefore σ_{00} can be ignored when considering transmission from transmitters to receivers. Hence, for a weakly coupled Fourier graphs with losses in the compact part of the graph,
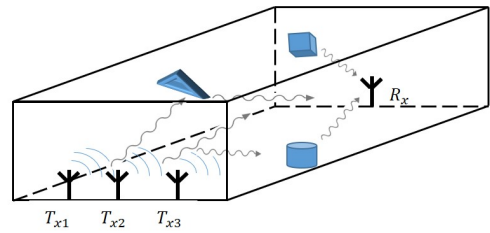
$$S^M = \left(\frac{\sin^2 \delta}{2B} e^{-\frac{\alpha \pi}{B}} \right) X \frac{1}{I_{2B} - \Lambda} X^\dagger, \qquad (151)$$

where the expression in the bracket is the non-statistical and system dependent part of the model, while $\xi = X(I_{2B} - \Lambda)^{-1} X^\dagger$ represents the statistical part with universal characteristics that can be predicted in RMT.

This means that, although the graph model was derived for wired networks, it is has the characteristics of wireless communication channels that are coupled to multiple transmitters and receivers. This idea is illustrated in Figure 45. In particular, Figure 45(a) is an illustration of a graph connected to three transmitters, T_{x1}, T_{x2} and T_{x3}, and one receiver R_x which we use to model the scenario of a chaotic cavity illustrated in Figure 45(b).
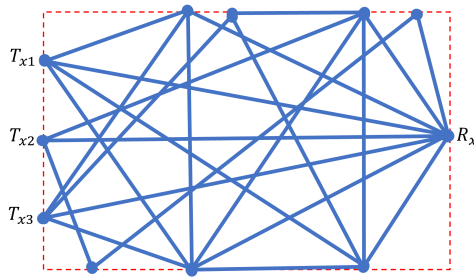
(a) Our wired scenario. (b) Wireless MIMO scenario.

Figure 45.: QG model as an analogue to MIMO system

If we consider the scenario in Figure 45(b) for example, then the transmission vector of the graph scattering matrix, S^M, is represented by elements of the sub-matrix, S_t^M, enclosed by the red box as shown in Figure 47. Across the frequency spectrum, the absolute values of these elements are presented in the various plots. The elements of S_t^M are denoted by S_{1i} where $i = 1, 2, \cdots, n_t$. Although these plots are for illustrative purposes, they have been obtained numerically by simulating a graph with a tetrahedral topology connected to three transmitters and one receiver. This is shown schematically in Figure 46, where the ith transmitter is denoted by T_{xi} and R_x denotes the receiver.
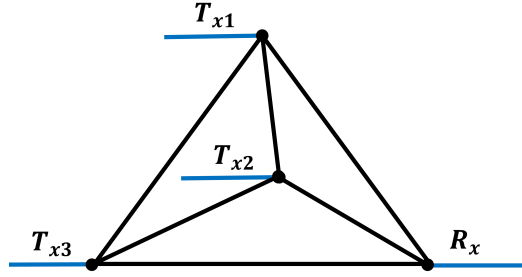

Figure 46.: Illustration of a tetrahedral connected to three transmitters, T_{x1}, T_{x2} and T_{x3}, and one receiver, R_x.

Using the scattering matrix S_t^M to model MISO systems, the channel capacity may then be written as

$$C = \log_2 \left[\det \left(1 + \frac{\rho}{n_t} |S_t^M|^2 \right) \right] \text{bps/Hz}, \tag{152}$$

where $|S_t^M|^2 = \sum_{i=1}^{n_t} |S_{1i}|^2 = \tau \sum_{i=1}^{n_t} |\xi_i|^2$. From (131) and the fact that $\tau = \sigma_Y^4$, we have

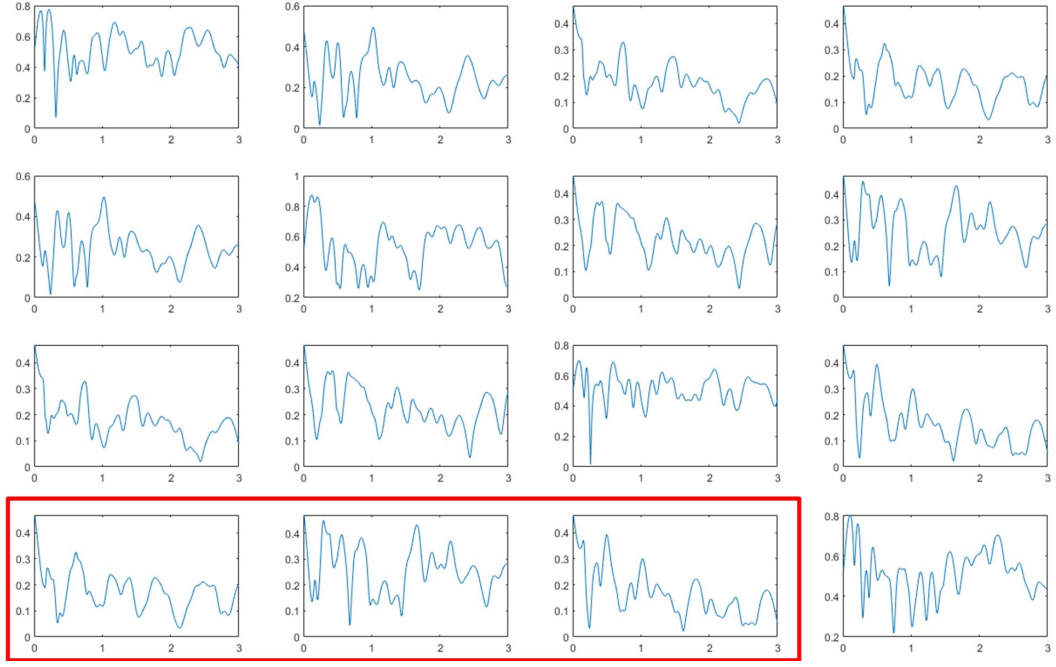$$\tau = \left(\frac{\sin^2 \delta}{2B} e^{-\epsilon} \right)^2, \tag{153}$$

Figure 47.: Extracted 1×3 transmission vector, S_i^M.

where τ is the coupling strength and depends on three attributes of the graph. Namely, graph size B, the damping factor $\exp(-\epsilon)$, and the free parameter δ, whose value allows us to control the strength of coupling to the leads, while keeping the vertex scattering matrix unitary. (NB: The expression of τ and the construction of a vertex scattering matrix which ensures weak coupling of leads were derived in Section 4.5.1).

It is essential to remember that both the statistical (system-independent) and the non-statistical (system-dependent) parts of the graph model are accounted for in (152) just like in random coupling model. We will use (152) in the next section to calculate the distribution of channel capacity.

6.3 DISTRIBUTION OF CHANNEL CAPACITY FOR SISO SYSTEMS

In this section, we begin with the simplest case of one transmitter ($n_t = 1$) and one receiver ($n_r = 1$). From (152), the channel capacity for SISO systems simplifies to

$$C = \log_2 \left[\det \left(1 + \rho \tau |\xi|^2 \right) \right] \text{ bits/Hz.} \tag{154}$$

The distribution of channel capacity may be derived in two ways:

1. Convolution Approach

2. Characteristic Function Approach.

Regardless of which method we use, we always start by constructing a model of the distribution of ξ.

From random coupling model, it was shown that ξ is Cauchy (or Lorentzian) distributed in the low-loss regime, and Gaussian distributed in the high-loss regime [38,152]. In the graph model however, we found (through numerical simulations graphs) that ξ is generally a t-distributed random variable. A t-distributed random variable interpolates smoothly between a Cauchy distribution and a Gaussian distribution. A Cauchy distribution is a special case of t-distribution where $\nu = 1$. In the limit of large ν, t-distribution becomes Gaussian. Since ξ is t-distributed, its probability density function (pdf) given by

$$f_\xi(x) = \frac{1}{\sigma \sqrt{\nu} \beta \left(\frac{1}{2}, \frac{\nu}{2} \right)} \left[1 + \frac{(x - \mu)^2}{\sigma^2 \nu} \right]^{-\frac{\nu+1}{2}}, \tag{155}$$

where $-\infty < x < \infty$. μ, σ and ν are the *location*, *scale* and *shape* parameters, respectively; and $\beta(\cdot, \cdot)$ denotes the beta function. When $\nu = 1$, then the pdf in (155) simplifies to that of Cauchy distribution as

$$f_{\tilde{\zeta}}(x) = \frac{1}{\sigma \pi} \left[1 + \left(\frac{x - \mu}{\sigma} \right)^2 \right]^{-1}. \tag{156}$$

Figure 48 shows an example of the distribution of the real and imaginary parts of ζ. The location parameter which is also the mean of the distribution is zero (i.e. $\mu = 0$) and so (155) leaves us with two parameters σ and ν which we will use in calculating the distribution of the channel capacity. ν is also known as the degree of freedom (dof) and we will use the two terms interchangeably. In (155), it must be noted that σ is not the standard deviation of the random variable ζ. In fact, in the special case when $\nu = 1$, the distribution has undefined standard deviation. For $\nu > 2$, the variance of a generalised t-distribution is rather given, in terms of the two parameters, by $\sigma_{\zeta}^2 = \sigma^2 \nu / (\nu - 2)$. However, in the limit of large ν, $\sigma_{\zeta}^2 \approx \sigma^2$ and the distribution of ζ becomes Gaussian with mean μ and variance σ^2. Since the transition between t-distribution and Gaussian distribution interpolates rather smoothly, it becomes difficult to pinpoint a particular value of ν for which 'Gaussianity' is attained. However, $\nu \geq 30$ always provides a good approximation to normal distribution and we shall use that as a rule of thumb to refer to a scenario when the distribution of ζ is approximately Gaussian.

Notation: Whenever a random variable X is t-distributed with parameters μ, ν and σ, we will write $X \sim t(\mu, \sigma, \nu)$. In the special case when $\mu = 0$,

we will simply write $X \sim t(\sigma, \nu)$. Similarly, we write $X \sim N(\mu, \sigma)$ when a random variable X is Gaussian distributed with mean μ and standard deviation σ. We classify as low-loss regime any regime where $\xi \sim t(\sigma, \nu)$ and as high-loss the regime where $\xi \sim N(\mu, \sigma_\xi)$.

The graph network simulated in Figure 48 consists of 120 bonds with HEX10 topology as shown in the inset of Figure 48(a). The graph is weakly coupled to two leads each with coupling strength, $\tau = 1.7269 \times 10^{-13}$. The loss parameter $\alpha = 0.1$ and the free parameter is $\delta = 0.01$. The lengths of the graphs were randomly chosen from a uniform distribution. Each plot in Figure 48(a) and (b) is created from 8000 realisations of such randomly chosen graphs. The distribution of ξ is compared with both t-distribution (red curve in the figure) and a Gaussian distribution (yellow curve) of the same variance. For this example with small damping (i.e. $\Im(k) = \epsilon = 2.618 \times 10^{-3}$), ξ is t-distributed with small dof, $\nu = 2.2$ as shown in the legend of the figure. Here, a Gaussian distribution, chosen to have the same variance, is quite different from the observed distribution. Figure 48(a) and (b) reveals that, the real and imaginary parts are identically distributed with equal variance. They are both t-distributed with equal parameter values.

From (138) in Chapter 4, we know that the loss parameter, $\alpha = \alpha_0 + \alpha_1$, where $\alpha_0 = B\epsilon_0/\pi$ and $\alpha_1 = B\epsilon/\pi$ denote losses due to radiating leads and losses within the compact part of the graph, respectively. The free parameter δ in (153) allows us to control the level of energy leakages due to radiating leads, while ϵ allows us to control the losses in the rest of the graph. As we

(a) Real part of ξ
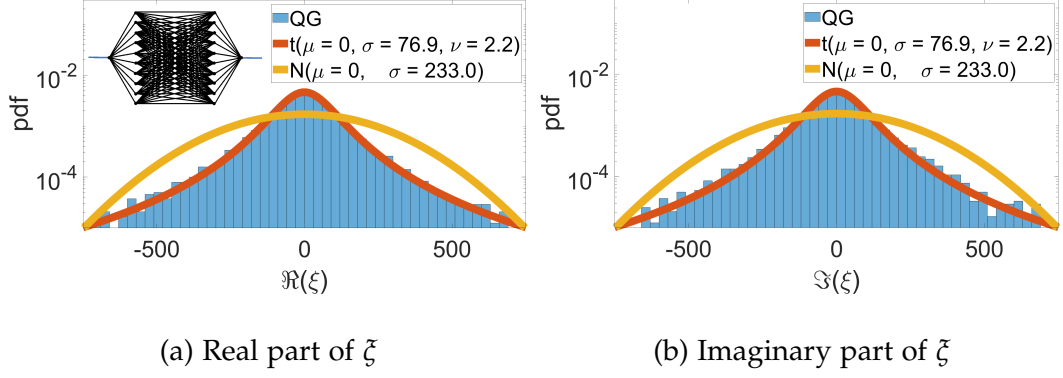
(b) Imaginary part of ξ

Figure 48.: The real and imaginary parts of ξ for a HEX10 Fourier graph with $\alpha = 0.1$, $\delta = 0.01$ and the number of bonds $B = 120$. Therefore the coupling strength, which depends on α, B and δ, is evaluated for each of the transmitter and the receiver as $\tau = 1.7269 \times 10^{-13}$. The red curve represents t-distribution with parameters $\sigma = 76.9$ and $\nu = 2.2$, while the yellow curve represents a Gaussian distribution with the same variance as the t-distribution.

increase the loss parameter in this way, ν also increases and consequently, the profile of ξ approaches a more Gaussian distribution. This transition is illustrated in Figure 49(a)-(d) and Figure 50(a)-(b), where the distribution of the real part of ξ, $\Re(\xi)$ for some selected values of $\alpha \in [0.5, \quad 5]$ are shown. Specifically, Figure 49(a)-(d) shows the distribution of $\Re(\xi)$ in the low-loss regime where $\nu < 30$. On the other hand, Figure 50(a)-(b) shows the distribution of $\Re(\xi)$ in the high-loss regime where $\nu > 30$. In each case, a HEX10 Fourier graph (see the inset in Figure 49(a)) was used with $B = 120$. The free parameter δ was fixed at $\delta = 0.5$, while ϵ values were chosen so that

the desired losses (i.e. α) are obtained. In Figure 49(a)-(d), $\alpha = 0.5, 1, 2, 3$, while in Figure 50(a)-(b), $\alpha = 4, 5$. Since the real and imaginary parts are identically distributed, we only show the effects of increasing losses on the distribution of the real part.

(a) $\alpha = 0.5, \tau = 9.1216 \times 10^{-7}$

(b) $\alpha = 1, \tau = 8.8859 \times 10^{-7}$

(c) $\alpha = 2, \tau = 8.4326 \times 10^{-7}$

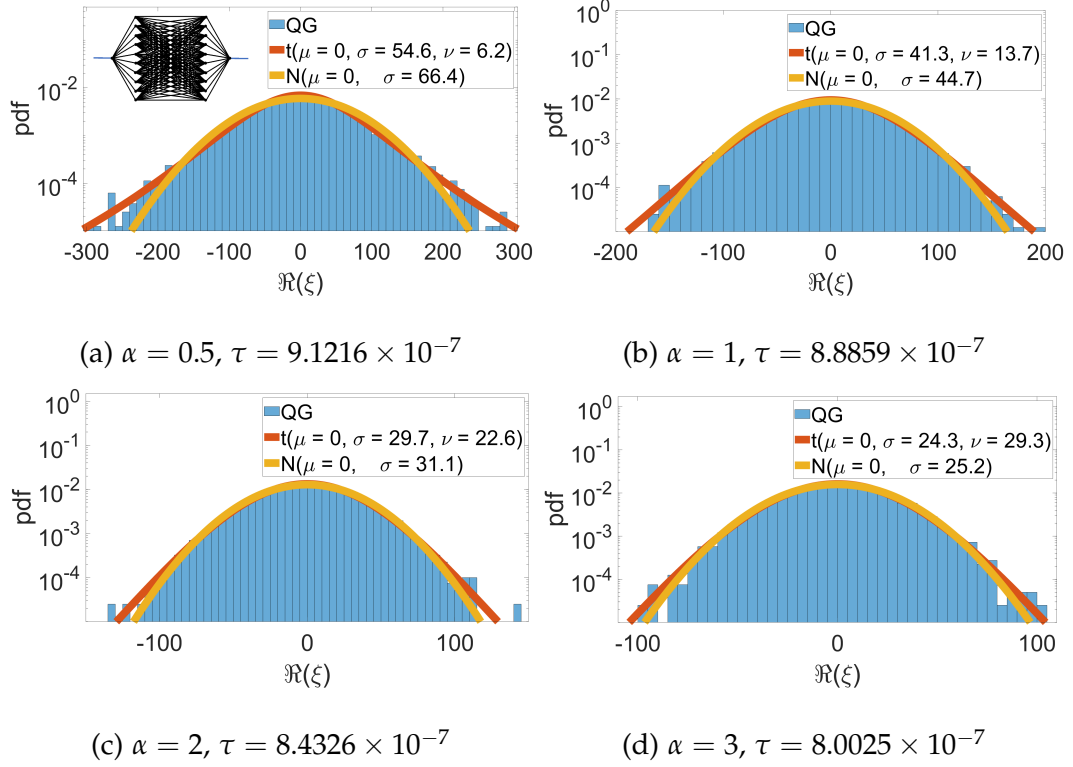(d) $\alpha = 3, \tau = 8.0025 \times 10^{-7}$

Figure 49.: The effect of increasing loss parameter on the distribution of $\Re(\xi)$ for a graph with HEX10 topology in the low-loss regime where $\nu < 30$. From (a)-(d), the distribution become more Gaussian as α increases. But in each case, the 'Gaussianity' criterion of $\nu > 30$ is not attained.

Figure 51 shows how the two parameters ν and σ change with increasing α. In this figure, we have divided the range of $\alpha \in [0.3949, \quad 5]$ into 21 equally-spaced incremental points. This helps us to see a more gradual

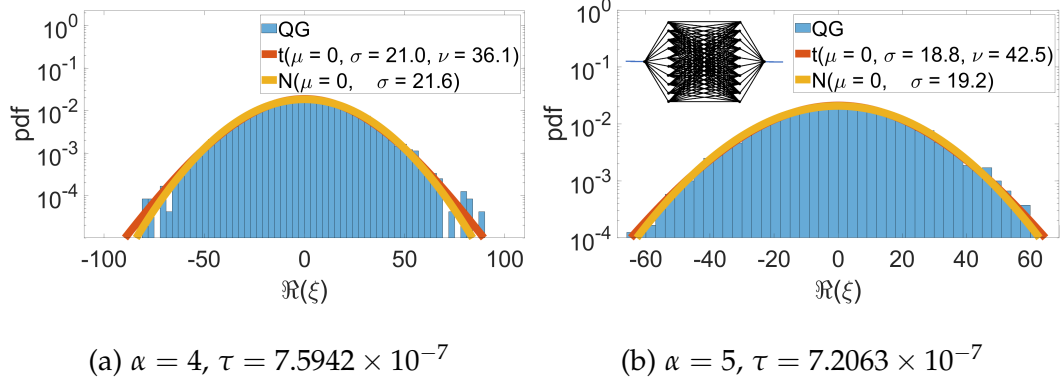(a) $\alpha = 4$, $\tau = 7.5942 \times 10^{-7}$ (b) $\alpha = 5$, $\tau = 7.2063 \times 10^{-7}$

Figure 50.: The distribution of $\Re(\xi)$ for a graph with HEX10 topology as in the inset of (b). Both (a) and (b) are in the high-loss regime where the degree of freedom $\nu > 30$. In (a) $\alpha = 4$ and the coupling strength $\tau = 7.5942 \times 10^{-7}$, while in (b), the loss parameter is increased to $\alpha = 5$ and $\tau = 7.2063 \times 10^{-7}$. In both figures, an ensemble average of 8000 randomly generated graphs were used.

transition of both parameters as we increase α. It can be seen that, the shape parameter ν increases with increasing α, while the scaling parameter, which is proportional to the variance, decreases with increasing losses. Increasing α reduces the 'fatness' of the tails and causes ξ to approach Gaussian distribution. This is in conformity with RCM predictions [38, 152]. For example, in Figure 50, $\nu > 30$ in each of the subplots (a) and (b). In both instances, we assume that ξ is effectively normally distributed because the shape parameter exceeded the threshold of $\nu = 30$.

From the distribution of ξ, we next calculate analytically the distribution of the channel capacity, $f_C(c)$, of a SISO system that works in both low and high loss regimes. We begin with the convolution method.
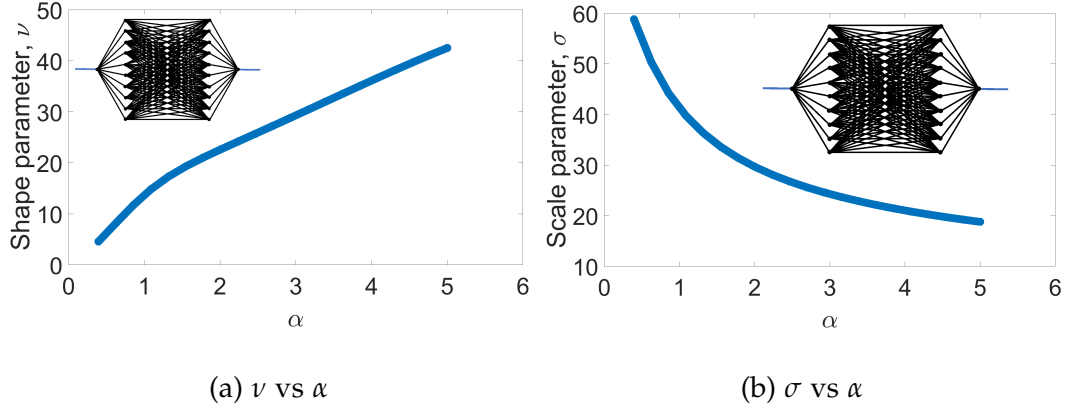
(a) ν vs α

(b) σ vs α

Figure 51.: Effects on increasing α on (a) the *shape* parameter and (b) *scale* parameter. Both plots were produced from an ensemble average of 2000 randomly chosen HEX10 Fourier graphs with coupling strength $\tau = 9.172 \times 10^{-7}$.

6.3.1 *Convolution method*

The convolution theorem states that: If X and Y are two independent continuous random variables with $f_X(x)$ and $f_Y(y)$ as their respective densities, then the density of $Z = X + Y$ may be written as

$$f_Z(z) = \int_{-\infty}^{\infty} f_Y(z - x) f_X(x)\, dx, \tag{157}$$

where $f_Z(z)$ is known as the convolution of $f_X(x)$ and $f_Y(y)$. From (154), we can use the distribution of $|\xi|^2$ to find the distribution of the channel capacity, C. We start with the distribution of $|\xi|^2$.

Since ξ is a complex variable, we can write it as $\xi = \xi_r + j\xi_i$, where ξ_r and ξ_i are the real and imaginary part of ξ, respectively. Consequently,

$$|\xi|^2 = \xi_r^2 + \xi_i^2. \tag{158}$$

This implies that $|\xi|^2$ is a sum of two random variables, ξ_r^2 and ξ_i^2, whose distributions we need to know first before calculating $f_{|\xi|^2}\left(|\xi|^2\right)$. Remembering that both $\xi_r \sim t(\sigma, \nu)$ and $\xi_i \sim t(\sigma, \nu)$, then each has a pdf given by

$$f_{\xi_r}(t) = f_{\xi_i}(t) = \frac{1}{\sigma\sqrt{\nu}\beta(\frac{1}{2}, \frac{\nu}{2})}\left[1 + \frac{t^2}{\sigma^2\nu}\right]^{-\frac{1+\nu}{2}}, \tag{159}$$

where $-\infty < t < \infty$ and $\beta(\cdot, \cdot)$ denotes the beta function.

We can use (159) to determine the distribution of ξ_r^2, by using a one-to-one transformation $X = g(T) = T^2$ from $\{t| -\infty < t < \infty\}$ to $\{x|x > 0\}$. This implies, for every value of X, there are two corresponding values of T. $T = g^{-1}(X) = \sqrt{X}$ and the Jacobian of transformation $\mathrm{d}T/\mathrm{d}X = 1/2\sqrt{X}$. Then

$$\begin{aligned} f_{\xi_r^2}(x) &= 2f_{\xi_r}\left(\sqrt{x}\right)\left|\frac{\mathrm{d}t}{\mathrm{d}x}\right| \\ &= \frac{1}{\sigma\sqrt{x\nu}\beta(\frac{1}{2}, \frac{\nu}{2})}\left[1 + \frac{x}{\sigma^2\nu}\right]^{-\frac{1+\nu}{2}}. \end{aligned} \tag{160}$$

ξ_r^2 is therefore a non-standard, F-distributed random variable with scaling parameter σ and degrees of freedoms $\nu_1 = 1$ and $\nu_2 = \nu$. We denote by $X \sim F(\sigma, 1, \nu)$, a random variable X, which is F-distributed with scaling parameter σ and degrees of freedoms $\nu_1 = 1$ and $\nu_2 = \nu$. This implies $\xi_r^2 \sim F(\sigma, 1, \nu)$. Similarly, $\xi_i^2 \sim F(\sigma, 1, \nu)$.

Figure 52 shows the distributions of ξ_r^2 and ξ_i^2 compared with the analytical expression in (160). The solid red curve represents an F-distribution while the histogram represents a network simulation of a graph with a HEX10 topology. The numerical results agrees well with the analytical pre-

diction, even in the tails. The irregular tails and their sudden termination are the result of finite-size effects.
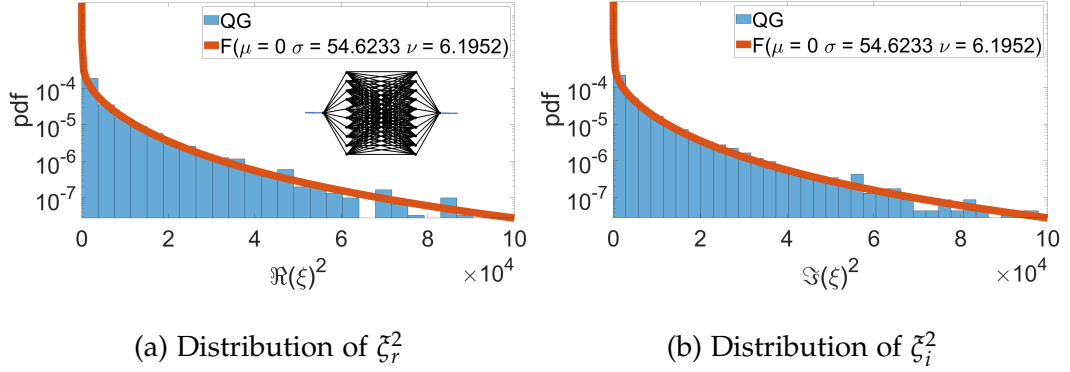

(a) Distribution of ξ_r^2

(b) Distribution of ξ_i^2

Figure 52.: Distributions of the squares of real and imaginary parts of ξ for a graph with a HEX10 topology. The number of bond in the graph is $B = 120$, the loss parameter $\alpha = 0.5$, the free parameter $\delta = 0.5$, and the coupling strength $\tau = 9.1216 \times 10^{-7}$.

From (158), if we let $Z = |\xi|^2$, $X = \xi_r^2$ and $Y = \xi_i^2$, then Z is a sum of two F-distributed random variables. Hence we can use the convolution equation in (157) to find the distribution of $|\xi|^2$ in terms of Z as

$$f_{|\xi|^2}(z) = \frac{1}{\sigma^2 \nu \beta(\frac{1}{2}, \frac{\nu}{2})^2} \int_{-\infty}^{\infty} \frac{1}{\sqrt{x(z-x)}} \left[1 + \frac{z-x}{\sigma^2 \nu}\right]^{-\frac{1+\nu}{2}} \left[1 + \frac{x}{\sigma^2 \nu}\right]^{-\frac{1+\nu}{2}}$$

(161)

$$\cdot H(x)H(z-x)\mathrm{d}x,$$

where $H(x)$ is the Heaviside step function. Since $x > 0$ and $y > 0$, then $z - x > 0$ which implies $x < z$. Consequently, the support of the integration is $0 < x < z$. Simplifying (161) and applying the support, we arrive at the pdf of $|\xi|^2$ being of the form

$$f_{|\xi|^2}(z) = \frac{1}{\sigma^2 \nu \beta(\frac{1}{2}, \frac{\nu}{2})^2} \int_0^z \frac{1}{\sqrt{x(z-x)\left(1 + \frac{z}{\sigma^2 \nu} + \frac{x(z-x)}{\sigma^4 \nu^2}\right)^{1+\nu}}} \mathrm{d}x. \qquad (162)$$

Figure 53 shows the distribution of $|\tilde{\xi}|^2$ using the same graph as indicated in Figure 52 and compared with the analytic calculation in (162). The red curve represents the theoretical prediction. It is important to note that $x > 0$ and $y = z - x > 0$ and therefore the pdf in (162) is defined only for $x, y > 0$.
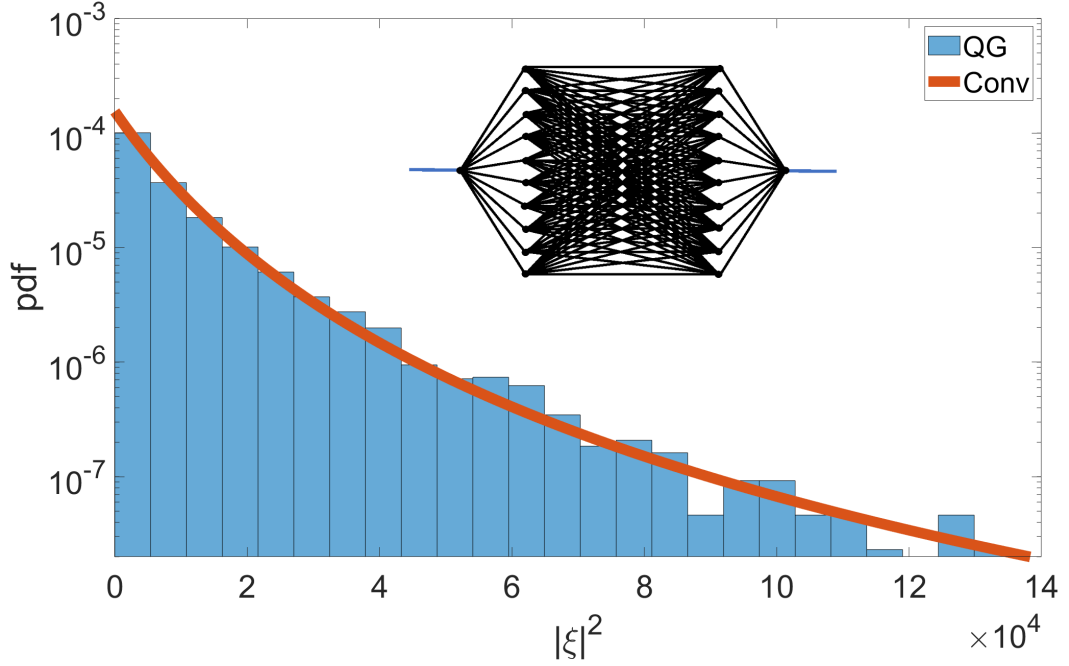

Figure 53.: Distribution of $|\tilde{\xi}|^2$ with $\alpha = 0.5$ for a graph of HEX10 topology with number of bonds $B = 120$, $\delta = 0.5$, the coupling strength $\tau = 9.1216 \times 10^{-7}$. The topology of the graph used is as in the inset.

Next, we use the distribution of $|\tilde{\xi}|^2$ to obtain the distribution of channel capacity, C. Remembering that the channel capacity formula in (154) relates $|\tilde{\xi}|^2$ with C, we can deduce the following:

$$f_C(c)\mathrm{d}C = f_{|\tilde{\xi}|^2}(z)\,\mathrm{d}|\tilde{\xi}|^2 \tag{163}$$

and

$$Z = |\xi|^2 = \frac{2^C - 1}{\rho\tau}. \tag{164}$$

The Jacobian of transformation is given by

$$\frac{d|\xi|^2}{dC} = \log(2)\frac{2^c}{\rho\tau}. \tag{165}$$

This implies

$$f_C(c) = f_{|\xi|^2}(z)\log(2)\frac{2^c}{\rho\tau}. \tag{166}$$

From (162), we know $f_{|\xi|^2}(z)$ and we can therefore substitute it in (166) to obtain the distribution of channel capacity as

$$f_C(c) = \frac{\log(2)2^c}{\rho\tau\sigma^2\nu\beta(\frac{1}{2},\frac{\nu}{2})^2}\int_0^z \frac{1}{\sqrt{x(z-x)\left(1 + \frac{z}{\sigma^2\nu} + \frac{x(z-x)}{\sigma^4\nu^2}\right)^{1+\nu}}}dx, \tag{167}$$

where $z = (2^c - 1)/\rho\tau$, ρ is the signal to noise ratio and the coupling parameter, τ, is as defined in (153). Comparison of the numerical results and the analytical expression in (167) is shown in Figure 54. The numerical simulation is done using the same HEX10 graph with the same low loss characteristics: $B = 120$, $\alpha = 0.5$, $\delta = 0.5$, $\tau = 9.1216 \times 10^{-7}$ and $\rho = 40$ dB. Typical values of $\rho > 20$ dB are required for applications involving data networks, while $\rho > 25$ dB are recommended in voice applications [153]. Therefore the choice of $\rho = 40$ dB is not uncommon in a typical communication system.

As the system losses increase, the pdf in (167) is still able to accurately predict the distribution of channel capacity irrespective of the level of losses, provided the graph is coupled to a single input and a single output devices. For example, Figure 54(b) shows distribution of channel capacity in the high-

loss regime where $\xi \sim N(\mu, \sigma)$ with $\alpha = 4$. In Figure 54(a), the losses in the channel are low ($\alpha = 0.5$) and so the capacity of the channel is larger than in a more lossy channel. This is evident, for example, when Figure 54(a) at $\alpha = 0.5$ is compared with Figure 54(b) at $\alpha = 4$. In Figure 54(a), the capacity reached as high as 11 bps/Hz, while in Figure 54(b), the highest value of the channel capacity is reduced to a little over 6 bps/Hz. This difference is significant. For example, if the two channels have equal bandwidths, then the channel with a lower loss will have a larger capacity than the one with a higher loss.

The main result of the present subsection is that, we have been able to analytically predict the distribution of channel capacity of Fourier graphs which are coupled to a single transmitter and a single receiver for both low- and high-loss scenarios.

However, when the number of transmitters is more than one, the convolution approach cannot be used to predict distribution of channel capacity. Under such circumstances, an alternative approach is required. In Section 6.3.2, we introduce such an alternative approach and we call it the *Characteristic Function Approach* (CFA).

6.3.2 *Characteristic Function Approach*

The characteristic function approach provides another angle of attack in finding the distribution of channel capacity. The underlying mathematical

(a) channel capacity at $\alpha = 0.5$
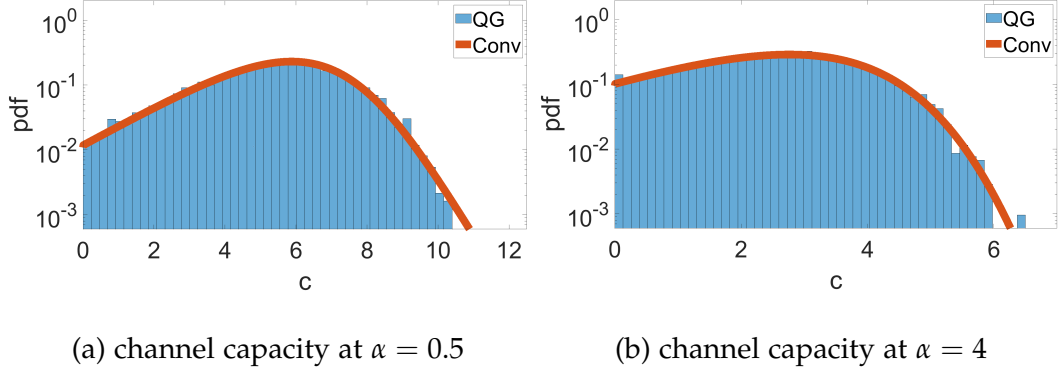
(b) channel capacity at $\alpha = 4$

Figure 54.: Predictions of distribution of channel capacity using the convolution approach (solid red curve) in the (a) low-loss regime when $\alpha = 0.5$ and (b) high-loss regime when $\alpha = 4$. In both cases, The graph size $B = 120$, $\delta = 0.5$. In (a), the coupling strength $\tau = 9.1216 \times 10^{-7}$, while in (b) $\tau = 7.5942 \times 10^{-7}$. The topology of the graph as indicated in the inset of Figure 53. The SNR $\rho = 40$ dB in each case.

manipulations are presented as follows:

Let X_i, be the ith random variable such that $X_1, X_2, X_3, \cdots, X_n$ are n independent and identically distributed random variables (iid's) each with pdf $f_{X_1}(x), f_{X_2}(x), f_{X_3}(x), \cdots, f_{X_n}(x)$ respectively. If Z is a another random variable such that

$$Z = \sum_{i=1}^{n} X_i, \tag{168}$$

then the pdf of Z, $f_Z(z)$ may be written in terms of a delta function $\delta(\cdot)$ as

$$f_Z(z) = \int_{R^n} dX_1 dX_2 \cdots dX_n f_{X_1}(x) f_{X_2}(x) \cdots f_{X_n}(x) \delta \left(Z - \sum_{i=1}^{n} X_i \right)$$

$$= \int_{R^n} \prod_{i=1}^{n} dX_i f_{X_i}(x) \left[\frac{1}{2\pi} \int_{-\infty}^{\infty} e^{jt(Z - \sum_{i=1}^{n} X_i)} dt \right]. \tag{169}$$

Therefore

$$
\begin{aligned}
f_Z(z) &= \frac{1}{2\pi} \int_{-\infty}^{\infty} e^{jtZ} dt \int_{R^n} \prod_{i=1}^{n} dX_i f_{X_i}(x) e^{-jtX_i} \\
&= \frac{1}{2\pi} \int_{-\infty}^{\infty} e^{jtZ} dt \left[\int_{-\infty}^{\infty} f_X(x) e^{-jtX} dX \right]^n .
\end{aligned}
\tag{170}
$$

The reason for the last step in (170) is because all X_i are identically distributed and we set $X = X_i$ for $X \in \{X_1, X_2, X_3, \cdots, X_n\}$. If we let

$$
\tilde{f}(t) = \int_{-\infty}^{\infty} f_X(x) e^{-jtX} dX,
\tag{171}
$$

then $\tilde{f}(t)$ is called the Fourier transform (FT) of $f_X(x)$. This means that $\tilde{f}(-t)$ is the characteristic function of $f_X(x)$ and (170) simplifies to

$$
f_Z(Z) = \frac{1}{2\pi} \int_{-\infty}^{\infty} \tilde{f}(t)^n e^{jtZ} dt.
\tag{172}
$$

Equation (172) is the inverse Fourier transform (IFT) of $\tilde{f}(t)^n$ which is the nth power of the Fourier transform of $f_X(x)$. Generally, for a graph with $n_t > 1$ transmitters,

$$
\begin{aligned}
Z &= \sum_{m=1}^{n_t} |\xi_m|^2 \\
&= \sum_{m=1}^{n_t} \xi_{r_m}^2 + \xi_{i_m}^2,
\end{aligned}
\tag{173}
$$

and each $|\xi_m|^2$ contributes $\tilde{f}(t)^2$ to (172). This implies that for $n_t > 1$

$$
f_Z(Z) = \frac{1}{2\pi} \int_{-\infty}^{\infty} \tilde{f}(t)^{2n_t} e^{jtZ} dt.
\tag{174}
$$

The characteristic function approach of finding $f_Z(z)$ can therefore be summarised in three(3) steps as follows:

1. Fourier Transform: Find the Fourier transform of $f_X(x)$

2. Exponentiation: Raise the result in step 1. to the power of $2n_t$, and

3. Inverse Fourier Transform: Find the inverse Fourier transform of the result in step 2., to obtain $f_Z(z)$.

For $n_t = 1$, Figure(55)(a) shows the comparison between the convolution approach and the characteristic function approach in the low-loss regime when $\alpha = 0.5$, while Figure (55)(b) shows a high-loss regime comparison when $\alpha = 4$. The dashed yellow curve is analytical prediction from the convolution approach, while the red curve results from the characteristic function approach. Predictably, the two results are identical. The difference at $|\xi|^2 = 0$ is due to low convergence accuracy in implementing the integrals of the characteristic function approach (This is one of the limitations of CFA). However, at $n_t = 1$, both methods give the same level of accuracy.

Similar to what was done in Section 6.3.1, we can now use the distribution of $|\xi|^2$ to find that of the channel capacity by using (166) which we can write more explicitly as

$$f_C(c) = f_{Z = \sum_{m=1}^{n_t} |\xi_m|^2} \left(\frac{n_t \left(2^c - 1 \right)}{\rho \tau} \right) \frac{\log(2) 2^c}{\rho \tau}. \tag{175}$$

This is what we refer to, in this thesis, as the characteristic function approach. However, as we add more transmitters to the underlying system, it is not possible to use the convolution approach in predicting the distribution of channel capacity. Therefore we can resort to the characteristic function approach for MISO systems which is a generalisation of the SISO architecture. Section 6.4 presents the MISO systems and how to accurately predict their distributions of channel capacity in low as well as high loss regimes. In summary, for SISO systems, both the convolution and characteristic function approach work well in predicting the distribution of channel capacity. This is true regardless of the level of losses in the system.

(a) Distribution of $|\xi|^2$ at $\alpha = 0.5$ (b) Distribution of $|\xi|^2$ at $\alpha = 4$
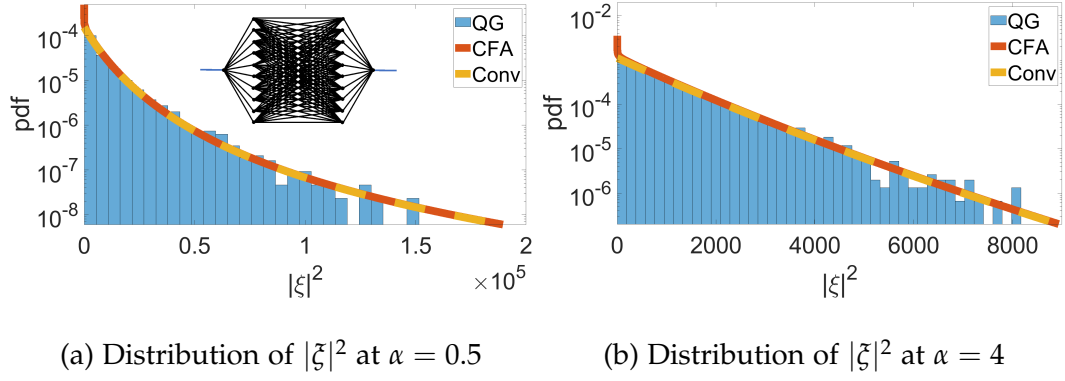
Figure 55.: Comparison between the predictions of the characteristic function approach (solid red curve) and the Convolution approach (dashed yellow curve) in estimating the distribution of $|\xi|^2$ in (a) low loss regime when $\alpha = 0.5$ and (b) high loss regime when $\alpha = 4$. In both cases, The graph size $B = 120$, $\delta = 0.5$. In (a), the coupling strength $\tau = 9.1216 \times 10^{-7}$, while in (b) $\tau = 7.5942 \times 10^{-7}$. The topology of the graph as indicated in the inset of (a).

6.4 GENERALISATION TO MISO SYSTEMS

For MISO systems, the channel capacity formula is given in (152). In this generalisation, the convolution approach is not possible. We therefore resort to the characteristic function approach (CFA) which works for all regimes of system losses and for any number of leads attached. This is significant because it creates the opportunity of obtaining a model which is 'one-model-fits-all'. The convergence of the integrations required in CFA is important

(a) Capacity distribution at $\alpha = 0.5$ (b) Capacity distribution at $\alpha = 4$
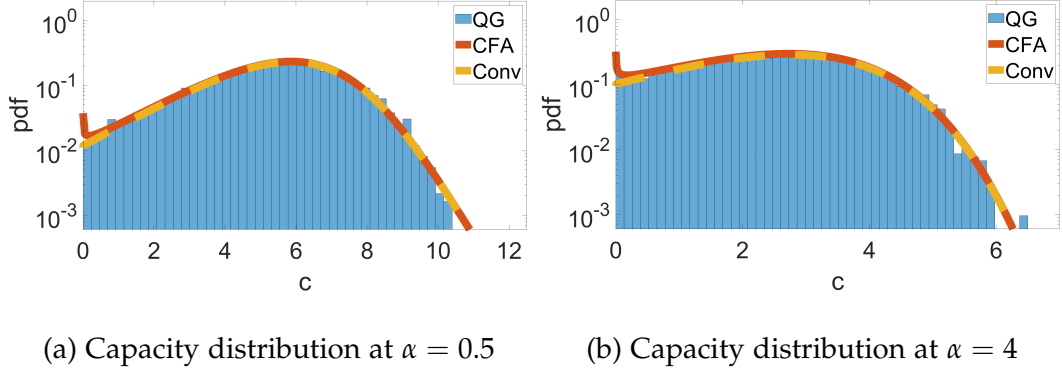
Figure 56.: Comparison between the characteristic function approach and the convolution method in the estimation of channel capacity in the low loss regime when $\alpha = 0.5$ and in the high loss regime when $\alpha = 4$. All other parameters are as in the caption of Figure 55 and graph topology is as indicated in the inset of Figure 55(a).

in obtaining an accurate theoretical predictions of the underlying channel capacity distribution.

Additionally, in the limit of high losses when the distribution of ξ becomes Gaussian, we will also derive a closed-form expression which efficiently predicts the distribution of channel capacity in this regime. With this closed-form solution, there is no need to worry about any convergence issues regarding the CFA implementation. Details of this calculation is presented in Section 6.4.2. We begin with characteristic function approach and subsequently show how to derive the closed form solution for systems with high losses.

6.4.1 *Characteristic Function Approach*

Going back to the characteristic function (CF) calculations in (174), we have shown that the method is able to predict the capacity distribution of a channel coupled to multiple transmitters from low to high losses. Examples of systems with low losses ($\alpha = 0.5$) are given in Figure 57 and it shows the distributions of channel capacity with varying number of transmitters, $n_t = 1, 2, 3$ and 4. Figures 58 and 59 show scenarios for medium ($\alpha = 2$) as well as high losses ($\alpha = 5$), respectively. In each case, the graph simulation result agrees well with the predictions of the CFA. However, as the number of transmitters is increased, a noticeable difference, between the graph simulation and the CFA predictions, begins to emerge particularly in the low loss regimes.

Increasing the number of transmitters (i.e. $n_t > 3$), further increases the error levels. This may be attributable to the numerical approximations involved in the implementation of the CFA mentioned in 6.3.2. The second step involves exponentiation, $\left[\tilde{f}(t)\right]^{2n_t}$, which depends on n_t. The error therefore increases in the limit of large n_t, especially in the low loss regime. To go round the challenge of implementing the characteristic function approach, a closed-form expression is derived in the high loss regime when the ξ is Gaussian distributed. This is presented in Section 6.4.2.

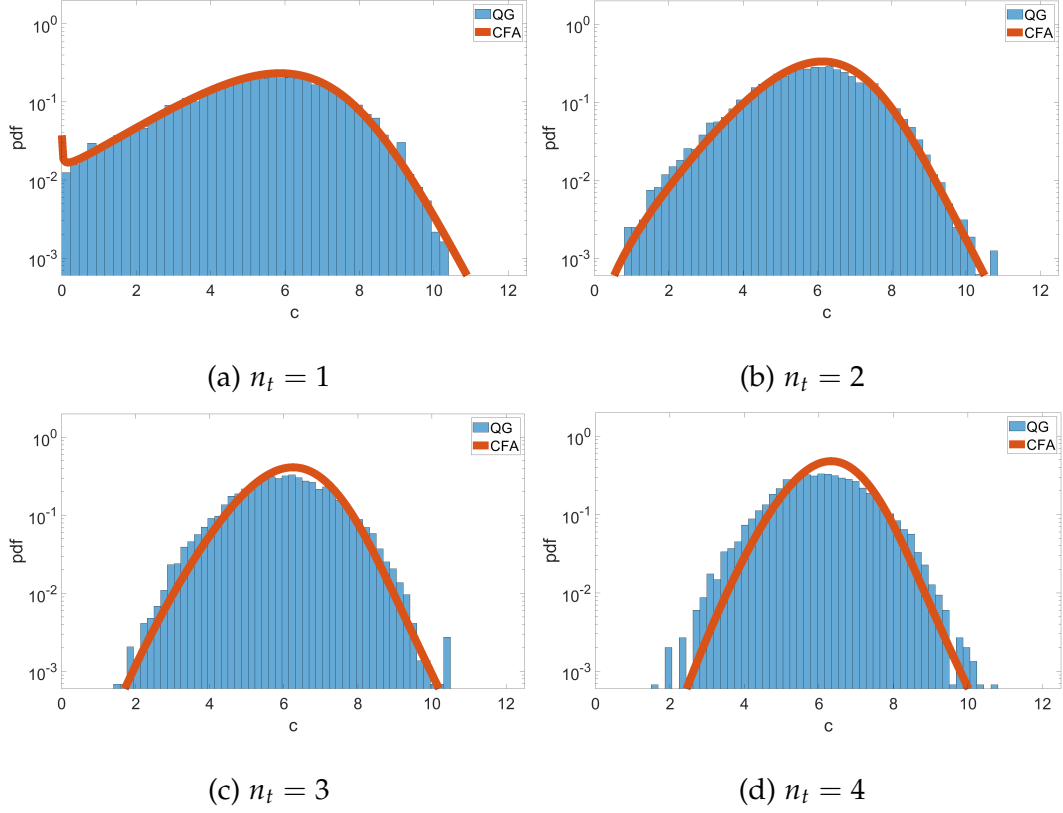(a) $n_t = 1$

(b) $n_t = 2$

(c) $n_t = 3$

(d) $n_t = 4$

Figure 57.: Characteristic function approach of predicting the distribution of channel capacity with transmitters ranging from one to four at $\alpha = 0.5$, $B = 120$, $\delta = 0.5$, $\tau = 9.1216 \times 10^{-7}$ and $\rho = 40$ dB

6.4.2 *High Loss Regime*

Previous section has results that are general across all loss regimes but not without some drawbacks. They are complicated to implement numerically, and involves several steps. We therefore introduce a simpler analytical approach where we derive a closed-form expression for the distribution of channel capacity in the high loss regime. This is important because it is com-

(a) $n_t = 1$

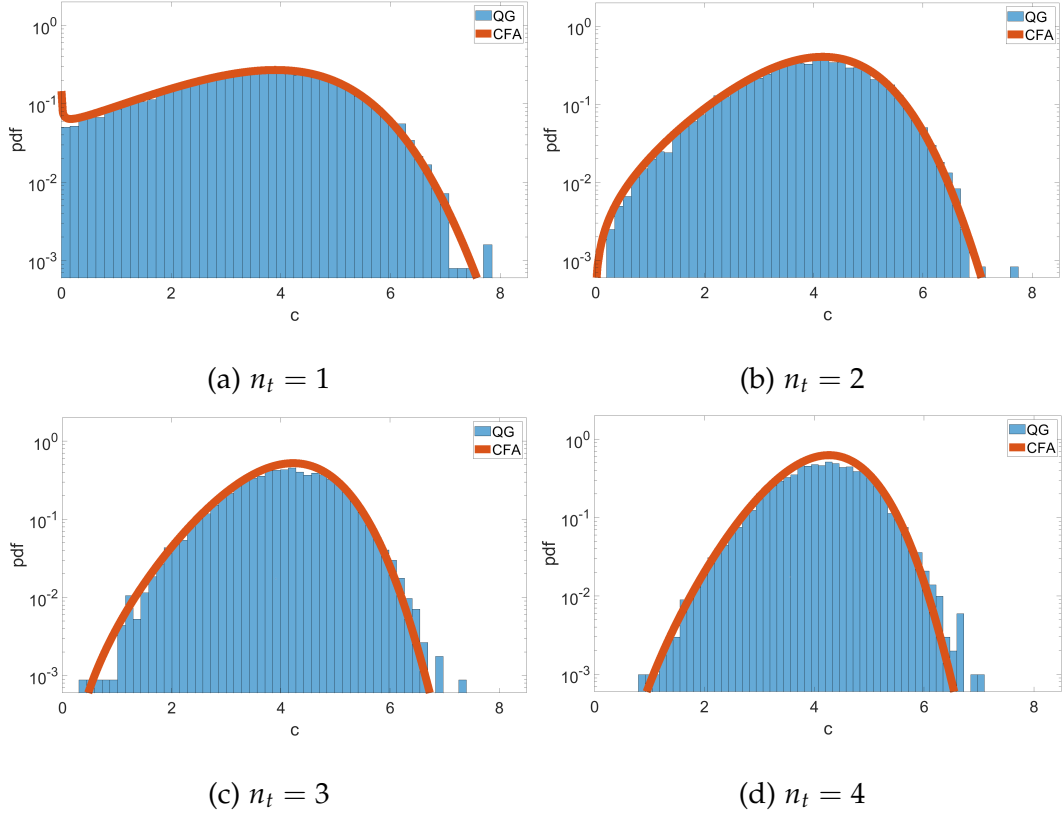(b) $n_t = 2$

(c) $n_t = 3$

(d) $n_t = 4$

Figure 58.: Distribution of channel capacity with transmitters ranging from one to four for a HEX10 Fourier graph at $\alpha = 2$, $B = 120$, $\delta = 0.5$, $\tau = 8.4326 \times 10^{-7}$ and $\rho = 40$ dB

monplace for communication channels to be modelled as having Rayleigh fading with high losses [150, 154–159].

As usual, we begin from the distribution of ξ. Since the distribution of ξ is Gaussian in high loss cases, then $|\xi|^2 = \xi_r^2 + \xi_i^2$ is a sum of two chi-squared distributions each with scaling parameter σ which is equal to

(a) $n_t = 1$

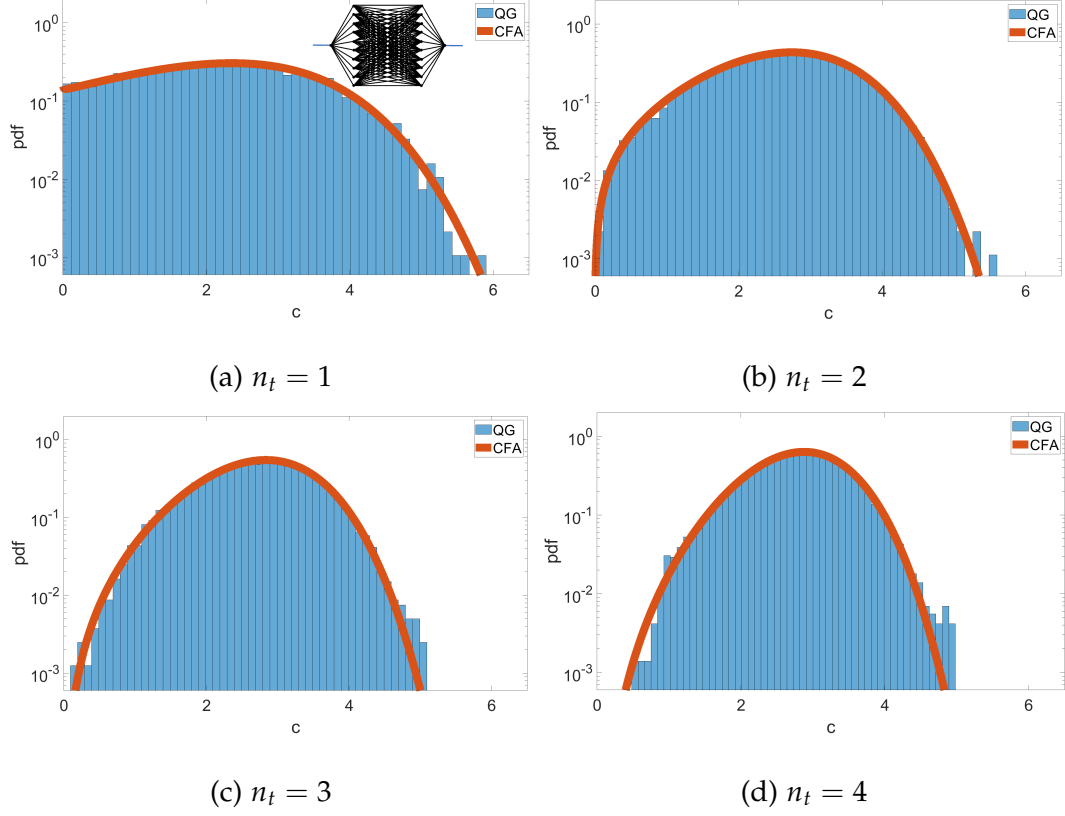(b) $n_t = 2$

(c) $n_t = 3$

(d) $n_t = 4$

Figure 59.: Distribution of channel capacity for a HEX10 Fourier graph with transmitters ranging from one to four at $\alpha = 5$, $B = 120$, $\delta = 0.5$, $\tau = 7.2063 \times 10^{-7}$ and $\rho = 40$ dB

standard deviation of the underlying Gaussian distribution, and degree of freedom $\nu = 1$. That is

$$
\begin{aligned}
f_{\xi_r^2}(x) = f_{\xi_i^2}(x) &= \frac{1}{\sigma\sqrt{2\pi}} x^{-\frac{1}{2}} e^{-\frac{x}{2\sigma^2}} \\
&= \frac{1}{\sigma 2^{\frac{\nu}{2}} \Gamma(\frac{\nu}{2})} x^{\frac{\nu}{2}-1} e^{-\frac{x}{2\sigma^2}},
\end{aligned}
\tag{176}
$$

where $\Gamma(\cdot)$ denotes the gamma function. In such cases we write $\xi_r^2 \sim \chi^2(\sigma, 1)$ and $\xi_i^2 \sim \chi^2(\sigma, 1)$, to denote that ξ_r^2 and ξ_i^2 are both chi-squared distributed with parameter scaling, σ and degree of freedom $\nu = 1$. Since

$|\tilde{\xi}|^2$ is the sum of two chi-squared distributed random variables, each with $\nu = 1$, then $|\tilde{\xi}|^2 \sim \chi^2(\sigma, 2)$ with pdf given by

$$f_{|\tilde{\xi}|^2}(x) = \frac{1}{2\sigma^2} e^{-\frac{x}{2\sigma^2}}. \tag{177}$$

Consequently, $Z = \sum_{m=1}^{n_t} |\tilde{\xi}_m|^2 \sim \chi^2(\sigma, 2n_t)$ with pdf given by

$$f_Z(z) = \frac{1}{(2\sigma^2)^{n_t} \Gamma(n_t)} z^{n_t-1} e^{-\frac{z}{2\sigma^2}}. \tag{178}$$

Figure 60 shows the distribution of Z with increasing number of transmitters. In each case the red curve represents the theoretical prediction derived in (178). The graph simulation was implemented for a HEX10 Fourier graph where the loss parameter $\alpha = 5$, $\delta = 0.5$, $B = 120$ and $\tau = 7.2063 \times 10^{-7}$. An ensemble average of 8000 realisations was used to produce the histogram in each of the plots. There is a good level of agreement between the closed-form expression in (178) and the numerical simulations even as we increase the number of transmitters.

We have calculated the pdf for Z. The pdf for C is easy to obtain from this by using equations (164), (166) and (178). Consequently, we obtain the pdf for C in the high-loss regime as

$$f_C(c) = \frac{\log(2)}{\Gamma(n_t)} \left(\frac{n_t}{2\sigma^2 \rho \tau} \right)^{n_t} 2^c (2^c - 1)^{n_t-1} e^{-\frac{n_t(2^c-1)}{2\sigma^2 \rho \tau}}. \tag{179}$$

Figure 61 shows a comparison between the characteristic function approach (CFA) and the closed form expression in (179). The red curve represents the CFA method, while the yellow curve is the prediction of the closed form expression. The number of transmitters $n_t = 1, 2, 3,$ and 4 in Figures 61 (a), (b), (c), and (d), respectively. The other parameters in this example are $\alpha = 5$, $B = 120$, $\delta = 0.5$, $\tau = 7.2063 \times 10^{-7}$ and $\rho = 40$ dB.

(a) $n_t = 1$

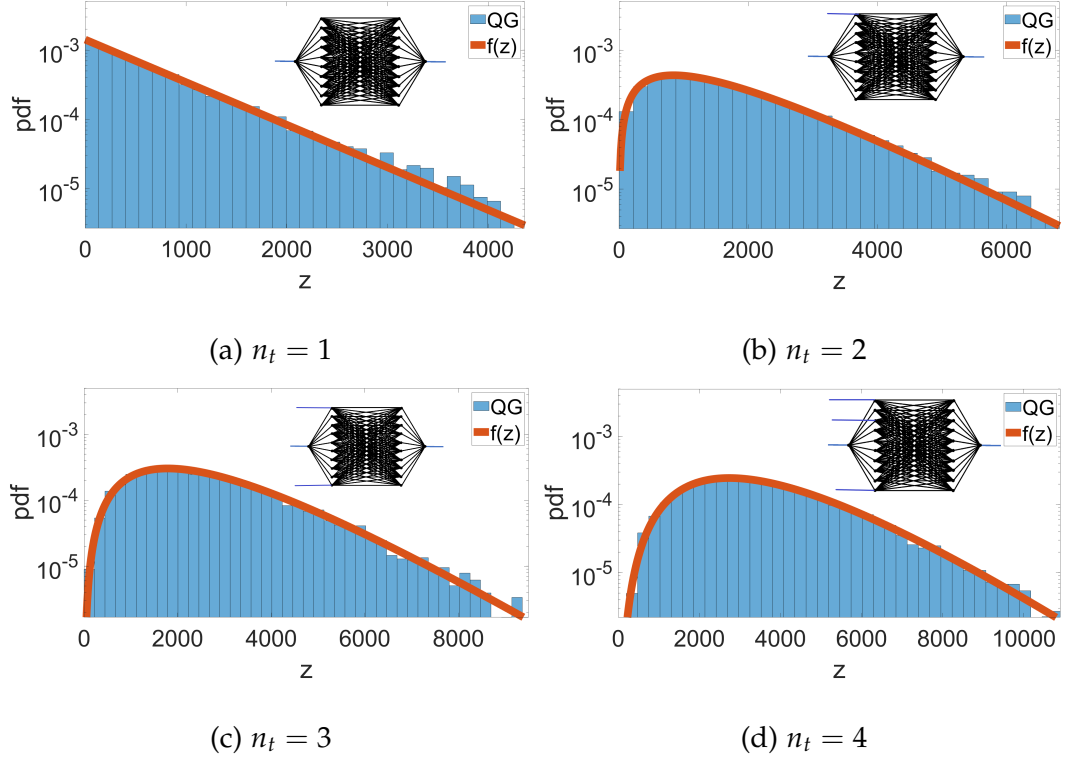(b) $n_t = 2$

(c) $n_t = 3$

(d) $n_t = 4$

Figure 60.: Comparison between the theoretical prediction (red solid curve) in (178) and the numerical simulation of an ensemble of 8000 HEX10 Fourier graphs (histogram) with number of transmitters ranging from one to four at $\alpha = 5$, $B = 120$, $\delta = 0.5$ and $\tau = 7.2063 \times 10^{-7}$.

Figures 62 (a) - (d) show examples with higher number of transmitters, from $n_t = 5$ to $n_t = 8$, respectively. The other parameters remain the same as those reported in Figure 61. The analytical results works well even with high number of input systems. While the closed-form expression in (179) and the CFA are two different ways of calculating the same pdf, they each have a unique advantage. The closed-form expression is a single equation, while the CFA involves several steps in its implementation (i.e. finding Fourier

(a) $n_t = 1$

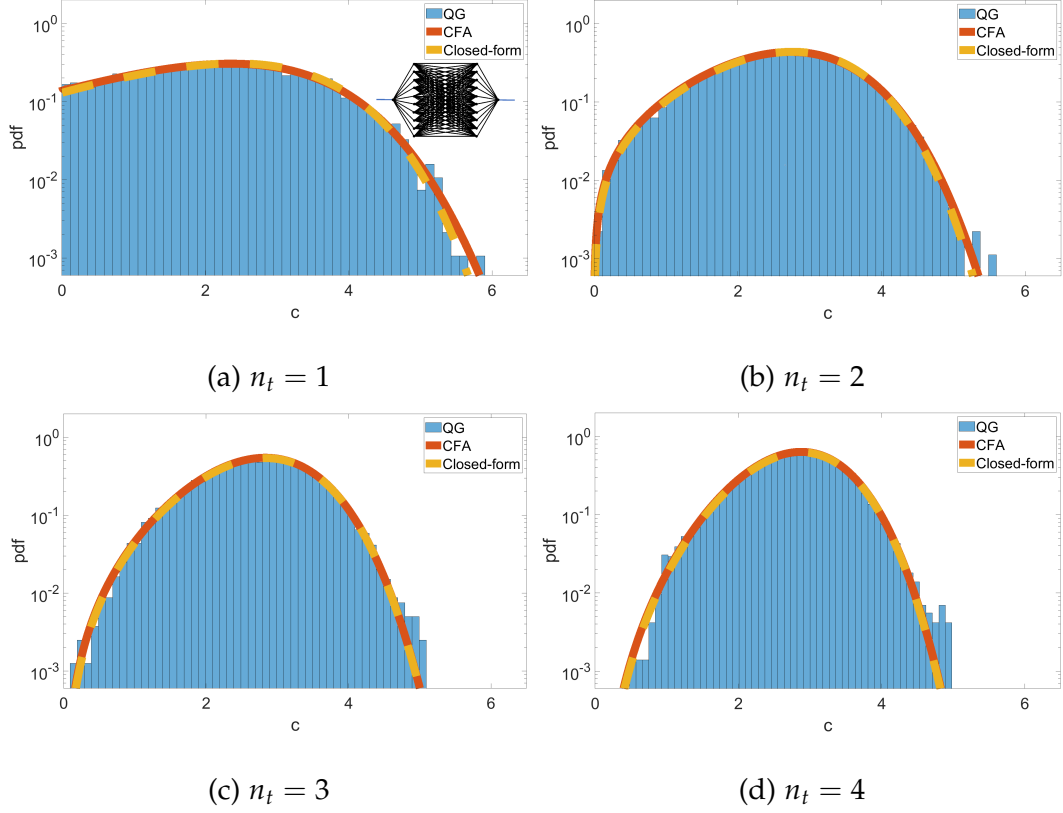(b) $n_t = 2$

(c) $n_t = 3$

(d) $n_t = 4$

Figure 61.: Comparison between the numerical simulation and analytical predictions of channel capacity distribution. The closed-form expression is the yellow curve and the CFA is the solid red. Other parameters are $\alpha = 5$, $B = 120$, $\delta = 0.5$, $\tau = 7.2063 \times 10^{-7}$ and $\rho = 40$ dB.

transform, exponentiation of result, and finding inverse Fourier transform), which may lead to problems of numerical convergence. However, the closed-form equation only works in high-loss regimes, whiles CFA works across all regimes.

(a) $n_t = 5$

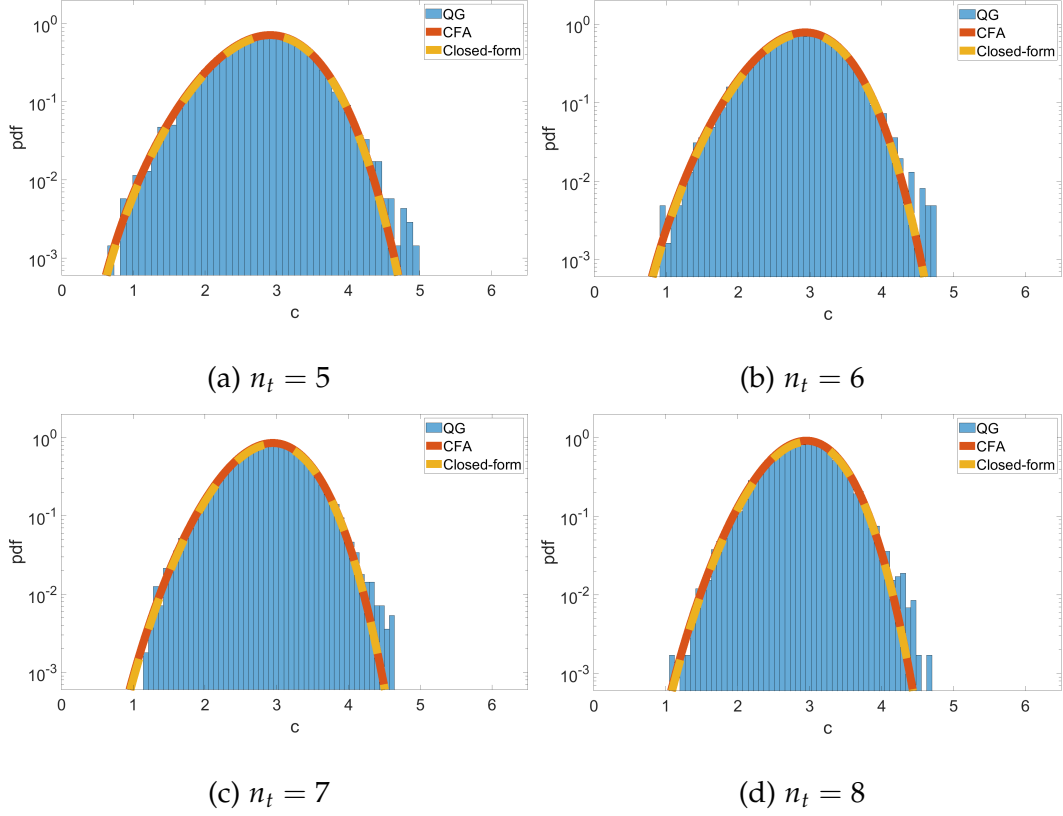(b) $n_t = 6$

(c) $n_t = 7$

(d) $n_t = 8$

Figure 62.: Comparison between the numerical simulation and analytical predictions of channel capacity distribution with $n_t = 5, 6, 7, 8$. All other parameters are as reported in Figure 61.

6.5 CONCLUSION

A simple model of quantum graphs on Fourier nodes weakly coupled to leads has been presented using an analogue of the Random Coupling Model. Although Fourier graphs can not be realised experimentally, it provides us with a simple alternative way of numerically simulating chaotic cavities using graph analogue RCM. This is because it satisfies all the assumptions of RCM in a natural way. It is therefore useful as a test-bed for numeri-

cal simulations of information transfer rates in both wired networks and communications within chaotic cavities.

We have shown different ways of obtaining the density functions for the distribution of capacity of communication channels. We began with the simple case of single-input single-out systems where we employed two methods. Both the *convolution* and the *characteristic function* approaches were shown to be able to describe the capacity distribution with remarkable level of accuracy. These worked both in the low loss regime as well as high loss regime in SISO systems.

However, in dealing with a more general scenario of multiple-input single-output systems, both the characteristic function approach and the closed-form expression are useful in predicting the channel capacity distribution in the high loss regime. The convolution method becomes unusable mainly because the distribution of sum of more than two F-distributed random variables is generally unknown in the form of explicit function. It remains an open problem in the field of probability theory to find the resultant distribution of the sum of F-distributed random variables. The convolution approach is therefore not suitable under such circumstances.

The characteristic function approach can be used for MISO/SIMO systems in across all regimes, but has convergence issues, especially in the low loss regime when the number of transmitters is increased. Therefore, in the high-loss regime where the distribution of ξ is Gaussian, we have derived a closed-form expression for the capacity distribution whose accuracy is

independent on the number of transmitters. Since many wireless applications involves high-loss communication channels with increasing number of transmit antennas, the closed-form expression provides a significant information in the study of channel capacities and the characteristics of wireless channels.

7

DISTRIBUTION OF CHANNEL CAPACITY ON NEUMANN GRAPHS

7.1 INTRODUCTION

Having calculated the distribution of the channel capacity for idealised Fourier graphs in the previous chapter, this chapter concentrates on a more realistic and experimentally accessible set of boundary conditions. These are graphs with Neumann boundary conditions at their vertices. We group these graphs into two main categories depending on the strength of lead coupling to the underlying graphs.

1. Weakly-coupled Neumann Graphs: These are graphs whose compact part are made of Neumann vertices and are weakly-coupled to leads.

2. Strongly-coupled Neumann Graphs: These are graphs where all the vertices, including those attached to leads, have Neumann boundary conditions.

In Chapter 6, the boundary conditions at the graph vertices are Fourier boundary conditions, which makes the random variable Y in (117) Gaussian distributed. However, Neumann boundary conditions make the distribution of Y a Laplace distribution. As discussed in Section 4.6.2, the variances of Y have been analytically determined for strongly-coupled Neumann graphs as well as for weakly-coupled graphs. It is important to note that, the expression of the variance of Y in (131) for a weakly-coupled graph remains unchanged whether the internal nodes have Fourier or Neumann boundary conditions. It is the distribution of Y that changes depending on the type of vertices under consideration.

In this chapter, we investigate the impact of Neumann boundary conditions on the distribution of channel capacity. Under each category, we will investigate the impact of the loss parameter α on the shape of the ζ distribution and hence on the capacity distribution. Additionally, we will explore the effects of increasing the number of transmitters while keeping the loss parameter constant. This will be done for both half-connected graphs (i.e. HEXv graphs with connectivity index, $\gamma \approx 0.5$) as well as fully-connected graphs (i.e. graphs with $\gamma = 1$).

We begin with the weakly-coupled Neumann graphs and subsequently discuss graphs that are strongly-coupled to leads.

This section treats graph networks with Neumann boundary conditions that are weakly-coupled to leads. Vertices that are not connected to leads have Neumann boundary conditions imposed on them, while vertices connected to leads have weakly-coupled boundary conditions discussed in Section 4.5.1 applied to them. This section explores the impact of weak coupling of leads on the distribution of channel capacity. We begin with the distributions of random variables X and Y.

7.2.1 *Distributions of Y and X*

In Chapter 6,we have seen that

$$
\begin{aligned}
S^M &= \sigma_{00} + Y \frac{1}{I_{2B} - \Lambda} Y^\dagger \\
&= \sigma_{00} + \sigma_Y X \frac{1}{I_{2B} - \Lambda} X^\dagger \sigma_Y \\
&= \sigma_{00} + \sigma_Y^2 \xi,
\end{aligned}
\tag{180}
$$

where Y (for Fourier graphs) is a non-standard Gaussian random variable, and X is the standardised version of Y.

In this section, we investigate the distributions of Y and X for Neumann graphs that are attached weakly to external leads. The distribution of Y is shown in Figure 63(a) for a Neumann graph with a HEX10 topology as shown in the inset. As we saw in Section 4.6.2, the variance of a Laplace distributed random variable with parameter b, is given by $2b^2$. Comparing

this with the analytical form of the variance of Y given in (131), we see that the parameter b can be written as $b = \exp(-\epsilon/2)\sin\delta/(2\sqrt{B})$ for complex Y. Keeping in mind that $\Re(Y)$ and $\Im(Y)$ are iid's, the parameter b for each of the real and imaginary parts is $b = \exp(-\epsilon/2)\sin\delta/(2\sqrt{2B})$. The variables δ and ϵ are free parameters whose values determine the level of losses through the leads and the compact part of the graph, respectively. For the distribution shown in Figure 63(a), the graph has $B = 120$ bonds and we chose $\delta = 0.5$ and $\epsilon = 1.9154 \times 10^{-3}$. This implies that $b \approx 0.0155$ and the coupling parameter is $\tau = (\exp(-\epsilon)\sin^2\delta/(2B))^2 = 9.1369 \times 10^{-7}$.

At $\alpha = 0.5$, Figure 63(b) shows the distribution of the standardised random variable $X = (1/\sigma_Y)Y$ scaled so that its variance is $\langle|X|^2\rangle = 1$. Therefore the variance of the real and imaginary parts of X after normalisation is 0.5 which corresponds to $b = 0.5$. The red curve is the distribution of Laplace random variable with variance $2b^2 = 0.5$.

7.2.2 Distribution of ξ

From (128), the normalised scattering matrix is given in terms of the random variable X

$$\xi = X\frac{1}{I_{2B} - \Lambda}X^\dagger, \tag{181}$$

where Λ is a $2B \times 2B$ diagonal matrix whose diagonal elements are eigenvalues of the transfer matrix $\hat{T}$.

(a) Distribution of $\Re(Y)$ at $\alpha = 0.5$ (b) Distribution of $\Re(X)$ at $\alpha = 0.5$
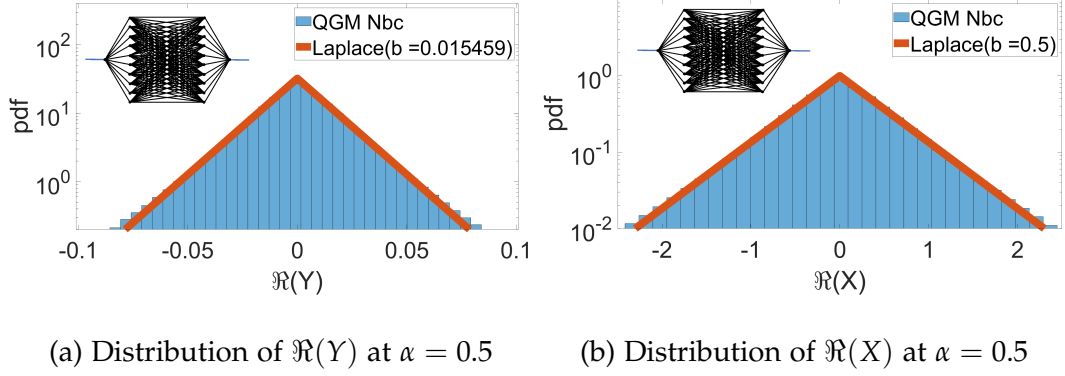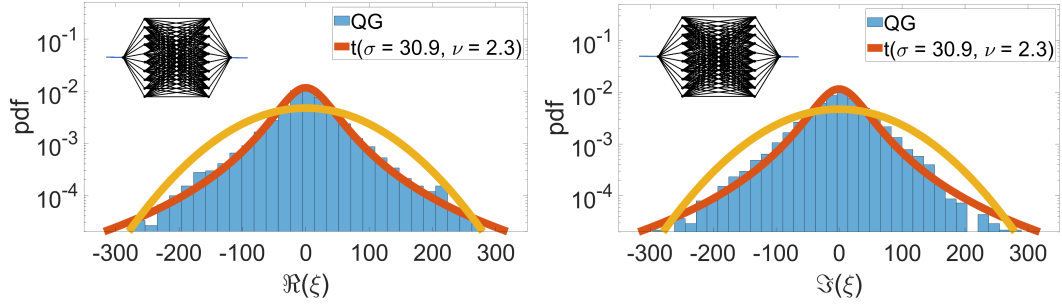
Figure 63.: Distribution of (a) $\Re(Y)$ and (b) $\Re(X)$ for a Neumann graph of HEX10 topology (histogram) at $\alpha = 0.5$, $B = 120$, $\delta = 0.5$, $\tau = 9.1369 \times 10^{-7}$ and $n_t = 1$. The variances of $\Re(Y)$ and $\Re(X)$ are 9.577×10^{-4} and 0.5 respectively. In both plots, an ensemble of 8000 graphs was used.

In this section, the distribution of ζ is investigated. Figure 64 shows the distribution of the real and the imaginary parts of ζ. As expected from Chapter 6, both the real and the imaginary parts are t-distributed in the low loss regime (note that $\alpha = 0.5$ in this example) with identical parameters σ and ν.

However, comparing the values of the two parameters here with those in an equivalent Fourier graph as in Figure 49(a), it is obvious that the values of both the scale parameter σ and the shape parameter ν are significantly different. It is important to note that both graphs are HEX10 graphs with equal attributes apart from boundary conditions. The HEX10 Fourier graph has $\sigma = 54.6$ and $\nu = 6.2$, while this HEX10 Neumann graph, as shown in Figure 64, has $\sigma = 30.9$ and $\nu = 2.3$. Consistently, the values of σ and ν

from Fourier graphs are large compared to those from equivalent Neumann graphs. This is true regardless of the amount of losses in the underlying system as will be seen later in this chapter. Despite the difference in the parameter values, ξ has the same functional form in both Neumann and Fourier graphs. The difference in the distributions of X has resulted in different values of σ and ν, where the Fourier graphs have their ξ closer to Gaussian distribution than the Neumann counterparts.

(a) Distribution of $\Re(\xi)$ at $\alpha = 0.5$

(b) Distribution of $\Im(\xi)$ at $\alpha = 0.5$

Figure 64.: Distribution of (a) $\Re(\xi)$ and (b) $\Im(\xi)$ for a Neumann graph of HEX10 topology (histogram) at $\alpha = 0.5$, $B = 120$, $\delta = 0.5$, $\tau = 9.1369 \times 10^{-7}$ and $n_t = 1$. In both plots, an ensemble of 8000 graphs was used.

7.2.3 *Distribution of Channel Capacity for SISO Systems*

From (128), the scattering matrix S^M is related to the normalised scattering matrix ζ through

$$
\begin{aligned}
S^M &= \sqrt{\tau}\zeta \\
&= \mathrm{e}^{-\epsilon}\frac{\sin^2 \delta}{2B}\zeta.
\end{aligned}
$$

(182)

This implies that the communication matrix H, which is modelled by S^M, can be used to calculate the distribution of channel capacity as we saw in Chapter 6. The convolution approach (CA) introduced in Section 6.3.1 and the characteristic function approach (CFA) in Section 6.3.2 together with the derived equations, are still applicable in this chapter. Again, since the ζ is t-distributed in the low loss regime, then $|\zeta|^2 = \zeta_r^2 + \zeta_i^2$ is a sum of two F-distributed random variables ζ_r^2 and ζ_i^2, where ζ_r and ζ_i are the real and imaginary of parts of ζ.

Figure 65 compares the distributions of ζ_r and ζ_i with the theoretical predictions (red curves) in (160). The theoretical calculations agree well with numerical simulations for a HEX10 Neumann graph. We can therefore use these predictions to calculate the distribution of their sum $|\zeta|^2$. This could be calculated in two different ways as was discussed in Chapter 7, where we used the CA (discussed in Section 6.3.1) and the CFA (discussed in Section 6.3.2) to calculate the pdf of the channel capacity.

The distribution of $|\zeta|^2$ is shown in Figure 66. This is compared with the two analytical solutions of Sections 6.3.1 and 6.3.2. The solid red curve is the
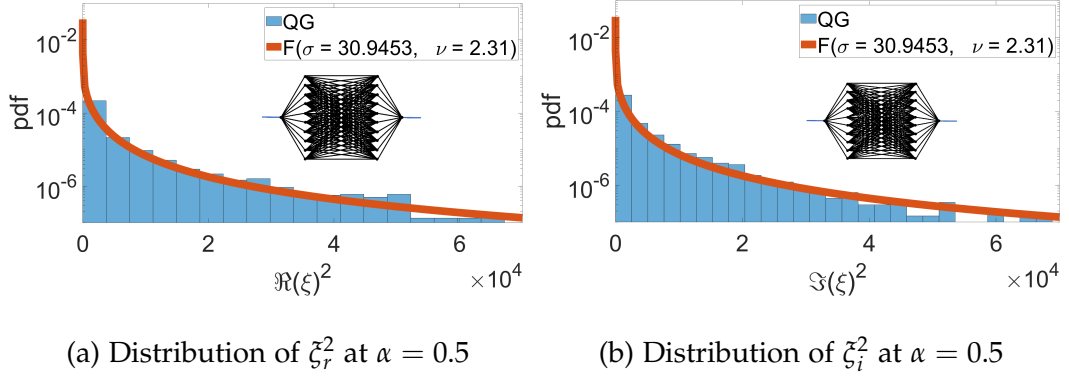
(a) Distribution of ξ_r^2 at $\alpha = 0.5$ (b) Distribution of ξ_i^2 at $\alpha = 0.5$

Figure 65.: (a) and (b) are the distributions of the squares of real and imaginary parts of ξ for a Neumann graph with HEX10 topology at $\alpha = 0.5$, $B = 120$, $\delta = 0.5$, $\tau = 9.1369 \times 10^{-7}$ and $n_t = 1$. In both plots, an ensemble of 8000 graphs was used.

prediction from the characteristic function approach, while the dashed yellow curve represents the convolution approach as presented in (167). Since the figure was generated from ξ distribution with a small value of $\nu = 2.3$, it cannot be compared with the closed-form solution, derived in (178), which was derived for $\nu > 30$. Both the convolution and the characteristic function approaches agree well with the numerical simulation.

As shown in Chapter 6, we can always derive the channel capacity distribution from the distribution of $|\xi|^2$ using the transformation $f_C(c) = f_{|\xi|^2}(z)\mathrm{d}Z/\mathrm{d}C$, where $z = n_t(2^c - 1)/(\rho\tau)$ and Jacobian of transformation $\mathrm{d}Z/\mathrm{d}C = \log(2)2^c/(\rho\tau)$. This was summarised in (175). Using both the convolution and characteristic function approaches, we compare the predictions of the two approaches with the numerical simulation of a HEX10 Neumann graph. This is shown in Figure 67 where the solid red and dashed
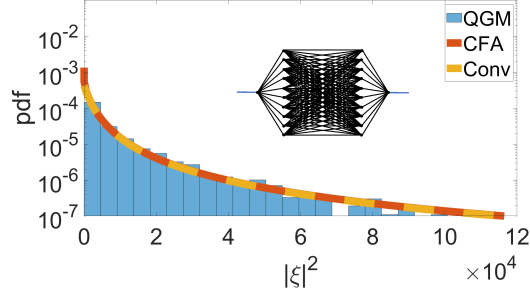
Figure 66.: Distribution of $|\xi|^2$ for a Neumann graph with HEX10 topology

at $\alpha = 0.5$, $B = 120$, $\delta = 0.5$, $\tau = 9.1369 \times 10^{-7}$ and $n_t = 1$. An

ensemble of 8000 graphs was used to create this distribution. The

solid red curve is the theoretical prediction of the characteristic

function approach, while the dashed yellow is the convolution

approach.

yellow curves are the theoretical predictions of the characteristic function
and the convolution approaches respectively.

However, from a critical examination of this figure as compared with Fig-
ure 56(a) of Chapter 6, we can see that the predictions in Figure 56(a) fit the
numerical simulation better. This is because, the more the distribution of
ξ approaches that of a Cauchy distribution (i.e. $\nu = 1$), the more challeng-
ing it is to maintain the level of accuracy we see in Figure 56. It is worth
mentioning that, although both figures are simulated at $\alpha = 0.5$, the Fourier
graph produces larger values of the degrees-of-freedom parameter ν than
the Neumann graph. This is ascribed to the fact that Fourier graphs ensure
equal scattering amplitudes at the nodes, while Neumann graphs favour
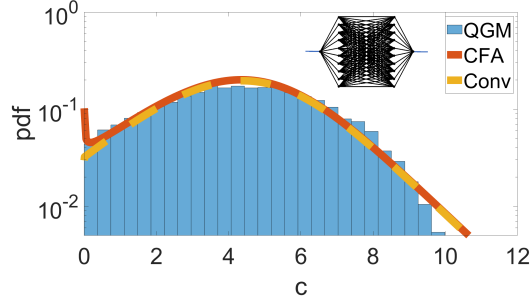back scattering with an increasing valency of the node.

Figure 67.: Distribution of channel capacity for a Neumann graph with HEX10 topology at $\alpha = 0.5$, $B = 120$, $\delta = 0.5$, $\tau = 9.1369 \times 10^{-7}$ and $n_t = 1$. An ensemble of 8000 graphs was used to create this distribution. The solid red curve is the theoretical prediction obtained from the characteristic function approach, while the dashed yellow is the result obtained from the convolution approach.

Next, we investigate the impact of augmenting system losses by increasing the value of α. Figure 68 shows the distribution of ξ when the loss parameter is $\alpha = 5$. It is instructive to note that the shape parameter $\nu = 7.1$ is still far below the threshold of $\nu = 30$ at which the distribution approximately Gaussian. The red curve is a t-distribution with $\sigma = 11.5$ and $\nu = 7.1$, while the yellow curve represents a Gaussian distribution with same variance as the t-distribution. It is obvious that the distribution of ξ in this plot is significantly different from the normal distribution. Again, comparing this plot with its Fourier graph equivalent, in terms of size and level of losses as depicted in Figure 50(b), one finds that the distribution of ξ

in Figure 50(b) is approximately Gaussian distributed, while Figure 68 still remains t-distributed.
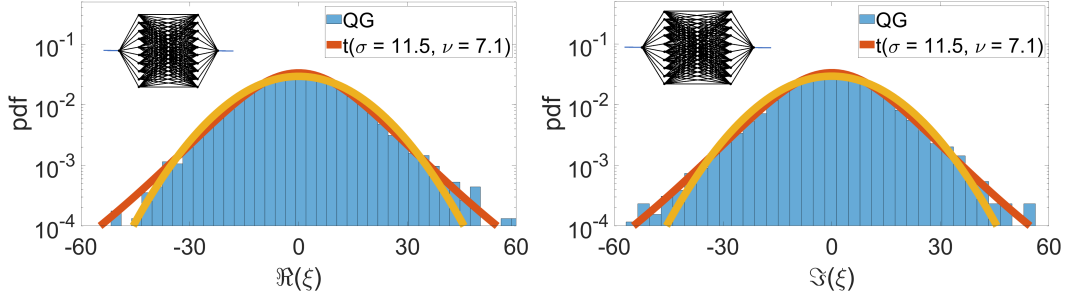
(a) Distribution of $\Re(\xi)$ at $\alpha = 5$ (b) Distribution of $\Im(\xi)$ at $\alpha = 5$

Figure 68.: Distribution of (a) $\Re(\xi)$ and (b) $\Im(\xi)$ for a Neumann graph of HEX10 topology (histogram) at $\alpha = 5$, $B = 120$, $\delta = 0.5$, $\tau = 7.2189 \times 10^{-7}$ and $n_t = 1$. In both plots, an ensemble of 8000 graphs was used.

In fact, for half-connected Neumann graphs that are weakly-coupled to leads, the distributions of ξ never attains 'Gaussianity' no matter what level of losses we consider. As α increases, the shape parameter ν initially increases rapidly and then plateaus. After it plateaus, the shape parameter broadly remains constant at $\nu = 7$. Figure 69 shows how the parameters of ξ changes with increasing system losses. In Figure 69(a), it can be observed that $\nu < 30$ regardless of how much we increase the value of α. Unlike Fourier graphs, which transition from t-distribution to Gaussian distribution with increasing losses, ξ is always t-distributed for half-connected Neumann graphs. Therefore the closed-form solution derived in section 6.4.2 does not apply for half-connected Neumann graphs with weakly-coupled

leads. However, we still have the choice between convolution approach and characteristic function approach (for SISO systems). On the other hand, under MISO or SIMO systems, we are stuck with using only the characteristic function approach for these graphs, since the convolution approach only applies to SISO systems.
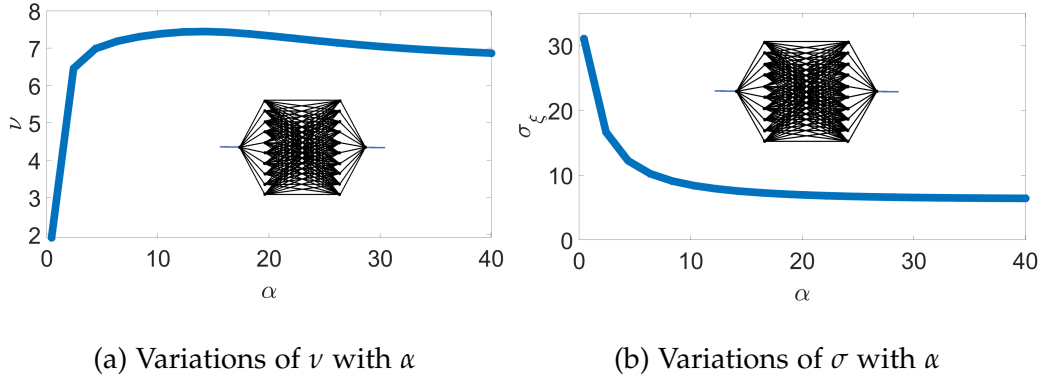

(a) Variations of ν with α (b) Variations of σ with α

Figure 69.: Effects of increasing losses on parameters of ξ for a Neumann graph of HEX10 topology (histogram). $B = 120$, $\delta = 0.5$ and $n_t = 1$. In both plots, an ensemble of 8000 graphs was used.

Figure 70 shows a comparison between the characteristic function approach (i.e. solid red curve in the figure) and the convolution approach (dashed yellow curve) for a HEX10 Neumann graph coupled to a single input and single output system at $\alpha = 5$. The theoretical predictions agree well with the numerical simulation. The topology of the simulated graph is shown in the inset of Figure 70, and an ensemble of 8000 such graphs were used to create the distribution. Despite the fact that both CA and CFA are different ways of computing the same formula, the CA cannot be used for

systems with multiple transmit antennas. In the next section, we discuss graph networks coupled to multiple transmit or multiple receive antennas.
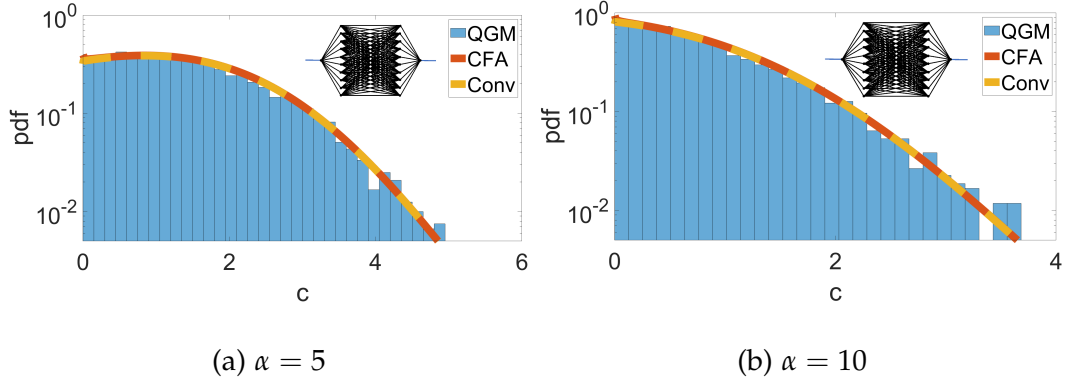

(a) $\alpha = 5$ (b) $\alpha = 10$

Figure 70.: Distribution of channel capacity for a weakly-coupled Neumann graph with HEX10 topology at $\alpha = 5$, $B = 120$, $\delta = 0.5$ and $n_t = 1$. In each case, an ensemble of 8000 graphs was used to create the distribution. The solid red curve is the theoretical prediction of the characteristic function approach, while the dashed yellow is the convolution approach. The coupling strength in (a) is $\tau = 7.2189 \times 10^{-7}$, while , $\tau = 5.5561 \times 10^{-7}$ in (b).

7.2.4 *Distribution of Channel Capacity for MISO Systems*

In this subsection, we focus on the effects of increasing the number of transmitters $n_t = 1, 2, 3, 4$. Since both the convolution approach and the closed-form expression cannot be applied in this scenario, we will only compare the simulations with the characteristic function approach at $\alpha = 10$, for an ensemble of 8000 randomly generated HEX10 Neumann graphs with weak

coupling of leads. The coupling parameter $\tau = 5.5561 \times 10^{-7}$, and the signal to noise ration $\rho = 40$ dB. In Figure 71, the prediction of the characteristic function approach (i.e. the red curve) agrees well with the numerical calculations in all the four sub-figures.
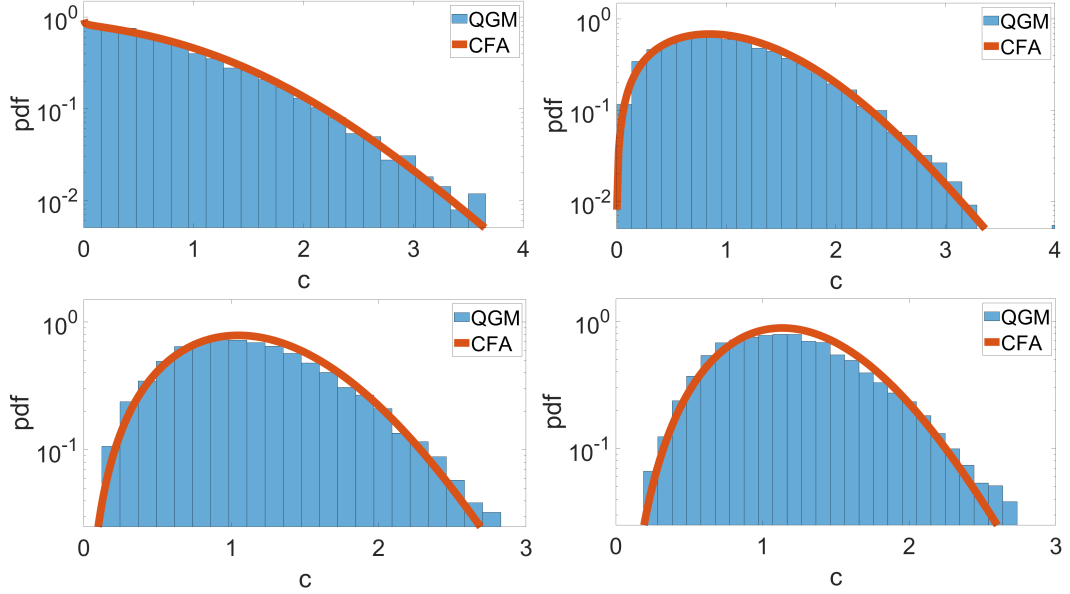

Figure 71.: Distribution of channel capacity for a weakly-coupled HEX10 Neumann graph with (a) $n_t = 1$, (b) $n_t = 2$, (c) $n_t = 3$, and (d) $n_t = 4$ at $\alpha = 10$, $B = 120$, $\delta = 0.5$ and $\rho = 40$ dB. The red curve is the theoretical prediction using the characteristic function approach. In each case, the coupling parameter is $\tau = 5.5561 \times 10^{-7}$.

In this section we discuss the distribution of channel capacity for Neumann graphs where all the nodes, including those attached to leads, have Neumann boundary conditions. This is what we refer to as the *strongly-coupled* Neumann graphs. It is important to note that, the coupling parameter τ for strongly-coupled Neumann graphs is an order of magnitude higher that its counterpart which is weakly-coupled. We begin with the distribution of the random variable Y and how it compares with Neumann as well as Fourier graphs that are weakly-coupled to leads. This comparison will also be done for ξ and for the channel capacity distributions for SISO systems. Finally, we will consider the general case of MISO systems with particular attention placed on how increasing the number of transmitters affect the channel capacity distribution.

7.3.1   *Distribution of X*

The variance of Y for strongly-coupled Neumann graphs is given by $\sigma_Y^2 = 2(v-1)/(v^2 B)$ as we saw in section 4.6.2.2. This implies that the normalised random variable $X = (1/\sigma_Y)Y = \sqrt{(v^2 B)/2(v-1)}Y$ has a variance of 1. Figure 72 shows the distributions of real and imaginary parts of X compared with a Laplace distribution of unit variance. Since the real and imaginary

parts of X are iid's, then each will have a variance of 0.5. This corresponds
to the Laplace distribution parameter $b = 0.5$ as indicated in the figure.

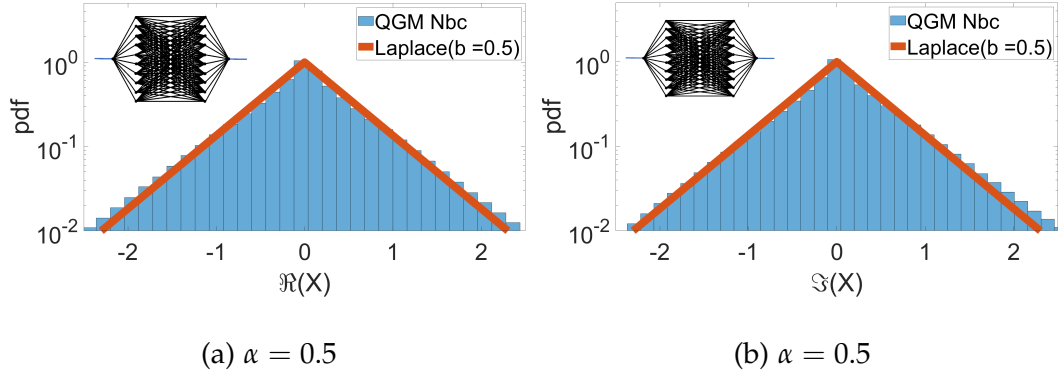(a) $\alpha = 0.5$ (b) $\alpha = 0.5$

Figure 72.: Distribution of real and imaginary parts of X for a strongly-coupled Neumann graph with HEX10 topology at $\alpha = 0.5$. In each case, an ensemble of 8000 graphs was used to create the distribution. The solid red curve is the theoretical prediction. The coupling strength is $\tau = 1.8544 \times 10^{-6}$.

7.3.2 *Distribution of ζ*

The next step is to find the distribution of the normalised scattering matrix ζ and use its distribution parameters σ and ν to calculate the channel capacity distributions by following the calculations discussed in Chapter 6. We first consider systems with small values of α, and then later deal with higher values of α. Figure 72 shows the distribution of ζ for a HEX10 strongly-coupled Neumann graph when $\alpha = 0.5$. This is compared with the distribution of a Gaussian random variable (yellow curve) of the same

variance as the t-distribution (red curve). Like its weakly-coupled counter-part, the distribution of ξ is t-distributed. However, the difference is that the value of the shape parameter ν has increased from $\nu = 2.3$ (see Figure 64) in the weakly-coupled case to $\nu = 3$ in the strongly-coupled graph of the same topology. There is also an increase in the scale parameter from $\sigma = 30.9$ to $\sigma = 34.2$. These changes result in a significant reduction in the range of ξ values from $[-300, \quad 300]$ in the case of weakly-coupled to $[-200, \quad 200]$ in the strongly-coupled case.

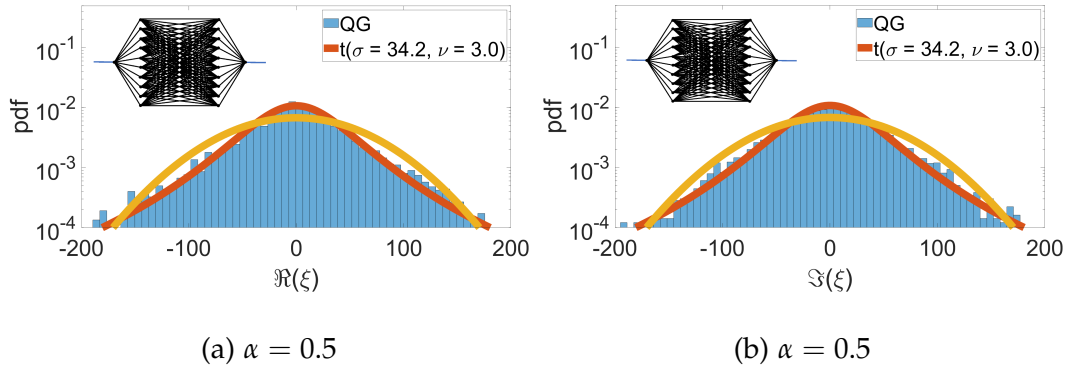(a) $\alpha = 0.5$

(b) $\alpha = 0.5$

Figure 73.: Distribution of real and imaginary parts of ξ for a strongly-coupled Neumann graph with HEX10 topology at $\alpha = 0.5$. In each case, an ensemble of 8000 graphs was used to create the distribution. The coupling strength is $\tau = 1.8544 \times 10^{-6}$. The t distribution (red curve) is compared with a Gaussian distribution (yellow) of the same variance.

The rest of the calculations remain the same as previously discussed. We use the parameter values σ and ν to calculate the distributions of ξ_r^2 and ξ_i^2 and use these identical distributions to find the distribution of $|\xi|^2 = \xi_r^2 + \xi_i^2$.

Finally we transform the distribution of $|\xi|^2$ in to the distribution of channel capacity. The rest of the figures in this chapter are based on the simulation of a strongly-coupled Neumann graph with a HEX10 topology. In each distribution presented, we use an ensemble average of 8000 randomly chosen graphs of the same topology.

7.3.3 *Distribution of Channel Capacity SISO Systems*

7.3.3.1 *HEXv or Half-connected Graphs*

We begin with the single-input single-output systems. Figure 74 shows the distribution of the squares of real and imaginary parts of ξ. The red curve in each case is the theoretical prediction based on the values of σ and ν obtained from Figure 73. Specifically, ξ_r^2 and ξ_i^2 are scaled F-distributed random variables each with degrees of freedoms $\nu_1 = 1$ and $\nu_2 = \nu$ and scale parameter σ.

The distribution of $|\xi|^2$, which is effectively the sum of two iid's obtained in Figure 74, is presented in Figure 75. We used the two approaches (i.e. convolution approach and the characteristic function approach) in predicting the pdf of $|\xi|^2$. The solid red curve represents characteristic function technique, while the dashed yellow curve represents the convolution approach. Again, this comparison is possible only when $n_t = 1$ and $n_r = 1$. For multiple transmitters, only the characteristic approach may be used when $\nu < 30$.
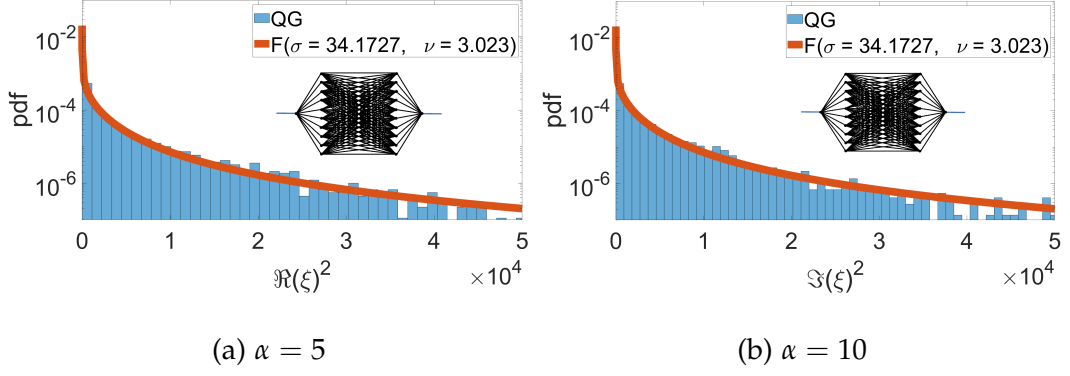
(a) $\alpha = 5$ (b) $\alpha = 10$

Figure 74.: Distribution of ξ_r^2 and ξ_i^2 for a strongly-coupled Neumann graph with HEX10 topology at $\alpha = 0.5$. In each case, an ensemble of 8000 graphs was used to create the distribution. The coupling strength is $\tau = 1.8544 \times 10^{-6}$. The red curve in each case is the theoretical prediction of a scaled F-distribution in (160).

Figure 76 shows the distribution of channel capacity at a small value of $\alpha = 0.5$. The solid red curve is the result of the characteristic function approach, while the dashed yellow curve represents the results obtained from the convolution approach. Even though the theoretical predictions of the channel capacity work well at low values of α, the accuracy of the prediction gets even better when the shape parameter increases. The increase in the shape parameter can be achieved by increasing the losses in the system.

When we increase the system losses to $\alpha = 5$, the shape parameter ν increases from $\nu = 3$ to $\nu = 6.9$. This is depicted in the legend of Figure 77(a) which shows the distribution of the real part of ξ at $\alpha = 5$. However, this increase in the value of ν does not go on indefinitely for half-connected Neu-
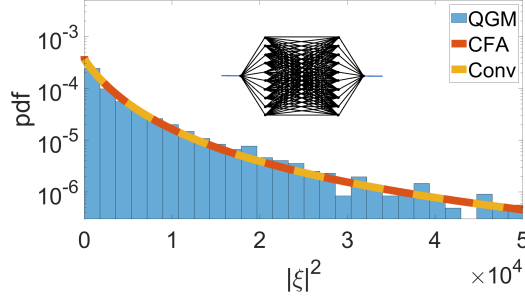
Figure 75.: Distribution of $|\xi|^2$ for a strongly-coupled Neumann graph with HEX10 topology, as indicated in the inset, at $\alpha = 0.5$. An ensemble of 8000 graphs was used to create the distribution. The coupling strength is $\tau = 1.8544 \times 10^{-6}$. The theoretical predictions using both the convolution approach (dashed yellow curve) and characteristic function approach (solid red curve) show a satisfactory agreement with the numerical simulation.

mann graphs. As we saw in the case of weakly-coupled graphs, the value of ν initially increases with increasing α but never reaches values that are high enough to make the distribution of the normalised scattering matrix ζ Gaussian.

In the specific case of strongly-coupled Neumann graphs, as the value of α increases, the shape parameter ν initially increases, then attains a peak value $\alpha = 5$ and then gradually decreases towards a saturated value of $\nu \approx 7$ for values of $\alpha > 5$. This is shown in Figure 79(a) for values of $\alpha \in [0.0396, \quad 40]$. Figure 77(a) shows the distribution of ζ at $\alpha = 5$, while Figure 77(b) shows the ζ distribution at $\alpha = 10$. As it can be seen, the value of ν at $\alpha = 5$ is greater than the value obtained at $\alpha = 10$.
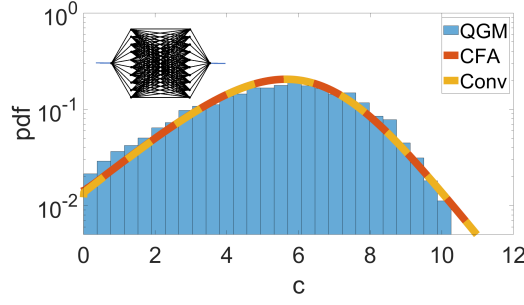
Figure 76.: Distribution of channel capacity for a strongly-coupled Neumann graph with HEX10 topology, as indicated in the inset, at $\alpha = 0.5$. An ensemble of 8000 graphs was used to create the distribution. The coupling strength is $\tau = 1.8544 \times 10^{-6}$. The theoretical predictions using both the convolution approach (dashed yellow curve) and characteristic function approach (solid red curve) agrees well with the numerical simulation.

Next, we use the parameter values in Figure 77(a) and (b) to calculate the distribution of channel capacity. The results are shown in Figure 78(a) and 78(b) respectively. It is obvious that the accuracy of the theoretical prediction here is better than what was found in the case when $\alpha = 0.5$ for the same strongly-coupled Neumann graph as depicted in Figure 76.

Just like in the case of half-connected weakly-coupled Neumann graphs, the distribution of ξ for strongly-coupled HEX10 Neumann graph remains t-distributed regardless of how high the value of the loss parameter α goes. Unlike the weakly-coupled Neumann graphs whose ν value approaches 7 with increasing α, the limiting value of ν in a strongly-coupled HEX10 Neumann graph is $\nu \approx 4$. The values of both parameters ν and σ are generally
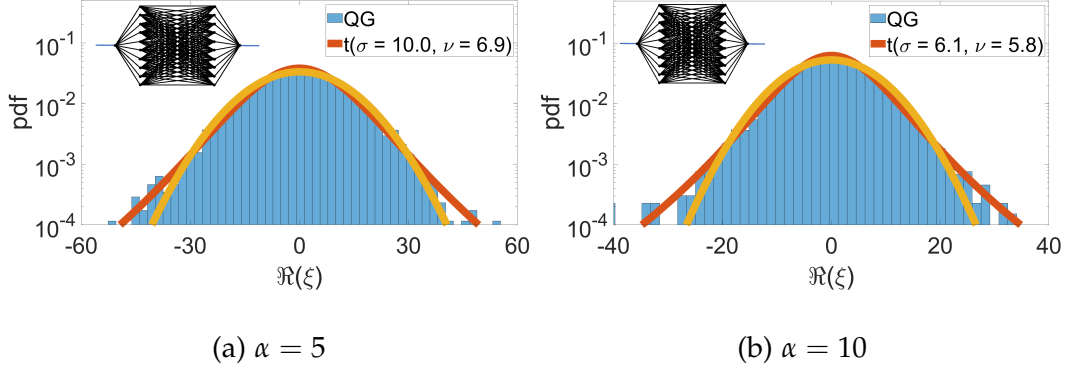
(a) $\alpha = 5$　　　　　　　　　(b) $\alpha = 10$

Figure 77.: Distribution of real parts of ξ for a strongly-coupled Neumann graph with HEX10 topology at $\alpha = 5$ in (a) and $\alpha = 10$ in (b). In each case, an ensemble of 8000 graphs was used to create the distribution. The coupling strength is $\tau = 1.4651 \times 10^{-6}$ for (a), while $\tau = 1.1277 \times 10^{-6}$ in (b).

lower in strongly-coupled graphs than in weakly-coupled graphs. For example, for a graph with HEX10 topology, the variations of both parameters are shown in Figure 79.

However, fully-connected graphs have a different story compared to half-connected graphs described above. The results for fully-connected graphs are presented next.

7.3.3.2 *Complete or Fully-connected Graphs*

As was discussed in chapter 3, fully-connected graphs have maximum connectivity $\gamma = 1$ where every vertex is connected to all other vertices. In this subsection, we focus on $K(v+1)$ graphs. $K(v+1)$ graphs are complete graphs with polygonal topology, and $v + 1$ vertices where the valency of
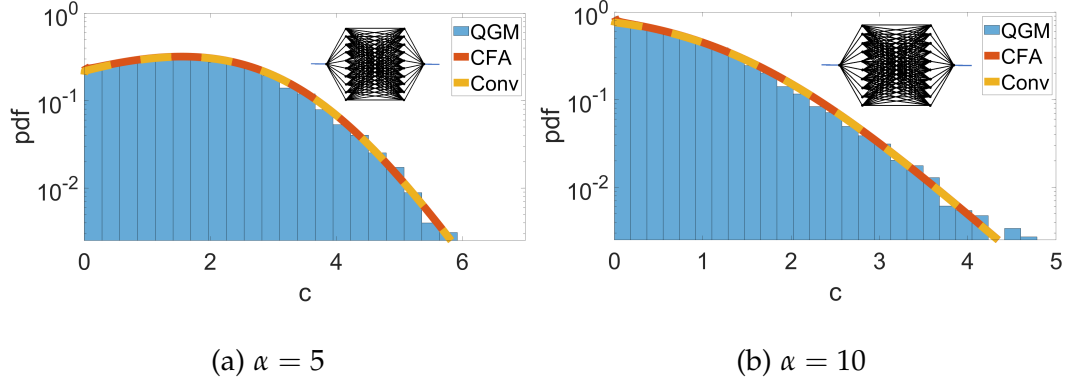
(a) $\alpha = 5$

(b) $\alpha = 10$

Figure 78.: Distribution of channel capacity for a strongly-coupled Neumann graph with HEX10 topology, as indicated in the inset, at $\alpha = 5$ in (a) and $\alpha = 10$ in (b) . An ensemble of 8000 graphs was used in each of the distributions with $n_t = 1$ and signal-to-noise ratio $\rho = 40$ dB. The coupling strength is $\tau = 1.4651 \times 10^{-6}$ in (a), while $\tau = 1.1277 \times 10^{-6}$ in (b). The theoretical predictions using both the convolution approach (dashed yellow curve) and characteristic function approach (solid red curve) agrees well with the numerical simulation.

each vertex is v. For example, Figure 80(a) illustrates a graph with K5 topology, while Figure 80(b) shows a K10 graph. A closer look at $K(v+1)$ graphs reveals that the number of bonds in such graphs

$$B = \frac{v(v+1)}{2}.$$ (183)

This is in contrast with HEXv graphs where the number of bonds is

$$B = v(v+2).$$ (184)

From (183) and (184) we can see that the number of bonds in both $K(v+1)$ graphs and HEXv graphs increases quadratically with increasing v, but
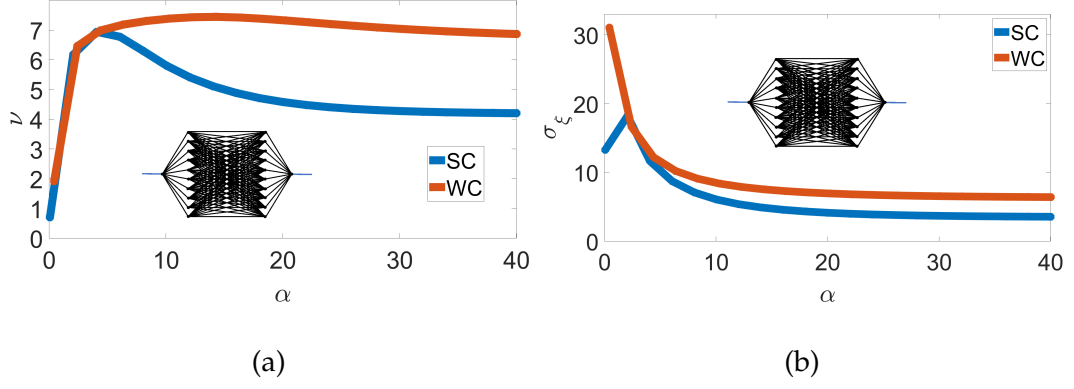
Figure 79.: An example of the comparison between the variations of (a) ν and (b) σ with increasing losses for a strongly-coupled (SC) and weakly-coupled (WC) HEXv Neumann graphs. In both plots, a HEX10 graph, as indicated in the inset, was used. From (a), it is obvious that the distribution of ξ is never Gaussian distributed no matter level of losses in the system.

the size of K$(v+1)$ graphs increase half as fast as that of HEXv in the limit of large v. But the connectivity index of K$(v+1)$ graphs is twice the connectivity of HEXv.

As we saw in chapter 3, the connectivity index γ for an arbitrary graph with n vertices and B bonds is given by

$$\gamma = \frac{2B}{n(n-1)}. \tag{185}$$

(a) K5 network.　　　　　　　　(b) K10 network
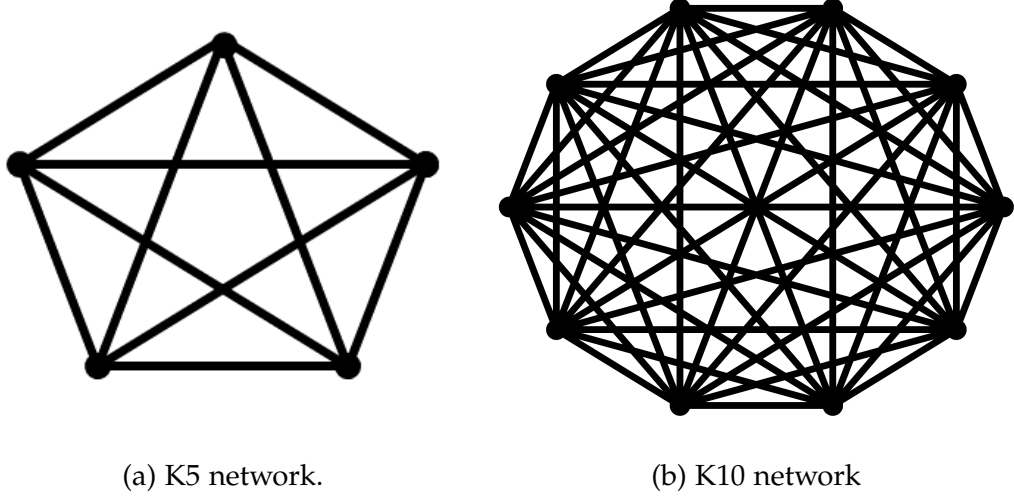
Figure 80.: Illustration of $K(v+1)$ graphs.

For $K(v+1)$ graphs, $n = v+1$, and from (183) and the formula for the connectivity index in (185), it implies that for all values of v in $K(v+1)$ graphs, the connectivity index is calculated as follows:

$$
\begin{aligned}
\gamma &= \frac{2B}{n(n-1)} \\
&= \frac{\frac{2v(v+1)}{2}}{(v+1)v} \\
&= 1.
\end{aligned}
\tag{186}
$$

As hinted before, the $K(v+1)$ graphs with Neumann boundary conditions have a rather different story when compared to HEXv graphs. Like the Neumann HEXv graphs, the normalised random variable X in (181) is also Laplace distributed in complete $K(v+1)$ graphs, but unlike the Neumann HEXv graphs, the distribution of the universal random variable ξ interpolates between t-distribution and Gaussian distribution with increasing loss parameter α.

Figure 81(a) shows the plot of the shape parameter ν versus the loss parameter $\alpha \in [0, \quad 3]$. The dashed turquoise curve indicates the threshold value of $\nu = 30$ above which the ξ distribution becomes approximately Gaussian. As can be seen from the figure, the distribution of ξ interpolates between t-distributed ($\nu < 30$) and Gaussian distributed ($\nu > 30$) with increasing losses. Generally, as the loss parameter α increases, the value of the shape parameter ν initially increases and later plateaus. Interestingly, $K(v+1)$ graphs with smaller number of bonds B plateau earlier compared to $K(v+1)$ graphs with a larger B. This is because, graphs with a relatively smaller B require a higher damping factor ϵ to achieve the same value of α (Remember that $\alpha = B(\epsilon_0 + \epsilon)/\pi$, and ϵ_0 remains constant for a particular coupling strength).

If we take a strongly-coupled K10 Neumann graph for example, the distribution of the non-normalised random variable Y and the corresponding normalised variable X are Laplace distributed as shown respectively in Figure 82(a) and (b). The red curves in the plot show the results obtained from the theoretical predictions.

However the real and imaginary parts of ξ may be t-distributed or Gaussian distributed depending on whether or not $\nu > 30$. This means that for fully-connected Neumann graphs, the distribution of ξ is not limited only to the t-distribution. It rather interpolates between t-distribution (in the low loss regime) and Gaussian distribution at high loss regime. The distribution shown in Figure 83 is for the real parts of ξ. The figure on the left shows the
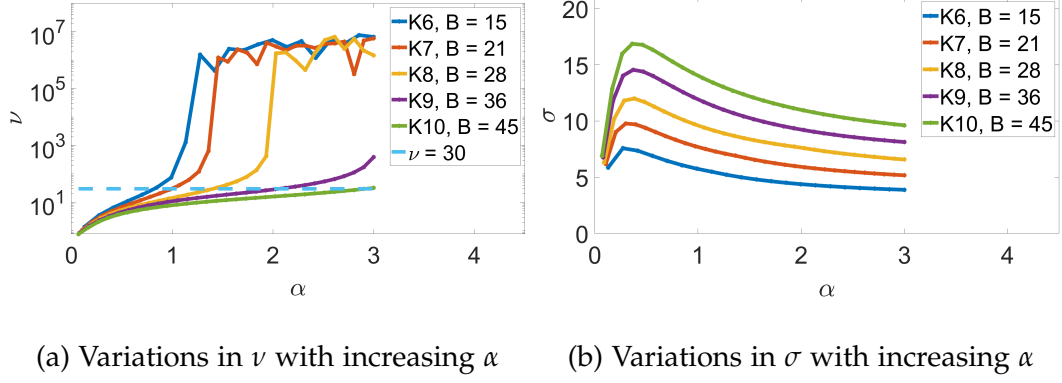
(a) Variations in ν with increasing α

(b) Variations in σ with increasing α

Figure 81.: Comparison between the variations of ν and σ with increasing losses for complete $K(\nu + 1)$ graphs which are strongly-coupled with Neumann boundary conditions. According to the ν values in (a), it is obvious that the distribution of ξ starts from being t-distributed ($\nu < 30$) to Gaussian distributed ($\nu > 30$) as the loss parameter increases. The dashed turquoise curve indicates the threshold value for the shape parameter ν.

distribution in the low-loss regime at $\alpha = 1$, while the figure on the right represents the ξ distribution in the high-loss regime where $\alpha = 4$. In each case, the solid red curve represents a t-distribution with scale parameter σ and shape parameter ν the values of which are shown in the legends. On the other hand, the dashed yellow curve is a Gaussian distribution whose variance is equal to the variance of the t-distribution shown. In (a), it obvious that the distribution of ξ is significantly different from Gaussian distribution, while in (b) the ξ is Gaussian distributed. From the values of σ and ν, we analytically estimate the distribution of the channel capacity as discussed before.

(a) Distribution of Y

(b) Distribution of X

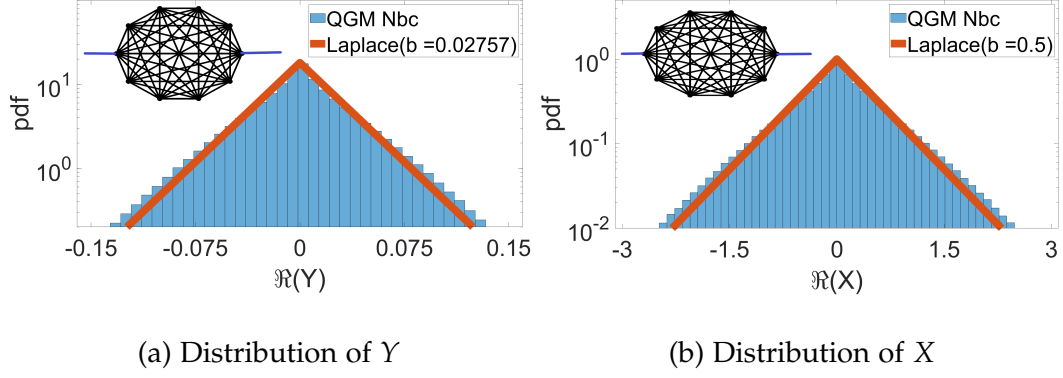Figure 82.: Distribution of the random variable Y and the standardised variable X for a strongly-coupled K10 Neumann graph at $\alpha = 4$.

(a) Distribution of ξ at $\alpha = 1$

(b) Distribution of ξ at $\alpha = 4$
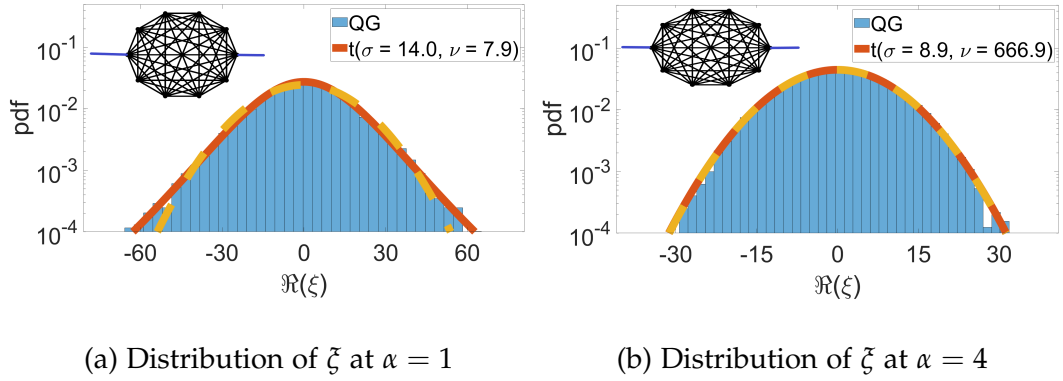
Figure 83.: Distribution of ξ for a strongly-coupled K10 Neumann graph at (a) $\alpha = 1$ and (b) $\alpha = 4$.

Figure 84(b) shows the distribution of channel capacity for a strongly-coupled K10 Neumann graph where $\epsilon = 0.2743$, $\rho = 40$ dB, $\alpha = 4$ and $\tau = 9.2442 \times 10^{-6}$. In each case, an ensemble of $20,000$ randomly chosen K10 graphs was used to generate the figure, and then compared with theoretical predictions. Since the simulation was done in high-loss regime (i.e. $\nu > 30$), and $n_t = 1$, each of the three theoretical approaches of predicting the capacity distribution may be used. The solid red curve represents the results

obtained from the characteristic function approach, the dashed yellow curve is the results from the convolution approach, while the dashed indigo curve represents the closed-form solution.

However, in the low-loss regime, we can only use the characteristic function approach or the convolution approach. This is shown in Figure 84(a), where $\epsilon = 0.06486$, $\rho = 40$ dB, $\alpha = 1$ and $\tau = 1.4054 \times 10^{-5}$. Predictably, the maximum value of the channel capacity in Figure 84(a) is greater than the one in Figure 84(b). This is because the range of the capacity is inversely proportional to the system losses.

(a) $\alpha = 1$ (b) $\alpha = 4$
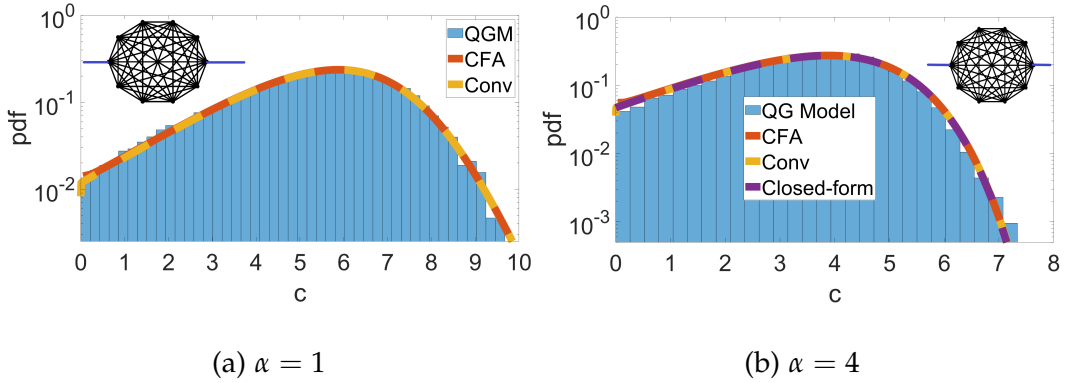
Figure 84.: Distribution of channel capacity for a strongly-coupled K10 Neumann graph at $\alpha = 4$.

After examining the capacity distribution of SISO systems for strongly-coupled Neumann half-connected (i.e. HEXv) graphs as well as complete graphs (i.e. K$(v+1)$) graphs, we next discuss what happens in MISO systems where multiple transmitters are coupled to the underlying graphs. We will start with half-connected graphs whose connectivity index $\gamma \approx 0.5$ for all v, and then subsequently treat fully-connected graphs where $\gamma = 1$.

7.3.4 *Distribution of Channel Capacity MISO Systems*

7.3.4.1 *HEXv Graphs*

In this subsection, we will keep the loss parameter constant at $\alpha \approx 5$, and inspect the effect of increasing the number of transmitters $n_t = 1, 2, 3, 4$. As can be seen in Figure 85, the theoretical prediction, using the characteristic function approach, fits the graph simulation well for multiple transmitters. As the number of transmitters increases, there is a corresponding increase in radiated losses through the leads. Although this increase in radiation is small compared to the total internal losses, it still affects the support of the channel capacity probability distribution. For example, the maximum value of c in Figure 85(a), which represent the scenario of a single transmitter, is $c = 6$ bits/s/Hertz, while the maximum value of c with $n_t = 4$ in 85(d) reduces to $c \approx 5.5$.

Increasing the number of transmitters may seem to bring about a negative effect. However the benefit of having MISO is to increase robustness against fading and interference effects, thus making the channel more stable and resilient. This is known, in the literature of wireless systems, as the *diversity* gain.

7.3.4.2 *Fully-connected Graphs*

Here, we focus on fully-connected graphs in general, but show an example for a K10 Neumann graph in particular. Specifically, we investigate the

(a) $n_t = 1$

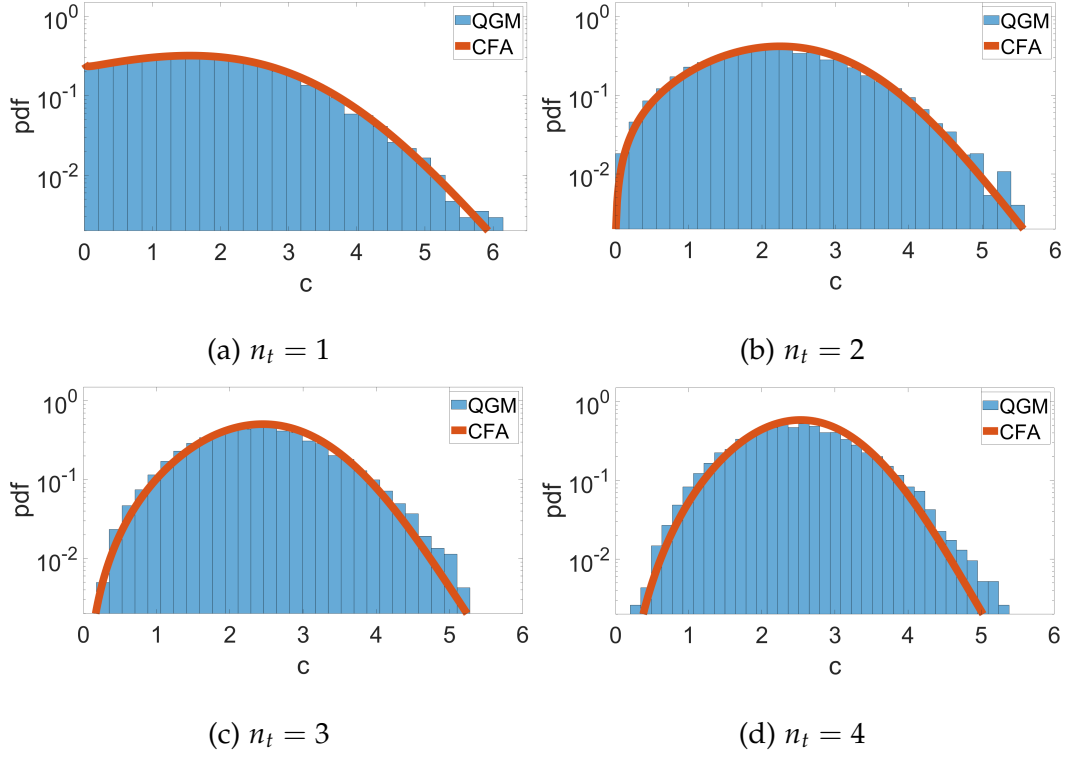(b) $n_t = 2$

(c) $n_t = 3$

(d) $n_t = 4$

Figure 85.: Distribution of channel capacity for a HEX10 strongly-coupled Neumann graph with increasing number of transmitters ($n_t = 1, 2, 3, 4$) at $\alpha \approx 5$, $B = 120$ and $\rho = 40$ dB. The red curve is the theoretical prediction using the characteristic function approach. In each case, the coupling parameter is $\tau = 1.4651 \times 10^{-6}$.

effects of increasing the number of transmitters n_t while keeping the loss parameter at $\alpha = 4$. We chose $\alpha = 4$ because it is large enough to make the distribution of ζ Gaussian, thus taking us well into the high-loss regime.

Figure 86 shows the distribution of channel capacity for graphs with K10 topology which are strongly-coupled to $1, 2, 3$ and 4 transmitters respectively. The boundary conditions at all vertices are Neumann. At $\alpha = 4$, the shape parameter for is $\nu = 47.04$, which verifies that the simulations

are made in the high-loss regime. When $n_t = 1$, all three approaches (i.e. characteristic function, convolution and closed-form solution) may be used to determine the pdf of the channel capacity. This is shown in Figure 86(a), where the red, yellow and indigo curves represent characteristic function, convolution and closed-form solution respectively.

(a) $n_t = 1$

(b) $n_t = 2$

(c) $n_t = 3$

(d) $n_t = 4$
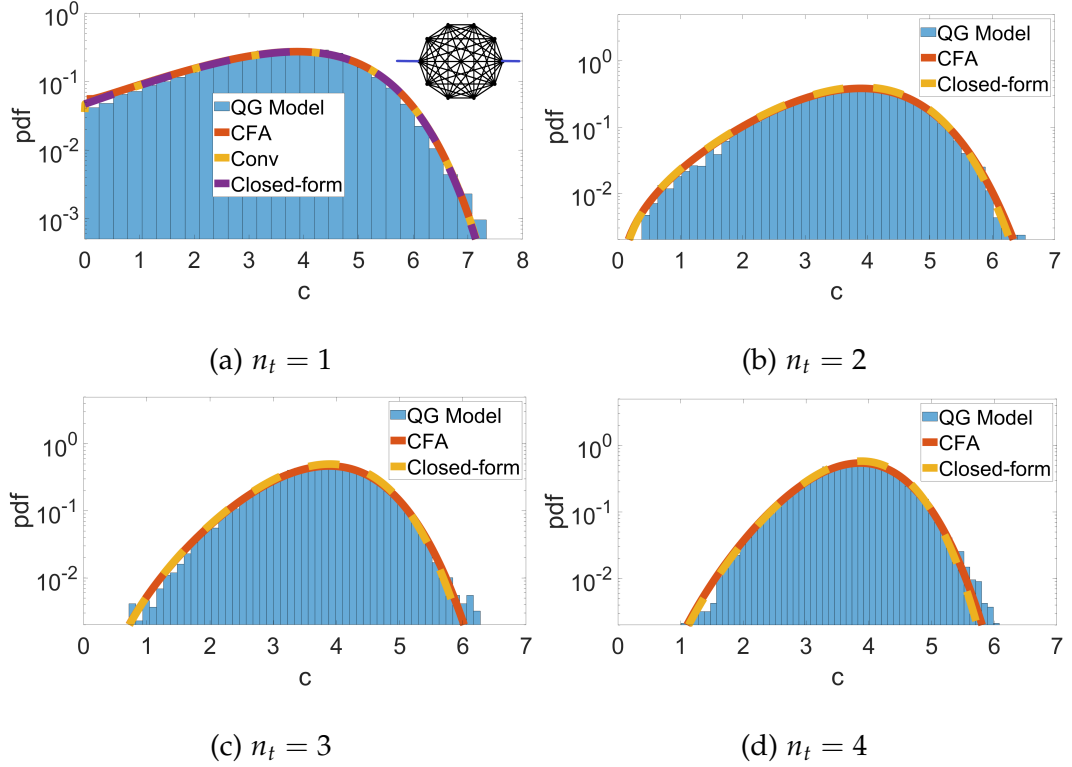
Figure 86.: Distribution of channel capacity for a K10 strongly-coupled Neumann graph with increasing number of transmitters ($n_t = 1, 2, 3, 4$) at $\alpha \approx 4$, $B = 45$ and $\rho = 40$ dB. The red curve is the theoretical prediction using the characteristic function approach. In each case, the coupling parameter is $\tau = 9.2442 \times 10^{-6}$.

However, the convolution approach cannot be used for $n_t > 1$. In such scenarios, we show the predictions of both characteristic function approach

(CFA) and the closed-form solution (CFS). For $n_t = 2, 3, 4$, the red curve in each case represents the CFA predictions, while the dashed-yellow curve denotes the CFS predictions. In all cases, the theoretical predictions agree well with the numerical simulations. In each case, we used $20,000$ realisations of randomly selected K10 graphs. After investigating other $K(v + 1)$ graphs, we have found the same level of accuracy in the theoretical predictions.

7.4 CONCLUSION

For graphs with medium connectivity, we have shown that, unlike Fourier graphs, the distribution of ζ never becomes Gaussian, when Neumann boundary conditions are applied and as losses increase. This is true whether the graphs are weakly- or strongly-coupled to leads. Therefore it is not possible to use the closed-form solution in (179) (which works only in the high-loss scenario) in predicting the probability density function of the channel capacity. However, in the case of single-input single-output systems, two approaches have been used to calculate the distribution of channel capacity. These are the *characteristic function* approach and the *convolution* approach. For multiple-input single-output systems, the only approach suitable for theoretically predicting the probability density function is that of the characteristic function approach. In general, the values of the shape parameter v of the universal random variable ζ are higher in weakly-coupled Neumann graphs than in its strongly-coupled counterparts. But, both are never high

enough to make the distribution of ξ Gaussian. Furthermore, the theoretical predictions in systems with higher values of ν are more accurate than those with lower value of ν.

However, for complete graphs with Neumann boundary conditions, the distribution of ξ starts as a t-distribution and gradually approaches Gaussian distribution as the system loss increases. Therefore, for SISO systems in low-loss regimes, both the convolution approach and the characteristic function approach may be used to calculate the pdf of their channel capacities. In the high loss regimes however, the closed-form expression in (179) can be used in addition to the other two approaches to predict the pdf of the channel capacity. In the generalised MISO systems, only the characteristic function approach can be used in the low-loss regime, while both the closed-form expression and characteristic function approach can be used in the high-loss regime.

The convolution approach is limited to SISO systems, while the closed-form expression is also limited to high-loss regimes. This makes the characteristic function approach superior to both convolution approach and the closed-form expression, because it works for MISO systems in both low- and high-loss regimes whenever the integrals involved behaves well in terms of convergence.

In conclusion, we have shown how to calculate the distribution of channel capacity of a more realistic and experimentally accessible boundary condition (i.e. the Neumann boundary condition). Although the universal ran-

dom variable ξ has one of its constituent variables Laplace distributed, we still have a structure of the graph scattering matrix that is identical to the RCM. This provides a simple but essential tool capable of predicting the distribution of channel capacities of both wired as well as wireless communication channel.

<div align="right">

8

</div>

WIRED COMMUNICATIONS SYSTEMS

8.1 INTRODUCTION

We have used quantum graph theory to model data transmission in chaotic cavities and have estimated the distribution of channel capacities for such multiple-input single-output (MISO) systems. Chapters 6 and 7 have focused on modelling wireless communication channels using Fourier and Neumann boundary conditions, respectively.

In this chapter, we focus on the applications of quantum graphs in *wired* communications, where we model data transmission within the Digital Subscriber Line (DSL) networks. A DSL network uses copper cables, on the existing telephone network infrastructure, as its channel to transmit data between the central office (CO) and subscribers (DSL end-users) [17]. An illustration of DSL network architecture is shown in Figure 87. Depending on the generation of DSL involved, the entire link from the CO to the end-users may be made up of copper cables or a combination of fibre optic cable and

copper. DSL technology is by far the most widely-used medium for broadband internet access. For example, by the end of the second quarter of 2018, there were in excess of 1 billion fixed broadband users worldwide [14]. Details of the DSL networks is treated next.
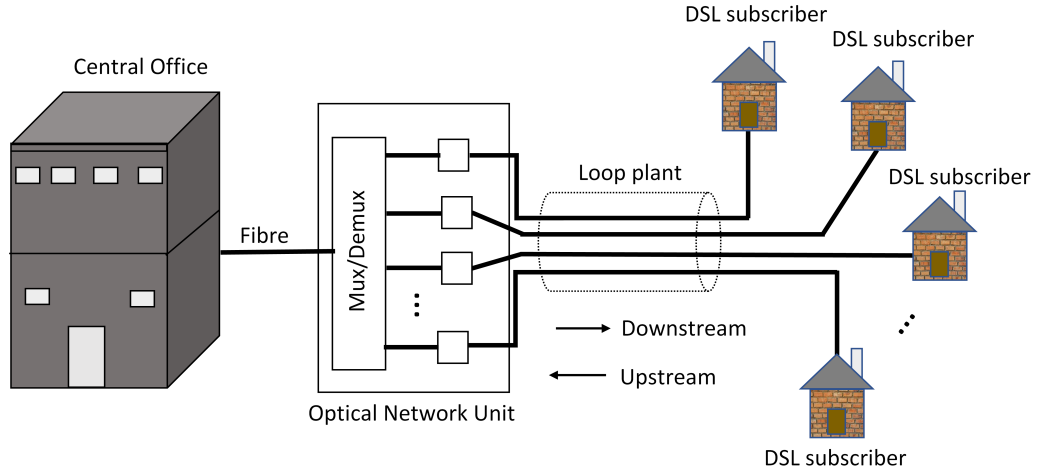

Figure 87.: Illustration of DSL Network connecting subscribers to the central office (adopted from [160]). Whenever there is no subscriber at a branch, all the data is redirected back onto the network. We implement that by applying Dirichlet boundary condition at the end of the branch.

The rest of the chapter is organised as follows. Section 8.2 summarises the theory behind DSL technologies, their types, and the evolutions they have undergone since inception. This is followed, in Section 8.3, by a treatment of the cable characteristics of DSL networks. Finally, the numerical simulations of in-house DSL networks is presented in Section 8.4, where we estimate the distribution of channel capacity of such realistic networks.

194

8.2 DSL TECHNOLOGIES

DSL technology has evolved over the years. The first generation leveraged the existing telephone networks, whose infrastructure is already widely available to prospective customers, to transmit both data and voice over different frequency ranges of the same copper wire. Typically, data is transmitted in the frequency range of $26 - 1104$ kHz, while the plain old telephone service (POTS) (i.e. the ordinary voice telephone communication) is transmitted at a lower frequency band of $30 - 4000$ Hz [161, 162], with sub-carrier separation of 4.3125 kHz.

DSL technologies can be separated into two categories according to whether the downstream and the upstream transmissions support equal data rates or not. These are symmetric DSL (SDSL) and asymmetric DSL (ADSL). In SDSL, both the downlink and the uplink have equal maximum speeds, while in ADSL the downlink speed is greater than the uplink. In practice however, many applications such as video-on-damand, 4K TV, require higher downstream speed more than upstream. This makes the ADSL the most commonly used technology. A power spectrum density (PSD) of the first generation ADSL is illustrated in Figure 88.

Since its inception, the ADSL has evolved chiefly as a result of ever-increasing demand for a faster broadband connectivity. So far, there are four main generations of DSL technologies that are classified according to

195
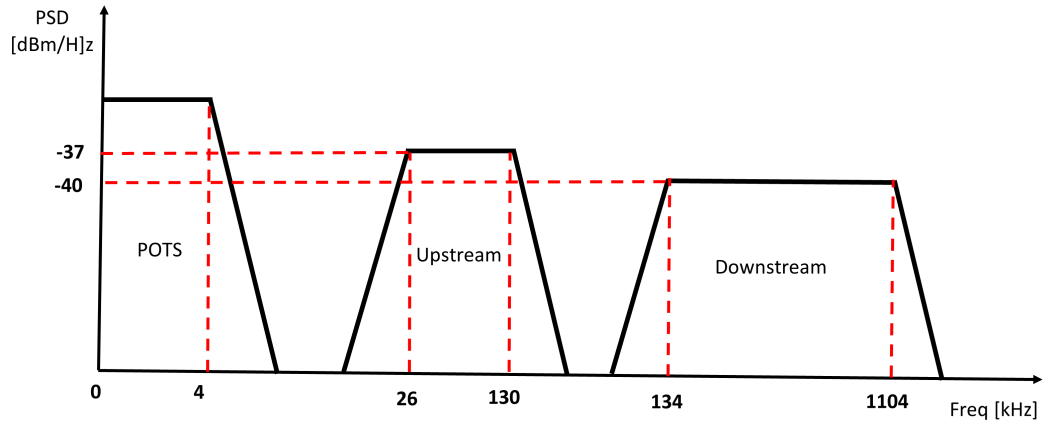
Figure 88.: An illustration of a PDP of first generation ADSL [163].

achievable data rates and improvement in technology [17, 164]. These generation of DSL technologies are illustrated in Figure 89.
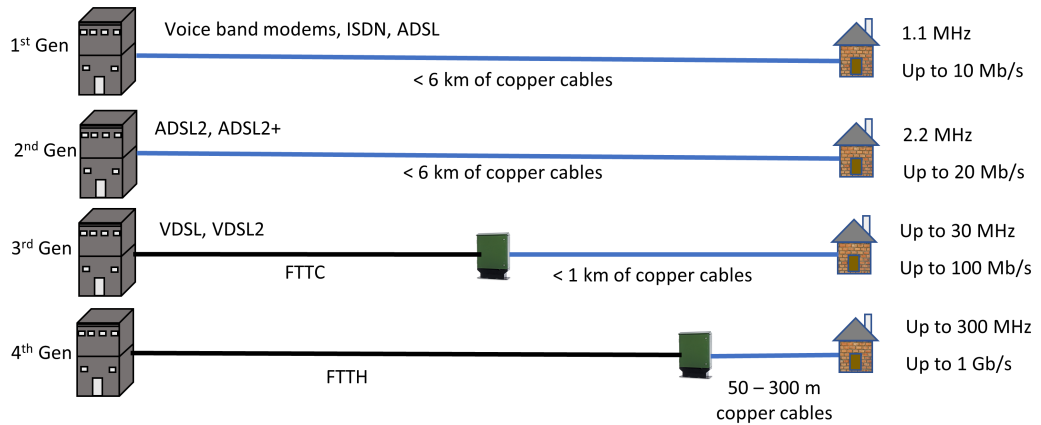
Figure 89.: Generations of DSL technology. The diagram is adopted and modified from [17].

The first and second generation DSL access networks are made up of entirely twisted pairs copper wires from the CO to customer premises with loop distances of several kilometres. The standards of the first generation DSL is the integrated services digital network (ISDN) followed by the International Telecommunication Union (ITU) (ITU-T, 1991), supporting a band-

width of 1.1 MHz with maximum achievable data rates of 10 Mb/s. The standards of the second generation DSL are governed by the ITU-T series 1999a, 2003, and 2005a, with data rates of up to 20 Mb/s. The doubling of the data rates was mainly effected by the wider bandwidth supported in the second generation. This was made possible by the improvements in the signal processing techniques such as the well-known dynamic spectrum management (DSM) [17, 164–167], which mainly reduced the crosstalk effects of the cables in DSL networks [144].

The improvements in the third and fourth generation DSL technologies were mainly achieved by minimizing the attenuation levels through the utilisation of shorter lengths of copper cables. Optical network units (ONU), also known as the *primary cross-connection point* (PCP) street cabinet, are placed between the CO and the customer premises. The link between the CO and ONU is replaced by fibre optic cables, which significantly reduces transmission losses and therefore increases achievable data rates (or throughput).

The third generation DSL technology reduces the final loop drop to less than 1 km, while the fourth generation reduces the length of the copper cable to less than 300m. The third and fourth generations DSL network can support a maximum of 30 MHz and up to 300 (depending on cable quality [168]) MHz in bandwidths, while data rates may reach up to 100 Mb/s and 1 Gb/s, respectively. However, the latest in the series of ITU standards for the fourth generation DSL (popularly known in the marketing circles as the

G.fast [169]) does not include the 300 MHz bandwidth. The latest standard is the ITU-T G.9701, which was approved in 2014. The updated standard was published in 2019, can be found in [16]. Although higher bit rates of up to 1 Gbps [161] and beyond [170, 171] have been achieved theoretically, it is almost impossible for the Internet Service Providers (ISPs) to practically implement such high speeds over copper networks.

The G.fast technology comes in two main profiles. The 106 MHz band plan and the 212 MHz band plan, with respective frequency range of $2.12175 - 105.984$ MHz and $2.12175 - 211.968$ MHz. The entire frequency spectrum from $0 - 211.968$ MHz is divided into 4096 tones with a frequency spacing of 51.75 kHz. The first 40 sub-carriers are used for telephone applications similar to the previous three generations. The 41st sub-carrier frequency is the first within the G.fast frequency band, and corresponds to 2.12175 MHz, while the last sub-carrier corresponds to 105.984 MHz or 211.968 MHz depending on the choice of profile. However, the first sub-carrier carrying data on a G.fast network is the 43rd tone and this corresponds to $f_{43} = 2.22525$ MHz [16].

Data transmission from the PCP street cabinet in the direction of DSL subscribers is known as the *downlink* or *downstream*, while the reverse transmission from subscribers towards the street cabinet is known as the *uplink* or *upstream* [160]. The downlink network is a single-input multiple-output (SIMO) system. But the system is MISO in the uplink, where data is transmitted from multiple DSL subscribers to the ONU. By swapping the role of

the transmitter(s) and the receiver(s), the network changes from a SIMO to a MISO. In both cases, the quantum graph model developed in Chapter 4 can provide an accurate prediction of the channel capacity statistics.

Unlike the three previous generations of DSL technology, which employ frequency-division duplexing, the G.fast scheme uses time-division duplexing (TDD), and so both the down and upstream transmission utilise the same frequency band. Table 1 gives a summary of the ITU-T G.9701 transmitter specifications for the 106 and 212 MHz profiles.

Table 1.: ITU-T G.9701 profiles

Parameter	106 MHz Profile	212 MHz Profile
Standard	ITU-T G.9701	ITU-T G.9701
Bandwidth	105.984 MHz	211.968 MHz
Sampling Frequency	211.968 MHz	423.936 MHz
No. of Tones	2048	4096
Tone spacing	51.75 kHz	51.75 kHz
UP- or Down-stream band plans	$2.12173 - 105.984$ MHz	$2.12173 - 211.968$ MHz
Transmit Power	4 dBm	8 dBm
No. of Bits per Sub-carrier	$0 - 12$	$0 - 12$
Symbol Rate	$48,000$ baud	$48,000$ baud
Noise Margin	6 dB	6 dB

At the customer premises, the DSL signal requires an in-house distribution network. A network interface device (NID) connects the rest of DSL

network to the in-house network, usually through a POTS splitter (which separates voice spectrum from the ADSL signal) [162].

The goal of the present research is to model data transmission within this in-premises network, starting from the NID to the end-users within the premises, or the reverse transmission from the end-users to the NID. In this scenario, we investigate the architecture proposed in Appendix I of the ITU-T G.9701 standard [16] as shown in Figure 90. The network is generally a cascade of sub-networks each with a star topology. The end of each branch is connected to an end-user (denoted a terminal A, B, etc) or terminated with a matched load so as to minimise signal reflections. This is because, within the premises, every phone jack is ideally terminated with a 100Ω impedance matching plug when not in use [162].
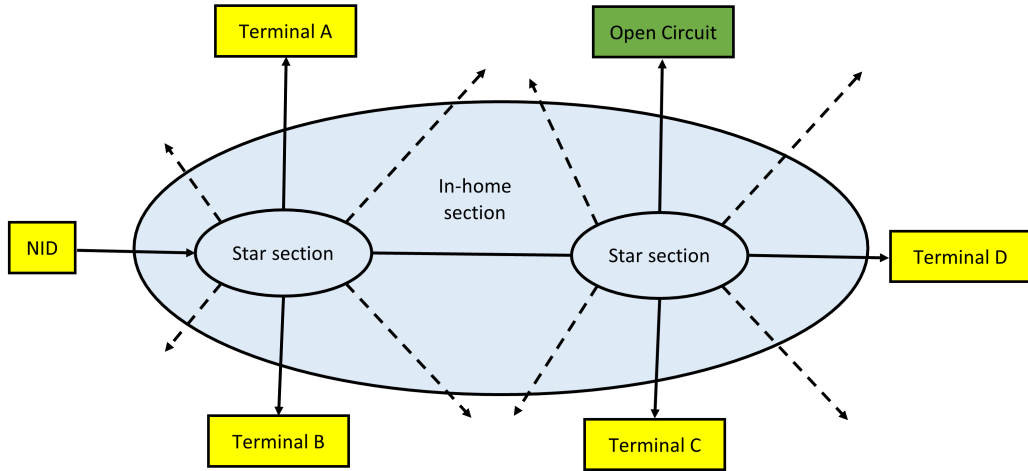

Figure 90.: Illustration of the topology of in-premises wiring of a G.fast network, adopted from Appendix I of [16].

In Chapter 3 Section 3.2.1, we have shown that the connectivity index of a cascade of star networks is $\gamma \leq 0.5$. This makes the DSL networks fall

into the category of networks with low connectivity index. Additionally, we have shown that the connectivity index of a cascade of star network with n vertices is given by

$$
\begin{aligned}
\gamma &= \frac{2B}{n(n-1)} \\
&= \frac{2(n-1)}{n(n-1)} \\
&= \frac{2}{n},
\end{aligned}
\tag{187}
$$

where the number of bonds $B = n - 1$ in a cascade of star networks. As the number of vertices n ($n \geq 4$ in a cascade of start networks) increases, the index of connectivity decreases (approaching zero in the limit of large n).

It is important to reiterate that, in Chapters 6 and 7, we have treated applications involving networks with medium connectivity (i.e. HEXv graphs with connectivity index of $\gamma \approx 0.5$), and fully-connected graphs (networks with $\gamma = 1$) respectively. By treating networks with low connectivity indices (such as in the in-house distribution network of G.fast) in this chapter, we will have completed examining the three main categories of graphs (in terms of their connectivity) in this thesis.

Next, we briefly discuss the channel (cable) characteristics of a G.fast network, before the numerical calculations are presented in Section 8.4.

8.3 DSL CABLE MODELLING

From the transmission line theory in Chapter 2, we have seen that the characteristic features of copper cables depend on four primary parameters, the

resistance (R), inductance (L), conductance (G), and capacitance (C). These frequency-dependent parameters can be used to define two secondary parameters as follows.

$$
\begin{aligned}
\kappa &= \sqrt{ZY} \\
&= \sqrt{(R + \mathrm{j}\omega L)(G + \mathrm{j}\omega C)} \\
&= \alpha_\kappa + \mathrm{j}\beta_\kappa
\end{aligned}
\tag{188}
$$

where Z and Y are the impedance and admittance of the underlying cable respectively, $\omega = 2\pi f$ is the angular frequency, α_κ and β_κ are the attenuation and phase constants respectively, and κ is the propagation constant.

The purpose of the subscript in α_κ is to differentiate it from the loss parameter α which was described in Chapter 4, Section 4.6. It is also important to note the difference between the two definitions of propagation constants κ (as defined in this chapter) and k (as defined in Chapters 3 and 4). In previous chapters, the $\Im(k)$ characterises the damping in the propagating waves, while the $\Re(\kappa)$ in this chapter represents the damping. The definition in (188) is popular in the Engineering community, while the k defined in (32), for example, is popular in the physics and mathematics communities.

The second of the two secondary parameters is the characteristic impedance of the cable and it is define as

$$
\begin{aligned}
Z_0 &= \sqrt{\frac{Z}{Y}} \\
&= \sqrt{\frac{R + \mathrm{j}\omega L}{G + \mathrm{j}\omega C}},
\end{aligned}
\tag{189}
$$

where Z_0 is the characteristic impedance of the underlying cable.

The goal of this section to discuss how κ is modelled for cables in DSL networks. Depending on the frequency range (hence the generation of the DSL) under consideration, several models have been studied [15, 172–177]. While [172–176] modelled κ for the cables in the frequency ranges of the first three generations of DSL networks (up to 30 MHz), [15, 16, 177, 178] modelled the propagation constant of cables in the G.fast frequency range.

However, of the many G.fast-compliant models, only the TNO-Ericsson (An acronym coined from Ireland's *Telephone Network Options Ltd*, and Sweden's *Ericsson*) model is currently adopted by ITU [16]. The TNO-Ericsson model, which depends on ten parameters, is given by

$$[Z, Y] = \text{model}\left(Z_{0\infty}, \eta_{VF}, R_{s0}, q_L, q_H, q_c, q_x, q_y, \phi, f_d\right), \qquad (190)$$

where

$$Z(\text{j}\omega) = \text{j}\omega L_{s\infty} + R_{s0}\left[1 - q_s q_x + \sqrt{q_s^2 q_x^2 + 2\frac{\text{j}\omega}{\omega_s}\left(\frac{q_s^2 + \text{j}\omega q_y/\omega_s}{q_s^2/q_x + \text{j}\omega q_y/\omega_s}\right)}\right] \qquad (191)$$

and

$$Y(\text{j}\omega) = \text{j}\omega C_{p0}\left(1 - q_c\right)\left(1 + \frac{\text{j}\omega}{\omega_d}\right)^{-2\phi/\pi} + \text{j}\omega q_c C_{p0} \qquad (192)$$

are the impedance and admittance of the underlying cable respectively, such that

$$L_{s\infty} = \frac{Z_{0\infty}}{\eta_{VF} \cdot c_0}, \qquad (193)$$

$$C_{p0} = \frac{1}{\eta_{VF} \cdot c_0} \times \frac{1}{Z_{0\infty}}, \qquad (194)$$

$$q_s = \frac{1}{q_H^2 \cdot q_L},$$ (195)

$$\omega_s = q_H^2 \cdot \omega_{s0} = q_H^2 \left(\frac{4\pi \cdot R_{s0}}{\mu_0} \right),$$ (196)

$$\omega_d = 2\pi f_d.$$ (197)

Here, $\omega = 2\pi f$ is the angular frequency $c_0 = 3 \times 10^8$ [m/s] is the speed of light, while $\mu_0 = 4\pi \times 10^{-7}$ [H/m] is the permeability in free space [16].

Different types of wires are used for different segments of G.fast network, and since our focus is the in-house distribution network, we consider a B05a (also known as the CAD55) cable. A CAD55 cable is a 0.5 mm unshielded aerial cable that is commonly used for household wiring. Fortunately, the values of all the ten parameters in the TNO-Ericsson model above have been reported in [16] for a $B05a$ cable. For a given frequency f, we could find $\kappa(f) = \sqrt{Z(\text{j}\omega)Y(\text{j}\omega)}$, where $\omega = 2\pi f$.

According to Appendix I of [16], the values of the ten parameters for $B05a$ cables (within the G.fast frequency range) are $Z_{0\infty} = 105.0694$, $\eta_{VF} = 0.6976$, $R_{s0} = 0.1871$, $q_L = 1.5315$, $q_H = 0.7415$, $q_x = 1$, $q_y = 0$, $q_c = 1.0016$, $\phi = -0.2356$, and $f_d = 1$. In the next section, we use these parameter values to simulate the in-house distribution of data at G.fast frequencies and compare it with the predictions our quantum graph model discussed in Chapter 4.

8.4 NUMERICAL SIMULATION OF DSL NETWORKS

In this section, the numerical results of how data is distributed within a household connected to a G.fast network, starting from the NID as illustrated in Figure 90. We do this analysis assuming the in-premises distribution network is made up entirely of CAD55 cables. Starting from the NID, if a branch in the star section of Figure 90 is not connected to a terminal, we terminate by a matching impedance (in this case a 100Ω for CAD55 cables).

In the following example, two star sections (made up of four branches each) forms the in-premises distribution network and are connected to terminals as illustrated in Figure 91. Figure 92 shows the distribution of real
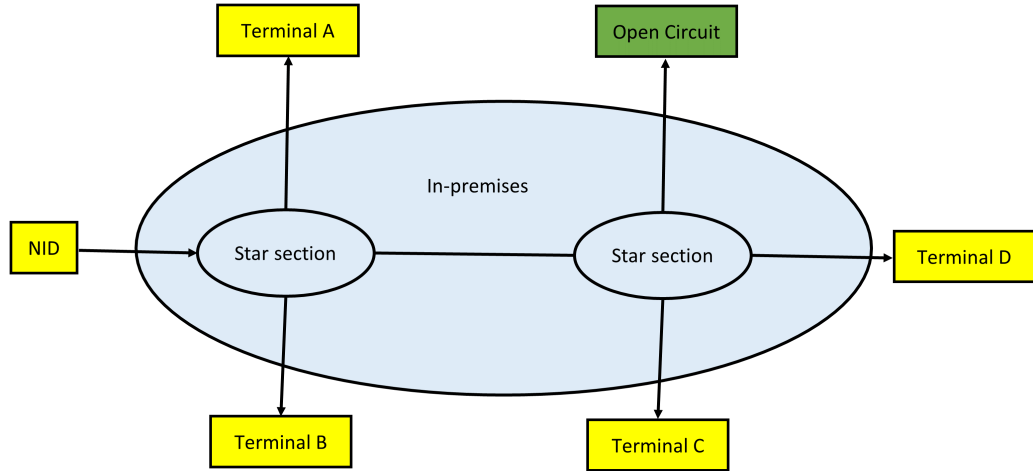

Figure 91.: Illustration of the topology of in-premises wiring of a G.fast network, adopted from Appendix I of [16].

and imaginary parts of ξ. The sub-carrier frequency $f = 105.93225$ MHz was used. This is the sub-carrier with the highest frequency in the 106 MHz profile of G.fast network. The loss parameter is $\alpha = 34.6$, while the coupling

parameter is $\tau = 4.6079 \times 10^{-4}$. The cable lengths are randomly chosen to be between 1 m and 30 m long. These are reasonable lengths of cables commonly found in households.
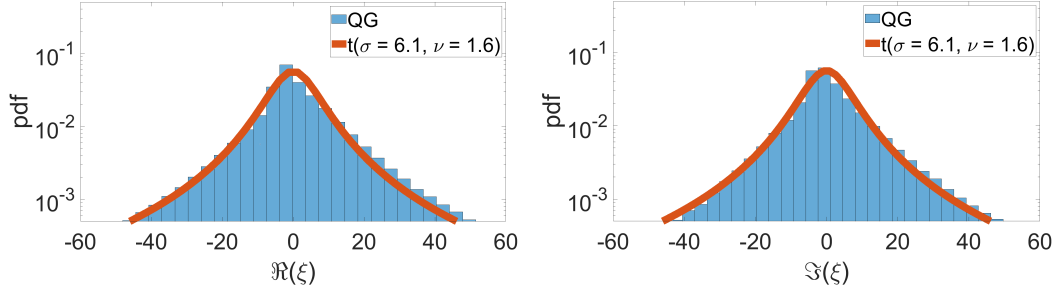

Figure 92.: The distribution of real and imaginary parts of ξ at $\alpha = 34.6$ and $\tau = 4.6079 \times 10^{-4}$ of a B05a wire with lengths randomly chosen between 1 m and 30 m, where 4 nodes are connected to the home network. An ensemble of $100,000$ simulations, each at a frequency of $f = 105.93225$ MHz, were used.

Since the cascade of star networks is sparsely connected (i.e. in terms of connectivity index), we expect the distribution of ξ to never approach Gaussian distribution regardless of the level of losses in the distribution network. This was discussed in Chapters 6, 7). Hence, the real and imaginary parts of ξ remain t-distributed even though the parameter α is significantly high for this scenario.

It follows that the random variables $\Re(\xi)^2$ and $\Im(\xi)^2$ are scaled F-distributed with scale parameter $\sigma = 6.1$ and shape parameter $\nu = 1.6$. Figures 93(a), (b) compare the numerical simulation (histograms) with the analytical results (red curve). Furthermore, the distribution of $|\xi|^2 = \Re(\xi)^2 + \Im(\xi)^2$ is shown
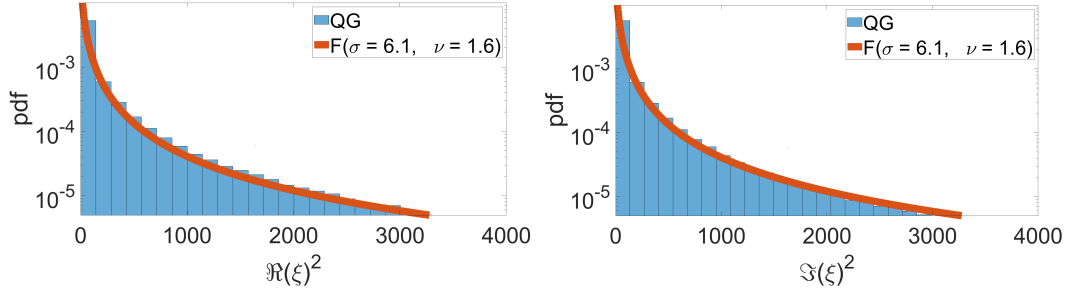
Figure 93.: The distribution of real and imaginary parts of ξ^2. The red curve denotes the analytical prediction (i.e. F-distribution with degree of freedom $\nu = 1.6$ and scale parameter $\sigma = 6.1$).

in Figure 94(a), while the pdf of the channel capacity was shown in Figure 94(b). In each case, the red curve represents the analytical calculation, and the histogram represents the numerical simulation of the in-premises distribution network depicted in Figure 91.
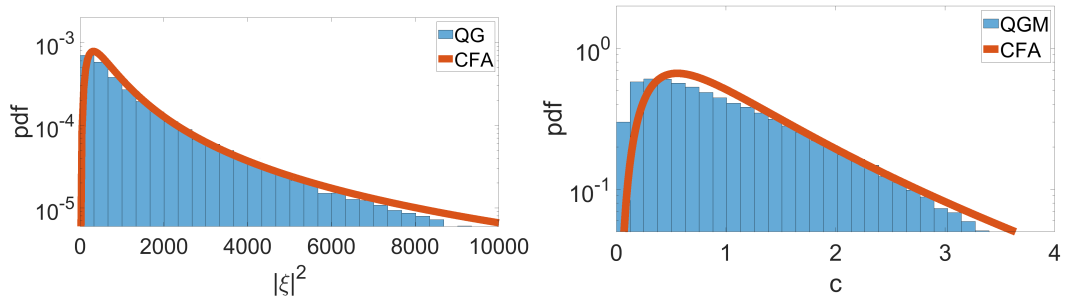
Figure 94.: The distribution of $|\xi|^2$ and channel capacity using the parameters of CAD55 wire of lengths between 1 m and 30 m at $\alpha = 34.6$, $\tau = 4.6079 \times 10^{-4}$, and sub-carrier frequency of $f = 105.93225$ MHz.

It is important to note that, even though the quantum graph model in Chapter 4 was derived for chaotic systems, the model works well even with the cascade of star topologies (which is generally 'non-chaotic') depicted in

Figure 91. In this specific case, the connectivity index is $\gamma = 2/8 = 0.25$, since the cable network is made up of 8 vertices. There is good agreement between the theoretical prediction and the numerical simulation. Since ξ in this scenario was t-distributed (and not Gaussian distributed, see Figure 92), and consists of multiple out-puts (four in this case), the characteristic function approach in (174) was used to predict the pdf of the channel capacity.

Figure 95 shows the effect of increasing sub-carrier frequency on channel capacity distribution. Higher sub-carrier frequency corresponds to higher data rates in bits/s/Hz. Increasing the sub-carrier frequency from $f = 20.02725$ MHz to $f = 80.0055$ MHz, increases the range of the capacity from 2 bits/s/Hz to 3 bits/s/Hz. The gaps between the graph simulations (blue histograms) and the analytical prediction (red curves) are attributed to the 'non-chaoticity', and the low connectivity of the underlying network topologies.

The next example shows the effects of increasing the number of terminals connected to the CAD55 cable network illustrated in Figure 96. In this scenario, six users are connected to the network, while three nodes are unused. The idle connection points are therefore terminated in a matched load. We are interested in analysing the impact of increased terminals on the pdf of channel capacity.

It is important note that the scenario of Figure 96 has longer total cable length than the scenario in Figure 91. Therefore the former will experience more losses on average than the latter, and this translates into a lower data

(a) $f = 20.02725$ MHz

(b) $f = 40.00275$ MHz

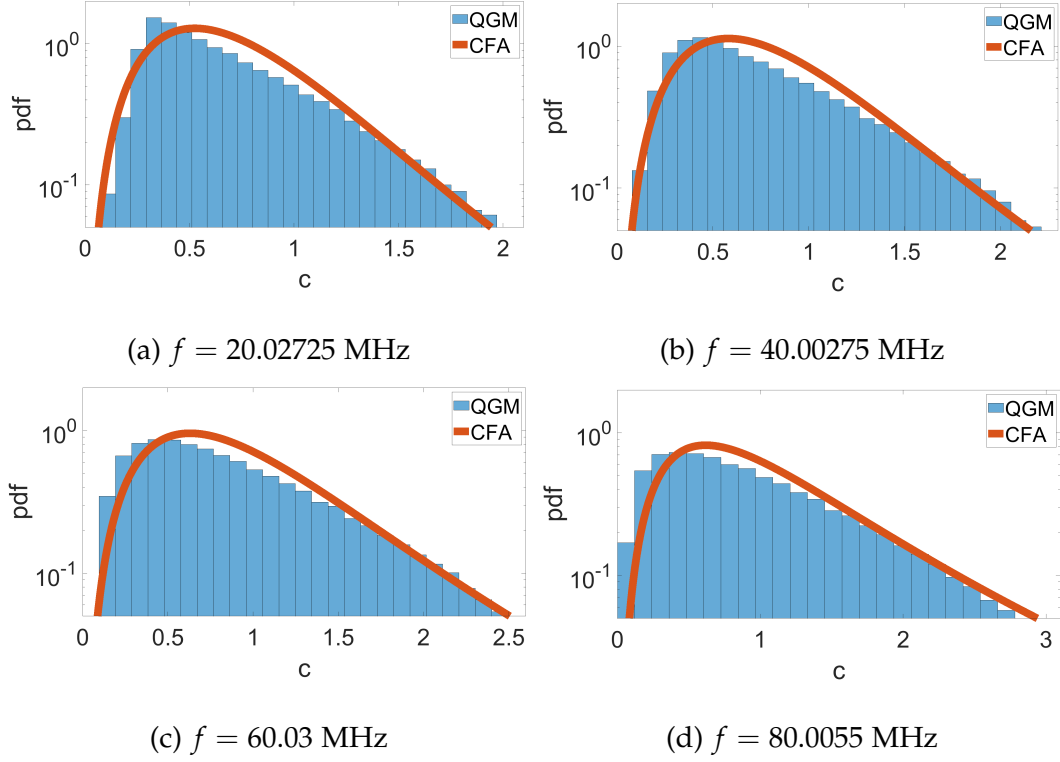(c) $f = 60.03$ MHz

(d) $f = 80.0055$ MHz

Figure 95.: The pdf of channel capacity of a network of CAD55 cables with Figure 91 topology at (a) $f = 20.02725$ MHz, (b) $f = 40.00275$ MHz, (c) $f = 60.03$ MHz, and (d) $f = 80.0055$ MHz. In each case, four terminals are active, and so $n_r = 4$

rate for the former, when both networks are operated at the same conditions. Figure 97 shows the results of the scenario in Figure 96, where there are six active terminals (i.e. $n_r = 6$).

For comparison purposes, we used the same frequencies (i.e. $f = 20.02725$ MHz, $f = 40.00275$ MHz, $f = 60.03$ MHz, and $f = 80.0055$ MHz) of the results in Figure 95. Comparing the two results at each frequency, Figure 95 results have superior performance, in terms of the range of capacity covered, than the results in Figure 97. This is a result of the increased number
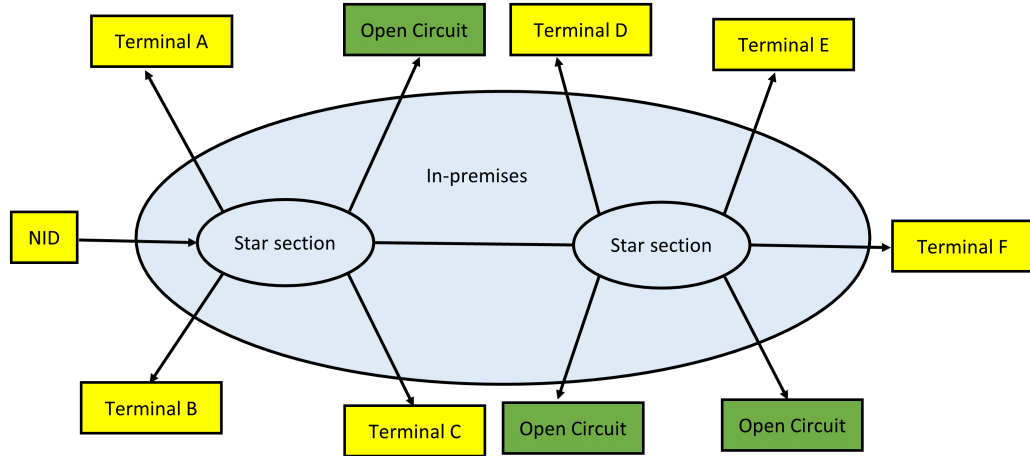
Figure 96.: Illustration of the topology of in-premises wiring of a G.fast network, where six nodes are attached to the network and three nodes are idle (i.e. those terminated as an open circuit to prevent back scattering).

of users on the network. This confirms what is experienced in every distribution networks, whether DSL or not. The higher the number of users on a network, the slower data rates.

8.5 CONCLUSION

The chapter presented the results of modelling the communication channel of fourth-generation DSL networks (G.fast networks), using realistic cable parameters from the so-called TNO-Ericsson model. In particular, we have shown that quantum graph modelling can be used to simulate the in-premises distribution network at G.fast frequencies. The parameters of CAD55 cables (which are commonly found in houses around the world),

(a) $f = 20.02725$ MHz

(b) $f = 40.00275$ MHz

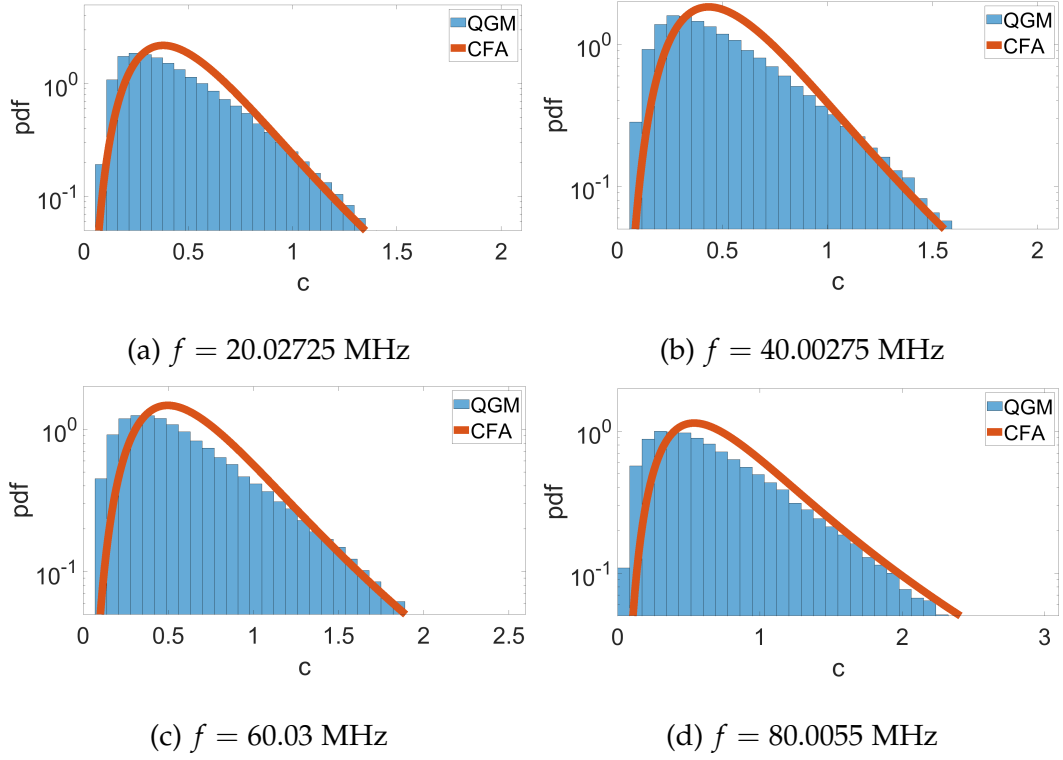(c) $f = 60.03$ MHz

(d) $f = 80.0055$ MHz

Figure 97.: The pdf of channel capacity of a network of CAD55 cables with topology as in Figure 96 at (a) $f = 20.02725$ MHz, (b) $f = 40.00275$ MHz, (c) $f = 60.03$ MHz, and (d) $f = 80.0055$ MHz. In each case $n_r = 6$

and the in-house distribution network (reported in the ITU documentation) were used in the simulations.

Even though such networks have low connectivity indices, which results in ξ behaving as a non-Gaussian random variable, we have shown that the characteristic function approach can accurately predict the pdf of channel capacity of the underlying cable networks. These predictions were accurate with as many as six nodes connected to the in-premises network, and operating at the high end of G.fast frequencies.

Combining the results in Chapters 6 and 7 with the results in this chapter, we have shown how distribution of channel capacity can be predicted, with high level of accuracy, regardless of the level of connectivity of the underlying communication networks. These predictions also work well with both wired and wireless systems as was shown in previous chapters.

9

FINAL CONCLUSIONS AND FUTURE OUTLOOK

This chapter provides a summary of the main achievements and findings in this research work, and offers suggestions as to how this work may be extended in future. We categorise the achievements according to chapters of this thesis.

9.1 SUMMARY OF ACHIEVEMENTS

Quantum Graph theory has been established as a successful paradigm for studying complex scattering problems. In this thesis, we have used the theory of quantum graphs to model the propagation of microwaves in complex networks. In Chapter 3, we have derived a unified mathematical expression for the vertex scattering matrix which includes both uniform and non-uniform cable networks.

We have derived an analogue of the so-called random coupling model. Although random coupling models are designed for microwave propaga-

tion in chaotic cavities, the analogue model derived in Chapter 4 is applicable to wired as well as wireless communication media. Additionally, the normalised scattering matrix of the analogue model depends on random variables that are not necessarily Gaussian. As a consequence, the distribution of the scattering parameters interpolates smoothly between scaled t-distribution and Gaussian distributions, as one graduates from low loss regimes into high loss regimes. The loss regimes were characterised by a dimensionless (i.e. depending only on the number of bonds in the graph network) parameter analogous to what is reported in random coupling models. In this case, we have calculated the statistics of communication channels that spans loss regimes.

Furthermore, we have successfully formulated a framework for implementing quasi-closed graphs, where the losses in the graph systems can be controlled, while maintaining the unitarity of the constituent vertex scattering matrices. Quasi-closed graphs allows for a more accurate verification of the level of 'chaoticity' (or lack thereof) within graphs networks. Also, controlling the amount of energy radiating through the coupled-leads, has direct applications in electromagnetic compatibility studies.

In Chapter 5 we have experimentally validated the graph model of Chapter 4, where we discussed how to correct for the additional lengths introduced by the T-junction connectors.

On one hand, Chapter 6 was based on idealised vertex scattering matrices (i.e. in Fourier graphs) that distribute energy equally at graphs nodes, and

the impact of such Fourier nodes on the statistics of scattering parameters. This has allowed us to learn about the main mechanisms of variability in the normalised scattering matrix ζ (as well as the channel capacity), before extending to more realistic models. On the other hand, Chapter 7 dealt with a more realistic (i.e. experimentally accessible) boundary conditions (i.e. Neumann boundary conditions) at the vertices of the underlying graph network. In both cases, we have shown *three* different approaches (to be used depending on the number of input and/or output systems, and loss regimes involved) of calculating the density functions for the distribution of channel capacity.

The *convolution* approach gives a closed-form expression that is applicable to single-input single-output systems, regardless of the regime. The second approach is the *characteristic function* approach, and it works for multiple-input single-output (or single-input multiple-output (SIMO)) systems, across all loss regimes. The third and final approach (a closed-form solution) is another SIMO/MISO-compliant approach that works only in the high loss regime, where the normalised scattering parameters are normally-distributed.

We have presented numerical results across graphs with varying levels of connectivity. For fully-connected graphs, we have shown that the distribution of the normalised scattering parameters approaches a Gaussian distribution when losses are increased. This is true for both Fourier and Neumann graphs. However, in the case of half-connected (and low-

connected) graphs, we have shown that, while Fourier graphs can gradu-ate to Gaussian-distributed scattering parameters (in the high loss regimes), Neumann graphs never escape the domain of the t-distribution.

Finally, in Chapter 8, we have successfully applied the statistical predic-tions of the graph model to a realistic scenario in G.fast network, which is the most current DSL technology as at the time of writing this thesis.

9.2 FUTURE OUTLOOK

It is worth noting that the statistical model predictions in this thesis do not apply to full MIMO systems, where multiple-input multiple-output are involved at the same time. A future perspective of this work will be to formulate predictions for fully MIMO systems. The main challenge in this scenario will be finding $\det\left(I_{n_r} + \frac{\rho}{n_t}HH^\dagger\right)$, where the number of transmit antennas n_t and the receive antennas n_r are simultaneously greater than one.

Another interesting research in future is to look into systems where the nodes in the graphs are replaced by electrical equipments having their own internal impedances.

Finally, there is a growing interest among telecom researchers in the area of reconfigurable intelligent surfaces (RIS) [22, 112, 114, 179–183]. In RIS-aided communication channels, some of the classical assumptions underpin-ning current communication systems (the idea that the radio environments

are beyond the control of scientists, and their dynamics are assumed to be solely controlled by natural phenomena) are dropped. The RIS can be used as smart surfaces made up programmable meta-materials (or large antennas arrays) that act as anomalous scatterers capable of modifying the properties of impinging radio waves from the transmitter to be reflected towards the receiver [22, 114]. The incident radio waves may be modified by controlling their reflection [179] (or refraction) angle, or applying phase shifts [181] or modifying their polarisations [182]. The incident radio waves may also be controlled by using the RIS as a passive beamformer which re-directs the impinging waves towards specified receive-antenna locations [180, 183]. There is convincing evidence among telecom researchers that the RIS may be implemented to solve a variety of problems in wireless communication, including enhancement in coverage, interference suppression, and security enhancement.

Recently, the work of Drinko et al. [112] have shown that simple structures of quantum graphs may act as filters. This may have a direct application in RIS-aided channels to suppress unwanted interference by allowing only signals of specific frequencies.

I propose the use of quantum graphs to model an RIS-aided communication system. Figure 98 shows an illustration of a communication system aided by an RIS when a line-of-sight (LOS) transmission may or may not be possible because of shielding of radio waves at high frequencies. The Figure is adopted from [181] and slightly modified for illustrative purposes. Data

transmission may take two possible routes. In the LOS transmission, data transfer takes the *Tx-Rx* link, while the non-LOS (NLOS) transmission goes through the *Tx-RIS* followed by the *RIS-Rx* sub-channels. Single or multiple transmit (receive)-antennas can be supported in this model.
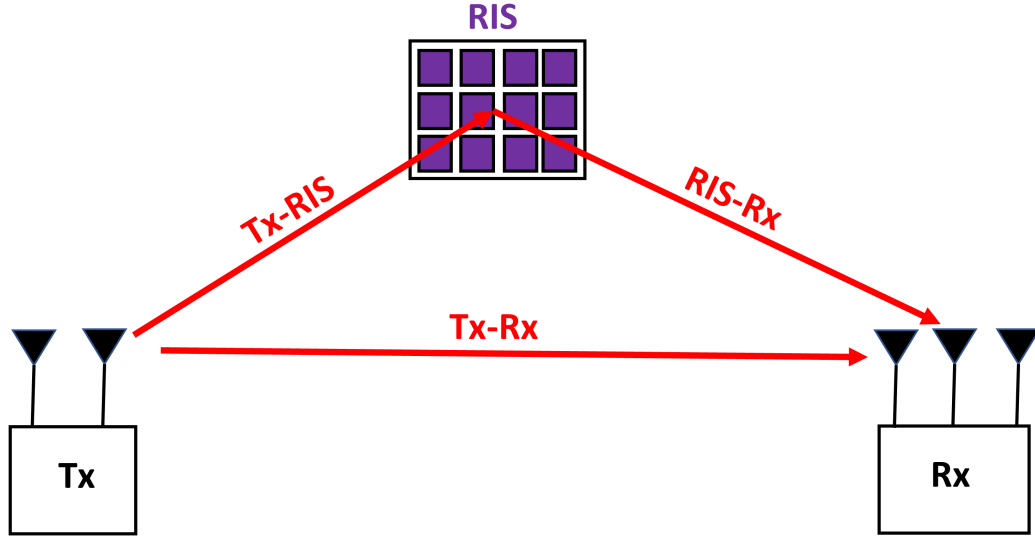

Figure 98.: An illustration of a communication system aided by a reconfigurable intelligent surface. The figure was adopted from [181], and simplified to suit current discussion.

The unit cells in the RIS system are envisaged to be modelled by quantum graphs of simple topological structures. In [112], a combination of equilateral triangle(s) and square(s) have shown promising indications to be able to suppress some frequencies ranges. An example is shown in Figure 99, where they proposed a square structure sandwiched by two equilateral triangles. The transmission coefficient depends jointly on the wave number k of the impinging radio waves and the length l of the edges connecting the nodes of the graph.
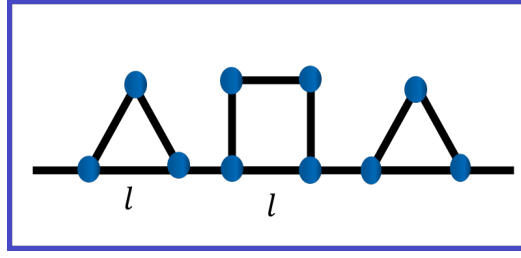
Figure 99.: A series representation of triangle-square-triangle

In the Drinko et al. however, the scale of bond lengths used are in the order of a metre. For example, figure 100 shows a repeat (reproduction) of their results in [112], where the length connecting any two vertices is 1 m long, and the wave number $0 \leq k \leq 2\pi$. The figure is the response of the transmission coefficient S_{12} as a function of the phase $0 \leq kl \leq 2\pi$. Although they used a Green's function approach to model the quantum graph, I reproduced this result using the graph model in this thesis, by finding the scattering matrices at each vertex, and aggregating them into the so-called graph scattering matrix (GSM). It is worth mentioning that their approach resulted in a closed-form expression of the transmission coefficient. However, their approach can only be applied to graphs with very low complexity, such as the examples in their paper. The approach in this thesis on the other hand, can model graphs with arbitrary complexity since, it only requires disaggregation of the problem into a set of vertex scattering matrices (VSM), and aggregating them, in a special way, to form the GSM.

Instead of using triangles and squares, I propose the use of simple loop structure as an equivalent, but a more efficient way of creating the building blocks. For instance, Figure 101 is an equivalent representation of Figure
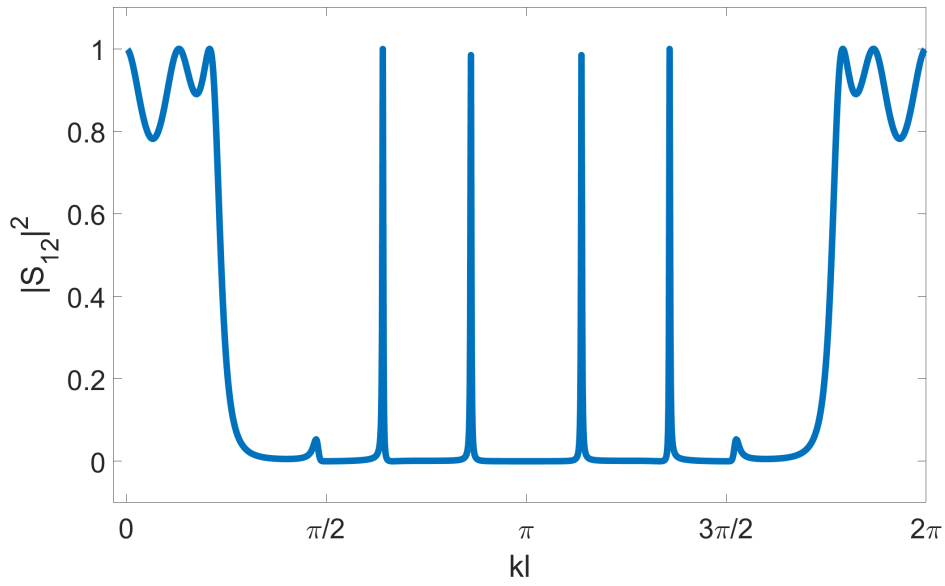
Figure 100.: Transmission power distribution for $0 \leq l \leq \lambda$ such that $0 \leq kl \leq 2\pi$, where $\lambda = 50$ mm.

99 when Neumann boundary conditions are imposed at the vertices. But this representation is more efficient because it reduces the size of the graph - in terms of the number of edges B in the graph - significantly. The reduction in B corresponds directly to a reduction in computational cost because majority of the matrices in the calculations are $2B \times 2B$ in dimensions.
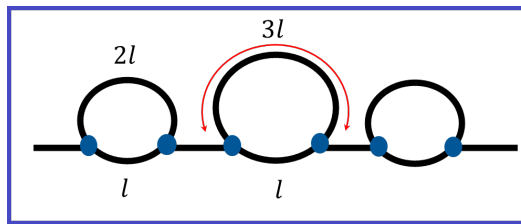

Figure 101.: An equivalent representation of the same scenario of Figure 99. This is more efficient because it reduces the matrix dimension we have to deal with, which in turn reduces the numerical cost.

For example, the representation in Figure 99 consists of 12 edges while that of Figure 101 requires only 8. This savings are for each unit cell in the RIS and so multiplying it by the number of unit cells in an RIS will amount to huge savings in numerical computation.

9.2.1 *Initial Calculations*

Preliminary calculations of the transmission amplitudes as a function of the wave number k and the graph length is presented in Figure 102. The horizontal and the vertical axes represent k and l respectively, while the transmission from input lead to output lead $|S_{12}|^2$ is represented by the *colour* bar. In all cases, the constraint that $0 \leq kl \leq 2\pi$ is satisfied. Additionally $l \leq \lambda/2$, where λ is the wavelength of the propagating wave. In this specific example, I chose $\lambda = 100$ mm, but in general λ can be chosen to be arbitrary small. This means that the so-called *homogenisable* [114] RIS surface can be implemented.

From Figure 102, we can see that for any given wave number k (and hence frequency f), we can find a length l which transmits the impinging wave but suppresses waves of other frequencies. This way, we could implement the RIS to suppress interference from other users. We could also use the proposed model for security enhancement to prevent an eavesdropper from listening to transmitted "message".
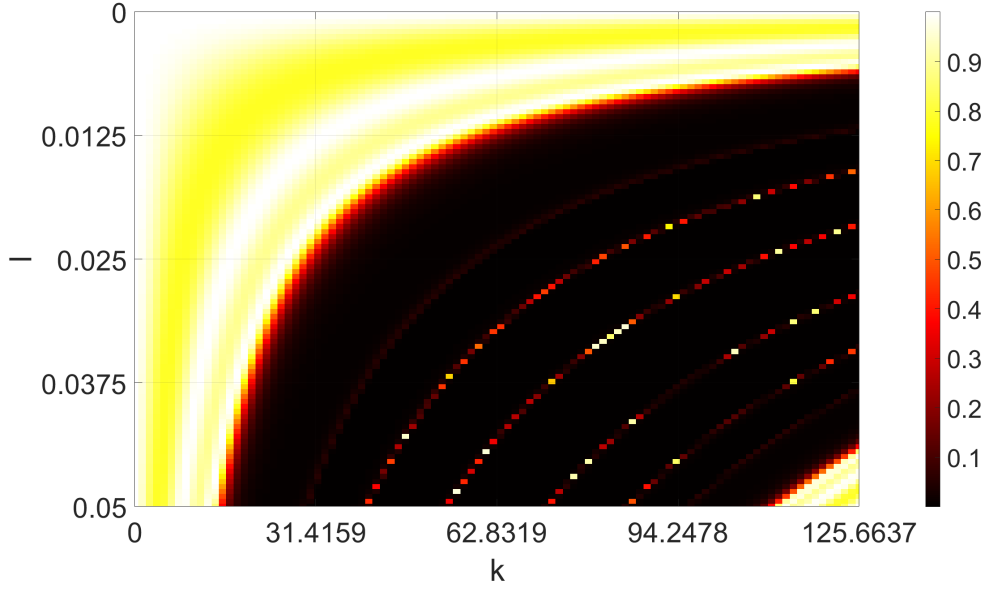
Figure 102.: Transmission power distribution for $0 \leq l \leq \lambda$ such that $0 \leq kl \leq 2\pi$, where $\lambda = 50$ mm.

The advantage of using quantum graph in this sense is that, unlike the dog-bone-shaped unit cell reported in [184] that require four degrees of freedom (and hence *four* variables to tweak for optimisation), the unit cells proposed here will require only one variable (i.e. *l*) for optimisation purposes. This significantly reduces the complexity of the optimisation problem that may be required if *joint-encoding* of the transmitter and the RIS is to be employed.

In each *super cell*, we may employ different arrangements of the building blocks and/or different edge lengths. This will be periodically repeated throughout the entire RIS surface.

A

In this appendix, we show the results of laboratory measurements that were not included in Chapter 5. The purpose of this appendix is to further buttress the point that the quantum graph model derived in Chapter 4 is useful for predicting the propagations microwaves in cable networks. We show two more examples of the graph model predictions compared with the laboratory measurements of real cable networks.

Figure 103(a) is the diagram of a cable network consisting of a single loop architecture. Care must be taken to include the extra cable length of 0.012 m introduced by the T-junction connector. The effective length of the main cable forming the loop is 2.014 m. The experimental results of the reflection coefficient, S_{11}, is shown in Figure 103(b) as the solid green curve. the blue curve is the graph model predictions.

Finally, we show the S_{11} results for a T-junction network, where all the three cables have different lengths. Figure 104(a) shows an illustration of the geometry and corresponding cable lengths of the underlying T-junction

(a) A single loop network

(b) S_{11} response for single loop network
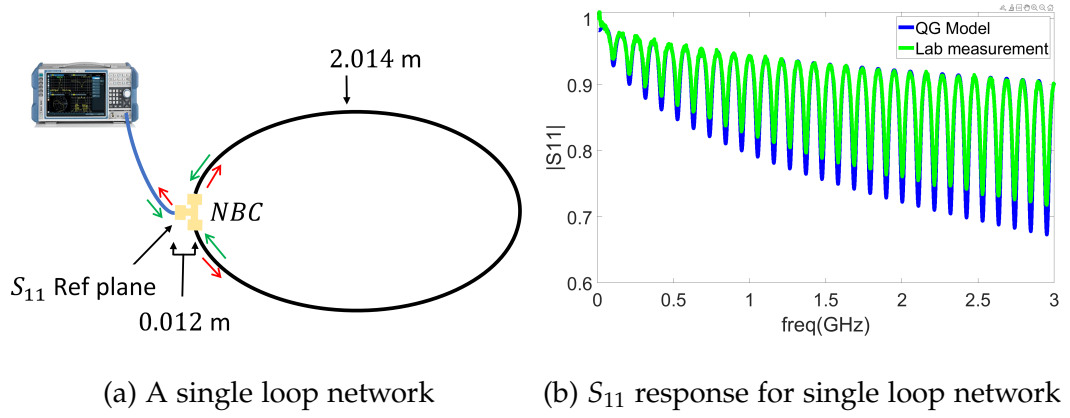
Figure 103.: Diagram and S_{11} response for a single loop network with cable lengths 0.012 m and 2.014 m.

network used in the laboratory, while Figure 104(b) shows the plot of $|S_{11}|$ against frequency up to 2 GHz. The graph model is able to predict even some of the minute details of the experimental results. We can therefore conclude that the graph model works well in predicting the propagation of high frequency waves in complex networks.

(a) T-junction network

(b) S_{11} response

Figure 104.: A schematic representation and a plot of $|S_{11}|$ for a T-junction network with cable lengths 0.3 m, 1.028 m, and 1.022 m.

BIBLIOGRAPHY

[1] B. Gentinne, J.-P. Eggermont, D. Flandre, and J.-P. Colinge, "Fully depleted soi-cmos technology for high temperature ic applications," *Materials Science and Engineering: B*, vol. 46, no. 1-3, pp. 1–7, 1997.
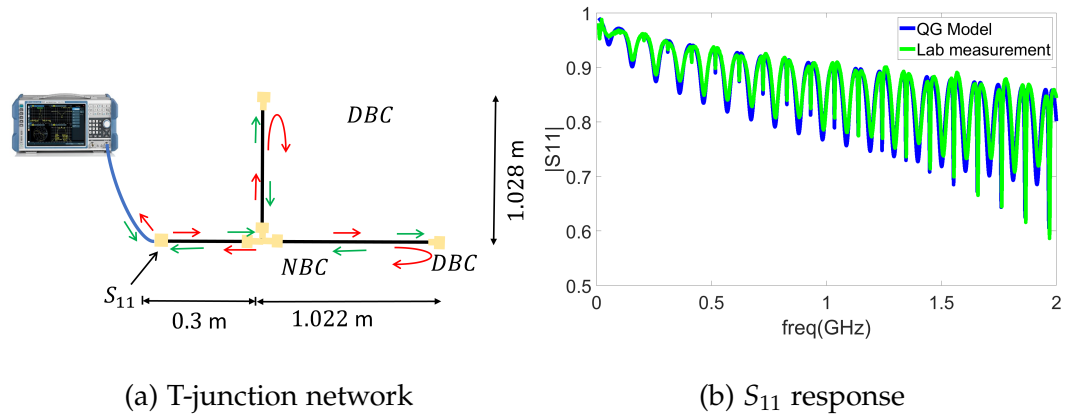
[2] J. B. McKitterick, G. Goetz, J. O'Connor, W. Maszara, and D. Boyko, "An soi smart-power solenoid driver for 300 c operation," in *Proceedings, Third International High Temperature Electronics Conference*, 1996.

[3] F. Kley, C. Lerch, and D. Dallinger, "New business models for electric cars—a holistic approach," *Energy policy*, vol. 39, no. 6, pp. 3392–3403, 2011.

[4] J. Stewart, "Uber's plan to launch flying cars in la by 2020 really could take off," https://www.wired.com/story/uber-flying-cars-los-angeles, july 2018.

[5] J. A. Hawkins, "Uber reportedly will sell its flying taxi business to secretive startup joby aviation," https://www.theverge.com/2020/12/2/22086597/uber-sells-flying-taxi-elevate-joby-aviation, december 2020.

[6] K. Pretz, "Ge aviation electrifies airplane engines to meet carbon emission goals," https://spectrum.ieee.org/the-institute/ieee-member-news/ge-aviation-electrifies-airplane-engines-to-meet-carbon-emission-goals, August 2019.

[7] C. T. U. Department of Measurement. (2019) Measurement and Monitoring of Energy Consumption in Aviation: Diagnostics and Detection of Degradations kernel description. [Online]. Available: https://meas.fel.cvut.cz/node/57

[8] E. M. Rogers, *Diffusion of innovations*. Simon and Schuster, 2010.

[9] P. Plötz, U. Schneider, J. Globisch, and E. Dütschke, "Who will buy electric vehicles? identifying early adopters in germany," *Transportation Research Part A: Policy and Practice*, vol. 67, pp. 96–109, 2014.

[10] K. Laurischkat, A. Viertelhausen, and D. Jandt, "Business models for electric mobility," *Procedia CIRP*, vol. 47, pp. 483–488, 2016.

[11] M. Hülsmann and D. Fornahl, *Evolutionary paths towards the mobility patterns of the future*. Springer, 2014.

[12] G. Wu, A. Inderbitzin, and C. Bening, "Total cost of ownership of electric vehicles compared to conventional vehicles: A probabilistic analysis and projection across market segments," *Energy Policy*, vol. 80, pp. 196–214, 2015.

[13] Davidson, "Rogers innovation adoption curve," www.davidsonwp.com/wp-content/uploads/2015/08/ Rogers-adoption-innovation-curve.png, july 2018.

[14] T. B. Forum, "Global fixed broadband subscribers exceed one billion," https://www.prnewswire.com/news-releases/ global-fixed-broadband-subscribers-exceed-one-billion-300735891. html, october 2018.

[15] D. Acatauassu, S. Höst, C. Lu, M. Berg, A. Klautau, and P. O. Börjesson, "Simple and causal copper cable model suitable for g. fast frequencies," *IEEE Transactions on Communications*, vol. 62, no. 11, pp. 4040–4051, 2014.

[16] I. ITU-T G, "9701 fast access to subscriber terminals (g. fast)—physical layer specification," *Recommendation ITU-T G.9701*, vol. 9701, 2019.

[17] D. Acatauassu, I. Almeida, F. Muller, A. Klautau, C. Lu, K. Ericson, and B. Dortschy, "Measurement and modeling techniques for the fourth generation broadband over copper," *Advance Topic In Measurement*, 2012.

[18] D. M. Pozar, *Microwave and RF design of wireless systems*. Wiley New Jersey, 2001.

[19] R. Collier, *Transmission lines: Equivalent circuits, electromagnetic theory, and photons*. Cambridge University Press, 2013.

[20] T. S. Rappaport, Y. Xing, O. Kanhere, S. Ju, A. Madanayake, S. Mandal, A. Alkhateeb, and G. C. Trichopoulos, "Wireless communications and applications above 100 ghz: Opportunities and challenges for 6g and beyond," *IEEE Access*, vol. 7, pp. 78 729–78 757, 2019.

[21] N. S. Perović, L.-N. Tran, M. Di Renzo, and M. F. Flanagan, "Achievable rate optimization for mimo systems with reconfigurable intelligent surfaces," *arXiv preprint arXiv:2008.09563*, 2020.

[22] V. Arun and H. Balakrishnan, "Rfocus: Beamforming using thousands of passive antennas," in *17th {USENIX} Symposium on Networked Systems Design and Implementation ({NSDI} 20)*, 2020, pp. 1047–1061.

[23] S. J. Orfanidis, *Electromagnetic waves and antennas*.   Rutgers University New Brunswick, NJ, 2002.

[24] J. Dobrowolski, *Microwave network design using the scattering matrix*. Artech House, 2010.

[25] W. R. Eisenstadt and Y. Eo, "S-parameter-based ic interconnect transmission line characterization," *IEEE transactions on components, hybrids, and manufacturing technology*, vol. 15, no. 4, pp. 483–490, 1992.

[26] L. N. Dworsky, *Modern transmission line theory and applications*.   Wiley, 1979.

[27] G. Images1, "Vector network analyser," https://www.google.com/ url?sa=i&rct=j&q=&esrc=s&source=images&cd=&cad=rja&uact=8&

ved=2ahUKEwi30JiRts7cAhVNQhoKHY4PAesQjRx6BAgBEAU&

url=https%3A%2F%2Fwww.testequity.com%2Fproducts%

2F34631%2F&psig=AOvVaw0FOyJAtQocHNkUdkmLoL44&ust=

1533301094077683, August 2018.

[28] L. Atzori, A. Iera, and G. Morabito, "The internet of things: A survey," *Computer networks*, vol. 54, no. 15, pp. 2787–2805, 2010.

[29] D. Giusto, A. Iera, G. Morabito, and L. Atzori, *The internet of things: 20th Tyrrhenian workshop on digital communications.* Springer Science & Business Media, 2010.

[30] P. M. Pontes, B. Lima, and J. P. Faria, "Izinto: a pattern-based iot testing framework," in *Companion Proceedings for the ISSTA/ECOOP 2018 Workshops*, 2018, pp. 125–131.

[31] Z. B. Drikas, J. G. Gil, S. K. Hong, T. D. Andreadis, J.-H. Yeh, B. T. Taddese, and S. M. Anlage, "Application of the random coupling model to electromagnetic statistics in complex enclosures," *IEEE Trans. Electromagn. Compat*, vol. 56, no. 6, pp. 1480–1487, 2014.

[32] X. Zheng, "Statistics of impedance and scattering matrices in microwave chaotic cavities: the random coupling model," Ph.D. dissertation, University of Maryland, 2005.

[33] X. Zheng, T. M. Antonsen, and E. Ott, "Statistics of impedance and scattering matrices in chaotic microwave cavities: Single channel case," *Electromagnetics*, vol. 26, no. 1, pp. 3–35, 2006.

[34] ——, "Statistics of impedance and scattering matrices of chaotic microwave cavities with multiple ports," *Electromagnetics*, vol. 26, no. 1, pp. 37–55, 2006.

[35] S. Hemmady, T. M. Antonsen, E. Ott, and S. M. Anlage, "Statistical prediction and measurement of induced voltages on components within complicated enclosures: A wave-chaotic approach," *IEEE Trans. Electromagn. Compat*, vol. 54, no. 4, pp. 758–771, 2012.

[36] S. Hemmady, X. Zheng, J. Hart, T. M. Antonsen Jr, E. Ott, and S. M. Anlage, "Universal properties of two-port scattering, impedance, and admittance matrices of wave-chaotic systems," *Physical Review E*, vol. 74, no. 3, p. 036213, 2006.

[37] S. D. Hemmady, "A wave-chaotic approach to predicting and measuring electromagnetic field quantities in complicated enclosures," Ph.D. dissertation, University of Maryland, 2006.

[38] G. Gradoni, J.-H. Yeh, B. Xiao, T. M. Antonsen, S. M. Anlage, and E. Ott, "Predicting the statistics of wave transport through chaotic cavities by the random coupling model: A review and recent progress," *Wave Motion*, vol. 51, no. 4, pp. 606–621, 2014.

[39] S. Gnutzmann‖ and U. Smilansky, "Quantum graphs: Applications to quantum chaos and universal spectral statistics," *Advances in Physics*, vol. 55, no. 5-6, pp. 527–625, 2006.

[40] T. Kottos and U. Smilansky, "Quantum chaos on graphs," *Physical review letters*, vol. 79, no. 24, p. 4794, 1997.

[41] T. Kottos and H. Schanz, "Quantum graphs: a model for quantum chaos," *Physica E: Low-dimensional Systems and Nanostructures*, vol. 9, no. 3, pp. 523–530, 2001.

[42] P. Exner, J. P. Keating, P. Kuchment, A. Teplyaev, and T. Sunada, *Analysis on Graphs and Its Applications: Isaac Newton Institute for Mathematical Sciences, Cambridge, UK, January 8-June 29, 2007*. American Mathematical Soc., 2008, vol. 77.

[43] M. Aizenman, R. Sims, and S. Warzel, "Fluctuation-based proof of the stability of ac spectra of," in *Quantum Graphs and Their Applications: Proceedings of an AMS-IMS-SIAM Joint Summer Research Conference on Quantum Graphs and Their Applications, June 19-23, 2005, Snowbird, Utah*, vol. 415. American Mathematical Soc., 2006, p. 1.

[44] G. Berkolaiko, "An elementary introduction to quantum graphs," *Geometric and Computational Spectral Theory*, vol. 700, p. 41, 2017.

[45] T. Kottos and U. Smilansky, "Periodic orbit theory and spectral statistics for quantum graphs," *Annals of Physics*, vol. 274, no. 1, pp. 76–124, 1999.

[46] L. Pauling, "The diamagnetic anisotropy of aromatic molecules," *The Journal of Chemical Physics*, vol. 4, no. 10, pp. 673–677, 1936.

[47] H. Kuhn, "Elektronengasmodell zur quantitativen deutung der lichtabsorption von organischen farbstoffen i," *Helvetica Chimica Acta*, vol. 31, no. 6, pp. 1441–1455, 1948.

[48] ——, "Quantenmechanische behandlung von farbstoffen mit verzweigtem elektronengas," *Helvetica Chimica Acta*, vol. 32, no. 7, pp. 2247–2272, 1949.

[49] J. R. Platt, "Classification of spectra of cata-condensed hydrocarbons," *The Journal of chemical physics*, vol. 17, no. 5, pp. 484–495, 1949.

[50] K. Ruedenberg and C. W. Scherr, "Free-electron network model for conjugated systems. i. theory," *The Journal of Chemical Physics*, vol. 21, no. 9, pp. 1565–1581, 1953.

[51] C. Coulson, "Note on the applicability of the free-electron network model to metals," *Proceedings of the Physical Society. Section A*, vol. 67, no. 7, p. 608, 1954.

[52] E. W. Montroll, "Quantum theory on a network. i. a solvable model whose wavefunctions are elementary functions," *Journal of Mathematical Physics*, vol. 11, no. 2, pp. 635–648, 1970.

[53] M. J. Richardson and N. Balazs, "On the network model of molecules and solids," *Annals of Physics*, vol. 73, no. 2, pp. 308–325, 1972.

[54] S. Alexander, "Superconductivity of networks. a percolation approach to the effects of disorder," *Physical Review B*, vol. 27, no. 3, p. 1541, 1983.

[55] C. Flesia, R. Johnston, and H. Kunz, "Strong localization of classical waves: a numerical study," *EPL (Europhysics Letters)*, vol. 3, no. 4, p. 497, 1987.

[56] J. Chalker and P. Coddington, "Percolation, quantum tunnelling and the integer hall effect," *Journal of Physics C: Solid State Physics*, vol. 21, no. 14, p. 2665, 1988.

[57] R. Klesse and M. Metzler, "Spectral compressibility at the metal-insulator transition of the quantum hall effect," *Physical review letters*, vol. 79, no. 4, p. 721, 1997.

[58] V. Kostrykin and R. Schrader, "Kirchhoff's rule for quantum wires," *Journal of Physics A: Mathematical and General*, vol. 32, no. 4, p. 595, 1999.

[59] T. Kottos and U. Smilansky, "Chaotic scattering on graphs," *Physical review letters*, vol. 85, no. 5, p. 968, 2000.

[60] ——, "Quantum graphs: a simple model for chaotic scattering," *Journal of Physics A: Mathematical and General*, vol. 36, no. 12, p. 3501, 2003.

[61] O. Hul, S. Bauch, P. Pakoński, N. Savytskyy, K. Życzkowski, and L. Sirko, "Experimental simulation of quantum graphs by microwave networks," *Physical Review E*, vol. 69, no. 5, p. 056205, 2004.

[62] M. Khalaj-Amirhosseini, "Closed form solutions for nonuniform transmission lines," *Progress In Electromagnetics Research*, vol. 2, pp. 243–258, 2008.

[63] S. Gnutzmann, U. Smilansky, and J. Weber, "Nodal counting on quantum graphs," *Waves in random media*, vol. 14, no. 1, pp. S61–74, 2004.

[64] S. Gnutzmann and A. Altland, "Universal spectral statistics in quantum graphs," *Physical review letters*, vol. 93, no. 19, p. 194101, 2004.

[65] ——, "Spectral correlations of individual quantum graphs," *Physical Review E*, vol. 72, no. 5, p. 056215, 2005.

[66] S. Gnutzmann, J. P. Keating, and F. Piotet, "Eigenfunction statistics on quantum graphs," *Annals of Physics*, vol. 325, no. 12, pp. 2595–2640, 2010.

[67] E. Akkermans, A. Comtet, J. Desbois, G. Montambaux, and C. Texier, "Spectral determinant on quantum graphs," *arXiv preprint cond-mat/9911183*, 1999.

[68] F. Barra and P. Gaspard, "On the level spacing distribution in quantum graphs," *Journal of Statistical Physics*, vol. 101, no. 1-2, pp. 283–319, 2000.

[69] ——, "Transport and dynamics on open quantum graphs," *Physical review E*, vol. 65, no. 1, p. 016205, 2001.

[70] H. Schanz and U. Smilansky, "Spectral statistics for quantum graphs: Periodic orbits and combinatories," *Philosophical Magazine B*, vol. 80, no. 12, pp. 1999–2021, 2000.

[71] P. Pakonski, K. Zyczkowski, and M. Kus, "Classical 1d maps, quantum graphs and ensembles of unitary matrices," *Journal of Physics A: Mathematical and General*, vol. 34, no. 43, p. 9303, 2001.

[72] P. Kuchment, "Quantum graphs: I. some basic structures," *Waves in Random media*, vol. 14, no. 1, pp. S107–128, 2004.

[73] ——, "Quantum graphs: Ii. some spectral properties of quantum and combinatorial graphs," *Journal of Physics A: Mathematical and General*, vol. 38, no. 22, p. 4887, 2005.

[74] ——, "Quantum graphs: an introduction and a brief survey," *arXiv preprint arXiv:0802.3442*, 2008.

[75] J. Boman and P. Kurasov, "Symmetries of quantum graphs and the inverse scattering problem," *Advances in Applied Mathematics*, vol. 35, no. 1, pp. 58–70, 2005.

[76] P. Kurasov and F. Stenberg, "On the inverse scattering problem on branching graphs," *Journal of Physics A: Mathematical and General*, vol. 35, no. 1, p. 101, 2001.

[77] P. Kurasov, G. Malenová, and S. Naboko, "Spectral gap for quantum graphs and their edge connectivity," *Journal of Physics A: Mathematical and Theoretical*, vol. 46, no. 27, p. 275309, 2013.

[78] P. Kurasov and S. Naboko, "Surgery of graphs and spectral gap: Titchmarsh-weyl operator-function approach," 2017.

[79] P. Kurasov, "Surgery of graphs: M-function and spectral gap." *Acta Physica Polonica, A.*, vol. 132, no. 6, 2017.

[80] ——, "Quantum graphs: spectral theory and inverse problems," *Journal of Spectral Theory*, 2018.

[81] R. Band, T. Shapira, and U. Smilansky, "Nodal domains on isospectral quantum graphs: the resolution of isospectrality?" *Journal of Physics A: Mathematical and General*, vol. 39, no. 45, p. 13999, 2006.

[82] R. Band, O. Parzanchevski, and G. Ben-Shach, "The isospectral fruits of representation theory: quantum graphs and drums," *Journal of Physics A: Mathematical and Theoretical*, vol. 42, no. 17, p. 175202, 2009.

[83] G. Dell'Antonio and L. Tenuta, "Quantum graphs as holonomic constraints," *Journal of mathematical physics*, vol. 47, no. 7, p. 072102, 2006.

[84] G. Tanner, "Unitary-stochastic matrix ensembles and spectral statistics," *Journal of Physics A: Mathematical and General*, vol. 34, no. 41, p. 8485, 2001.

[85] P. Exner and K. Nemcová, "Leaky quantum graphs: approximations by point-interaction hamiltonians," *Journal of Physics A: Mathematical and General*, vol. 36, no. 40, p. 10173, 2003.

[86] P. Exner and O. TUREK, "Approximations of singular vertex couplings in quantum graphs," *Reviews in Mathematical Physics*, vol. 19, no. 06, pp. 571–606, 2007.

[87] P. Exner, "Leaky quantum graphs: a review," *arXiv preprint arXiv:0710.5903*, 2007.

[88] P. Exner and J. Lipovskỳ, "Resonances from perturbations of quantum graphs with rationally related edges," *Journal of Physics A: Mathematical and Theoretical*, vol. 43, no. 10, p. 105301, 2010.

[89] S. A. Fulling, P. Kuchment, and J. H. Wilson, "Index theorems for quantum graphs," *Journal of Physics A: Mathematical and Theoretical*, vol. 40, no. 47, p. 14165, 2007.

[90] S. Fulling, L. Kaplan, and J. Wilson, "Vacuum energy and repulsive casimir forces in quantum star graphs," *Physical review A*, vol. 76, no. 1, p. 012118, 2007.

[91] J. Harrison, U. Smilansky, and B. Winn, "Quantum graphs where back-scattering is prohibited," *Journal of Physics A: Mathematical and Theoretical*, vol. 40, no. 47, p. 14181, 2007.

[92] U. Smilansky, "Irreversible quantum graphs," *Waves in Random Media*, vol. 14, no. 1, pp. S143–154, 2004.

[93] ——, "Quantum chaos on discrete graphs," *Journal of Physics A: Mathematical and Theoretical*, vol. 40, no. 27, p. F621, 2007.

[94] J. Bolte and S. Endres, "The trace formula for quantum graphs with general self adjoint boundary conditions," in *Annales Henri Poincaré*, vol. 10, no. 1.   Springer, 2009, pp. 189–223.

[95] T. Cheon, P. Exner, and O. Turek, "Approximation of a general singular vertex coupling in quantum graphs," *Annals of Physics*, vol. 325, no. 3, pp. 548–578, 2010.

[96] E. B. Davies, P. Exner, and J. Lipovskỳ, "Non-weyl asymptotics for quantum graphs with general coupling conditions," *Journal of Physics A: Mathematical and Theoretical*, vol. 43, no. 47, p. 474013, 2010.

[97] E. B. Davies and A. Pushnitski, "Non-weyl resonance asymptotics for quantum graphs," *Analysis & PDE*, vol. 4, no. 5, pp. 729–756, 2012.

[98] L. Erdős and H.-T. Yau, "Universality of local spectral statistics of random matrices," *Bulletin of the American Mathematical Society*, vol. 49, no. 3, pp. 377–414, 2012.

[99] A. Hussein, D. Krejčiřík, and P. Siegl, "Non-self-adjoint graphs," *Transactions of the American Mathematical Society*, vol. 367, no. 4, pp. 2921–2957, 2015.

[100] M. Ławniczak, O. Hul, S. Bauch, and L. Sirko, "Experimental simulation of quantum graphs by microwave networks-closed and open systems," *Chaotic Modeling and Simulation*, vol. 1, p. 105, 2011.

[101] M. Ławniczak, S. Bauch, V. Yunko, M. Białous, J. Wrochna, and L. Sirko, "Investigation of the wigner reaction matrix of microwave networks simulating quantum graphs with broken time reversal symmetry-one-port investigation," *Acta Physica Polonica, A.*, vol. 136, no. 5, 2019.

[102] M. Ławniczak, J. Lipovskỳ, S. Bauch, and L. Sirko, "Unexpected properties of open quantum graphs and microwave networks," in *Chaotic Modeling and Simulation International Conference*.   Springer, 2019, pp. 181–191.

[103] V. Ivrii, "100 years of weyl's law," *Bulletin of Mathematical Sciences*, vol. 6, no. 3, pp. 379–452, 2016.

[104] Z. Pluhař and H. A. Weidenmüller, "Universal chaotic scattering on quantum graphs," *Physical review letters*, vol. 110, no. 3, p. 034101, 2013.

[105] C. W. Beenakker, "Random-matrix theory of quantum transport," *Reviews of modern physics*, vol. 69, no. 3, p. 731, 1997.

[106] A. M. Tulino, S. Verdú *et al.*, "Random matrix theory and wireless communications," *Foundations and Trends® in Communications and Information Theory*, vol. 1, no. 1, pp. 1–182, 2004.

[107] U. Smilansky, "Delay-time distribution in the scattering of time-narrow wave packets.(i)," *Journal of Physics A: Mathematical and Theoretical*, vol. 50, no. 21, p. 215301, 2017.

[108] U. Smilansky and H. Schanz, "Delay-time distribution in the scattering of time-narrow wave packets (ii)—quantum graphs," *Journal of Physics A: Mathematical and Theoretical*, vol. 51, no. 7, p. 075302, 2018.

[109] E. P. Wigner, "Lower limit for the energy derivative of the scattering phase shift," *Physical Review*, vol. 98, no. 1, p. 145, 1955.

[110] F. T. Smith, "Lifetime matrix in collision theory," *Physical Review*, vol. 118, no. 1, p. 349, 1960.

[111] S. C. Brewer, "Wave propagation and complexity: A transfer operator approach," Ph.D. dissertation, University of Nottingham, 2018.

[112] A. Drinko, F. Andrade, and D. Bazeia, "Simple quantum graphs proposal for quantum devices," *The European Physical Journal Plus*, vol. 135, no. 6, p. 451, 2020.

[113] N. DOCOMO, "Docomo conducts world's first successful trial of transparent dynamic metasurface," 2020.

[114] G. Gradoni and M. Di Renzo, "End-to-end mutual-coupling-aware communication model for reconfigurable intelligent surfaces: An electromagnetic-compliant approach based on mutual impedances," *arXiv preprint arXiv:2009.02694*, 2020.

[115] G. Berkolaiko and P. Kuchment, *Introduction to quantum graphs.* American Mathematical Soc., 2013, no. 186.

[116] S. Hemmady, X. Zheng, E. Ott, T. M. Antonsen, and S. M. Anlage, "Universal impedance fluctuations in wave chaotic systems," *Physical review letters*, vol. 94, no. 1, p. 014102, 2005.

[117] D. Lu and T. Wu, "The zero-divisor graphs of posets and an application to semigroups," *Graphs and Combinatorics*, vol. 26, no. 6, pp. 793–804, 2010.

[118] R. Nikandish and F. Shaveisi, "On the structure of compact graphs," *Opuscula Mathematica*, vol. 37, no. 6, 2017.

[119] A. Duca, "Bilinear quantum systems on compact graphs: well-posedness and global exact controllability," *arXiv preprint arXiv:1710.06022*, 2017.

[120] B. Basavanagoud, V. R. Desai, and S. Patil, "(β, α)- connectivity index of graphs," *Applied Mathematics and Nonlinear Sciences*, vol. 2, no. 1, pp. 21–30, 2017.

[121] G. Caporossi, I. Gutman, P. Hansen, and L. Pavlović, "Graphs with maximum connectivity index," *Computational Biology and Chemistry*, vol. 27, no. 1, pp. 85–90, 2003.

[122] H. S. Ramane and A. S. Yalnaik, "Status connectivity indices of graphs and its applications to the boiling point of benzenoid hydrocarbons,"

Journal of Applied Mathematics and Computing, vol. 55, no. 1-2, pp. 609–627, 2017.

[123] S. Gupta, M. Singh, and A. Madan, "Application of graph theory: Relationship of eccentric connectivity index and wiener's index with anti-inflammatory activity," *Journal of Mathematical Analysis and Applications*, vol. 266, no. 2, pp. 259–268, 2002.

[124] M. Binu, S. Mathew, and J. N. Mordeson, "Connectivity index of a fuzzy graph and its application to human trafficking," *Fuzzy Sets and Systems*, vol. 360, pp. 117–136, 2019.

[125] P. L. Knight and W. E. Marshall, "The metrics of street network connectivity: their inconsistencies," *Journal of Urbanism: International Research on Placemaking and Urban Sustainability*, vol. 8, no. 3, pp. 241–259, 2015.

[126] C. Ducruet and J.-P. Rodrigue, "Graph theory: Measures and indices," https://transportgeography.org/?page_id=5981, May 2020.

[127] J.-P. Rodrigue, *The geography of transport systems*.   Taylor & Francis, 2020.

[128] M. Allgaier, S. Gehler, S. Barkhofen, H.-J. Stöckmann, and U. Kuhl, "Spectral properties of microwave graphs with local absorption," *Physical Review E*, vol. 89, no. 2, p. 022925, 2014.

[129] X. Zheng, S. Hemmady, T. M. Antonsen Jr, S. M. Anlage, and E. Ott, "Characterization of fluctuations of impedance and scattering matri-

ces in wave chaotic scattering," *Physical Review E*, vol. 73, no. 4, p. 046208, 2006.

[130] S. Hemmady, X. Zheng, T. M. Antonsen Jr, E. Ott, and S. M. Anlage, "Universal statistics of the scattering coefficient of chaotic microwave cavities," *Physical Review E*, vol. 71, no. 5, p. 056215, 2005.

[131] M. L. Mehta, *Random matrices*. Elsevier, 2004.

[132] C. Poli, G. A. Luna-Acosta, and H.-J. Stöckmann, "Nearest level spacing statistics in open chaotic systems: generalization of the wigner surmise," *Physical review letters*, vol. 108, no. 17, p. 174101, 2012.

[133] H.-J. Stöckmann, "Quantum chaos: an introduction," 2000.

[134] Y. V. Fyodorov and H.-J. Sommers, "Statistics of resonance poles, phase shifts and time delays in quantum chaotic scattering: Random matrix approach for systems with broken time-reversal invariance," *Journal of Mathematical Physics*, vol. 38, no. 4, pp. 1918–1981, 1997.

[135] H. Weyl, "The asymptotic distribution law for the eigenvalues of linear partial differential equations (with applications to the theory of black body radiation)," *Math. Ann*, vol. 71, no. 1, pp. 441–479, 1912.

[136] C. Smartt, S. Greedy, D. Thomas, C. Christopoulos, and P. Sewell, "Shielded cable model development for time domain cem techniques," in *IET 8th International Conference on Computation in Electromagnetics (CEM 2011)*. IET, 2011, pp. 1–2.

[137] J. Paul, C. Christopoulos, D. W. Thomas, and X. Liu, "Time-domain modeling of electromagnetic wave interaction with thin-wires using tlm," *IEEE transactions on electromagnetic compatibility*, vol. 47, no. 3, pp. 447–455, 2005.

[138] A. J. Wlodarczyk, V. Trenkic, R. A. Scaramuzza, and C. Christopoulos, "A fully integrated multiconductor model for tlm," *IEEE Transactions on Microwave Theory and Techniques*, vol. 46, no. 12, pp. 2431–2437, 1998.

[139] J. Paul, C. Christopoulos, and D. W. Thomas, "Correction to" time-domain modeling of electromagnetic wave interaction with thin-wires using tlm"[aug 05 447-455]," *IEEE Transactions on Electromagnetic Compatibility*, vol. 50, no. 2, pp. 450–451, 2008.

[140] P. Russer, *Electromagnetics, microwave circuit and antenna design for communications engineering*.   Artech House, 2003.

[141] O. U. Guide, "Set up measurements," http://na.support.keysight.com/vna/help/latest/S1_Settings/Select_a_Measurement_State.htm, july 2020.

[142] G. Andrieu, N. Ticaud, F. Lescoat, and L. Trougnou, "Fast and accurate assessment of the "well stirred condition" of a reverberation chamber from s_{11} measurements," *IEEE Transactions on Electromagnetic Compatibility*, vol. 61, no. 4, pp. 974–982, 2018.

[143] L. Bastianelli, F. Moglie, G. Gradoni, and V. M. Primiani, "Full wave computation of the electromagnetic field in chaotic reverberation chambers," in *2019 International Conference on Electromagnetics in Advanced Applications (ICEAA)*. IEEE, 2019, pp. 1104–1106.

[144] J. W. Cook, R. H. Kirkby, M. G. Booth, K. T. Foster, D. E. Clarke, and G. Young, "The noise and crosstalk environment for adsl and vdsl systems," *IEEE Communications Magazine*, vol. 37, no. 5, pp. 73–78, 1999.

[145] Y. Jiang, J. Li, and W. W. Hager, "Uniform channel decomposition for mimo communications," *IEEE Transactions on Signal Processing*, vol. 53, no. 11, pp. 4283–4294, 2005.

[146] G. J. Foschini and M. J. Gans, "On limits of wireless communications in a fading environment when using multiple antennas," *Wireless personal communications*, vol. 6, no. 3, pp. 311–335, 1998.

[147] J. R. Pierce and E. C. Posner, *Introduction to communication science and systems*. Springer Science & Business Media, 2013.

[148] R. M. Fano and D. Hawkins, "Transmission of information: A statistical theory of communications," *American Journal of Physics*, vol. 29, pp. 793–794, 1961.

[149] R. G. Gallager, *Information theory and reliable communication*. Springer, 1968, vol. 2.

[150] B. Sklar, "Rayleigh fading channels in mobile digital communication systems. i. characterization," *IEEE Communications magazine*, vol. 35, no. 7, pp. 90–100, 1997.

[151] C. L. Holloway, H. A. Shah, R. J. Pirkl, W. F. Young, D. A. Hill, and J. Ladbury, "Reverberation chamber techniques for determining the radiation and total efficiency of antennas," *IEEE transactions on antennas and propagation*, vol. 60, no. 4, pp. 1758–1770, 2012.

[152] G. Gradoni, T. M. Antonsen, E. Ott *et al.*, "Impedance and power fluctuations in linear chains of coupled wave chaotic cavities," *Physical Review E*, vol. 86, no. 4, p. 046204, 2012.

[153] meraki, "Signal-to-noise ratio (snr) and wireless signal strength," https://documentation.meraki.com/MR/WiFi_Basics_and_Best_ Practices/Signal-to-Noise_Ratio_(SNR)_and_Wireless_Signal_ Strength, April 2020.

[154] H. S. Wang and P.-C. Chang, "On verifying the first-order markovian assumption for a rayleigh fading channel model," *IEEE Transactions on Vehicular Technology*, vol. 45, no. 2, pp. 353–357, 1996.

[155] J. Boutros and E. Viterbo, "Signal space diversity: a power-and bandwidth-efficient diversity technique for the rayleigh fading channel," *IEEE Transactions on Information theory*, vol. 44, no. 4, pp. 1453–1467, 1998.

[156] C. C. Tan and N. C. Beaulieu, "On first-order markov modeling for the rayleigh fading channel," *IEEE Transactions on Communications*, vol. 48, no. 12, pp. 2032–2040, 2000.

[157] M. Lapointe, A. Vareljian, and R. Badalone, "Fully adaptive equalization for high loss communications channels," May 10 2011, uS Patent 7,940,839.

[158] R. Payne, P. Landman, B. Bhakta, S. Ramaswamy, S. Wu, J. D. Powers, M. U. Erdogan, A.-L. Yee, R. Gu, L. Wu *et al.*, "A 6.25-gb/s binary transceiver in 0.13-/spl mu/m cmos for serial data transmission across high loss legacy backplane channels," *IEEE Journal of Solid-State Circuits*, vol. 40, no. 12, pp. 2646–2657, 2005.

[159] A. Perrig, R. Canetti, J. D. Tygar, and D. Song, "Efficient authentication and signing of multicast streams over lossy channels," in *Proceeding 2000 IEEE Symposium on Security and Privacy. S&P 2000.* IEEE, 2000, pp. 56–73.

[160] G. Ginis and J. M. Cioffi, "Vectored transmission for digital subscriber line systems," *IEEE Journal on selected areas in communications*, vol. 20, no. 5, pp. 1085–1104, 2002.

[161] A. Tarantola, "The next generation of dsl can pump 1gbps through copper phone lines," https://gizmodo.com/the-next-generation-of-dsl-can-pump-1gbps-through-coppe-1484256467, december 2013.

[162] P. S. Chow and J. M. Cioffi, "A multi-drop in-house adsl distribution network," in *Proceedings of ICC/SUPERCOMM'94-1994 International Conference on Communications*. IEEE, 1994, pp. 456–460.

[163] T. Regan, "Adsl line driver/receiver design guide," *Part l/II, Linear Technology, 2OOO*, vol. 10, no. 1.

[164] V. Oksman, H. Schenk, A. Clausen, J. M. Cioffi, M. Mohseni, G. Ginis, C. Nuzman, J. Maes, M. Peeters, K. Fisher *et al.*, "The itu-t's new g. vector standard proliferates 100 mb/s dsl," *IEEE Communications Magazine*, vol. 48, no. 10, pp. 140–148, 2010.

[165] K. B. Song, S. T. Chung, G. Ginis, and J. M. Cioffi, "Dynamic spectrum management for next-generation dsl systems," *IEEE Communications Magazine*, vol. 40, no. 10, pp. 101–109, 2002.

[166] R. Cendrillon and M. Moonen, "Iterative spectrum balancing for digital subscriber lines," in *IEEE International Conference on Communications, 2005. ICC 2005. 2005*, vol. 3. IEEE, 2005, pp. 1937–1941.

[167] R. B. Moraes, B. Dortschy, A. Klautau, and J. R. i Riu, "Semiblind spectrum balancing for dsl," *IEEE Transactions on Signal Processing*, vol. 58, no. 7, pp. 3717–3727, 2010.

[168] R. van den Brink, "Enabling 4gbb via hybrid-ftth, the missing link in ftth scenarios," *Proc. BBF*, pp. 1–33, 2010.

[169] M. Jackson, "G.fast broadband gets commercial uk launch by openreach," https://www.ispreview.co.uk/index.php/2020/03/g-fast-broadband-gets-commercial-uk-launch-by-openreach.html, march 2020.

[170] N. Owano, "Alcatel-lucent sets broadband speed record using copper," https://techxplore.com/news/2014-07-alcatel-lucent-broadband-copper.html, july 2014.

[171] B. Matt, "Researchers get record broadband speeds out of old-school copper wire," https://www.engadget.com/2014-07-10-alcatel-lucent-broadband-copper-world-record.html, july 2014.

[172] J. W. Cook, "Parametric modeling of twisted pair cables for vdsl," *ETSI contribution TD22, Vienna, Austria*, 1996.

[173] W. Y. Chen, *DSL: Simulation Techniques and Standards Development for Digital Subscriber Lines*. Alpel Publishing, 1997.

[174] P. Boets and L. Van Biesen, "Metallic 2-wire parametric line models—a survey," in *XVIII Imeko World Congress*, 2006.

[175] T. Magesacher, J. R. i Riu, M. Jakovljević, M. Loiola, P. Ödling, and P. O. Börjesson, "Measurement and modeling of short copper cables for ultra-wideband communication," in *Broadband Access Communication Technologies*, vol. 6390. International Society for Optics and Photonics, 2006, p. 639006.

[176] F. Lindqvist, P. O. Börjesson, P. Ödling, S. Höst, K. Ericson, and T. Magesacher, "Low-order and causal twisted-pair cable modeling by means of the hilbert transform," in *AIP Conference Proceedings*, vol. 1106, no. 1. American Institute of Physics, 2009, pp. 301–310.

[177] D. Acatauassu, S. Höst, C. Lu, M. Berg, A. Klautau, and P. O. Börjesson, "Simple and causal twisted-pair channel models for g. fast systems," in *2013 IEEE Global Communications Conference (GLOBECOM)*. IEEE, 2013, pp. 2834–2839.

[178] R. Van Den Brink and B. Van Den Heuvel, "G. fast: Wideband modeling of twisted pair cables as two-ports," *ITU-T SG15 Q4 Contrib. 11GS3-028*, 2011.

[179] N. Yu, P. Genevet, M. A. Kats, F. Aieta, J.-P. Tetienne, F. Capasso, and Z. Gaburro, "Light propagation with phase discontinuities: generalized laws of reflection and refraction," *science*, vol. 334, no. 6054, pp. 333–337, 2011.

[180] V. Arun and H. Balakrishnan, "Rfocus: Practical beamforming for small devices," *arXiv preprint arXiv:1905.05130*, 2019.

[181] R. Karasik, O. Simeone, M. Di Renzo, and S. S. Shitz, "Beyond max-snr: Joint encoding for reconfigurable intelligent surfaces," in *2020 IEEE International Symposium on Information Theory (ISIT)*. IEEE, 2020, pp. 2965–2970.

[182] F. H. Danufane, M. Di Renzo, J. de Rosny, and S. Tretyakov, "On the path-loss of reconfigurable intelligent surfaces: An approach based on green's theorem applied to vector fields," *arXiv preprint arXiv:2007.13158*, 2020.

[183] X. Qian, M. Di Renzo, J. Liu, A. Kammoun, and M.-S. Alouini, "Beamforming through reconfigurable intelligent surfaces in single-user mimo systems: Snr distribution and scaling laws in the presence of channel fading and phase noise," *arXiv preprint arXiv:2005.07472*, 2020.

[184] M. Di Renzo, A. Zappone, M. Debbah, M.-S. Alouini, C. Yuen, J. de Rosny, and S. Tretyakov, "Smart radio environments empowered by reconfigurable intelligent surfaces: How it works, state of research, and road ahead," *arXiv preprint arXiv:2004.09352*, 2020.